Université du Québec
Institut National de la Recherche Scientifique
Centre Energie Matériaux Télécommunications

Energy-Efficient Reconfigurable Intelligent Surfaces Aided Wireless Information and Power Transfer

by

Zina Mohamed

A dissertation submitted in partial fulfillment of the requirements for the degree of
Doctor of Philosophy in Telecommunications

Evaluation Jury

External examiner:	Dr. Amine Maaref Huawei Technologies Canada
External examiner:	Prof. Benoit Champagne McGill University
Internal examiner:	Prof. Leszek Szczecinski INRS, Université du Québec
Research supervisor:	Prof. Sonia Aïssa INRS, Université du Québec

Abstract

Recently, reconfigurable intelligent surfaces (RIS) have attracted great attention from both industry and academia as a potential solution to path loss, shadowing, and multipath effects and a promising technology to enhance future network performances. RIS are planar arrays, consisting of nearly passive and low-cost reflecting elements, that control the propagation environment by reflecting the incident signal in a special direction by properly designing and adjusting the phase shift values of the reflecting elements. This dissertation aims to design a framework for RIS-aided wireless information and power transfer. We focus on assessing, designing, and enhancing the energy efficiency (EE) and reliability for different kinds of systems: wireless power transfer (WPT), wireless information transfer (WIT), and simultaneous wireless information and power transfer (SWIPT) systems. In particular, in the first part of this work, a cooperative RIS-aided WPT system with high efficiency is designed. As a starting point, we exploit the potential of cooperative energy beamforming, and we develop a design framework for a cooperative WPT system. Specifically, we focus on improving the efficiency of transmission by addressing the most important metrics characterizing the system's performance, i.e., the WPT coverage probability and data transmission probability. The developed framework and design are then extended to the case of multiple RIS-aided WPT system. In the second part of this work, we focus on designing an energy-efficient RIS-aided WIT system for cell edge users. Particularly, we focus on designing the optimal solution in order to maximize the EE for two deployment scenarios: the single service or unicast and multiple services or the joint broadcast unicast. In the third part of this work, we focus on the design of the RIS-aided SWIPT system based on the null space. The main objective of this part is to achieve a balance between the harvested energy at energy receivers and the sum-rate of the information receivers. A framework to evaluate and optimize a multi-objective function taking into account the total harvested energy and the sum-rate, is proposed.

Chapter 1 introduces the state of the art of the RIS technology focusing on comparisons with relaying technology, the optimization oriented works, channel estimation, RIS design and applications, and the limitations and challenges. On the other hand, the concept and the challenges of the wireless information and power transfer are also presented.

The first part of this dissertation is about designing a cooperative RIS-aided WPT. In particular, stochastic geometry tools to model the Poisson point process (PPP) distributed network nodes (access points (APs), device, RIS) and to determine the closed-form expressions of the WPT coverage probability and the data transmission probability for different types of devices are leveraged. The obtained expressions are a function of the extended generalized multivariate MeijerG function (EGMMGF). A new implementation of the EGMMGF is also presented. The proposed formulae in this part avoid most of the complexity and time-consumption issues already in the literature. The findings provide a guideline for deriving similar tractable formulas for different system models.

The second part of this dissertation is about designing an energy-efficient RIS-aided WIT for the cell-edge users for two deployment scenarios: the single service (unicast) and multi-service (joint broadcast-unicast). In particular, a UAV equipped with RIS is leveraged to assist the downlink and uplink communication. The main objective is to maximize the EE of the cell-edge users by properly designing the active and passive beamforming matrices. Optimal solutions to solve the optimization problems are presented. Numerical results show that significant performance enhancements are achieved by the RIS-UAV compared to its counterpart but with standard relaying techniques and validate that the RIS-UAV can be leveraged to serve cell-edge users with high EE. Moreover, a framework design for joint unicast-broadcast downlink communication assisted with an aerial dual-polarized RIS is proposed. Results show the superiority of leveraging polarization for the joint transmission of different kinds of traffic patterns.

Unlike parts I and II which only deal with WPT or WIT, part III of this dissertation explores the SWIPT system. More specifically, a framework design for RIS-aided SWIPT based on the degree of freedom provided by the null space of the composite channel matrix between the AP and the information receivers is proposed to send additional energy signals. The main objective is to achieve a balance between the harvested energy at the energy receivers and the sum-rate of the information receivers. Based on the multi-objective optimization framework and the weighted Tchebycheff approach, the equivalent sum-rate maximization problem is formulated first. Then, an efficient two-layer algorithm is proposed to design the active information beamforming vectors at the AP and the passive beamforming matrix at the RIS. The results of this part are novel and highlight the importance of integrating RIS and exploiting the null space while designing SWIPT systems.

Finally, chapter 9 concludes this dissertation and proposes future works.

Acknowledgment

First, I would like to show my gratitude for my supervisor, Prof. Sonia Aïssa, for her contribution to my life and career. She helped me set a clear direction to follow. I am also thankful to Fonds de Recherche du Québec Nature et technologies and Natural Sciences and Engineering Research Council of Canada for their financial support during this journey.

Second, my sincere appreciation goes to Prof. Benoit Champagne from McGill University, Dr. Amine Maaref from Huawei Technologies Canada, and Prof. Leszek Szczecinski from INRS, for honoring me by judging my work.

Finally, I would like to thank my parents for their support, love and prayers throughout my research years.

Contents

List of Figures

List of Abbreviations

5G Fifth Generation of Telecommunication

6G Sixth Generation of Telecommunication

A2G Air-to-Ground

AF Amplify-and-Forward

AP Access Point

AWGN Additive White Gaussian Noise

BS Base Station

CDF Cumulative Distribution Function

CoMP Coordinated Multiple Points

CoMPe Coordinated Multipoint Energy Beamforming

CSI Channel State Information

DC Direct Current

DF Decode-and-Forward

EE Energy Efficiency

EGMMGF extended generalized multivariate MeijerG function

EH Energy Harvesting

EM Electromagnetic

ER Energy Receiver

G2G Ground-to-Ground

IR Information Receiver

LDM Layered-Division Multiplexing

LoS Line-of-Sight

MGF Moment Generating Function

MIMO Multiple-Input Multiple-Output

MISO Multiple-Input Single-Output

MMSE Minimum Mean Square Error

MOO Multi-Objective Optimization

MRT Maximum Ratio Transmission

NLoS Non-Line-of-Sight

PB Power Beacon

PDF Probability Density Function

PS Power Splitting

QCQP Quadratically-Constraint Quadratic Problem

RF Radio Frequency

RIS Reconfigurable Intelligent Surfaces

SDP Semi-Definite Program

SDR Semi-Definite Relaxation

SE Spectral Efficiency

SINR Signal-to-Interference-Plus-Noise Ratio

SVD Singular Value Decomposition

SWIPT Simultaneous Wireless Information and Power Transfer

TS Time Switching

UAV Unmanned Aerial Vehicles

WIPT Wireless Information and Power Transfer

WIT Wireless Information Transfer

WPCN Wireless Powered Communication Network

WPT Wireless Power Transfer

XPD Cross-Polar Discrimination

ZF Zero Forcing

Chapter 1

Introduction and Objectives

1.1 Introduction to RIS

1.1.1 Scope and Motivation

Nowadays, with the development of technologies, the next-generation wireless networks will convey numerous applications and conveniences to make lives easier, smoother, and more comfortable with better quality of service (QoS), lower costs, and complexity [1]. The researches show that 6G communications are intended to provide massive connectivity, larger coverage, higher throughput, enhanced capacity, higher reliability, and low latency through its use cases of machine-type communications, ultra-reliable and low-latency communication (uRLLC), extremely low-power communications and long-distance and high-mobility communications.

To meet the stringent requirements of the device connectivity which is expected to be larger than 107 devices/km2; the reliability which is intended to be higher than 99.9999%, the latency which is expected to be smaller than 0.1 ms; the data rate that will be higher than 1 Tb/s and the energy efficiency that is expected to be 10 to 100 times higher than that of 5G [1–3], researches have been proliferated. In particular, the focus has been directed to the connectivity interruptions caused by the randomness of the communication environment, i.e., wireless channels, path loss, shadowing effects, and blockage (obstacles). As a solution, deploying more base stations (BSs), more antennas at the BS, or the use of more spectrum were proposed to deal with these limitations.

However, these techniques result in high power consumption, high deployment and maintenance costs, and high signal processing complexity. Hence, the main research goal has been turned to the design of sophisticated techniques at the transmitter and the receiver to compensate for the propagation's effects, and to turn the propagation environment itself into an optimization variable, i.e., the creation of a smart radio environment. Among the cost-effective emerging technologies, reconfigurable intelligent surface (RIS) has received widespread interest from both the industry and academia as a promising technology for low-cost, agile, and intelligent communications [4].

1.1.2   Potentials of RIS

RIS also comes under other names, such as large intelligent surface (LIS) [3,5], intelligent walls [6], software-controlled meta-surfaces [7,8]. Generally speaking, RIS is a digitally-controlled metasurface with massive nearly passive, and low-cost reflecting elements, with unique capabilities enabling the communication means to be reconfigurable, and the entire radio environment to be intelligent. In particular, by reconfiguring the impinging radio waves in real-time and by manipulating their EM characteristics, specific functions such as wave steering, blocking, splitting, polarizing, creating a virtual line-of-sight (LoS) link, adding extra signal paths towards desired directions, refining the channel statistics/distribution [9–11] can be fulfilled.

The elements of the RIS are a highly energy-efficient unit as they do not consume any power for amplification and/or transmission [4,12], and they only require minimal signal processing capabilities to configure the phase shifts and amplitude of reflecting elements. Furthermore, RIS are introduced as a new player in the whole communication process that may provide several solutions for the limitations of the random wireless channel and the requirements of the emerging new applications. By turning the wireless environment into a controllable block system, the performance of the communication network including enlarging the coverage and improving the transmission robustness, the spectrum efficiency and EE [11], is enhanced.

To summarize RIS has come to the forefront with the following distinguishable features that made it a key technology in future wireless communications:

- Nearly passive reflecting elements: the RIS elements are assumed to be perfect reflectors, i.e., they do not comprise any active converters (analog-to-digital/digital-to-analog) and/or power amplifiers, and they operate in the full-duplex mode.

- The reflecting elements, a.k.a., meta-atoms, reconfigure and modify the overall impedance of the surface, thus manipulating the impinging EM wave and achieving polarization control or beam-steering.

- RIS can work at high-frequency bands such as mmWave and Terahertz (THz). Therefore, RIS can be used to mitigate the blockage effects and the high penetration losses [11], which are judged to be more severe at high frequencies. This feature is very important for future communication networks.

- Easy deployment and implementation: RIS are intended to be deployed on the facades of buildings, ceilings of factories, aerial platforms, and indoor spaces.

1.1.3   State of the Art

As aforementioned, RIS are considered as a promising technology for future wireless networks and have spurred extensive research. It is worth pointing out that several articles have appeared in the literature providing an overview of the recent research works on RIS such as implementation, design, channel modeling and estimation, etc. [4, 7, 13]. In this section, the state-of-the-art, focusing on comparisons with relaying technology, optimization, channel estimation, and RIS design is reviewed. The challenges and limitations of this technology are also presented.

Comparison with Relaying

RIS are very promising to fill the gap in the area of relay-assisted wireless systems by responding to the question of achieving full-duplex relaying with low power consumption. In the literature, two types of relays are considered: transparent and non-transparent relays [14]. For instance, the former re-transmits the signals after amplification, e.g., amplify-and-forward (AF) relays, however, the latter re-transmits the signals after regeneration, e.g., decode-and-forward (DF) relays. It is noteworthy that classical active relays usually operate in half-duplex, i.e., re-transmission and reception of signals are separated temporally whereas the RIS operate in full-duplex since they

re-transmit the signal without generating new radio signals or amplification. Researchers focused on comparing the performance gains of the RIS-assisted systems and the relaying-assisted systems. In fact, the most notable works are presented in [3, 15]. For instance, [15] compared the achievable EE of RIS-aided system and its counterpart based on the AF relaying. This work showed that the RIS-aided system achieves higher EE as compared to AF. This can be explained by the fact that received signal strengths are enhanced without using power amplifiers, but by appropriate phase-shift design in the case of RIS-aided communications. Another meaningful comparison between the RIS-aided system and the DF relaying was presented in [3] and showed that the RIS-based system needs a large number of reflecting elements to remain competitive with DF relaying technology.

Reflecting Element modeling

Designing the RIS elements model is one of the most important research directions. In this regard, a paucity of papers has appeared recently to propose different methods and designs. In particular, circuits/models based on loading PIN diodes [16], varactor diodes [17], micro-electromechanical system (MEMS) switches [18] and liquid crystal [19] were proposed. Few comparisons between these designs have been conducted and showed that the MEMS switches outperform the PIN diodes in the mmWave band [18].

Performance Analysis and Optimization

It is of capital importance to investigate the performance analysis of the RIS-aided systems in terms of achievable capacity, SE, sum-rate, harvested power, coverage, and EE, which are nowadays widely recognized as essential metrics in system design. Very limited theoretical works have been carried out to perform system performance analysis in the literature [20, 21].

On the other hand, maximizing some utilities, such as EE [22], SE [21] and the received power [15, 23], by designing the RIS phase shifts values, the active beamforming and the optimal power allocation matrices based on conventional optimization techniques are extensively explored in the literature. In fact, designing RIS phase-shift matrix has been studied in [15, 24, 25] where the proposed solutions are based on the semi-definite relaxation (SDR). Moreover, authors in [15, 24, 26] focused on jointly optimizing transmit beamforming matrix at the BS and the phase-shift ma-

trix at the RIS to meet certain goals, such as maximizing the EE [15], maximizing minimum user SINR [24], [25] sum-rates or minimize transmit power [26] while satisfying some quality of service (QoS) constraints. Most of the previous works are solved based on alternating optimization techniques based on matrix decomposition methods, zero-forcing techniques (ZF), the Minimum mean square error (MMSE), SDR, etc.

Although conventional optimization techniques ensure optimal and/or near-optimal solutions, they are time-consuming and need complex structures. To deal with this, machine learning appears as a promising solution [27–31], as it is based on self-supervised learning and outperforms the existing limits of matrix decomposition methods, the non-convexity of the optimization problem and the calculation complexity. For instance, deep learning and deep reinforcement learning techniques consider the wireless propagation environment as a deep neural network, where RIS units are neurons and their cross-interactions are links. After the training phase, the source (BS or AP) learns the propagation basics of RISs and configures them to the optimal settings.

Channel Estimation

Most existing works on RIS-aided communication assume perfect channel state information (CSI) available at the BS and the RIS, which is an impractical assumption. One big challenge is the inability of the RIS to estimate the channel or to assist the estimation process by transmitting pilot symbols. This issue is due to the passivity of the RIS elements. Hereafter, we report some of the proposed works in this field [2, 22, 24, 32–34]. For instance, the pioneering work presented in [35] is the first estimation protocol for a single-user RIS-assisted MISO system, known as the ON/OFF protocol. In this work, all RIS-assisted links are estimated one-by-one by serially turning one element ON while keeping the others OFF. This protocol was significantly improved in terms of the normalized mean squared error (NMSE) performance in [36] for a single-user system and in [24] for a multi-user system. Most of the above works require optimal values for RIS phase shifts, which resulted in an increase in the training overhead. To deal with this, [37] introduced the idea of grouping adjacent RIS elements into sub-surfaces, then performing the estimation using the maximum likelihood approach.

1.1.4 Challenges of RIS

Despite the distinctive potentials of RIS that make it involved in a wide range of applications for indoor/outdoor communications, smart cities, and the internet of things (IoT) in general, they introduce important design challenges, where the most important are:

Accurate Physical Models

As previously mentioned, designing an accurate model for the RIS elements is very important for system performance analysis. Actually, most of the current models that describe RISs as a function of their EM properties suffer from a lack of accuracy and tractability since they rely on the assumption that the RIS acts as a perfect reflector. However, RISs can do functions other than reflection, such as polarization and transmission [38]. Moreover, their response to the incident radio waves leans on many other parameters such as the angle of incidence, the angle of reflection, the angle of refraction, the polarization state, and the fabrication materials. Therefore, a deep rethink and study of the existent models are required to obtain new designs and physical models with quite practical performance.

Integration of RISs with Emerging Technologies

To respond to the requirements of the aforementioned next-generation networks (cf. Section 1.1), different cost-effective technologies such as massive-MIMO, beamforming, mmWave communications, unmanned aerial vehicles (UAV), wireless power transfer (WPT) and simultaneous wireless information and power transfer, THz communications, short packet communications, and mobile edge computing were proposed. Motivated by the potentials of the RIS technology presented in Section. 1.1.2, it can be leveraged and implemented with these technologies and comes to the front with additional degrees of freedom and advantages to enhance the main communication performance metrics such as the coverage, SE, and EE, with low-cost and low complexity.

In this dissertation, we are interested in leveraging the potentials of RIS with emerging technologies and tackling the shortcomings related to this research field.

1.2 Inroduction to WIPT

1.2.1 Scope and Motivation

In recent years, energy harvesting (EH) has emerged as an enabling technology to address the key challenge of sustainability in ever-growing communication networks. In particular, to deal with the tremendous energy demands of wireless devices, radio frequencies (RF) have been considered to provide a stable and controllable source of energy [39, 40] and constituted a promising solution to improve the future wireless networks by prolonging their lifetime. EH has been receiving great attention from the research and industry community and has been integrated into many applications, including wireless sensor networks, smart-home industries, and the internet of things (IoT) in general [41].

As a result, integrating EH technology capabilities into existing wireless communication systems has become a competitive research field. In fact, the efforts of researchers have been focused on unifying the information and energy transmission processes. This unification leads to a new paradigm for 6G, which enables devices to wirelessly communicate while harvesting their required operation energy, a.k.a., wireless-powered communications (WPC). In WPC, both wireless information and power transfer coexist, in contrast to conventional wireless networks wherein only WIT exists. There are three operation modes for WIPT: WPT, WPC, and SWIPT [40, 42]. In particular, in WPC networks, the receiver is a low-power device that harvests energy in DL via WPT and uses it to send data on the UL. However, in SWIPT, energy and information are simultaneously transferred on the DL from one or multiple APs to one or multiple receivers.

SWIPT has received widespread interest as a promising solution to the problem of limited efficiency, which is of paramount importance and one of the most challenging design aspects of emerging wireless communication systems. Without being interrupted by energy depletion due to communication usage, SWIPT is expected to improve user experience and convenience, with higher and more sustainable throughput performance as compared to conventional battery-powered communication systems. Several research works have been conducted in the literature to study the SWIPT from a design point of view, performance evaluation, and optimization. For instance, a comprehensive survey of the state-of-the-art of SWIPT and related ideas such as practical transceiver architectures, SWIPT models, and interference exploitation is provided in [43]. Moreover, the rate

and energy (R-E) trade-off is studied in several works, e.g., [40, 44–46]. Motivated by the potentials of the coordinated multi-point transmission (CoMP) and multi-antenna beamforming in enhancing the signal strength and the efficiency of transmission, CoMP-SWIPT systems were investigated in [47, 48].

1.2.2   Challenges of SWIPT

Despite the performance improvements brought by SWIPT and CoMP-SWIPT, certain challenges still exist and need to be addressed before implementation to exploit the full potentials of these emerging technologies, such as:

Path-loss and Channel Fading Effects

One of the most important factors upsetting the levels of harvested energy from the RF signals is that the wireless propagation channel between the transmitter and the receiver suffers from path-loss, shadowing, and multi-path fading, which extremely reduce the amount and efficiency of the harvested power and hence deteriorate the whole wireless communication system performance.

Power Constraints

Knowing that information receivers (IRs) and energy receivers (ERs) in practice operate with different power sensitivity [49] (e.g., -10 dBm for ERs, -60 dBm for IRs [43]), one big challenge is to study the performance trade-off between information and energy transfer that do not exist in traditional wireless information transfer systems.

For SWIPT systems, two kinds of receiver architectures were proposed: the separate receivers and the integrated or co-located receivers [44]. Most of the existing works rely on the assumption that the receiver is able to extract power and information simultaneously from the received signal (co-located receivers). However, in practice, the receiver's circuits for harvesting energy from RF signals are not yet able to directly decode the information. Consequently, in order to coordinate SWIPT at the receiver side, two splitting mechanisms were proposed, known as, time switching (TS) and power splitting (PS) [44, 50].

The above challenges motivate researchers to carry out deep studies and performance analyses in order to understand the limitations of a SWIPT system in practice.

1.2.3 RIS-Aided SWIPT

Recall that the main target of next-generation wireless communication systems is to enhance connectivity by increasing data rates, coverage, bandwidths, and reliability while reducing energy consumption. In response to these major requirements, developing green communications and enhancing EE become a necessity. To this end, one of the promising solution that has recently attracted the attention of researchers is to leverage RIS to assist SWIPT. It is pointing out that this research field is still in its infancy and few research works have recently appeared in the literature [51–53]. For instance, in [52], the weighted sum-power maximization problem was studied for a RIS-aided SWIPT system, with no dedicated energy-carrying signals. In [51], the minimum rate maximization problem was formulated and solved under ideal and non-ideal channel conditions based on an iterative algorithm. In [53], the weighted sum-rate is maximized under QoS constraints, by jointly optimizing the active beamforming matrices and the passive RIS reflection matrix for SWIPT system.

Recently, research works have focused on improving the wireless power efficiency and reducing the transmit power as well as providing more flexibility and degree of freedom for designing the beamforming for energy and information and thus improving both the sum-rate and the amount of harvested energy in SWIPT systems [2, 52]. Typically, the beamforming design becomes more challenging due to the trade-off and the conflicting design objectives for the information and power transfers. This motivates the need for a deep rethink of the existing beamforming techniques. In order to adequate the proposed solution to the above conflicting purposes, an optimization problem with intractable non-convex constraints was proposed and solved in [51, 54, 55].

Note that the aforementioned studies were based on conventional optimization techniques to design the energy and information beamforming vectors of RIS-aided SWIPT systems.

1.3   Overview of the Research Goal

The objective of this dissertation is to design a framework for RIS-aided wireless information and power transfer, with a focus on assessing, optimizing, and enhancing the energy efficiency and reliability of a wireless communication systems. To this end, different systems models are considered such as WPT, WIT, and SWIPT. The specific objectives stemming from the ultimate one are summarized as follows:

- Design a cooperative RIS-aided WPT system with high transmission efficiency. As a starting point, we aim to design a cooperative WPT system by taking advantage of the cooperative energy beamforming potentials. The main objective of this work is to develop a framework for improving and evaluating the efficiency of the system by addressing the most important metrics characterizing the performance, i.e., WPT coverage probability and data transmission probability. Then, the developed framework and design will be extended to cover the case of multiple RIS cooperating for WPT to meet the main goal of this part.

- Design an energy-efficient RIS-aided WIT for cell-edge users. Two deployment scenarios are investigated in this part: the single service or unicast (downlink and uplink communication) and multiple services (the joint unicast-broadcast transmission).

- Design an efficient RIS-aided SWIPT system based on the degree of freedom provided by the null space of the composite channel between the AP and the IRs. The main objective of this part is to achieve a balance between the sum-rate of the IRs and the harvested power at the ERs.

1.4   Methodology

1.4.1   Part I: RIS-Aided WPT

The aim of the first part of this dissertation is to improve the efficiency of the WPT system, to increase the signal power at the harvesting devices, and thus the energy coverage and the energy for data transmission. To this end, this work proposes to leverage cooperative energy beamforming and coordinated transmission.

The first chapter of this part considers a wireless-powered communication network, where multiple APs, distributed according to PPP, collaborate to transfer wireless power to the devices on the downlink, which is then used for data transmission on the uplink. The main goal of this chapter is to derive the WPT coverage probability and the data transmission probability in their closed-form expressions and to provide a comparative study of the cooperative mechanism with the conventional non-cooperative scheme. Particularly, the Poisson-Voronoi tessellation is considered, and each device is served by the nearest active AP(s). This motivates the categorization of the devices into three types: inner-cell, cell-edge, and vertex-cell. By leveraging stochastic geometry tools and based on the moment-generating function (MGF) approach, the expressions for the three types of devices are provided and evaluated. Such analyses will emphasize the importance of exploiting cooperative beamforming and the stochastic geometry tools for designing WPT systems with high efficiency.

Motivated by the fact that cooperative energy beamforming enhances transmission efficiency, the performance of coordinated multipoint energy beamforming (CoMPe) in a triangular Poisson-Delaunay is studied in the second chapter of part I. Particularly, APs are distributed according to PPP and cooperate together to meet the energy requirements of devices uniformly distributed in the coverage area. The typical device is served by three APs. According to the distance between the serving AP and the target device, three types of devices are considered here. The main objective is to provide tractable closed-form formulae for the WPT coverage probability and to conduct a comparative study with a non-cooperative WPT scheme. To this end, first, the distance probability density functions (PDFs) are derived, as they are not explored before for this kind of tessellation. Then, the stochastic geometry tools, the MGF approach, and the newly derived PDFs are used to derive the closed-form expressions of the WPT coverage probability. A comparison with the Poisson-Voronoi tessellation is also presented in this chapter.

Despite the gain achieved with CoMPe, certain devices still suffer from low efficiency, especially in the presence of obstacles or when they are located at high distances. To deal with this issue, the third chapter of this part proposes to leverage cooperative RIS to assist the WPT system. In particular, the devices and the RISs are distributed according to a PPP. For the analysis, a typical device D is considered, which is assumed to be in the far-field of the power beacon (PB) with no direct LoS in between. Two configurations of designs are considered: (i) the cascaded configuration, where the signal transmitted by the PB reaches the end device via the cascaded channel between K RISs, (ii) the distributed configuration, where K RISs simultaneously relay the PB's signal to

the end device. The main objective of this chapter is to present the theoretical framework for the derivation of the WPT coverage probability based on stochastic geometry tools and the MGF approach for the cooperative RIS-assisted WPT system for both aforementioned configurations and to provide a comparative study with single RIS-aided WPT.

1.4.2 Part II: RIS-Aided WIT

The second part of this dissertation aims to design a WIT system that improves the communication performance of starving users (i.e, users in dead zone or at the cell-edge). This work proposes to leverage the aerial RIS to assist communication since UAVs are a very promising solution that provides good connectivity conditions, enhanced channel capacity, extended coverage area, and flexible deployment. Consequently, fairness among users is guaranteed, and high-performance gains are achieved at the cell-edge users. Motivated by this, assessing, designing, and improving the EE of aerial RIS aided WIT systems in two deployment scenarios, namely, single service and multi-services, is explored.

In the first chapter of this part, the system under study consists of a BS with M antenna that sends independent data streams to K single antenna ground UEs at a far distance from the BS, i.e., cell-edge users. The downlink communication is assisted by a UAV equipped with N reflecting elements. The aim of this chapter is to maximize the EE by jointly designing the active and passive beamforming matrices. To this end, the limiting case of the MRT technique is used to design the beamforming vectors at the BS. Then, the optimization problem is reduced to seeking an efficient power allocation algorithm and phase-shift matrix design. As a solution, an efficient iterative algorithm based on alternating optimization techniques is proposed. In particular, the power allocation matrix is obtained based on the interior point method, and the phase-shift matrix is obtained based on SDR.

In the second chapter of part II, the uplink cellular communication assisted with RIS-UAV is investigated. The main objective is to jointly design the transmit powers of the users, the active beamforming at the base stations, and the passive beamforming at the RIS while satisfying the quality of service requirements in order to maximize the EE to the cell-edge users. To deal with the highly intractable non-convex problem, an iterative solution based on alternating optimization techniques is proposed. In particular, the power allocation is designed based on the Dinkelbach

algorithm; the beamforming vectors are obtained based on MMSE, and the phase-shift matrix is designed based on SDR.

In the third chapter of part II, the potential performance benefits brought by a dual-polarized RIS-UAV in transmitting two kinds of traffic patterns with high EE, namely, unicast and broadcast transmissions, are investigated. The downlink communication assisted with aerial dual-polarized RIS, where the BS simultaneously transmits independent data streams to a set of UEs, and broadcasts another data stream to another set of UEs, at a far distance from the BS. The main objective of this work is to maximize the EE of the system by jointly designing the beamformers at the BS for both unicast and broadcast messages and the phase-shift matrix at the aerial RIS while taking into account the QoS requirements of all services and the unit-modulus constraints at the aerial RIS. To this end, an efficient low-complexity two-stage algorithm is proposed to solve the formulated problem. In the first stage, the passive beamforming matrix of the dual-polarized aerial RIS is designed based on the Gaussian randomization method, which relaxes the inhomogeneous non-convex QCQP into a semi-definite program. In the second stage, the active beamforming at the BS is designed based on a dual-structured beamforming approach, in which the interior point method is used to obtain the prebeamforming matrix, and the beamforming matrices pertaining to the unicasting and broadcasting are obtained based on low-complexity zero-forcing and successive convex approximation, respectively.

1.4.3   Part III: RIS-Aided SWIPT

Unlike the previous two parts that deal only with either power transfer or information transfer, part III of this dissertation focuses on the SWIPT system assisted with RIS. A design framework to coordinate and balance the sum-rate of IRs and the harvested energy at the ERs is proposed. In particular, the degrees of freedom of the channel between the IRs and the AP are used to construct the energy signal. First, the null space of the matrix is computed based on the SVD. Second, the energy signal is chosen as the eigenvector corresponding to the largest eigenvalue of the projected version of the channel between the ERs and the AP in the computed null space. Third, a MOO problem is formulated and aims to jointly design the active transmit information beamforming matrix at the AP and the passive beamforming matrix at the RIS while satisfying quality of service requirements. Finally, to solve the highly non-convex formulated maximization problem, the MOO

framework and the weighted Tchebycheff approach are exploited to formulate the equivalent sum rates (ESR) maximization problem that can be solved with a two-layer algorithm based on the alternating optimization techniques. In particular, the active beamforming at the AP is designed based on low-complexity ZF techniques in the first layer, and the passive beamforming matrix at RIS is designed based on the Gaussian randomization method and SDR after relaxing the non-convex QCQP into an SDP in the second layer.

Part I

RIS-Aided Wireless Power Transfer

The main objective of this part is to design a cooperative RIS-aided WPT with high efficiency. As starting point, the design of cooperative WPT is considered with the focus on improving the efficiency of transmission by addressing the most important metrics characterizing the system's performance, i.e., WPT coverage and data transmission probabilities of two tessellations the Poison-Voronoi (chapter 2) and the Poisson-Delaunay (chapter 3). Then, the developed framework and design will be extended to the case of multiple RIS-aided WPT systems (chapter 4).

Chapter 2

Coordinated Wireless Powered Communication

2.1 Introduction

Coordinated transmissions from multiple sources are a promising solution to enhance performances of the network such as capacity, coverage, and EE. On the other hand, energy beamforming consists in focusing energy towards the EH devices. It is useful to improve the network performance as it increases the signal power at the target devices, and thus the energy coverage, and decreases the interference. Motivated by these facts, a question arises as to the benefits that can be achieved if the coordinated communication and the energy beamforming are both used to enhance the power coverage and the transmission probability.

Taking the above question as a starting point, we consider wireless powered communications where multiple access points (APs) collaborate to meet the energy demands of the harvesting devices on the downlink, which are then used for their data transmission on the uplink. The coverage area of the network is a Poisson-Voronoi tessellation, in which each device connects to the nearest active AP(s) [57]. The devices are categorized into three types: *inner-cell*, *cell-edge*, and *vertex-cell*. Taking advantage of the benefits of distributed beamforming and the optimality of maximum-ratio transmission, the harvested energy at a typical device is first derived. Then, closed-form analytical

---

[0]The contents of this chapter are extracted from [56].

expressions for the wireless power coverage and the transmission probability are obtained for the three device types. Numerical results are provided, and show the gains in coverage and transmission probabilities that can be achieved with coordinated WPT as compared to the single-source WPT and/or when the density of the network APs increases.

The organization of the chapter is as follows. The system model is detailed in Section 2.2. Then, in Section 2.3, the wireless coverage probability formulae for three type of devices are provided. In Section 2.4, the transmission probability expressions are provided. Through extensive simulations in Section 2.5, We show that the gains in coverage and transmission probabilities that can be achieved with coordinated WPT are higher than that obtained with the single-source WPT. Section 2.6 concludes the chapter.

2.2   The Wireless Powered Network

Each device harvests energy from the WPT by cooperating APs, and then uses the harvested energy for its information transmission on the uplink. The APs, which are equipped with a large number of antennas, N, are distributed in a two-dimensional infinite plane according to a homogeneous Poisson point process (HPPP), denoted by Φ, with intensity λ (cf. Fig. 2.1). The devices, which are single-antenna devices, are uniformly distributed in the plane. The power transfer and the information transfer are frame-based in the time domain, and we assume the harvest-use protocol at the devices. Each frame, of duration T, consists of $M > 1$ slots, indexed from 0 to $M - 1$, and the slots among cooperating APs and a typical device are synchronized. The first $M - 1$ slots correspond to the downlink phase, in which the set of cooperating APs, denoted Φ_{c} with cardinality $|\Phi_{\mathrm{c}}| = K$, transmit energy to a target device. The Mth time slot is dedicated for the uplink phase, where the device uses the harvested energy to transmit its always available data to its associated nearest AP. Without loss of generality, we set T to unity.

Denote the channel between the kth AP in Φ_c and a typical device by $\mathbf{g}_k \in \mathbb{C}^{N \times 1}$. Channels follow the block-fading model, and are assumed to be independent from each other.[1] The channel gains include the path loss and the fast fading effects. Thus, $\mathbf{g}_k = \mathbf{h}_k \sqrt{\mathbf{D}_k}$, where $\mathbf{D}_k \in \mathbb{R}^K$ is a diagonal matrix modeling the path loss effects, with elements $[\mathbf{D}]_{k,k} = d_k^{-\alpha}$, $k \in \{1, 2, \cdots, K\}$,

---

[1]We assume full knowledge of the channel state information (CSI), and leave investigations of cases with partial and imperfect CSI for future work.
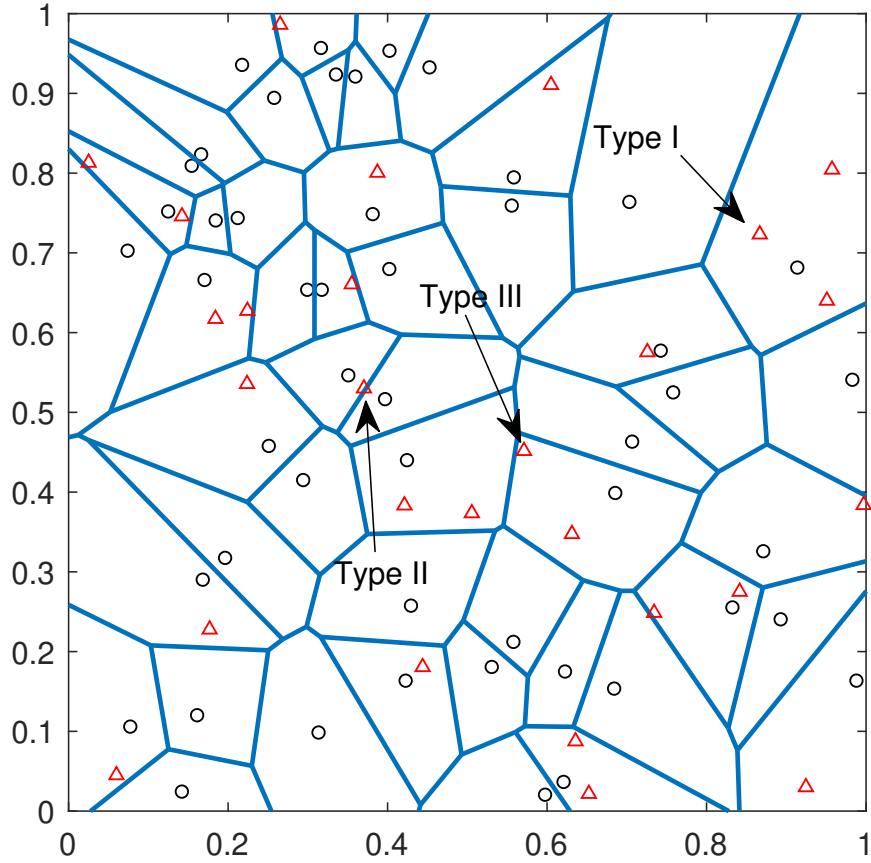
Figure 2.1: The wireless powered network: APs are marked with circles, and devices with triangles; polygons are the Poisson-Voronoi tessellation centered with APs.

$\alpha = 4$ is the path loss exponent, d_k is the Euclidian distance between the kth AP and the typical device, and $\mathbf{h}_k \in \mathbb{C}^{N \times 1}$ is the fast fading component modeled as $\mathbf{h}_k = \mathbf{h}_k^{\text{LoS}} + \mathbf{h}_k^{\text{NLoS}}$, where $\mathbf{h}_k^{\text{LoS}}$ and $\mathbf{h}_k^{\text{NLoS}}$ are the line-of-sight (LoS) and non line-of-sight (NLoS) components. The random channel vectors are i.i.d. such that the path gains are Nakagami distributed, with parameters (m_L, Ω_L) for $\mathbf{h}_k^{\text{LoS}}$ and (m_N, Ω_N) for $\mathbf{h}_k^{\text{NLoS}}$ [58]. Hence, the channel is expressed as

$$\mathbf{g}_k = \left[\mathbf{h}_k^{\text{LoS}} + \mathbf{h}_k^{\text{NLoS}} \right] \mathbf{D}^{\frac{1}{2}}. \tag{2.1}$$

The received signal at a typical device is given by

$$y = \sum_{k \in \Phi_c} \mathbf{g}_k^H \mathbf{x}_k + z, \tag{2.2}$$

where $\mathbf{x}_k = [x_{k,1}, \cdots, x_{k,N}]^T$ is the energy signal vector determined by the beamforming, and z is a zero-mean AWGN with spectral power N_0. Signals originating from the adjacent cooperation sets are not shown in (2.2), given that we neglect their incremental contribution to the aggregate harvested energy at each device. The transmit energy signal is written as

$$\mathbf{x}_k = \sqrt{P_k}\mathbf{w}_k u_k, \tag{2.3}$$

where $\mathbf{w}_k = [w_{k,1}, \cdots, w_{k,N}]^T$ is the beamforming weight vector representing the phase shift of the tone transmitted from the kth AP, and u_k is the source baseband signal with $\mathbb{E}\{|u_k|^2\} = 1$. P_k denotes the transmit power of the kth AP, assumed equal for all elements in the cooperation set Φ_{c}, i.e., $P_k = P_{\text{t}} \ \forall k$, and we assume $u_k = u \ \forall k$. Hence, the received signal at the typical device can be written as

$$y = \sum_{k \in \Phi_c} \sqrt{P_{\text{t}}}\mathbf{g}_k^H \mathbf{w}_k u + z. \tag{2.4}$$

To maximize the harvested power at the device, maximum ratio transmission is used [59]. The energy beamforming vector can be written as $\mathbf{w}_k = \frac{\mathbf{g}_k}{\|\mathbf{g}_k\|}$. By using the energy conversion law and assuming no harvesting from the AWGN, the input power at the device's rectifier, during the WPT from Φ_{c}, is given by

$$E_{\text{in}} = P_{\text{t}} \left| \sum_{k \in \Phi_c} \frac{\mathbf{g}_k^H \mathbf{g}_k}{\|\mathbf{g}_k\|} \right|^2 = P_{\text{t}} \sum_{k \in \Phi_c} \|\mathbf{g}_k\|^2. \tag{2.5}$$

Therefore, the instantaneous received power at the device is

$$P_{\text{in}} = P_{\text{t}} \sum_{k \in \Phi_c} \left\| \mathbf{h}_k^{\text{LoS}} + \mathbf{h}_k^{\text{NLoS}} \right\|^2 d_k^{-\alpha}. \tag{2.6}$$

Considering the generally adopted piece-wise linear energy harvesting model [60], the output direct current (DC) power can be obtained according to

$$P_{\text{EH}} = \begin{cases} \eta P_{\text{in}}, & P_{\text{in}} \leq P_{\text{th}}; \\ \eta P_{\text{th}}, & P_{\text{in}} > P_{\text{th}}, \end{cases} \tag{2.7}$$

where $0 < \eta < 1$ denotes the power conversion efficiency [61], and P_{th} is the saturation threshold of the rectifier. It is clear that the piece-wise model reduces to the conventional linear model when P_{th} goes to infinity.

2.3   Wireless Power Coverage Probability

We study the WPT performance using the power coverage metric, which is defined as the probability that the received power at a typical device is higher than a predefined threshold,

$$P_{\text{cov}} = \mathbb{P}\left(P_{\text{EH}} \geq \gamma_{\text{th}}\right), \tag{2.8}$$

where P_{EH} is the harvested power in one WPT block time. The coverage probability is interpreted as the complementary cumulative distribution function of the harvested power and expressed as:[2]

$$P_{\text{cov}} = \begin{cases} 1 - \mathbb{P}\left(\eta P_{\text{t}} \sum\limits_{k \in \Phi_c} \left\|\mathbf{h}_k^{\text{LoS}} + \mathbf{h}_k^{\text{NLoS}}\right\|^2 d_k^{-\alpha} < \gamma_{\text{th}}\right) \\ \qquad\qquad\qquad\qquad\qquad \text{for } \gamma_{\text{th}} \leq P_{\text{th}}; \\ 1 \qquad \text{for } \gamma_{\text{th}} > P_{\text{th}}. \end{cases} \tag{2.9}$$

Since P_{EH} is the sum of K random variables involving the random channel vectors and the random distances between the device and the K serving APs, direct computation of P_{cov} when $\gamma_{\text{th}} \leq P_{\text{th}}$ is not possible. Thus, we adopt the moment generating function (MGF) based approach to calculate P_{cov}. The MGF of the harvested power is given by

$$\mathcal{M}_{P_{\text{EH}}}(s) = \prod_{k=1}^{K} \mathcal{M}_{P_k}(s), \tag{2.10}$$

where $\mathcal{M}_{P_k}$ is the MGF of the harvested power from the kth AP. The power coverage at typical device is calculated as

$$P_{\text{cov}} = 1 - \int_0^{\gamma_{\text{th}}} f_{P_{\text{EH}}}(x)\mathrm{d}x, \tag{2.11}$$

where $f_{P_{\text{EH}}}(x)$ is the probability density function (PDF) of the harvested power, which can be found using

$$f_{P_{\text{EH}}}(x) = \frac{1}{2\pi} \int_{-\infty}^{\infty} \mathcal{M}_{P_{\text{EH}}}(js) \exp(-jsx)\mathrm{d}s. \tag{2.12}$$

To proceed, we first present necessary PDFs pertaining to the distances and the channel gain vectors.

---

[2]As it is clear from the context, P_{cov} will refer to the case when $\gamma_{\text{th}} \leq P_{\text{th}}$.

Distribution of d_k

Three typical device types are considered (cf. Fig. 2.1): *(i)* Type I: such devices are located inside Poisson-Voronoi cells; *(ii)* Type II: the device is on the edge of the Poisson-Voronoi cells; and *(iii)* Type III: the device is at the vertex of the dual Poisson-Voronoi cells. The number K of cooperating APs can be determined according to the device type. We assume that only the closest APs are active [57]. If the device is located inside the Poisson-Voronoi cells, then $K = 1$ [57], and the PDF of distance d_k is given by

$$f_{\mathrm{d}}(d) = 2\lambda\pi d \exp\left(-\lambda\pi d^2\right). \tag{2.13}$$

If the device is located on the edge of the Poisson-Voronoi cells, then $K = 2$ and d_k is distributed according to [62]:

$$f_{\mathrm{d}}(d) = 4\pi\lambda^{\frac{3}{2}} d^2 \exp\left(-\lambda\pi d^2\right). \tag{2.14}$$

For a typical device at the vertex of the Voronoi cells, we have $K = 3$, and the PDF of the distance is given by [57]:

$$f_{\mathrm{d}}(d) = 2(\lambda\pi)^2 d^3 \exp\left(-\lambda\pi d^2\right). \tag{2.15}$$

Distribution of $\mathbf{h}_k$ and $\|\mathbf{h}_k\|^2$

As aforementioned, each element of $\mathbf{h}_k = [h_{k,1}, \cdots, h_{k,N}]^{\mathrm{T}}$ is the sum of two Nakagami distributed random variables with parameters (m_L, Ω_L) and (m_N, Ω_N) for the LoS and NLoS components, respectively. The distribution of the sum variable can be modeled by a Nakagami function [63], namely,

$$f_{h_{k,n}}(x) = \frac{2m^m x^{2m-1}}{\Gamma(m)\Omega^m} \exp\left(-\frac{mx^2}{\Omega}\right), \tag{2.16}$$

where $h_{k,n}$ is the amplitude, $\Omega = \mathbb{E}\left[h_{k,n}^2\right]$ and $m = \frac{\Omega^2}{\mathrm{Var}\left[h_{k,n}^2\right]} = \frac{\Omega^2}{\mathbb{E}\left[h_{k,n}^4\right]-\Omega^2}$. The moments $\mathbb{E}\left[h_{k,n}^2\right]$ and $\mathbb{E}\left[h_k^4\right]$ can be calculated using [63, (6)]. The ith moment of h_k is given by

$\mathbb{E}\left[h_{k,n}^i\right] = \sum_{i_1=0}^{i}\sum_{i_2=0}^{i_1} \begin{pmatrix} i \\ i_1 \end{pmatrix}\begin{pmatrix} i_1 \\ i_2 \end{pmatrix} \mathbb{E}\left[h_{1,n}^{i-i_1}\right]\mathbb{E}\left[h_{2,n}^{i_1-i_2}\right]$, and we have $\mathbb{E}\left[h_{1,n}^i\right] = \mathbb{E}\left[(h_{k,n}^{\mathrm{LoS}})^i\right] =$

$\frac{\Gamma(m_L+\frac{n}{2})}{\Gamma(m_L)}\left(\frac{\Omega_L}{m_L}\right)^{\frac{i}{2}}$ and $\mathbb{E}\left[h_{2,n}^i\right] = \mathbb{E}\left[(h_{k,n}^{\mathrm{NLoS}})^i\right] = \frac{\Gamma(m_N+\frac{n}{2})}{\Gamma(m_N)}\left(\frac{\Omega_N}{m_N}\right)^{\frac{i}{2}}$. Besides, $\|h_{k,n}\|^2$ follows the

Erlang distribution, which is a special case of the Gamma distribution, given by

$$f_{\|h_{k,n}\|^2}(x) = \frac{m^m x^{m-1}}{\Omega^m \Gamma(m)} \exp\left(-\frac{mx}{\Omega}\right). \tag{2.17}$$

Inner-Cell Typical Device

Now, we focus on calculating the power coverage probability for Type-I typical device. For such, we need to determine the CDF of the harvested energy. Given the distance distribution shown in (2.13), the CDF of $d^{-\alpha}$ is required, which can be expressed as $F_{d^{-\alpha}} = 1 - F_d\left(d^{\frac{-1}{\alpha}}\right) = 1 - \exp\left(-\lambda \pi d^{\frac{-2}{\alpha}}\right)$. Then, the CDF of the harvested energy is obtained as

$$
\begin{aligned}
F_{P_{\mathrm{EH}}}(\gamma_{\mathrm{th}}) &= \int_0^\infty \mathbb{P}\left(d^{-\alpha} < \frac{\gamma_{\mathrm{th}}}{\eta P_t y}\right) f_{\|\mathbf{h}\|^2}(y)\mathrm{d}y \\
&= \frac{m^m}{\Omega^m \Gamma(m)} \int_0^\infty \left(1 - \exp\left(-\lambda\pi\left(\frac{\eta P_t y}{\gamma_{\mathrm{th}}}\right)^{\frac{2}{\alpha}}\right)\right) y^{m-1} \exp\left(-\frac{my}{\Omega}\right)\mathrm{d}y \\
&= 1 - {}_1F_1\left(m; \frac{1}{2}; \frac{\eta P_t \Omega(\lambda\pi)^2}{4m\gamma_{\mathrm{th}}}\right) + \frac{\lambda\pi\sqrt{\frac{\eta P_t}{\gamma_{\mathrm{th}}}}}{\sqrt{\frac{m}{\Omega}}\Gamma(m)}\Gamma\left(\frac{1}{2}+m\right){}_1F_1\left(\frac{1}{2}+m; \frac{3}{2}; \frac{\eta P_t \Omega(\lambda\pi)^2}{4m\gamma_{\mathrm{th}}}\right),
\end{aligned} \tag{2.18}
$$

where the confluent hypergeometric function of the first kind is defined as the series ${}_1F_1(a; b; t) \triangleq \sum_{k=0}^\infty \frac{a^{(k)}}{b^{(k)}}\frac{t^k}{k!}$, with $a^{(0)} = 1, a^{(k)} = a(a+1)(a+2)\cdots(a+n-1)$ [64].

The coverage probability of a typical device at the inner cell is then found in closed-form using

$$P_{\mathrm{cov}}(\lambda, \gamma_{\mathrm{th}}) = 1 - F_{P_{\mathrm{EH}}}(\gamma_{\mathrm{th}}). \tag{2.19}$$

Cell-Edge Typical Device

In this case, the distance distribution is shown in (2.14). The MGF of the harvested energy from the kth AP is given by

$$
\begin{aligned}
\mathcal{M}_{P_k}(s) &= \mathbb{E}_{x,d}\left[\exp\left(-s\eta P_{\text{t}}\left\|\mathbf{h}_k\right\|^2 d_k^{-\alpha}\right)\right] \\
&= \frac{m^m}{\Omega^m \Gamma(m)} \times \int_0^{+\infty}\int_0^\infty \exp\left(-s\eta P_{\text{t}}xd^{-\alpha} - \frac{mx}{\Omega}\right) x^{m-1} f_{\text{d}}(d)\mathrm{d}x\mathrm{d}d \\
&= \frac{4\pi\lambda^{\frac{3}{2}}m^m}{\Omega^m \Gamma(m)} \int_0^{+\infty} d^2 \exp\left(-\lambda\pi d^2\right)\left(s\eta P_{\text{t}}d^{-\alpha} + \frac{m}{\Omega}\right)^{-m}\mathrm{d}d \\
&= \frac{4\pi\lambda^{\frac{3}{2}}m^m}{\Gamma(m)\Omega^m} \times \underbrace{\int_0^{+\infty} d^2 \exp\left(-\lambda\pi d^2\right) G_{1,1}^{1,1}\left(\frac{s\eta P_{\text{t}}\Omega d^{-\alpha}}{m}\middle|\begin{array}{c}1-m\\0\end{array}\right)\mathrm{d}d}_{I_1}.
\end{aligned}
\tag{2.20}
$$

By making the change of variable $u = d^2$, the integral I_1 shown above can be written as $I_1 = 2\int_0^{+\infty}\exp\left(-\lambda\pi u\right)uG_{1,1}^{1,1}\left(\frac{s\eta P_{\text{t}}\Omega u^{-2}}{m}\middle|\begin{array}{c}1-m\\0\end{array}\right)\mathrm{d}u$. Then, using the proprieties of the Meijer-G function, we get

$$
\begin{aligned}
I_1 &= 2\int_0^{+\infty}\exp\left(-\lambda\pi u\right)uG_{1,1}^{1,1}\left(\frac{s\eta P_{\text{t}}\Omega u^2}{m}\middle|\begin{array}{c}m\\1\end{array}\right)\mathrm{d}u \\
&= \frac{2}{\sqrt{\pi}(\lambda\pi)^2}G_{3,1}^{1,3}\left(\frac{4s\eta P_{\text{t}}\Omega}{m(\lambda\pi)^2}\middle|\begin{array}{c}\frac{-1}{2},0,1-m\\1\end{array}\right),
\end{aligned}
\tag{2.21}
$$

which, upon substitution in (2.20) and then in (2.10), yields the MGF of the harvested energy, namely,

$$
\mathcal{M}_{P_{\text{EH}}}(s) = \left(\frac{8\lambda\sqrt{\pi\lambda}m^m}{\Omega^m\Gamma(m)(\lambda\pi)^2}G_{3,1}^{1,3}\left(z\middle|\begin{array}{c}\frac{-1}{2},0,1-m\\1\end{array}\right)\right)^K,
\tag{2.22}
$$

where $z = \frac{4s\eta P_{\text{t}}\Omega}{m(\lambda\pi)^2}$.

The PDF of the harvested power is calculated using (2.12) after substitution of the above MGF therein. To find $f_{P_{\text{EH}}}(x)$, we should calculate the product of the K Meijer-G functions shown in (2.22), which we denote as G_K for simplicity. As the WPT cooperation set in this case is formed

by $K = 2$ active APs, we have

$$G_2 = \left(G_{3,1}^{1,3} \left(\frac{4s\eta P_t \Omega}{m(\lambda\pi)^2} \middle| \begin{matrix} \frac{-1}{2}, 0, 1-m \\ 1 \end{matrix} \right) \right)^2 = G_{0,0:3,1:3,1}^{0,0:1,3:1,3} \left(z, z \middle| \begin{matrix} \mathbf{v}_1 \\ \mathbf{v}_2 \end{matrix} \middle| \begin{matrix} \mathbf{v}_1 \\ \mathbf{v}_2 \end{matrix} \right), \qquad (2.23)$$

where $\mathbf{v}_1 = [\frac{-1}{2}, 0, 1-m]$ and $\mathbf{v}_2 = [1]$. Then, substituting G_2 in the expression of the PDF (2.12), and taking advantage of the integral representation of the Meijer-G function, we obtain

$$f_{P_{EH}}(x) = \frac{-1}{2\pi x} \left(\frac{8\lambda\sqrt{\pi\lambda}m^m}{\Omega^m \Gamma(m)(\lambda\pi)^2} \right)^2 G_{1,0:1,3:1,3}^{0,1:3,1:3,1} \left(\frac{-4\eta P_t \Omega}{xm(\lambda\pi)^2}, \frac{-4\eta P_t \Omega}{xm(\lambda\pi)^2} \middle| \begin{matrix} 0 \\ - \end{matrix} \middle| \begin{matrix} \mathbf{v}_1 \\ \mathbf{v}_2 \end{matrix} \middle| \begin{matrix} \mathbf{v}_1 \\ \mathbf{v}_2 \end{matrix} \right). \qquad (2.24)$$

Finally, using (2.11) and further calculations, the power coverage probability at a cell-edge typical device is obtained as

$$P_{cov}(\lambda, \gamma_{th}) = 1 + \frac{1}{2\pi} \left(\frac{8\lambda\sqrt{\pi\lambda}m^m}{\Omega^m \Gamma(m)(\lambda\pi)^2} \right)^2 G_{1,0:1,3;1,3}^{0,1:3;1:3,1} \left(\frac{-4\eta P_t \Omega}{\gamma_{th} m(\lambda\pi)^2}, \frac{-4\eta P_t \Omega}{\gamma_{th} m(\lambda\pi)^2} \middle| \begin{matrix} 0 \\ - \end{matrix} \middle| \begin{matrix} \mathbf{v}_1 \\ \mathbf{v}_2 \end{matrix} \middle| \begin{matrix} \mathbf{v}_1 \\ \mathbf{v}_2 \end{matrix} \right).$$

$$(2.25)$$

For comparison purposes, we determine the coverage probability for the WPT case from a single AP. For such, we first find the CDF of $d^{-\alpha}$, which is given by $F_{d^{-\alpha}} = 4\pi\lambda^{\frac{3}{2}} \left(\frac{\exp\left(-\lambda\pi d^{\frac{-1}{\alpha}} \right)}{2(\lambda\pi)d^{\frac{-1}{\alpha}}} + \frac{\sqrt{\pi}\,\mathrm{erf}\left(\sqrt{\pi}d^{\frac{-1}{\alpha}} \right)}{4(\lambda\pi)^{\frac{3}{2}}} \right)$, in which erf(.) is the error function. The CDF of the harvested energy is then found as

$$F_{P_{EH}}(\gamma_{th}) = 1 - \frac{2\sqrt{\lambda}\Omega^{\frac{3}{4}}}{m^{\frac{3}{4}}\Gamma(m)} \left(\frac{\eta P_t}{\gamma_{th}} \right)^{\frac{1}{4}}$$

$$\left[\sqrt{\frac{m}{\Omega}}\Gamma\left(\frac{1}{4} + m \right) {}_1F_1\left(\frac{1}{4} + m; \frac{1}{2}; \frac{\eta P_t \Omega(\lambda\pi)^2}{4m\gamma_{th}} \right) - \lambda\pi\sqrt{\frac{\eta P_t}{\gamma_{th}}}\Gamma\left(\frac{3}{4} + m \right) {}_1F_1\left(\frac{3}{4} + m; \frac{3}{2}; \frac{\eta P_t \Omega(\lambda\pi)^2}{4m\gamma_{th}} \right) \right]$$

$$+ \frac{2\Omega^{\frac{3}{4}}\left(\frac{\eta P_t}{\gamma_{th}} \right)^{\frac{1}{4}}}{m^{\frac{3}{4}}\Gamma(m)} \left[\frac{\sqrt{\frac{m\pi}{\Omega}}}{4} G_{2,3}^{3,2}\left(-\frac{\eta P_t \Omega(\lambda\pi)^2}{4m\gamma_{th}} \middle| \begin{matrix} \frac{3}{4}, \frac{3}{4} - m \\ 0, \frac{1}{2}, \frac{-1}{4} \end{matrix} \right) - \frac{\sqrt{\frac{\eta P_t}{\gamma_{th}}}\pi^{\frac{3}{4}}}{8} G_{2,3}^{3,2}\left(\frac{-\eta P_t \Omega(\lambda\pi)^2}{4m\gamma_{th}} \middle| \begin{matrix} \frac{1}{4}, \frac{1}{4} - m \\ 0, \frac{-1}{2}, \frac{-3}{4} \end{matrix} \right) \right],$$

$$(2.26)$$

which, upon substitution in (2.19), yields the closed-form expression for the power coverage probability of a cell-edge device serviced by a single AP.

Vertex-Cell Typical Device

For a typical device of Type III, the distance distribution is as shown in (2.15). In this case, the MGF of the harvested energy from K APs is obtained as

$$\mathcal{M}_{P_{\mathrm{EH}}}(s) = \left(\frac{4m^m}{\Gamma(m)\Omega^m\sqrt{\pi}}\right)^K \left(G_{3,1}^{1,3}\left(\frac{4s\eta P_{\mathrm{t}}\Omega}{m(\lambda\pi)^2}\bigg|\begin{array}{c}\frac{-1}{2},0,1-m\\1\end{array}\right)\right)^K.$$
(2.27)

Here, three APs are active. Therefore, we have

$$G_3 = \left(G_{3,1}^{1,3}\left(\frac{4s\eta P_{\mathrm{t}}\Omega}{m(\lambda\pi)^2}\bigg|\begin{array}{c}\frac{-1}{2},0,1-m\\1\end{array}\right)\right)^3.$$
(2.28)

Then, substituting G_3 in the expression of the PDF, we obtain

$$f_{P_{\mathrm{EH}}}(x) = \frac{-1}{2\pi x}\left(\frac{4m^m}{\Gamma(m)\Omega^m\sqrt{\pi}}\right)^3 G_{1,0:1,3:1,3:1,3}^{0,1:3,1:3,1:3,1}\left(\frac{-\omega}{x},\frac{-\omega}{x},\frac{-\omega}{x}\bigg|\begin{array}{c}0\\-\end{array}\bigg|\begin{array}{c}\mathbf{v}_1\\\mathbf{v}_2\end{array}\bigg|\begin{array}{c}\mathbf{v}_1\\\mathbf{v}_2\end{array}\bigg|\begin{array}{c}\mathbf{v}_1\\\mathbf{v}_2\end{array}\right),$$
(2.29)

where $\mathbf{v}_1 = [\frac{-1}{2},0,1-m]$, $\mathbf{v}_2 = [1]$ and $\omega = \frac{4\eta P_{\mathrm{t}}\Omega}{m(\lambda\pi)^2}$.

Finally, using (2.11) and mathematical manipulations, the power coverage probability for a typical device of Type III is obtained as follows:

$$P_{\mathrm{cov}}(\lambda,\gamma_{\mathrm{th}}) = 1 + \frac{1}{2\pi}\left(\frac{4m^m}{\Gamma(m)\Omega^m\sqrt{\pi}}\right)^3 G_{1,0:1,3:1,3:1,3}^{0,1:3,1:3,1:3,1}\left(\frac{-\omega}{\gamma_{\mathrm{th}}},\frac{-\omega}{\gamma_{\mathrm{th}}},\frac{-\omega}{\gamma_{\mathrm{th}}}\bigg|\begin{array}{c}0\\-\end{array}\bigg|\begin{array}{c}\mathbf{v}_1\\\mathbf{v}_2\end{array}\bigg|\begin{array}{c}\mathbf{v}_1\\\mathbf{v}_2\end{array}\bigg|\begin{array}{c}\mathbf{v}_1\\\mathbf{v}_2\end{array}\right).$$
(2.30)

In this case, the CDF of $d^{-\alpha}$ is given by $F_{\mathrm{d}^{-\alpha}} = 1 - \exp(-\lambda\pi d^{\frac{-2}{\alpha}}) - (\lambda\pi)d^{\frac{-2}{\alpha}}\exp(-\lambda\pi d^{\frac{-2}{\alpha}})$, and the CDF of the harvested energy is obtained as follows:

$$F_{P_{\mathrm{EH}}}(\gamma_{\mathrm{th}}) = \int_0^\infty \mathbb{P}\left(d^{-\alpha} < \frac{\gamma_{\mathrm{th}}}{\eta P_{\mathrm{t}}y}\right) f_{\|\mathbf{h}\|^2}(y)\mathrm{d}y$$

$$= 1 - {}_1F_1\left(m;\frac{1}{2};\frac{\eta P_{\mathrm{t}}\Omega(\lambda\pi)^2}{4m\gamma_{\mathrm{th}}}\right) + \frac{\lambda\pi\sqrt{\frac{\eta P_{\mathrm{t}}}{\gamma_{\mathrm{th}}}}\Gamma\left(\frac{1}{2}+m\right)}{\Gamma(m)\sqrt{\frac{m}{\Omega}}}{}_1F_1\left(\frac{1}{2}+m;\frac{3}{2};\frac{\eta P_{\mathrm{t}}\Omega(\lambda\pi)^2}{4m\gamma_{\mathrm{th}}}\right)$$

$$- \frac{\Omega\lambda\pi\sqrt{\frac{\eta P_{\mathrm{t}}}{\gamma_{\mathrm{th}}}}}{\Gamma(m-1)}\left[\sqrt{\frac{m}{\Omega}}\Gamma\left(\frac{1}{2}+m\right){}_1F_1\left(\frac{1}{2}+m;\frac{1}{2};\frac{\eta P_{\mathrm{t}}\Omega(\lambda\pi)^2}{4m\gamma_{\mathrm{th}}}\right)\right.$$

$$\left. - \lambda\pi\sqrt{\frac{\eta P_{\mathrm{t}}}{\gamma_{\mathrm{th}}}}\Gamma(1+m){}_1F_1\left(1+m;\frac{3}{2};\frac{\eta P_{\mathrm{t}}\Omega(\lambda\pi)^2}{4m\gamma_{\mathrm{th}}}\right)\right].$$
(2.31)

Then, substituting (2.31) into (2.19), the coverage probability of Type-III typical device when serviced by one AP is obtained.

2.4 Data Transmission Probability

This metric, defined as the probability that the device can transmit on the uplink, is now analyzed for the three device types.

Let C be the battery capacity of typical device, and assume that $C \to \infty$. The battery level S_t evolves as

$$S_t = S_{t-1} + P_{\mathrm{EH}}(t) - P_{\mathrm{UE}} I\left(S_{t-1} \geq P_{\mathrm{UE}}\right), \tag{2.32}$$

where t is the time frame index, $S_0 = 0$, P_{EH} is the DC power at the UE, P_{UE} is its data transmit power, and $I(x)$ is the indicator function [65]. We consider fixed-power transmission. As per [65, (9)], assuming random walk model, the transmission probability can be computed using

$$P_{\mathrm{tr}} = \min\left(1, (M-1)\mathbb{E}\left[P_{\mathrm{EH}}\right] P_{\mathrm{UE}}^{-1}\right), \tag{2.33}$$

with $\mathbb{E}\left[P_{\mathrm{EH}}\right] = \int_0^\infty x f_{P_{\mathrm{EH}}}(x)\mathrm{d}x$, in which $f_{P_{\mathrm{EH}}}$ denotes the PDF of the harvested energy.

Inner-Cell Device

The transmission probability of a typical device at the inner of cells, i.e., Type I, is obtained as

$$
\begin{aligned}
P_{\mathrm{tr}} = \min\Bigg(1, \frac{(M-1)P_{\mathrm{th}}^2}{2\pi P_{\mathrm{UE}}} \Bigg[&\frac{\lambda\pi\Gamma\left(\frac{1}{2}+m\right)a_1}{4\Gamma(1+m)^2} G_{2,3}^{1,2}\left(z_1 \,\middle|\, \begin{matrix} \frac{3}{2}, -m \\ 0, \frac{1}{2}, \frac{-1}{2} \end{matrix}\right) \\
&+ \frac{(\lambda\pi)^2\sqrt{\pi}\eta P_{\mathrm{t}}\Omega}{4\Gamma(1+m)} G_{2,3}^{2,1}\left(z_1 \,\middle|\, \begin{matrix} -m, 1 \\ 0, 0, \frac{-1}{2} \end{matrix}\right) + \frac{(\lambda\pi)^3\sqrt{\pi}\eta P_{\mathrm{t}}\Omega(\frac{1}{2}+m)}{(8m+4)\Gamma(m+1)\sqrt{\frac{m}{\Omega}}} G_{2,3}^{1,2}\left(z_1 \,\middle|\, \begin{matrix} \frac{1}{2}, \frac{-1}{2}-m \\ 0, \frac{-1}{2}, \frac{-3}{2} \end{matrix}\right) \Bigg]\Bigg),
\end{aligned}
\tag{2.34}
$$

where $a_1 = \sqrt{\frac{m\pi\eta P_{\mathrm{t}}\Omega}{P_{\mathrm{th}}}}$ and $z_1 = \frac{-\eta P_{\mathrm{t}}\Omega(\lambda\pi)^2}{4mP_{\mathrm{th}}}$.

Cell-Edge Device

For this type, the transmission probability is found as

$$P_{\text{tr}} = \min\left(1, -\frac{(M-1)}{2\pi P_{\text{UE}}}\left(\frac{8\lambda\sqrt{\pi\lambda}m^m}{\Omega^m\Gamma(m)(\lambda\pi)^2}\right)^2 G_{1,0:1,3:1,3}^{0,1:3,1:3,1}\left(\frac{-\omega}{P_{\text{th}}}, \frac{-\omega}{P_{\text{th}}}\middle| \begin{array}{c}0\\-\end{array}\middle| \begin{array}{c}\mathbf{v}_1\\\mathbf{v}_2\end{array}\middle| \begin{array}{c}\mathbf{v}_1\\\mathbf{v}_2\end{array}\right)\right), \qquad (2.35)$$

where $\omega = \frac{4\eta P_{\text{t}}\Omega}{m(\lambda\pi)^2}$, where $\mathbf{v}_1 = [\frac{-1}{2}, 0, 1-m]$ and $\mathbf{v}_2 = [1]$.

For comparison, we also consider when the Type-II UE is served by a single AP. The transmission probability is given by Eq. (2.36), where $b_1 = \frac{9(\lambda\pi)^{\frac{3}{2}}\left(\frac{\Omega\eta P_{\text{t}}}{mP_{\text{th}}}\right)^{\frac{3}{4}}}{\Gamma(m)}$, $b_2 = \frac{3(\lambda\pi)^{\frac{7}{2}}\eta P_{\text{t}}\Omega\left(\frac{\Omega\eta P_{\text{t}}}{P_{\text{th}}}\right)^{\frac{3}{4}}}{2m^{\frac{7}{4}}\Gamma(m)}$,

$b_3 = \frac{3(\frac{\Omega}{m})^{\frac{7}{4}}(\lambda\pi)^2\eta P_{\text{t}}\left(\frac{\pi\eta P_{\text{t}}}{P_{\text{th}}}\right)^{\frac{3}{4}}}{4\Gamma(m)}$, $b_4 = \frac{9P_{\text{th}}\left(\frac{\Omega\pi\eta P_{\text{t}}}{mP_{\text{th}}}\right)^{\frac{3}{4}}}{4\Gamma(m)}$, $b_5 = \frac{3\left(\frac{\eta P_{\text{t}}}{P_{\text{th}}}\right)^{\frac{1}{4}}}{\Gamma(\frac{1}{4})\Gamma(\frac{5}{4})}$, $b_6 = \frac{2P_{\text{th}}\sqrt{\frac{m\pi\lambda}{\Omega}}\Gamma(\frac{3}{4}+m)\Gamma(\frac{1}{4})^2}{4\left(\frac{m}{\Omega}\right)^{\frac{3}{4}}\Gamma(m)\Gamma(\frac{1}{4}+m)}$,

$b_7 = \frac{\Gamma(\frac{1}{4})2\sqrt{\frac{m}{\Omega}}\Gamma(\frac{5}{4})(\lambda\pi)^{\frac{5}{2}}\eta P_{\text{t}}\Omega^{\frac{7}{4}}}{m^{\frac{3}{4}}\Gamma(m)}$, $b_8 = \frac{\Gamma(\frac{1}{4})\sqrt{\frac{m\pi}{\Omega}}\Omega^{\frac{3}{4}}}{2m^{\frac{3}{4}}\Gamma(\frac{5}{4})}$, $b_9 = \frac{(\lambda\pi)^2\eta P_{\text{t}}\Omega}{m}$, $w = \frac{-\eta P_{\text{t}}\Omega(\lambda\pi)^2}{4mP_{\text{th}}}$.

$$P_{\text{tr}} = \min\left(1, \frac{(M-1)}{12P_{\text{UE}}}\left[b_1 G_{2,3}^{3,2}\left(w\middle| \begin{array}{c}\frac{5}{4}, \frac{1}{4}-m\\0, \frac{1}{4}, \frac{-1}{2}\end{array}\right) + b_2 G_{2,3}^{3,2}\left(w\middle| \begin{array}{c}\frac{1}{4}, \frac{-3}{4}-m\\0, \frac{-3}{4}, \frac{-3}{2}\end{array}\right) + b_3 G_{3,4}^{4,3}\left(w\middle| \begin{array}{c}\frac{-3}{4}, \frac{-3}{4}-m, \frac{1}{4}\\\frac{-7}{4}, \frac{-3}{2}, \frac{-3}{4}, 0\end{array}\right)\right.\right.$$

$$+ b_4 G_{3,4}^{4,3}\left(w\middle| \begin{array}{c}\frac{1}{4}, \frac{1}{4}-m, \frac{5}{4}\\\frac{-3}{4}, \frac{-1}{2}, 0, \frac{1}{4}\end{array}\right) - b_5\left[b_6 G_{2,3}^{3,2}\left(w\middle| \begin{array}{c}\frac{7}{4}, \frac{3}{4}-m\\0, \frac{3}{4}, \frac{1}{2}\end{array}\right) + b_7 G_{2,3}^{3,2}\left(w\middle| \begin{array}{c}\frac{3}{4}, \frac{-1}{4}-m\\0, \frac{-1}{4}, \frac{-1}{2}\end{array}\right)\right.$$

$$\left.\left.\left. + b_8 b_9 G_{3,4}^{4,3}\left(w\middle| \begin{array}{c}\frac{-1}{4}, \frac{-1}{4}-m, \frac{3}{4}\\\frac{-5}{4}, \frac{-1}{2}, \frac{-1}{4}, 0\end{array}\right) + b_8 P_{\text{th}} G_{3,4}^{4,3}\left(w\middle| \begin{array}{c}\frac{3}{4}, \frac{3}{4}-m, \frac{7}{4}\\\frac{-1}{4}, 0, \frac{1}{2}, \frac{3}{4}\end{array}\right)\right]\right]\right). \qquad (2.36)$$

where $\omega = \frac{4\eta P_{\text{t}}\Omega}{m(\lambda\pi)^2}$.

Vertex-Cell Device

The transmission probability of Type-III typical device is

$$P_{\text{tr}} = \min\left(1, -\frac{(M-1)}{2\pi P_{\text{UE}}}\left(\frac{4m^m}{\Gamma(m)\Omega^m\sqrt{\pi}}\right)^3 G_{1,0:1,3:1,3:1,3}^{0,1:3,1:3,1:3,1}\left(\frac{-\omega}{P_{\text{th}}}, \frac{-\omega}{P_{\text{th}}}, \frac{-\omega}{P_{\text{th}}}\middle| \begin{array}{c}0\\-\end{array}\middle| \begin{array}{c}\mathbf{v}_1\\\mathbf{v}_2\end{array}\middle| \begin{array}{c}\mathbf{v}_1\\\mathbf{v}_2\end{array}\middle| \begin{array}{c}\mathbf{v}_1\\\mathbf{v}_2\end{array}\right)\right).$$

$$(2.37)$$
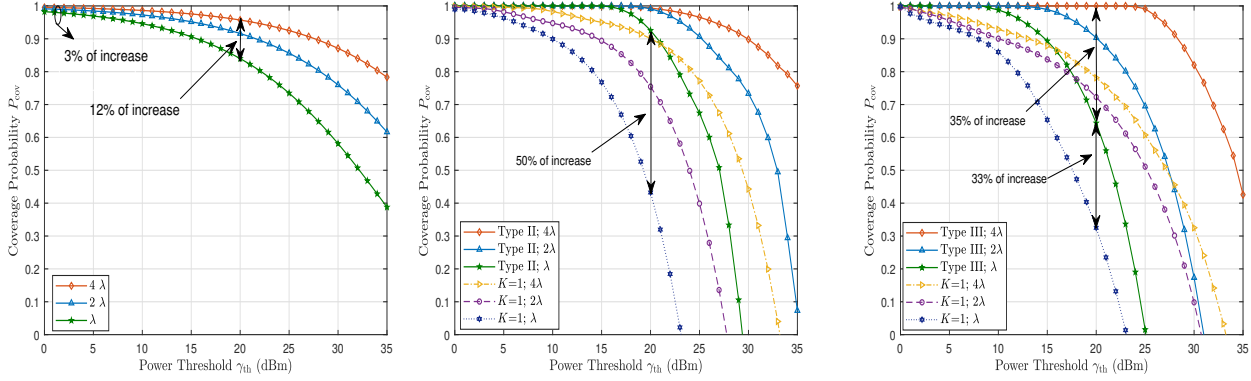
Figure 2.2: The coverage probability versus the power threshold γ_{th} for typical UE at (a) inner cell, (b) edge of cells and (c) vertex of Voronoi cells.

where $\omega = \frac{4\eta P_t \Omega}{m(\lambda\pi)^2}$. Also, when the Type-III device is served by a single AP, its transmission probability is given by:

$$
P_{\text{tr}} = \min\left(1, \frac{(M-1)\sqrt{\frac{\eta P_t}{P_{\text{th}}}}}{3P_{\text{UE}}}\left[c_1 G_{2,3}^{3,2}\left(w_1 \left|\begin{array}{c} \frac{3}{2}, \frac{-1}{2} - m \\ 0, \frac{1}{2}, \frac{1}{2} \end{array}\right.\right)\right.\right.
$$

$$
+ c_2 G_{2,3}^{3,2}\left(w_1 \left|\begin{array}{c} \frac{3}{2}, \frac{1}{2} - m \\ 0, \frac{1}{2}, \frac{-1}{2} \end{array}\right.\right) + c_3\left[c_1 G_{2,3}^{3,2}\left(w_1 \left|\begin{array}{c} \frac{1}{2}, \frac{-1}{2} - m \\ 0, \frac{-1}{2}, \frac{-1}{2} \end{array}\right.\right) + \frac{3c_2}{P_{\text{th}}} G_{2,3}^{3,2}\left(w_1 \left|\begin{array}{c} \frac{1}{2}, \frac{-1}{2} - m \\ 0, \frac{-1}{2}, \frac{-3}{2} \end{array}\right.\right)\right]
$$

$$
+ c_4\left[{}_1F_1\left(1+m; \frac{3}{2}; -w_1\right) - 1\right] - c_5 G_{2,3}^{3,2}\left(w_1 \left|\begin{array}{c} -m, 1 \\ 0, 0, \frac{-1}{2} \end{array}\right.\right) + c_6 G_{2,3}^{3,2}\left(z_1 \left|\begin{array}{c} -m, 1 \\ 0, 0, \frac{-1}{2} \end{array}\right.\right)\right), \quad (2.38)
$$

where $c_1 = \frac{-3\lambda\pi\Omega\sqrt{\frac{\pi m}{\Omega}}P_{\text{th}}}{2\Gamma(m-1)}$, $c_2 = \frac{\lambda\pi^{\frac{3}{2}}P_{\text{th}}}{4\Gamma(m)\sqrt{\frac{m}{\Omega}}}$, $c_3 = \frac{2\lambda\pi\Gamma\left(\frac{1}{2}+m\right)}{\Gamma(m)\sqrt{\frac{m}{\Omega}}}$, $c_4 = (\lambda\pi)^2 m(m-1)\eta P_t \Omega$, $c_5 = \frac{3(\lambda\pi)^2\Omega\sqrt{\pi}}{6\Gamma(m-1)}$, $c_6 = \frac{(\lambda\pi)^2\eta P_t \Omega\sqrt{\pi}}{4\Gamma(1+m)}$, $z_1 = \frac{-\eta P_t \Omega(\lambda\pi)^2}{4mP_{\text{th}}}$ and $w_1 = \frac{-\lambda\pi\Gamma\left(\frac{1}{2}+m\right)}{\Gamma(m)\sqrt{\frac{m}{\Omega}}P_{\text{th}}}$.

2.5 Performance Evaluation

Numerical results for the coverage and transmission probabilities as per the developed analysis are now presented. Unless otherwise stated, the simulation parameters are as follows: $P_t = 50$ dBm, $P_{\text{UE}} = 10$ dBm, $\eta = 0.75$, $\Omega = 7.7$, $\alpha = 4$, $m = 3$, and $M = 4$. The nominal value for the density of APs is $\lambda = 0.005$, and the unit of density is $1/\text{m}^2$.

Figure 2.2(a) illustrates the power coverage probability versus the power threshold, for a typical device of Type I, i.e., at the inner cell. For a given threshold value, the higher the density of the

APs is, the higher the coverage probability will be. For instance, when the AP density is four times the nominal density λ, a gain of 12% can be attained when $\gamma_{\text{th}} = 20$ dBm, and reaches 40% when $\gamma_{\text{th}} = 35$ dBm. For very low thresholds $\gamma_{\text{th}} \leq 5$ dBm, the coverage probability is similar for the three density values. Significant coverage gain is obtained for high threshold values. Therefore, target power coverage can be reached with reduced AP densities, thereby reducing the implementation complexity for practical deployment.

Figure 2.2(b) shows the coverage metric versus γ_{th}, for different numbers of APs servicing a typical device at the edge of Voronoi cells, and different APs' densities. Plots validate that coordinated beamforming enhances the power coverage of the network, e.g., when the density is λ, a gain of 50% is attained when $\gamma_{\text{th}} = 20$ dBm and two APs are used, compared to the case with $K = 1$ AP. Increasing density enhances the power coverage as it brings the APs closer to the devices, e.g., a gain of 10% can be reached for the scenario with $\gamma_{\text{th}} = 20$ dBm, $K = 2$, and a density of four times the nominal λ, compared to the same setting but with density 2λ.

The same behaviors w.r.t. the number of servicing APs and the densities are observed in Fig. 2.2(c), which illustrates the coverage probability at a vertex-cell device. For the case with density λ and $\gamma_{\text{th}} = 20$, a 33% gain is attained with three cooperative APs compared to the case with $K = 1$.
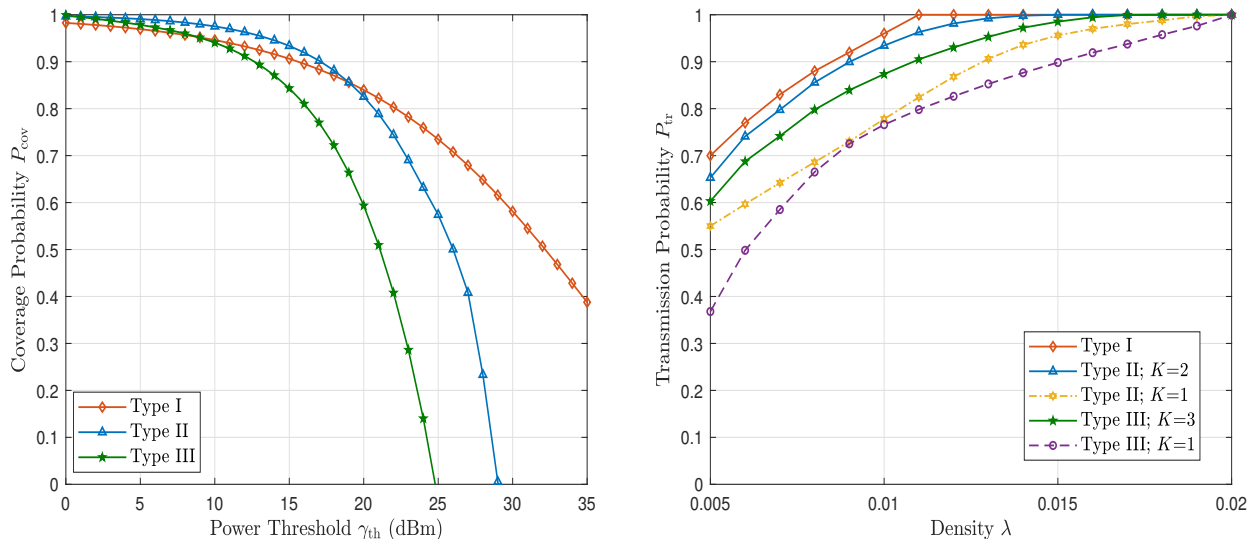
Figure 2.3: (a) Coverage probability versus the power threshold γ_{th} for the three device types, with $\lambda = 0.005$; (b) Transmission probability versus the AP density for the three device types, with $P_{\text{th}} = 15$ dBm.

Figure 2.3(a) compares the coverage probability for the three device types in a network with AP density $\lambda = 0.005$. As the received signal decays with the distance, all types of devices experience large path loss, and the coverage decreases drastically for high threshold values. A typical device at the vertex of cells, i.e., Type III, corresponds to the worst case, due to the highest path loss compared to the two other cases which leads to significant decrease in wireless power coverage.

Figure 2.3(b) shows the transmission probability for the three device types versus the AP density. Here, the energy harvesting saturation threshold is set at $P_{\text{th}} = 15$ dBm. Plots validate that cooperative WPT enhances performance. For a given density value, the higher the number of servicing APs, the higher the transmission probability. As expected, P_{tr} increases with higher density. Indeed, increasing density will shorten the distance between the devices and the servicing AP(s), which improves the efficiency of the WPT, thus enhancing the transmission probability. Besides, it is confirmed that a typical device at the vertex of cells, i.e., Type III, exhibits the lowest transmission probability.

2.6   Concluding Remarks

For wireless powered communication networks, where access points transmit power to the devices on the downlink for their data transmission on the uplink, we considered distributed energy beamforming to maximize the harvested energy, and obtained the power coverage and transmission probabilities for three typical device types. The developed formulae and the ensuing numerical results confirm the gains of the cooperative wireless power transfer, and are useful for network optimization and dimensioning with low complexity.

Chapter 3

Coordinated Energy Beamforming: Triangular Poisson-Delaunay

3.1   Introduction

In the literature, two distinct methodologies are used for the investigation of coordinated transmissions in cellular networks. The deterministic approach, which is based on the regular hexagonal cellular model, has been widely used and is known to be non-suitable for modeling the network in practical deployment scenarios [67–69]. The second approach is based on the theory of stochastic geometry, and has been shown to outclass the first in the modeling and analysis of cellular networks [70, 71]. Stochastic geometry is in fact an efficient tool for capturing the average behavior of networks and their randomness nature [72, 73]. Generally, a Poisson point process (PPP) is used to describe the distribution of APs in such networks, while devices are assumed to be uniformly distributed in the coverage area of the network [56, 57, 72].

In the context of cooperative WPT, the work in [32] investigated a cooperative transmission strategy for energy-harvesting based small-cell APs, and derived the cell load distributions, the average user capacity, and the coverage probability via Gamma approximation. The work in [74] investigated a multi-cell network with cooperative non-orthogonal multiple access and energy harvesting, and derived closed-form expressions for the coverage probability, ergodic rate, and energy

---

[0]The contents of this chapter are extracted from [66].

efficiency. In [58], the authors considered a large-scale network where multiple devices were wirelessly charged by power beacons in the millimeter wave. Using stochastic geometry, the work derived an approximate expression for the power coverage probability while considering only one type of devices randomly distributed in the coverage area. In [75], an analytical and experimental study on a distributed antenna system for WPT was presented and its effects on the coverage probability were analyzed. In the aforementioned works, a device is assumed to connect only to the nearest AP(s) in its cooperating set. For instance, our recent work [56] investigated the power coverage and transmission probability in Poisson-Voronoi tessellations, and showed the superiority of using coordinated WPT in enhancing performances.

When using stochastic geometry for the modeling and analysis of wireless networks, be it for WPT, data trainer, or joint power and data transfer, distributions of the distances between the network nodes are required. Such distance distributions can be used to study important network characteristics, including interference, outage, connectivity, routing, energy consumption, etc. [76, 77]. In general, there are two types of distance distributions that are needed in the stochastic geometry modelling, (i) the distribution of the distance between a given reference node and a random node located inside a cell, and (ii) the distribution of the distance between two random nodes (located in different cells). An example of the former is the nearest neighbor distance distribution when the reference node (e.g., AP) is located at the center of the cell [57, 73, 78], and an example of the latter is the distribution of the distance between randomly located nodes in different cells. In the last decade, many works have investigated the first type of distance distribution. The most general result in the literature, summarized in [57], can compute distance distributions in Voronoi cells. However, this model does not accurately reflect the distance distributions in many practical network deployment scenarios where a finite number of nodes are uniformly and independently distributed over a finite area such as square, hexagon, triangle, or disk region.

Different from previous works, the focus of this work is on the second type of distance distributions, i.e., when the points belong to different cells. The derivations are significantly more complicated, and consequently the literature is not completed. Obtaining closed-form expressions for the distance distributions in this case has almost exclusively been limited to the scenario where points are randomly distributed [76, 78–80]. The most common strategy for obtaining the distance distributions is by first computing the cumulative distribution function (CDF) and then differentiating it to find the probability density function (PDF). Computing the CDF amounts to finding the

area of intersection of a given circle and the region in question, so computing this area of intersection is the main mathematical challenge.

Keeping the above challenges in mind, we propose a wireless powered communication network, where multiple APs collaborate together to meet the energy demands of the harvesting devices on the downlink. The APs are distributed according to a PPP, and the devices are uniformly distributed in the coverage area. We study the performance of the coordinated transmissions based on a Poisson-Delaunay triangulation forming the cooperating set. According to the Euclidean distances from a device to its three serving APs, devices in the network are classified into three types, namely, Type-I, Type-II and Type-III. In the Poisson-Delaunay triangular tessellation, the PDF of the distance between a device and the APs is still unknown, and so is the wireless power coverage of such type of devices.

Motivated by these facts, the main contributions are threefold:

- Presenting a general framework for analytically computing the closed-form PDF of the distance between random nodes. With the obtained formulae, commonly used statistical metrics such as variance, skewness, and kurtosis, of the distance distribution can be easily calculated. Here, they are used for simplifying and calculating the integrals to obtain closed-form expressions for the power coverage probabilities, which help to overcome the complexity of the numerical implementation of these kinds of metrics.

- Using the obtained distance PDFs, we derive the downlink wireless power coverage probabilities in their closed forms for the three device types mentioned above. The formulae involved the extended generalized multivariate MeijerG function (EGMMGF) whose evaluation poses some challenges. Herein, we develop a Matlab code to numerically evaluate this function.

- Providing numerical results for the cooperative and the non-cooperative WPT, and also presenting comparisons for transmission cases over Rayleigh and Nakagami-m fading channels.

In detailing the organization of the chapter is as follows. Section 3.2 elaborates the proposed wireless powered cooperative model. The wireless power coverage framework is presented in Section 3.3. In particular, the fundamental statistics for the coverage probability calculation are provided in Section 3.3.1 and the coverage probability analysis for different device types is then pre-

sented in Section 3.3.2. The numerical results are provided in Section 3.4, and Section 3.5 concludes the chapter.

3.2 Cooperative WPT

We consider a WPT network, where each device harvests energy from the WPT from a set of cooperating APs. The APs, each equipped with N antennas, are distributed in a two-dimensional infinite plane according to a homogeneous PPP, denoted by Φ, with intensity λ (cf. Fig. 3.1). The single-antenna devices are uniformly distributed in the plane. The set of cooperating APs, denoted by Φ_c of cardinality $|\Phi_c| = K$, sends energy to a target device. Without loss of generality, we set the transmission duration T to unity.
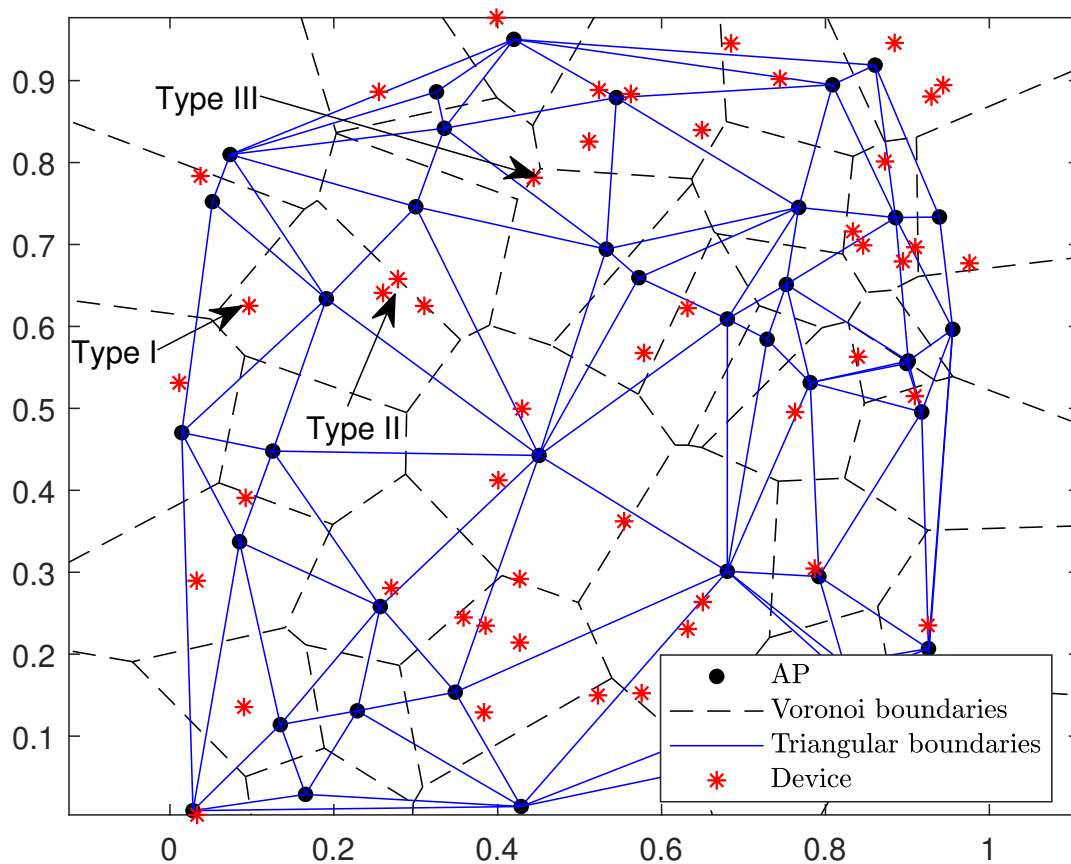
Figure 3.1: The wireless network: polygons with black dash-lines indicate the Poisson-Voronoi tessellation centered with the access points (APs); triangles with blue solid-lines are formed by the cooperating APs; the black filled circles represent the APs; and the red stars denote the devices.

Let us denote the channel between the kth AP in Φ_c and a typical device by $\mathbf{g}_k \in \mathbb{C}^{N \times 1}$. The channel gains include the effects of the path loss and the fast fading.[1] Here, $\mathbf{g}_k = \mathbf{h}_k \sqrt{\mathbf{D}_k}$, where $\mathbf{D}_k \in \mathbb{R}^K$ is a diagonal matrix modeling the path loss effects, with elements $[\mathbf{D}]_{k,k} = d_k^{-\alpha_1}$, $k \in \{1, 2, \cdots, K\}$, in which $\alpha_1 = 4$ is the path loss exponent and d_k is the Euclidian distance between the kth AP and the typical device, and where $\mathbf{h}_k = [h_{k,1}, \cdots, h_{k,N}]^T \in \mathbb{C}^{N \times 1}$ is the fast fading component modeled as $\mathbf{h}_k = \mathbf{h}_k^{\text{LoS}} + \mathbf{h}_k^{\text{NLoS}}$, in which $\mathbf{h}_k^{\text{LoS}}$ and $\mathbf{h}_k^{\text{NLoS}}$ are the line-of-sight (LoS) and non line-of-sight (NLoS) components. The random channel gains $h_{k,i}$ are assumed i.i.d. to avoid complex expressions, following Nakagami-m distributions with parameters (m_L, Ω_L) for $\mathbf{h}_k^{\text{LoS}}$ and (m_N, Ω_N) for $\mathbf{h}_k^{\text{NLoS}}$ [58]. Hence, the channel can be expressed as

$$\mathbf{g}_k = \left[\mathbf{h}_k^{\text{LoS}} + \mathbf{h}_k^{\text{NLoS}}\right] \mathbf{D}^{\frac{1}{2}}. \tag{3.1}$$

The received signal at a typical device is expressed as

$$y = \sum_{k \in \Phi_c} \mathbf{g}_k^H \mathbf{x}_k + z, \tag{3.2}$$

where $\mathbf{x}_k = [x_{k,1}, \cdots, x_{k,N}]^T$ is the energy signal vector determined by the beamforming, and z is a zero-mean AWGN with spectral power N_0. Signals originating from the adjacent cooperation sets are not shown in (3.2), given that we neglect their incremental contribution to the aggregate harvested energy at the device. The transmit energy signal shown in (3.2) is given by

$$\mathbf{x}_k = \sqrt{P_k} \mathbf{w}_k u_k, \tag{3.3}$$

where $\mathbf{w}_k = [w_{k,1}, \cdots, w_{k,N}]^T$ is the beamforming weight vector representing the phase shift of the signal transmitted from the kth AP, and u_k is the source base-band signal assumed to be unitary, i.e., $\mathbb{E}\{|u_k|^2\} = 1$. In (3.3), P_k denotes the transmit power of the kth AP. Assuming equal power for all elements in the cooperation set Φ_c, we can write $P_k = P_t \ \forall k$, and we assume $u_k = u \ \forall k$. Hence, the received signal at the typical device can be written as

$$y = \sum_{k \in \Phi_c} \sqrt{P_t} \mathbf{g}_k^H \mathbf{w}_k u + z. \tag{3.4}$$

---

[1]We assume full knowledge of the channel state information (CSI), and defer investigations of cases with partial and imperfect CSI to future work.

To maximize the harvested power at the device, maximum ratio transmission is used [59]. The energy beamforming vector can be written as $\mathbf{w}_k = \frac{\mathbf{g}_k}{\|\mathbf{g}_k\|}$. By using the energy conversion law and assuming no harvesting from the AWGN, the input power at the device's rectifier during the WPT from $\Phi_{\rm c}$, is given by

$$E_{\rm in} = P_{\rm t} \left| \sum_{k \in \Phi_c} \frac{\mathbf{g}_k^H \mathbf{g}_k}{\|\mathbf{g}_k\|} \right|^2 = P_{\rm t} \sum_{k \in \Phi_c} \|\mathbf{g}_k\|^2. \tag{3.5}$$

Therefore, the instantaneous received power at the device is

$$P_{\rm in} = \frac{E_{\rm in}}{T} = P_{\rm t} \sum_{k \in \Phi_c} \left\| \mathbf{h}_k^{\rm LoS} + \mathbf{h}_k^{\rm NLoS} \right\|^2 d_k^{-\alpha_1}. \tag{3.6}$$

Considering the generally adopted piece-wise linear energy-harvesting model [56], the output direct current power can be obtained as

$$P_{\rm EH} = \begin{cases} \eta P_{\rm in}, & P_{\rm in} \leq P_{\rm th}, \\ \eta P_{\rm th}, & P_{\rm in} > P_{\rm th}, \end{cases} \tag{3.7}$$

where $0 < \eta < 1$ denotes the power conversion efficiency, and $P_{\rm th}$ is the saturation threshold of the energy rectifier. It is clear that the piece-wise model reduces to the traditional linear model when $P_{\rm th}$ goes to infinity. Based on the geometric locations of the APs, the Poisson-Delaunay tessellation (PDT) dual to the Poisson-Voronoi tessellation can be constructed. Therefore, if the device is inside the Poisson-Delaunay triangular cell, the three APs at the vertices of the triangle are picked up to form its cooperating set. If the device is at the edge of the triangle, there must be another triangle sharing the same edge, and they together form a quadrilateral.

According to the Euclidean distances from the three cooperating APs, all devices in the network are classified into three types. Type-I device are those located at the centroids of triangular cells. Thus, such a device is equidistant from the three serving APs. Type-II devices are equidistant from two APs, but have another distance from the third one. Type-III devices have distinct distances from their three serving APs.

3.3 Wireless Power Coverage

3.3.1 Fundamental Statistics

We study the WPT performance using the power coverage metric, which is defined as the probability that the received power at a typical device is higher than a predefined threshold,

$$P_{\text{cov}} = \mathbb{P}\left(P_{\text{EH}} \geq \gamma_{\text{th}}\right), \tag{3.8}$$

where P_{EH} is the harvested power in one WPT block time. The coverage probability is interpreted as the complementary cumulative distribution function (CCDF) of the harvested power and expressed as [58]:[2]

$$P_{\text{cov}} = \begin{cases} 1 - \mathbb{P}\left(\eta P_{\text{t}} \sum_{k \in \Phi_c} \left\|\mathbf{h}_k^{\text{LoS}} + \mathbf{h}_k^{\text{NLoS}}\right\|^2 d_k^{-\alpha_1} < \gamma_{\text{th}}\right) \\ \qquad\qquad\qquad\qquad\qquad\qquad \text{for } \gamma_{\text{th}} \leq P_{\text{th}}; \\ 1 \qquad \text{for } \gamma_{\text{th}} > P_{\text{th}}. \end{cases} \tag{3.9}$$

As P_{EH} is the sum of K random variables involving the random channel vectors and the random distances between the device and the K serving APs, direct computation of P_{cov} when $\gamma_{\text{th}} \leq P_{\text{th}}$ is not possible. Thus, to calculate P_{cov}, we adopt an approach based on the moment generating function (MGF) [81]. The MGF of the harvested power is given by

$$\mathcal{M}_{P_{\text{EH}}}(s) = \prod_{k=1}^{K} \mathcal{M}_{P_k}(s), \tag{3.10}$$

where $\mathcal{M}_{P_k}$ is the MGF of the harvested power from the kth AP. The power coverage at a typical device is calculated as

$$P_{\text{cov}} = 1 - \int_{-\infty}^{\gamma_{\text{th}}} f_{P_{\text{EH}}}(x)\mathrm{d}x, \tag{3.11}$$

where $f_{P_{\text{EH}}}(x)$ is the PDF of the harvested power, which can be evaluated using [69, 82],

$$f_{P_{\text{EH}}}(x) = \frac{1}{2\pi} \int_{-\infty}^{\infty} \mathcal{M}_{P_{\text{EH}}}(js) \exp(-jsx)\mathrm{d}s. \tag{3.12}$$

To proceed, we first present necessary PDFs pertaining to the distances and the channel gain vectors.

---

[2]Hereafter, as it is clear from the context, P_{cov} will refer to the case when $\gamma_{\text{th}} \leq P_{\text{th}}$.

Distance PDF Derivation of Typical Devices

The space of the wireless network can be decomposed into disjoint triangles for the analysis of the devices' distances to their serving APs according to their types. The cell is modelled as a triangle as shown in Fig. 3.2, the vertices are formed by the cooperating APs, and the device is a random point distributed uniformly in the triangle.

For ease of presentation, we adopt the following symbols. Consider a triangular cell. First, we denote the cell as $\triangle A_0 A_1 A_2$, and consider the vertex A_0 as the reference point. The area of the triangular cell is denoted by $\mathcal{A}$, h is the altitude length, and $|A_0 A_1|$, $|A_0 A_2|$ and $|A_1 A_2|$ are the edges' lengths of the cell. According to the value of angle $\angle A_0 A_1 A_2$, two cases are distinguished:

- If $0 < \angle A_0 A_1 A_2 \leq \frac{\pi}{2}$, then the altitude with the base edge $A_1 A_2$ is inside the triangle as illustrated in Fig. 3.2 (a).

- If $\angle A_0 A_1 A_2 > \frac{\pi}{2}$, then the altitude with the base edge $A_1 A_2$ falls outside the triangle as shown in Fig. 3.2 (b).
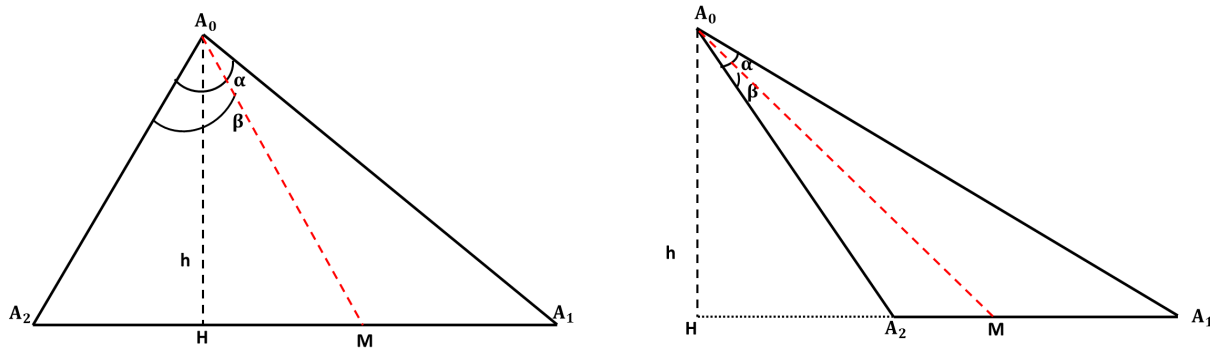
Figure 3.2: Illustration of (a) the acute case (inside altitude) and (b) the obtuse case (outside altitude).

Next, we derive the PDF of the distances for the different types of devices based on the above geometrical modelling.

Let P denote a random point representing the location of the target device within the triangle. Our goal is to study the statistical properties of $r = |A_0 P|$, that is, the Euclidean distance between the reference point A_0 and the random point P. We start by computing the CDF of r, denoted here as $F_r(r)$.
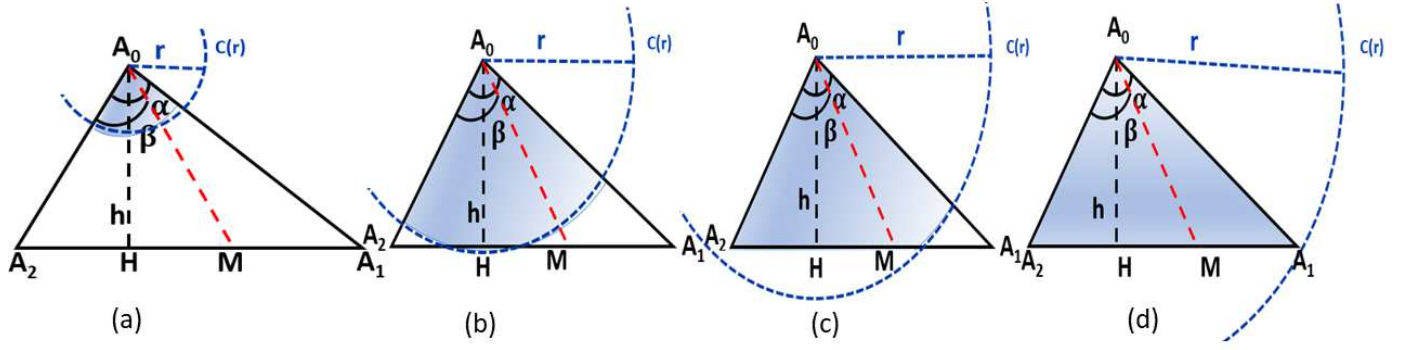
Figure 3.3: Distance distributions from vertex A_0 to a uniformly distributed random point in $\triangle A_0 A_1 A_2$: (a) Case 1: $0 < r \leq h$; (b) Case 2: $h < r \leq |A_0 A_2|$; (c) Case 3: $|A_0 A_2| < r \leq |A_0 A_1|$; and (d) Case 4: $r > |A_0 A_1|$.

Taking the approach in [79] as starting point, we draw a circle $C(r)$ of radius r and centered on the reference point A_0 to determine the desired distance distribution. The CDF $F_r(r)$ is the area colored in blue in Fig. 3.3, which corresponds to the intersection of the triangle and the circle $C(r)$, i.e., $\triangle A_0 A_1 A_2 \cap C(r)$, divided by the area of $\triangle A_0 A_1 A_2$.

According to the range of r, different cases are treated here:

- **Case 1**: $0 < r \leq h$ as shown in Fig. 3.3 (a);

- **Case 2**: $h < r \leq |A_0 A_2|$ as shown in Fig. 3.3 (b);

- **Case 3**: $|A_0 A_2| < r \leq |A_0 A_1|$ as shown in Fig. 3.3 (c);

- **Case 4**: $r > |A_0 A_1|$ as shown in Fig. 3.3 (d).

Distance PDF of Type-I Devices

The distance r between the device and each of the three APs is an identical random variable and its PDF is expressed as in [83]

$$f_r(r) = 2(\pi\lambda)^2 r^3 \exp\left(-\lambda\pi r^2\right). \tag{3.13}$$

Distance PDF of Type-II Devices

3.0

Theorem 3.1. *The PDF of the distance r of Type-II devices is expressed as*

$$f_r(r) = \begin{cases} \frac{2r}{3\pi\mathcal{A}}(4+\pi^2), & 0 < r \leq h \\ \frac{4r}{3\pi\mathcal{A}}(\pi^2-1), & h < r \leq |A_0 A_2| \\ 0, & \text{otherwise,} \end{cases} \qquad (3.14)$$

and the corresponding CDF is given by

$$F_r(r) = \begin{cases} \frac{r^2}{3\pi\mathcal{A}}(4+\pi^2), & 0 < r \leq h \\ \frac{2r^2}{3\pi\mathcal{A}}(\pi^2-1), & h < r \leq |A_0 A_2| \\ 0, & \text{otherwise.} \end{cases} \qquad (3.15)$$

The proof is provided in Appendix C.

Distance PDF of Type-III Devices

Theorem 3.2. *The PDF of the distance r of Type-III devices is given by*

$$f_r(r) = \begin{cases} 0, & r \leq 0 \\ \frac{(4+\pi^2)r}{3\pi\mathcal{A}}, & 0 < r \leq h \\ \frac{(4+\nu(\pi^2-2\pi)+\pi^2)r}{3\pi\mathcal{A}}, & h < r \leq |A_0 A_2| \\ \frac{2(\pi^2-1)r}{3\pi\mathcal{A}}, & |A_0 A_2| < r \leq |A_0 A_1| \\ \frac{3\pi^2}{2}, & r > |A_0 A_1|, \end{cases} \qquad (3.16)$$

and the CDF is expressed as

$$F_r(r) = \begin{cases} 0, & r \leq 0 \\ \frac{(4+\pi^2)r^2}{6\pi\mathcal{A}}, & 0 < r \leq h \\ \frac{(4+\nu(\pi^2-2\pi)+\pi^2)r^2}{6\pi\mathcal{A}} & h < r \leq |A_0 A_2| \\ \frac{(\pi^2-1)r^2}{3\pi\mathcal{A}}, & |A_0 A_2| < r \leq |A_0 A_1| \\ \frac{3\pi^2 r}{4}, & r > |A_0 A_1|. \end{cases} \qquad (3.17)$$

The proof is provided in Appendix C.

Distributions of $\mathbf{h}_k$ and $\|\mathbf{h}_k\|^2$

Recall that $\mathbf{h}_k = \mathbf{h}_k^{\text{LoS}} + \mathbf{h}_k^{\text{NLoS}}$, where each vector entry is the sum of two Nakagami distributed random variables with parameters (m_L, Ω_L) and (m_N, Ω_N) for the LoS and NLoS components, respectively. Hence, the entries of $\mathbf{h}_k$ can be modeled by a Nakagami distribution [63], i.e.,

$$f_{h_{k,i}}(x) = \frac{2m^m x^{2m-1}}{\Gamma(m)\Omega^m} \exp\left(-\frac{mx^2}{\Omega}\right), \tag{3.18}$$

where $\Omega = \mathbb{E}\left[h_{k,i}^2\right]$ and $m = \frac{\Omega^2}{\text{Var}\left[h_{k,i}^2\right]} = \frac{\Omega^2}{\mathbb{E}\left[h_k^4\right] - \Omega^2}$. The moments $\mathbb{E}\left[h_{k,i}^2\right]$ and $\mathbb{E}\left[h_{k,i}^4\right]$ can be calculated using [63, (6)].

The nth moment of $h_{k,i}$ is given by $\mathbb{E}[h_{k,i}^n] = \sum\limits_{n_1=0}^{n} \sum\limits_{n_2=0}^{n_1} \binom{n}{n_1} \binom{n_1}{n_2} \mathbb{E}\left[h_1^{n-n_1}\right] \mathbb{E}\left[h_2^{n_1-n_2}\right]$, and we have $\mathbb{E}\left[h_1^n\right] = \mathbb{E}[(h_{k,i}^{\text{LoS}})^n] = \frac{\Gamma(m_L+\frac{n}{2})}{\Gamma(m_L)}\left(\frac{\Omega_L}{m_L}\right)^{\frac{n}{2}}$ and $\mathbb{E}\left[h_2^n\right] = \mathbb{E}[(h_{k,i}^{\text{NLoS}})^n] = \frac{\Gamma(m_N+\frac{n}{2})}{\Gamma(m_N)}\left(\frac{\Omega_N}{m_N}\right)^{\frac{n}{2}}$. The magnitude of the element $h_{k,i}$ denoted as $|h_{k,i}|$ follows a Nakagami-m distribution and, as such, $|h_{k,i}|^2$ follows the Erlang distribution, which is a special case of the Gamma distribution. Hence, $\|\mathbf{h}_k\|^2$ is also of an Erlang distribution given by [84]

$$f_{\|\mathbf{h}_k\|^2}(x) = \frac{m^m x^{m-1}}{\Omega^m \Gamma(m)} \exp\left(-\frac{mx}{\Omega}\right). \tag{3.19}$$

3.3.2 Analysis

Coverage Probability for Type-I Devices

For a typical device of Type-I, the distance distribution is as shown in Eq. (3.13). In this case, the MGF of the harvested energy from K APs is as given by [56]

$$\mathcal{M}_{P_{\text{EH}}}(s) = \left(\frac{4m^m}{\Gamma(m)\Omega^m \sqrt{\pi}}\right)^K \left(G_{3,1}^{1,3}\left(\begin{array}{c} \frac{-1}{2}, 0, 1-m \\ 1 \end{array} \middle| \frac{4s\eta P_{\text{t}}\Omega}{m(\lambda\pi)^2}\right)\right)^K. \tag{3.20}$$

46

Therefore, the PDF of the harvested power is expressed as

$$f_{P_{\text{EH}}}(x) = \frac{-1}{2\pi x} \left(\frac{4m^m}{\Gamma(m)\Omega^m\sqrt{\pi}} \right)^3 G^{0,1:1,3:1,3:1,3}_{1,0:3,1:3,1:3,1} \left(\begin{array}{c} 0 \\ - \end{array} \middle| \begin{array}{c} \mathbf{v}_1 \\ \mathbf{v}_2 \end{array} \middle| \begin{array}{c} \mathbf{v}_1 \\ \mathbf{v}_2 \end{array} \middle| \begin{array}{c} \mathbf{v}_1 \\ \mathbf{v}_2 \end{array} \middle| \frac{-\omega}{x}, \frac{-\omega}{x}, \frac{-\omega}{x} \right), \qquad (3.21)$$

where $\mathbf{v}_1 = [-\frac{1}{2}, 0, 1-m]$, $\mathbf{v}_2 = [1]$ and $\omega = \frac{4\eta P_t \Omega}{m(\lambda\pi)^2}$. Then, using Eq. (3.11) and some mathematical manipulations, the power coverage probability for a typical device of Type-I is obtained as follows:

$$P_{\text{cov}}(\lambda, \gamma_{\text{th}}) = 1 + \frac{1}{2\pi} \left(\frac{4m^m}{\Gamma(m)\Omega^m\sqrt{\pi}} \right)^3 G^{0,1:1,3:1,3:1,3}_{1,0:3,1:3,1:3,1} \left(\begin{array}{c} 0 \\ - \end{array} \middle| \begin{array}{c} \mathbf{v}_1 \\ \mathbf{v}_2 \end{array} \middle| \begin{array}{c} \mathbf{v}_1 \\ \mathbf{v}_2 \end{array} \middle| \begin{array}{c} \mathbf{v}_1 \\ \mathbf{v}_2 \end{array} \middle| \frac{-\omega}{\gamma_{\text{th}}}, \frac{-\omega}{\gamma_{\text{th}}}, \frac{-\omega}{\gamma_{\text{th}}} \right). \qquad (3.22)$$

Coverage Probability for Type-II Devices

For this type of devices, the distance distribution is as shown in Eq. (3.14). Next, the coverage probability is calculated separately for the four cases defined in Section 3.3.1.

Case 1: The MGF of the harvested energy from the kth AP is given by

$$\begin{aligned}
\mathcal{M}_{P_k}(s) &= \mathbb{E}_{x,d}\left[\exp\left(-s\eta P_t \|\mathbf{h}_k\|^2 d_k^{-\alpha_1} \right) \right] \\
&= \frac{m^m}{\Omega^m\Gamma(m)} \int_0^{+\infty} \int_0^{\infty} \exp\left(-s\eta P_t x d^{-\alpha_1} - \frac{mx}{\Omega} \right) x^{m-1} f_d(d)\mathrm{d}x\mathrm{d}d \\
&= \frac{2(4+\pi^2)m^m}{3\pi\mathcal{A}\Omega^m\Gamma(m)} \int_0^{+\infty} \int_0^h \exp\left(-s\eta P_t x d^{-\alpha_1} - \frac{mx}{\Omega} \right) x^{m-1}\mathrm{d}d\mathrm{d}x\mathrm{d}d \\
&= \frac{2(4+\pi^2)m^m}{3\pi\mathcal{A}\Omega^m\Gamma(m)} \int_0^h d\left(s\eta P_t d^{-\alpha_1} + \frac{m}{\Omega} \right)^{-m} \mathrm{d}d \\
&= \frac{2(4+\pi^2)m^m}{3\pi\mathcal{A}\Omega^m\Gamma(m)} \underbrace{\int_0^h dG^{1,1}_{1,1}\left(\begin{array}{c} 1-m \\ 0 \end{array} \middle| \frac{s\eta P_t \Omega d^{-\alpha_1}}{m} \right) \mathrm{d}d}_{I_1}. \qquad (3.23)
\end{aligned}$$

Direct evaluation of Eq. (3.23) is not available in the literature. Using the proprieties of the MeijerG function, and setting $\alpha_1 = 4$, I_1 can be expressed as

$$\begin{aligned}
I_1 &= \int_0^h dG^{1,1}_{1,1}\left(\begin{array}{c} 1 \\ m \end{array} \middle| \frac{m}{s\eta P_t \Omega d^{-\alpha_1}} \right) \mathrm{d}d \\
&= \frac{h^2(\frac{mh^4}{s\eta P_t\Omega})^m\Gamma(m)_2F_1\left(m; \frac{1}{2}+m; \frac{3}{2}+m; \frac{-h^4 m}{s\eta P_t\Omega} \right)}{2+4m}, \qquad (3.24)
\end{aligned}$$

which, upon substitution in Eq. (3.23) and then in Eq. (3.10), yields the MGF of the harvested energy. That is,

$$
\begin{aligned}
\mathcal{M}_{P_{\mathrm{EH}}}(s) &= \mathbb{E}_{x,d}\left[\exp\left(-s\eta P_{\mathrm{t}}\|\mathbf{h}_k\|^2 d_k^{-\alpha_1}\right)\right] \\
&= \frac{m^m}{\Omega^m\Gamma(m)}\int_0^{+\infty}\int_0^{\infty}\exp\left(-s\eta P_{\mathrm{t}}xd^{-\alpha_1}-\frac{mx}{\Omega}\right)x^{m-1}f_{\mathrm{d}}(d)\mathrm{d}x\mathrm{d}d \\
&= \left(\frac{2(4+\pi^2)m^m h^2}{3\pi\mathcal{A}\Omega^m(2+4m)}\right)^3\left(\frac{mh^4}{s\eta P_{\mathrm{t}}\Omega}\right)^{3m} {}_2F_1\left(m;\frac{1}{2}+m;\frac{3}{2}+m;\frac{-h^4m}{s\eta P_{\mathrm{t}}\Omega}\right)^3 \\
&= \left(\frac{2(4+\pi^2)m^m h^2}{3\pi\mathcal{A}\Omega^m(2+4m)}\right)^3\left(\frac{mh^4}{s\eta P_{\mathrm{t}}\Omega}\right)^{3m}\left(\frac{\Gamma(\frac{3}{2}+m)}{\Gamma(m)\Gamma(\frac{1}{2}+m)}G_{2,2}^{1,2}\left(\begin{array}{c}1-m,\frac{1}{2}-m\\0,\frac{-1}{2}-m\end{array}\Big|\frac{h^4m}{s\eta P_{\mathrm{t}}\Omega}\right)\right)^3,
\end{aligned}
$$

(3.25)

where $h = \sqrt{\frac{3\pi\mathcal{A}}{4+\pi^2}}$. The PDF of the harvested power is calculated using (3.12) after substitution of the above MGF therein. To find $f_{P_{\mathrm{EH}}}(x)$, we should first calculate the product of three MeijerG functions, i.e., $G_{2,2}^{2,1}\left(\begin{array}{c}1,\frac{3}{2}+m\\m,\frac{1}{2}+m\end{array}\Big|\frac{s\eta P_{\mathrm{t}}\Omega}{h^4m}\right)$. Using the integral representation of the MeijerG function [85, Eqs. (5) & (6)], the PDF is found as

$$
f_{P_{\mathrm{EH}}}(x) = (-x)\left(\frac{\eta P_t\Omega}{h^4m}\right)^{-3m}\frac{K_1}{2\pi}G_{1,0:2,2:2,2:2,2}^{0,1:1,2:1,2:1,2}\left(\begin{array}{c}3m\\-\end{array}\Big|\begin{array}{c}\mathbf{b}_3\\\mathbf{b}_4\end{array}\Big|\begin{array}{c}\mathbf{b}_3\\\mathbf{b}_4\end{array}\Big|\begin{array}{c}\mathbf{b}_3\\\mathbf{b}_4\end{array}\Big|\begin{array}{c}\frac{-\gamma_1}{x},\frac{-\gamma_1}{x},\frac{-\gamma_1}{x}\end{array}\right),\quad(3.26)
$$

where $K_1 = \left(\frac{2(4+\pi^2)m^m h^2}{3\pi\mathcal{A}\Omega^m(2+4m)}\right)^3$, $\mathbf{b}_3 = [1,\frac{3}{2}+m]$, $\mathbf{b}_4 = [m,\frac{1}{2}+m]$ and $\gamma_1 = \frac{\eta P_t\Omega}{h^4m}$. Finally, the wireless power coverage probability is obtained as

$$
P_{\mathrm{cov}} = 1 + \frac{K_1\gamma_{\mathrm{th}}^2}{4\pi}\left(\frac{\eta P_t\Omega}{h^4m}\right)^{-3m}G_{1,0:2,2:2,2:2,2}^{0,1:1,2:1,2:1,2}\left(\begin{array}{c}3m\\-\end{array}\Big|\begin{array}{c}\mathbf{b}_3\\\mathbf{b}_4\end{array}\Big|\begin{array}{c}\mathbf{b}_3\\\mathbf{b}_4\end{array}\Big|\begin{array}{c}\mathbf{b}_3\\\mathbf{b}_4\end{array}\Big|\begin{array}{c}\frac{-\gamma_1}{\gamma_{\mathrm{th}}},\frac{-\gamma_1}{\gamma_{\mathrm{th}}},\frac{-\gamma_1}{\gamma_{\mathrm{th}}}\end{array}\right).\quad(3.27)
$$

Case 2: In this case, the MGF is expressed as

$$
\mathcal{M}_{\mathrm{P_{EH}}}(s) = \left(\frac{m^m 4(\pi^2-1)}{3\pi\mathcal{A}\Omega^m(c_1+2c_1m)}\right)^3
$$
$$
\left(e_1^{4m+2}\left(c_1+e_1^4\right)^{1-m}{}_2F_1\left(1;\frac{3}{2};\frac{3}{2}+m;\frac{-e_1^4m}{s\eta P_{\mathrm{t}}\Omega}\right)-h^{4m+2}\left(c_1+h^4\right)^{1-m}{}_2F_1\left(1;\frac{3}{2};\frac{3}{2}+m;\frac{-h^4m}{s\eta P_{\mathrm{t}}\Omega}\right)\right)^3,
$$

(3.28)

where $e_1 = |A_0 A_1| = \sqrt{\frac{3\pi\mathcal{A}}{2(\pi^2-1)} + h^2}$, h is as defined after Eq. (3.25), and $c_1 = \frac{s\eta P_t \Omega}{m}$. The PDF of the harvested power is expressed as in Eq. (3.29),

$$
f_{P_{\mathrm{EH}}}(x) = \frac{K_2}{2\pi} \int_{-\infty}^{+\infty} (js)^{-3} \left(e_1^6 G_{3,3}^{2,2} \left(\begin{array}{c} 1, \frac{3}{2}+m, 1 \\ 1, \frac{3}{2}, m-1 \end{array} \middle| \frac{js\eta P_t \Omega}{e_1^4 m} \right) - h^6 G_{3,3}^{2,2} \left(\begin{array}{c} 1, \frac{3}{2}+m, 1 \\ 1, \frac{3}{2}, m-1 \end{array} \middle| \frac{js\eta P_t \Omega}{h^4 m} \right) \right)^3 \exp(-jsx)\mathrm{d}s
$$

$$
= \frac{K_2}{2\pi} \left(\left(e_1^6\right)^3 I_2 - 3 \left(e_1^6\right)^2 h^6 I_3 + 3 \left(h^6\right)^2 e_1^6 I_4 - \left(e_1^6\right)^3 I_5 \right). \tag{3.29}
$$

where $K_2 = \left(\frac{4m^m(\pi^2-1)}{3\pi\mathcal{A}\Omega^m} \right)^3$, and where I_2, I_3, I_4 and I_5 are obtained as shown in Appendix D, in which e and c are respectively substituted by e_1 and h to obtain Eq. (3.29) in closed form. Finally, the coverage probability is expressed as

$$
\begin{aligned}
P_{\mathrm{cov}} = 1 - \frac{K_2}{6\pi} \Bigg(& v_1 G_{1,0:3,3:3,3:3,3}^{0,1:2,2:2,2:2,2} \left(\begin{array}{c} 3 \\ - \end{array} \middle| \begin{array}{c} \mathbf{b}_5 \\ \mathbf{b}_6 \end{array} \middle| \begin{array}{c} \mathbf{b}_5 \\ \mathbf{b}_6 \end{array} \middle| \begin{array}{c} \mathbf{b}_5 \\ \mathbf{b}_6 \end{array} \middle| \frac{-\gamma_2}{\gamma_{\mathrm{th}}}, \frac{-\gamma_2}{\gamma_{\mathrm{th}}}, \frac{-\gamma_2}{\gamma_{\mathrm{th}}} \right) \\
& - v_2 G_{1,0:3,3:3,3:3,3}^{0,1:2,2:2,2:2,2} \left(\begin{array}{c} 3 \\ - \end{array} \middle| \begin{array}{c} \mathbf{b}_5 \\ \mathbf{b}_6 \end{array} \middle| \begin{array}{c} \mathbf{b}_5 \\ \mathbf{b}_6 \end{array} \middle| \begin{array}{c} \mathbf{b}_5 \\ \mathbf{b}_6 \end{array} \middle| \frac{-\gamma_2}{\gamma_{\mathrm{th}}}, \frac{-\gamma_2}{\gamma_{\mathrm{th}}}, \frac{-\gamma_1}{\gamma_{\mathrm{th}}} \right) \\
& + v_3 G_{1,0:3,3:3,3:3,3}^{0,1:2,2:2,2:2,2} \left(\begin{array}{c} 3 \\ - \end{array} \middle| \begin{array}{c} \mathbf{b}_5 \\ \mathbf{b}_6 \end{array} \middle| \begin{array}{c} \mathbf{b}_5 \\ \mathbf{b}_6 \end{array} \middle| \begin{array}{c} \mathbf{b}_5 \\ \mathbf{b}_6 \end{array} \middle| \frac{-\gamma_2}{\gamma_{\mathrm{th}}}, \frac{-\gamma_1}{\gamma_{\mathrm{th}}}, \frac{-\gamma_1}{\gamma_{\mathrm{th}}} \right) \\
& - v_4 G_{1,0:3,3:3,3:3,3}^{0,1:2,2:2,2:2,2} \left(\begin{array}{c} 3 \\ - \end{array} \middle| \begin{array}{c} \mathbf{b}_5 \\ \mathbf{b}_6 \end{array} \middle| \begin{array}{c} \mathbf{b}_5 \\ \mathbf{b}_6 \end{array} \middle| \begin{array}{c} \mathbf{b}_5 \\ \mathbf{b}_6 \end{array} \middle| \frac{-\gamma_1}{\gamma_{\mathrm{th}}}, \frac{-\gamma_1}{\gamma_{\mathrm{th}}}, \frac{-\gamma_1}{\gamma_{\mathrm{th}}} \right) \Bigg),
\end{aligned} \tag{3.30}
$$

where $\mathbf{b}_5 = [1, \frac{3}{2}+m, 1]$, $\mathbf{b}_6 = [1, \frac{3}{2}, m-1]$, $v_1 = \left(e_1^6\right)^3 \gamma_{\mathrm{th}}^3$, $v_2 = 3\left(e_1^6\right)^2 h^6 \gamma_{\mathrm{th}}^3$, $v_3 = 3\left(h^6\right)^2 e_1^6 \gamma_{\mathrm{th}}^3$, $v_4 = \left(h^6\right)^3 \gamma_{\mathrm{th}}^3$, $\gamma_2 = \frac{\eta P_t \Omega}{e_1^4 m}$, and $\gamma_1 = \frac{\eta P_t \Omega}{h^4 m}$.

Case 3: In this case, the coverage probability is unity, i.e., $P_{\mathrm{cov}} = 1$.

Coverage Probability for Type-III Devices

For this type of energy harvesting devices, the distance distribution is as shown in (3.16). Once again, four cases are treated.

Case 1: The PDF of the harvested power is calculated as in the previous type, i.e., Type-II, with $K = 3$, which yields

$$f_{P_{\text{EH}}}(x) = \frac{1}{2\pi} \left(\frac{2(4+\pi^2)m^m c^2 \Gamma(\frac{3}{2}+m)}{3\pi \mathcal{A}\Omega^m(2+4m)\Gamma(\frac{1}{2}+m)} \right)^3$$

$$\int_{-\infty}^{+\infty} \exp\left(-jsx\right) \left(\frac{js\eta P_{\text{t}}\Omega}{c^4 m} \right)^{-3m} G_{2,2}^{2,1} \left(\begin{array}{c} 1, \frac{3}{2}+m \\ m, \frac{1}{2}+m \end{array} \middle| \frac{js\eta P_{\text{t}}\Omega}{c^4 m} \right)$$

$$G_{2,2}^{2,1} \left(\begin{array}{c} 1, \frac{3}{2}+m \\ m, \frac{1}{2}+m \end{array} \middle| \frac{js\eta P_{\text{t}}\Omega}{c^4 m} \right) G_{2,2}^{2,1} \left(\begin{array}{c} 1, \frac{3}{2}+m \\ m, \frac{1}{2}+m \end{array} \middle| \frac{js\eta P_{\text{t}}\Omega}{c^4 m} \right) ds$$

$$= (-x) \left(\frac{\eta P_t \Omega}{c^4 m} \right)^{-3m} K_3 G_{1,0:2,2:2,2:2,2}^{0,1:2,1:2,1:2,1} \left(\begin{array}{c} 3m \\ - \end{array} \middle| \begin{array}{c} \mathbf{b}_3 \\ \mathbf{b}_4 \end{array} \middle| \begin{array}{c} \mathbf{b}_4 \\ \mathbf{b}_4 \end{array} \middle| \begin{array}{c} \mathbf{b}_3 \\ \mathbf{b}_4 \end{array} \middle| \frac{-\gamma_5}{x}, \frac{-\gamma_5}{x}, \frac{-\gamma_5}{x} \right), \qquad (3.31)$$

where $K_3 = \frac{1}{2\pi} \left(\frac{2(4+\pi^2)m^m c^2 \Gamma(\frac{3}{2}+m)}{3\pi \mathcal{A}\Omega^m(2+4m)\Gamma(\frac{1}{2}+m)} \right)^3$, $\mathbf{b}_3 = [1, \frac{3}{2}+m]$, $\mathbf{b}_4 = [m, \frac{1}{2}+m]$ and $\gamma_5 = \frac{\eta P_t \Omega}{c^4 m}$. Substituting this PDF in Eq. (3.11), the coverage probability is found as

$$P_{\text{cov}} = 1 - \frac{K_3 \left(\frac{\eta P_t \Omega}{c^4 m} \right)^{-3m}}{(2\pi j)^4} \int_{\mathcal{R}_1} \int_{\mathcal{R}_2} \int_{\mathcal{R}_3} \int_{\mathcal{R}_4} \prod_{i=1}^3 \frac{\Gamma(m+r_i)\Gamma(\frac{1}{2}+m-r_i)\Gamma(-r_i)}{\Gamma(\frac{3}{2}+m+r_i)}$$

$$\times \Gamma(1-r_4) \int_{-\infty}^{\gamma_{\text{th}}} \left(\frac{\gamma_5}{x} \right)^{-r_i} (x)^{3m-1} dr_1 dr_2 dr_3 dr_4 dx$$

$$= 1 + K_3 \left(\frac{\eta P_t \Omega}{c^4 m} \right)^{-3m} \frac{\gamma_{\text{th}}^2}{2} G_{1,0:2,2:2,2:2,2}^{0,1:2,1:2,1:2,1} \left(\begin{array}{c} 3m \\ - \end{array} \middle| \begin{array}{c} \mathbf{b}_3 \\ \mathbf{b}_4 \end{array} \middle| \begin{array}{c} \mathbf{b}_3 \\ \mathbf{b}_4 \end{array} \middle| \begin{array}{c} \mathbf{b}_3 \\ \mathbf{b}_4 \end{array} \middle| \frac{-\gamma_5}{\gamma_{\text{th}}}, \frac{-\gamma_5}{\gamma_{\text{th}}}, \frac{-\gamma_5}{\gamma_{\text{th}}} \right). \qquad (3.32)$$

Case 2: In this case, the PDF of the harvested power is obtained as shown in (3.33),

$$f_{P_{\text{EH}}}(x) = \frac{K_4}{2\pi} \int_{-\infty}^{\infty} (js)^{-3} \left(e^6 G_{3,3}^{2,2} \left(\begin{array}{c} 1, \frac{3}{2}+m, 1 \\ 1, \frac{3}{2}, m-1 \end{array} \middle| \frac{js\eta P_{\text{t}}\Omega}{e^4 m} \right) - c^6 G_{3,3}^{2,2} \left(\begin{array}{c} 1, \frac{3}{2}+m, 1 \\ 1, \frac{3}{2}, m-1 \end{array} \middle| \frac{js\eta P_{\text{t}}\Omega}{c^4 m} \right) \right)^3 \exp(-jsx) ds$$

$$= \frac{K_4}{2\pi} \left(\left(e^6 \right)^3 I_2 - 3 \left(e^6 \right)^2 c^6 I_3 + 3 \left(c^6 \right)^2 e^6 I_4 - \left(c^6 \right)^3 I_5 \right). \qquad (3.33)$$

where $K_4 = \left(\frac{m^m(4+\nu(\pi^2-2\pi)+\pi^2)2\Gamma(\frac{3}{2}+m)m}{6\pi \mathcal{A}\Omega^m \sqrt{\pi}\Gamma(m-1)\eta P_t \Omega(1+2m)} \right)^3$, $e = |A_0 A_1| = \sqrt{2\left(\frac{3\pi \mathcal{A}}{4+\nu(\pi^2-2\pi)+\pi^2} + 1 \right)}$ and $c = \sqrt{\frac{6\pi \mathcal{A}}{4+\pi^2}}$, and where I_2, I_3, I_4 and I_5 are as provided in Appendix D. Therefore, the coverage proba-

bility in this case is given by

$$
\begin{aligned}
P_{\text{cov}} = 1 - \frac{K_4}{6\pi} & \left(v_5 G^{0,1:2,2:2,2:2,2}_{1,0:3,3:3,3:3,3} \left(\begin{array}{c} 3 \\ - \end{array} \middle| \begin{array}{c} \mathbf{b}_5 \\ \mathbf{b}_6 \end{array} \middle| \begin{array}{c} \mathbf{b}_5 \\ \mathbf{b}_6 \end{array} \middle| \begin{array}{c} \mathbf{b}_5 \\ \mathbf{b}_6 \end{array} \middle| \frac{-\gamma_6}{\gamma_{\text{th}}}, \frac{-\gamma_6}{\gamma_{\text{th}}}, \frac{-\gamma_6}{\gamma_{\text{th}}} \right) \right. \\
& - v_6 G^{0,1:2,2:2,2:2,2}_{1,0:3,3:3,3:3,3} \left(\begin{array}{c} 3 \\ - \end{array} \middle| \begin{array}{c} \mathbf{b}_5 \\ \mathbf{b}_6 \end{array} \middle| \begin{array}{c} \mathbf{b}_5 \\ \mathbf{b}_6 \end{array} \middle| \begin{array}{c} \mathbf{b}_5 \\ \mathbf{b}_6 \end{array} \middle| \frac{-\gamma_6}{\gamma_{\text{th}}}, \frac{-\gamma_6}{\gamma_{\text{th}}}, \frac{-\gamma_5}{\gamma_{\text{th}}} \right) \\
& + v_7 G^{0,1:2,2:2,2:2,2}_{1,0:3,3:3,3:3,3} \left(\begin{array}{c} 3 \\ - \end{array} \middle| \begin{array}{c} \mathbf{b}_5 \\ \mathbf{b}_6 \end{array} \middle| \begin{array}{c} \mathbf{b}_5 \\ \mathbf{b}_6 \end{array} \middle| \begin{array}{c} \mathbf{b}_5 \\ \mathbf{b}_6 \end{array} \middle| \frac{-\gamma_6}{\gamma_{\text{th}}}, \frac{\gamma_5}{\gamma_{\text{th}}}, \frac{-\gamma_5}{\gamma_{\text{th}}} \right) \\
& \left. - v_8 G^{0,1:2,2:2,2:2,2}_{1,0:3,3:3,3:3,3} \left(\begin{array}{c} 3 \\ - \end{array} \middle| \begin{array}{c} \mathbf{b}_5 \\ \mathbf{b}_6 \end{array} \middle| \begin{array}{c} \mathbf{b}_5 \\ \mathbf{b}_6 \end{array} \middle| \begin{array}{c} \mathbf{b}_5 \\ \mathbf{b}_6 \end{array} \middle| \frac{-\gamma_5}{\gamma_{\text{th}}}, \frac{-\gamma_5}{\gamma_{\text{th}}}, \frac{-\gamma_5}{\gamma_{\text{th}}} \right) \right),
\end{aligned} \tag{3.34}
$$

where $\mathbf{b}_5$ and $\mathbf{b}_6$ are defined after Eq. (3.30), $v_5 = \left(e^6\right)^3 \gamma_{\text{th}}^3$, $v_6 = 3\left(e^6\right)^2 c^6 \gamma_{\text{th}}^3$, $v_7 = 3\left(c^6\right)^2 e^6 \gamma_{\text{th}}^3$, $v_8 = \left(c^6\right)^3 \gamma_{\text{th}}^3$ and $\gamma_6 = \frac{\eta P_{\text{t}} \Omega}{e^4 m}$.

Case 3: Here, the PDF of the harvested power is expressed as

$$
\begin{aligned}
f_{P_{\text{EH}}}(x) = K_5 & \int_{-\infty}^{\infty} (js)^{-3} \left(d^6 G^{2,2}_{3,3} \left(\begin{array}{c} 1, \frac{3}{2}+m, 1 \\ 1, \frac{3}{2}, m-1 \end{array} \middle| \frac{js\eta P_{\text{t}}\Omega}{d^4 m} \right) - e^6 G^{2,2}_{3,3} \left(\begin{array}{c} 1, \frac{3}{2}+m, 1 \\ 1, \frac{3}{2}, m-1 \end{array} \middle| \frac{js\eta P_{\text{t}}\Omega}{e^4 m} \right) \right)^3 \exp(-jsx)\mathrm{d}s \\
& = K_5 \left(\left(d^6\right)^3 I_2 - 3\left(d^6\right)^2 e^6 I_3 + 3\left(e^6\right)^2 d^6 I_4 - \left(e^6\right)^3 I_5 \right).
\end{aligned} \tag{3.35}
$$

where $K_5 = \frac{\left((\pi^2-1)m^m\right)^3}{2\pi(3\pi\mathcal{A}\Omega^m)^3}$, $d = |A_0 A_2| = \sqrt{2\left(\frac{3\pi\mathcal{A}}{2(\pi^2-1)} + \frac{e^2}{2}\right)}$, e is as defined after Eq. (3.33), and where I_2, I_3, I_4 and I_5 are obtained as shown in Appendix D, in which c and e are respectively substituted with e and d to obtain Eq. (3.35) in closed form. Subsequently, the wireless power coverage probability is expressed as

$$
\begin{aligned}
P_{\text{cov}} = 1 - \frac{K_5}{3} & \left(v_9 G^{0,1:2,2:2,2:2,2}_{1,0:3,3:3,3:3,3} \left(\begin{array}{c} 3 \\ - \end{array} \middle| \begin{array}{c} \mathbf{b}_5 \\ \mathbf{b}_6 \end{array} \middle| \begin{array}{c} \mathbf{b}_5 \\ \mathbf{b}_6 \end{array} \middle| \begin{array}{c} \mathbf{b}_5 \\ \mathbf{b}_6 \end{array} \middle| \frac{-\gamma_7}{\gamma_{\text{th}}}, \frac{-\gamma_7}{\gamma_{\text{th}}}, \frac{-\gamma_7}{\gamma_{\text{th}}} \right) \right. \\
& - v_{10} G^{0,1:2,2:2,2:2,2}_{1,0:3,3:3,3:3,3} \left(\begin{array}{c} 3 \\ - \end{array} \middle| \begin{array}{c} \mathbf{b}_3 \\ \mathbf{b}_4 \end{array} \middle| \begin{array}{c} \mathbf{b}_3 \\ \mathbf{b}_4 \end{array} \middle| \begin{array}{c} \mathbf{b}_3 \\ \mathbf{b}_4 \end{array} \middle| \frac{-\gamma_7}{\gamma_{\text{th}}}, \frac{-\gamma_7}{\gamma_{\text{th}}}, \frac{-\gamma_6}{\gamma_{\text{th}}} \right) \\
& + v_{11} G^{0,1:2,2:2,2:2,2}_{1,0:3,3:3,3:3,3} \left(\begin{array}{c} 3 \\ - \end{array} \middle| \begin{array}{c} \mathbf{b}_5 \\ \mathbf{b}_6 \end{array} \middle| \begin{array}{c} \mathbf{b}_5 \\ \mathbf{b}_6 \end{array} \middle| \begin{array}{c} \mathbf{b}_5 \\ \mathbf{b}_6 \end{array} \middle| \frac{-\gamma_7}{\gamma_{\text{th}}}, \frac{-\gamma_6}{\gamma_{\text{th}}}, \frac{-\gamma_6}{\gamma_{\text{th}}} \right) \\
& \left. - v_{12} G^{0,1:2,2:2,2:2,2}_{1,0:3,3:3,3:3,3} \left(\begin{array}{c} 3 \\ - \end{array} \middle| \begin{array}{c} \mathbf{b}_5 \\ \mathbf{b}_6 \end{array} \middle| \begin{array}{c} \mathbf{b}_5 \\ \mathbf{b}_6 \end{array} \middle| \begin{array}{c} \mathbf{b}_5 \\ \mathbf{b}_6 \end{array} \middle| \frac{-\gamma_6}{\gamma_{\text{th}}}, \frac{-\gamma_6}{\gamma_{\text{th}}}, \frac{-\gamma_6}{\gamma_{\text{th}}} \right) \right),
\end{aligned} \tag{3.36}
$$

where $\mathbf{b}_5$, $\mathbf{b}_6$ are defined as after Eq. (3.30), $v_9 = \left(d^6\right)^3 \gamma_{\text{th}}^3$, $v_{10} = 3\left(d^6\right)^2 e^6 \gamma_{\text{th}}^3$, $v_{11} = 3\left(e^6\right)^2 d^6 \gamma_{\text{th}}^3$, $v_{12} = \left(e^6\right)^3 \gamma_{\text{th}}^3$, $\gamma_7 = \frac{\eta P_{\text{t}} \Omega}{d^4 m}$, and $\gamma_6 = \frac{\eta P_{\text{t}} \Omega}{e^4 m}$.

Case 4: In this case, we have $P_{\text{cov}} = 1$.

Non-Cooperative WPT

For comparison purposes, we determine the coverage probability when energy is harvested from a single AP, i.e., $K = 1$. First, we need to determine the CDF of the harvested energy $F_{P_{\text{EH}}}$. For such, the CDF of $d^{-\alpha_1}$ is required, which is expressed as shown in Eq. (3.17). As per (3.17), four cases are distinguished.

Case 1: Here, the CDF of the harvested energy is obtained as per Eq. (3.37), where c is defined after Eq. (3.33).

$$F_{P_{\text{EH}}}(\gamma_{\text{th}}) = \frac{m^m c^m \Omega}{\Omega^m \Gamma(m) m} \left(\frac{cm}{\Omega}\right)^{-m} \left[\Gamma(1+m) - \Gamma\left(1+m, \frac{cm}{\Omega}\right) - \frac{(4+\pi^2)\left(\frac{\eta P_{\text{t}} \Omega}{\gamma_{\text{th}} m}\right)^{\frac{4}{\alpha_1}}}{6\pi\mathcal{A}} \right.$$
$$\left. \left(\Gamma\left(\frac{4+\alpha_1}{\alpha_1}+m\right) - \Gamma\left(\frac{4+\alpha_1}{\alpha_1}+m, \frac{cm}{\Omega}\right) \right) \right]. \tag{3.37}$$

Case 2: In this case, we have

$$F_{P_{\text{EH}}}(\gamma_{\text{th}}) = \frac{m^m}{3\Omega^m \Gamma(m) m} \left[e^m \left(\frac{em}{\Omega}\right)^{-m} \left(-m\Gamma\left(m, \frac{em}{\Omega}\right) - \frac{(4+\nu(\pi^2-2\pi)+\pi^2)\eta P_{\text{t}} \Gamma\left(1+m, \frac{em}{\Omega}\right)}{6\pi\mathcal{A}\gamma_{\text{th}}} \right) \right.$$
$$\left. -c^m \left(\frac{cm}{\Omega}\right)^{-m} \left(-m\Gamma\left(m, \frac{cm}{\Omega}\right) - \frac{(4+\nu(\pi^2-2\pi)+\pi^2)\eta P_{\text{t}} \Gamma\left(1+m, \frac{cm}{\Omega}\right)}{6\pi\mathcal{A}\gamma_{\text{th}}} \right) \right], \tag{3.38}$$

where c and e are as defined after Eq. (3.33).

Case 3: In this case, we obtain the following expression, where d and e are as defined after Eq. (3.35).

$$F_{P_{\text{EH}}}(\gamma_{\text{th}}) = \frac{m^m}{3\Omega^m \Gamma(m) m} \left[d^m \left(\frac{dm}{\Omega}\right)^{-m} \left(-m\Gamma\left(m, \frac{dm}{\Omega}\right) - \frac{(\pi^2-1)\eta P_{\text{t}}}{3\pi\mathcal{A}\gamma_{\text{th}}} \Gamma\left(1+m, \frac{dm}{\Omega}\right) \right) - e^m \left(\frac{cm}{\Omega}\right)^{-m} \right.$$
$$\left. \left(-m\Gamma\left(m, \frac{em}{\Omega}\right) - \frac{(\pi^2-1)\eta P_{\text{t}}}{3\pi\mathcal{A}\gamma_{\text{th}}} \Gamma\left(1+m, \frac{em}{\Omega}\right) \right) \right]. \tag{3.39}$$

Case 4: $F_{P_{\text{EH}}}(\gamma_{\text{th}}) = 0$.

Depending on the location of the device w.r.t. the serving AP, we choose the corresponding CDF from the above equations and calculate the coverage probability of a Type-III typical device in the non-cooperative WPT case in closed-form, by using

$$P_{\text{cov}}(\gamma_{\text{th}}) = 1 - F_{P_{\text{EH}}}(\gamma_{\text{th}}). \tag{3.40}$$

3.4 Performance Evaluation

Now, we evaluate the obtained coverage probability expressions, and compare the ensuing numerical results with the non-cooperative WPT. Unless otherwise stated, the simulation parameters are $P_{\text{t}} = 40$ dBm, $\eta = 0.85$, $\Omega = 1$, $f = 2.5$ GHz and $\lambda = 1/100^2$ m^{-2}. For fair comparisons, we consider the cooperative WPT system of [75], where K APs modeled according to a deterministic approach, are used to transmit power to a target device located at coordinate $\mathbf{c}$ in the coverage area. The corresponding coverage probability is defined as $P_{\text{cov}} = \frac{\int_{\mathbf{c} \in \mathcal{A}} \exp(-\gamma_{\text{th}}/m_r(\mathbf{c}))}{|\mathcal{A}|}$ [75, Eq. (23)], where $m_r(\mathbf{c})$ is the average harvested power by the device when it is located at the coordinate $\mathbf{c}$. Here, we consider the case with $K = 3$, and $\mathcal{A}$ is the area of the triangle formed by the APs distributed according to deterministic model. We use Matlab platform for all calculations. The results are also compared to Monte-Carlo results obtained by up to 10^7 simulation realizations.

Figures 3.4, 3.5 & 3.6 plot the coverage probability versus the power threshold γ_{th} for different values of the Nakagami parameter, i.e, $m = 3$ and $m = 1$ (referred to by Nakagami and Rayleigh in the figures), for the Type-I, Type-II and Type-III devices, respectively. Results are shown for the cooperative ($K = 3$) and non-cooperative ($K = 1$) WPT. First, it is observed that P_{cov} is a decreasing function of γ_{th}, which is intuitively expected since the energy transferred via WPT may suffer a considerable loss due to the long-range transmission. Further, P_{cov} is an increasing function of the density λ of APs. This can be explained by the fact that an increase of λ means that the APs and the devices are located in a more compact manner, i.e., the triangular cell size decreases. Therefore, the distance of the power transfer decreases, which means that the received signal quality will be enhanced as the effects of the path loss, fading, and shadowing will be reduced. Besides, it is observed that the simulation results match the analytical results fairly well, which demonstrates the correctness of our analytical results. The slight difference between the simulation and analytical
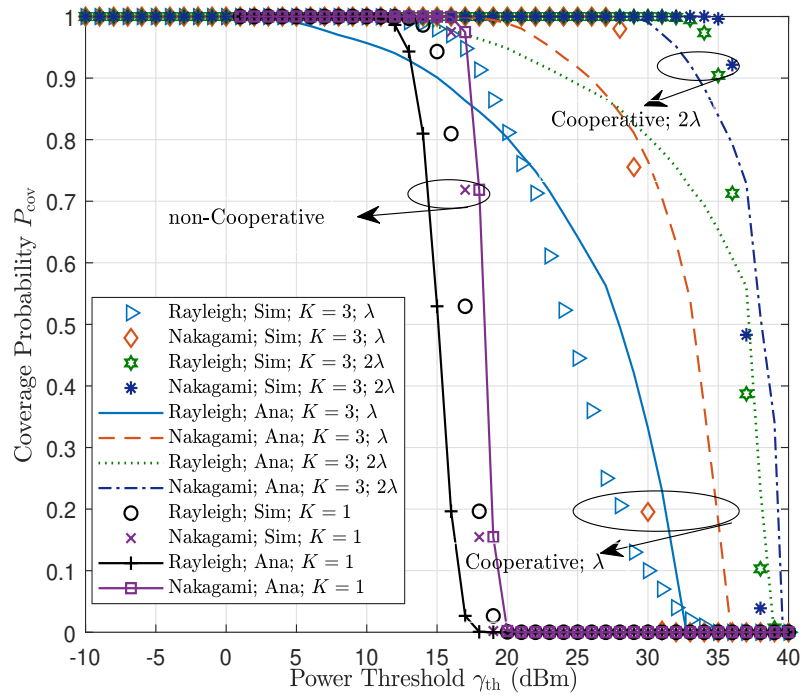
Figure 3.4: Coverage variation with the power threshold of cooperative WPT for Type-I.
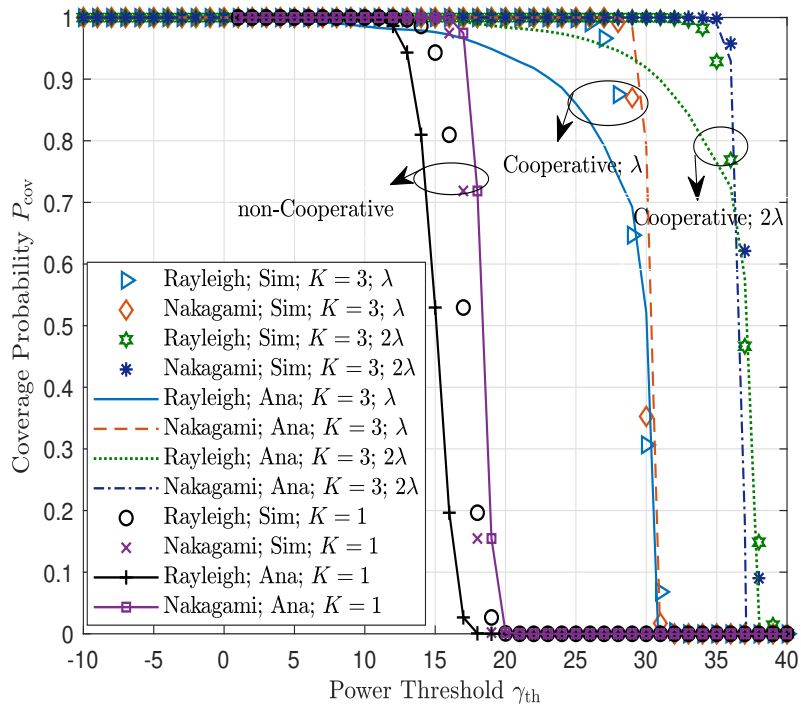
Figure 3.5: Coverage variation with the power threshold of cooperative WPT for Type-II.
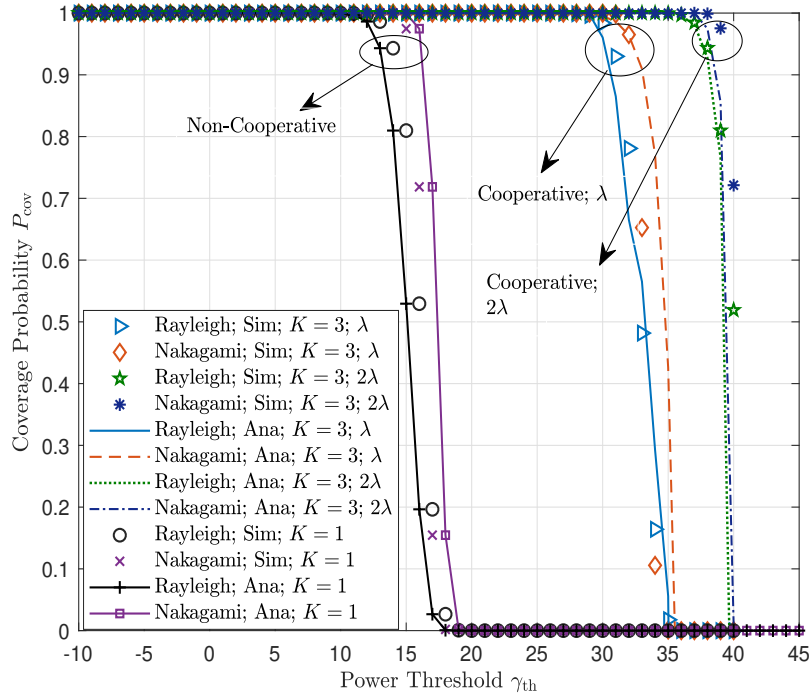
Figure 3.6: Coverage variation with the power threshold of cooperative WPT for Type-III.

results can be explained by the fact that we rely on the Mellin-Barnes integral form of the MeijerG which is an approximation of this function.

As expected, the figures prove that cooperative WPT does improve the coverage probability significantly. Indeed, the results of cooperative Type-I, Type-II, and Type-III are superior to the non-cooperative cases. The coverage seems sensitive to variation of the shape factor m for all devices' types. Indeed, as m increases while keeping Ω and P_{t} fixed, the coverage probability increases. This can be explained by the fact that the fluctuations of the signal envelope become weaker as m gets higher, hence leading to an increase in the coverage probability. For instance, Type-I performs better under the Nakagami fading model than the Rayleigh initially (around 2 dB variation of threshold power), but as the power threshold increases, the fading effects are nearly similar and, hence, the coverage results are almost similar irrespective of the m values.

Figures 3.7 and 3.8 show the coverage probability versus the power threshold for different values of the transmit power P_{t}. The three devices' types are considered. As observed, the coverage probability gains obtained as per this work's analysis outperform those of the benchmark for all the types of devices, especially for high power thresholds. This can be explained by the fact that the
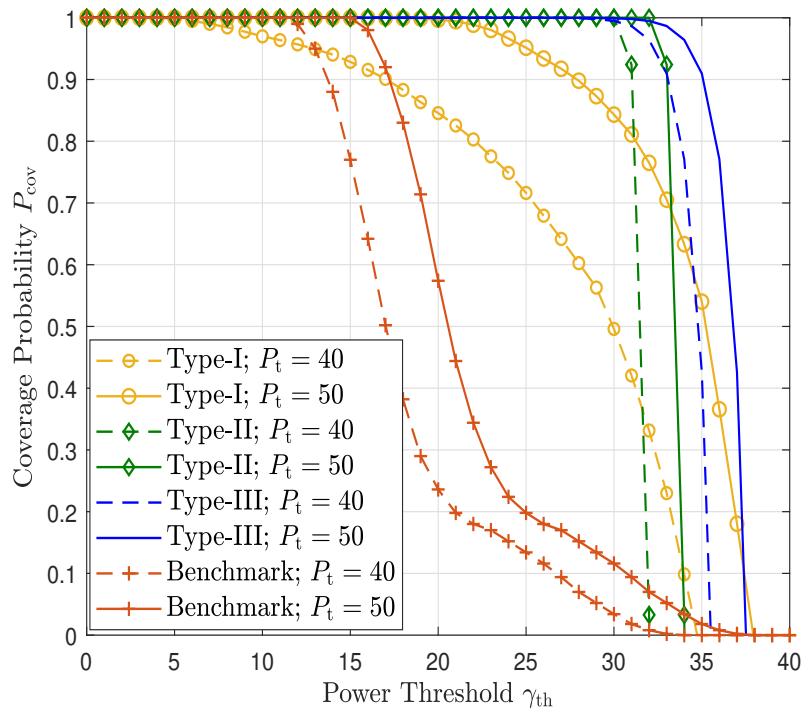
Figure 3.7: Coverage variation with the power threshold of cooperative WPT for the three device types in the Nakagami case.

distance distributions and the coverage probabilities derived in this work are more accurate as they are obtained using stochastic geometry tools. Furthermore, as expected, the coverage probability increases when the transmit power increases. Indeed, the received signal at a typical device becomes stronger and the average harvested energy gets enhanced. For the cooperative case, we observe that the coverage performance pertaining to Type-III devices is better than that of Type-I and Type-II for medium values of the power threshold γ_{th}. It is also pertinent to note that Type-III devices require an additional power threshold of about 5 dB as compared to Type-I and Type-II before its coverage starts decreasing from 1. Further, higher network density (2λ) cases offer about 5 dB variation in the power threshold required to maintain high coverage as compared to the networks with a density of λ. Finally, one can conclude that the Type-III devices exhibit high coverage probability irrespective of the channel conditions; an inference which can be used for future WPT-based cellular network deployment.
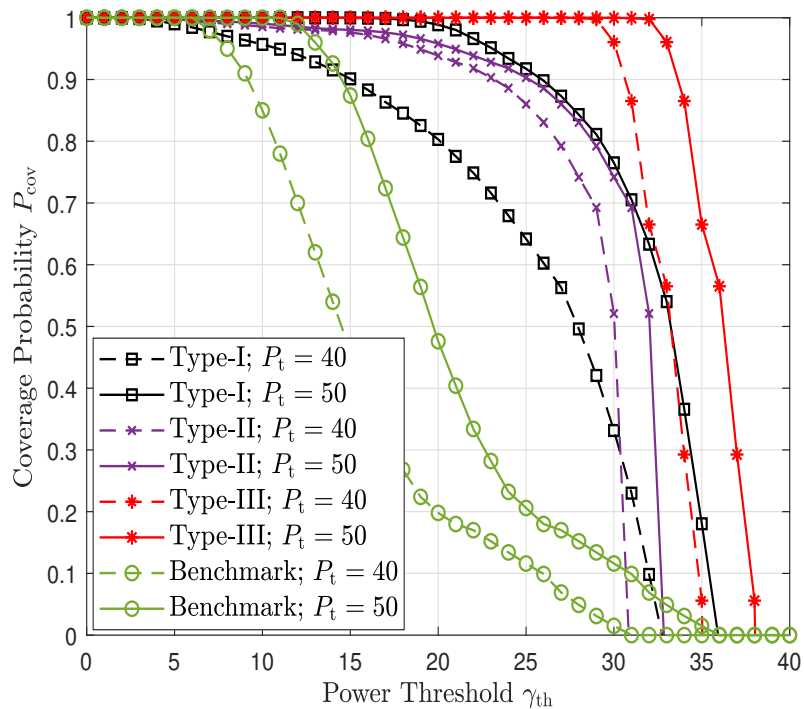
Figure 3.8: Coverage variation with the power threshold of cooperative WPT for the three device types in the Rayleigh case.

3.5 Concluding Remarks

In this chapter, we considered a wireless powered communication network, where access points distributed according to Poisson-Delaunay triangulation jointly transmit power to the network devices. We leveraged the distributed energy beamforming and stochastic geometry tools to maximize the harvested energy and obtain the power coverage for three typical device types in their closed forms. The developed formulae include the extended generalized multivariate MeijerG function, for which an implementation algorithm was also proposed. Comparative numerical results confirm the gains of the cooperative wireless power transfer, and are useful for network optimization and dimensioning with low complexity.

Chapter 4

WPT Aided with Cooperative RIS: Design and Coverage Analysis

4.1 Introduction

Motivated by the results obtained in Chapters 5 & 6 and the potentials of the RIS technology summarized in 1.1.2, this chapter leverages the use of multiple RISs for the design of WPT with enhanced performance in terms of harvested energy and wireless power coverage. In the WPT system, the energy transmitter, a.k.a. power beacon, is aided by multiple RISs to transfer energy to the harvesting devices. Assuming practical scenarios, where the devices and the RISs are distributed according to Poisson point processes (PPP), we investigate the coverage probability of the WPT system in two design schemes. Specifically, two possible RIS cooperation schemes are considered: cascaded and distributed. Adopting the moment generating function (MGF) based approach, we assess the system's wireless power coverage, by providing closed-form expressions for the coverage probability in the two types of system operations, as well as when the WPT is aided by a single RIS. Apart from validating the exactness of the analysis via Monte-Carlo simulations, the numerical results demonstrate the effectiveness of the cooperative WPT, showing how an increase in the number of cooperating RISs or in the number of their reflecting elements can improve the coverage probability significantly, and also the merits of the cascaded and distributed RIS configurations.

---

[0] The contents of this chapter are extracted from [86].

The organization of the chapter is as follows. The system model is detailed in Section 4.2. Then, the wireless power coverage framework is presented in Section 4.3. In particular, the fundamental statistics for the coverage probability calculation are provided in Section 4.3.1and the coverage probability analysis for different configurations of RIS is then presented in Section 4.3.2. The numerical results are provided in Section 4.4. Section 4.5 concludes the chapter.

4.2 The RIS-Aided WPT Model

The power transmission from the power beacon to U devices in the system is aided by multiple RISs (cf. Fig. 4.1). Considering practical distributions for the system nodes, the devices are assumed to be distributed according to a PPP ϕ_D with density λ_D, and the K_RIS RISs, each equipped with N_k reflecting elements, are spatially distributed according to a homogeneous PPP ϕ_RIS with density λ_RIS. The power beacon is equipped with a uniform linear array of M_t antennas, and the devices are single-antenna equipment. For the analysis, a typical device is considered, which is assumed to be in the far-field of the power beacon with no direct LoS in between. We assume that a selection scheme is in place to choose the most suitable set of K RISs for the signal transmission from the power beacon to the harvesting device. The selection can be based on the closest RISs to the power beacon [87], RISs that lead to high-quality end-to-end connection [88], or the ones that form a feasible end-to-end LoS path [88].[1] The WPT follows one of two designs: the cascaded, where the signal transmitted by the power beacon reaches the end device via the cascaded channel between K RISs (cf. Fig. 4.1(a), where $K = 2$), or the distributed, where K RISs simultaneously relay the power beacon signal to the end device (cf. Fig. 4.1(b), where $K = 2$).

For notation simplicity, we refer to the power beacon as node B, and to the typical harvesting device as node D. Let us denote the channels of links B-RIS$_k$, RIS$_k$-RIS$_{k+1}$, and RIS$_k$-D, by $\mathbf{H}_{\mathrm{B},k} \in \mathbb{C}^{M_\mathrm{t} \times N_k}$, $\mathbf{H}_{k,k+1} \in \mathbb{C}^{N_k \times N_{k+1}}$, and $\mathbf{h}_{k,\mathrm{D}} \in \mathbb{C}^{N_k \times 1}$, respectively, with $[\mathbf{H}_{\mathrm{B},k}]_{i,j} = d_{\mathrm{B},k}^{-\frac{\alpha}{2}} c_{i,j,k} e^{-j\phi_{i,j,k}}$, $[\mathbf{H}_{k,k+1}]_{j,l} = d_{k,k+1}^{-\frac{\alpha}{2}} \beta_{j,l,k,k+1} e^{-j\xi_{j,l,k,k+1}}$, and $[\mathbf{h}_{k,\mathrm{D}}]_l = d_{k,\mathrm{D}}^{-\frac{\alpha}{2}} b_{k,l} e^{-j\psi_{k,l}}$, where $d_{\mathrm{B},k}$, $d_{k,k+1}$ and $d_{k,\mathrm{D}}$ are the distances of links B-RIS$_k$, RIS$_k$-RIS$_{k+1}$, and RIS$_k$-D, respectively. Here, $c_{i,j,k}$, $\beta_{j,l,k,k+1}$ and $b_{k,l}$ denote the channels' amplitudes, $\phi_{i,j,k}$, $\xi_{j,l,k,k+1}$ and $\psi_{k,l}$ are the corresponding phases, and α is the

---

[1]The selection scheme is out of the scope of this chapter.
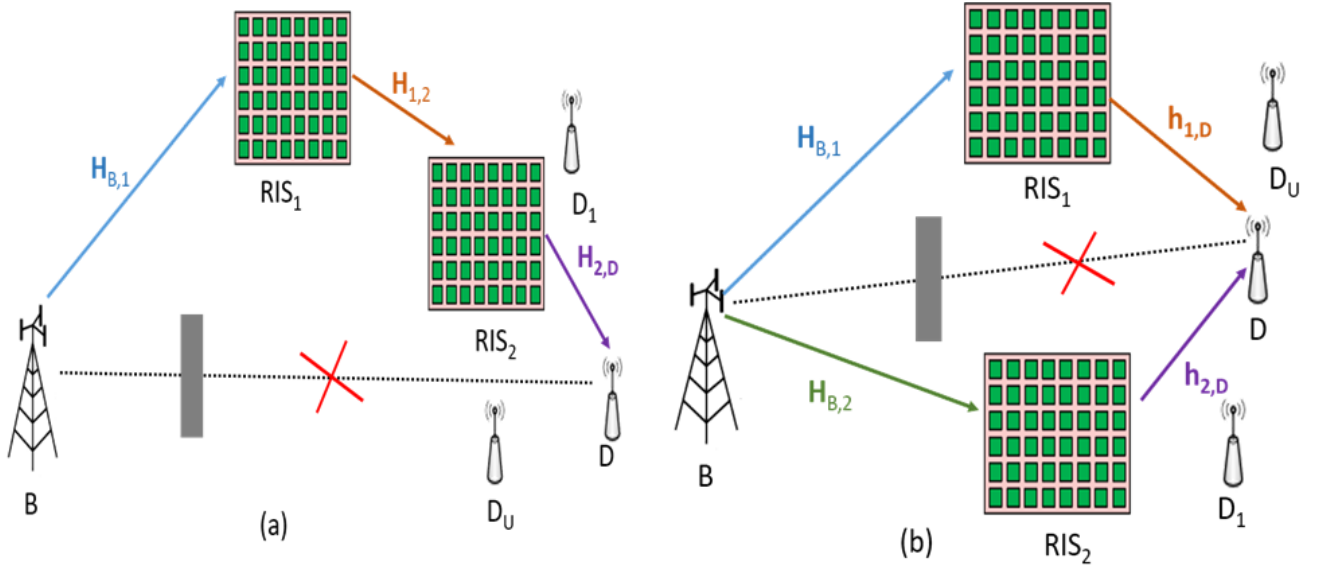
Figure 4.1: Illustration of the WPT from the power beacon, B, to a typical device, D, aided with (a) cascaded RISs or (b) distributed RISs.

path-loss exponent.[2] We assume that the channels' amplitudes are Nakagami distributed, i.e.,

$$f_\zeta(x) = \frac{2m^m x^{2m-1}}{\Omega^m \Gamma(m)} \exp\left(\frac{-mx^2}{\Omega}\right), \; x > 0, \tag{4.1}$$

where ζ is the amplitude, i.e., $c_{i,j,k}$, $\beta_{j,l,k,k+1}$ or $b_{k,l}$, and where $m \geq 0.5$ is the fading severity parameter and Ω denotes the mean fading power.

Cascaded RISs

As the WPT channel is the concatenation of the first-hop link, i.e., B-RIS$_1$, links RIS$_k$-RIS$_{k+1}$ ($k = 1, \cdots, K$), and the last-hop link, i.e., RIS$_K$-D, the received signal at the typical device D can be expressed as

$$y = \left(\mathbf{h}_{K,\mathrm{D}}^{\mathrm{H}} \prod_{k=1}^K \boldsymbol{\Theta}_k \mathbf{H}_{k,k+1}^{\mathrm{H}} \mathbf{H}_{\mathrm{B},1}^{\mathrm{H}}\right) \mathbf{w}s + z, \tag{4.2}$$

where $\boldsymbol{\Theta}_k \triangleq diag\left(a_{k,1} e^{j\theta_{k,1}}, \cdots, a_{k,N_k} e^{j\theta_{k,N_k}}\right)$ denotes the reflection matrix of RIS$_k$, with $\theta_{k,n} \in [0, 2\pi]$ and $a_{k,n}$ denoting, respectively, the phase shift and the amplitude reflection coefficient associated with the nth element of RIS$_k$.[3] Here, $\mathbf{w} \in \mathbb{C}^{M_t \times 1}$ denotes the energy beamforming vector

---

[2]We assume that the channel coefficients of all links can be estimated, e.g., by using the parallel factor (PARAFAC) decomposition technique to decompose the cascaded channel model as detailed in [33].

[3]Hereafter, we assume that $a_{k,n} = 1, \forall k, \forall n$.

at node B, s is the transmit signal modeled as a random variable with zero mean and unit variance, and z denotes the additive white Gaussian noise (AWGN) having zero mean and variance σ^2. Therefore, the received signal power at the device D can be calculated as

$$P_{\text{in}} = \left| \left(\mathbf{h}_{K,D}^H \prod_{k=1}^{K} \boldsymbol{\Theta}_k \mathbf{H}_{k,k+1}^{\text{H}} \mathbf{H}_{\text{B},1}^{\text{H}} \right) \mathbf{w} \right|^2. \tag{4.3}$$

For any specific phase-shift matrix $\boldsymbol{\Theta}_k$, $k = 1, \cdots, K$, it is not difficult to show that the optimal transmit beamforming corresponds to the maximum-ratio transmission (MRT) method [?]. Hence, $\mathbf{w}$ is given by

$$\mathbf{w} = \sqrt{P_{\text{t}}} \frac{\left(\mathbf{h}_{K,D}^{\text{H}} \prod_{k=1}^{K} \boldsymbol{\Theta}_k \mathbf{H}_{k,k+1}^{\text{H}} \mathbf{H}_{\text{B},1}^{\text{H}} \right)^{\text{H}}}{\left\| \mathbf{h}_{K,D}^{\text{H}} \prod_{k=1}^{K} \boldsymbol{\Theta}_k \mathbf{H}_{k,k+1}^{\text{H}} \mathbf{H}_{\text{B},1}^{\text{H}} \right\|^2}, \tag{4.4}$$

where P_{t} is the transmit power of the power beacon. By substituting this beamforming vector into (4.3), while considering the generally adopted piece-wise linear energy harvesting model [61], and assuming no harvesting from the AWGN, the output direct-current power at the typical device can be obtained according to

$$P_{\text{EH}} = \eta P_{\text{t}} \left\| \mathbf{h}_{K,D}^{\text{H}} \prod_{k=1}^{K} \boldsymbol{\Theta}_k \mathbf{H}_{k,k+1}^{\text{H}} \mathbf{H}_{\text{B},1}^{\text{H}} \right\|^2, \tag{4.5}$$

where $0 < \eta < 1$ denotes the power conversion efficiency [61]. Let us use $\mathbf{h}_i$ to represent the term $\mathbf{h}_{K,D}^{H} \prod_{k=1}^{K} \boldsymbol{\Theta}_k \mathbf{H}_{k,k+1}^{\text{H}} \mathbf{H}_{\text{B},1}^{\text{H}} \in \mathbb{C}^{1 \times M_t}$ of (4.5). The expression can then be rewritten as $P_{\text{EH}} = \eta P_{\text{t}} \sum_{i=1}^{M_t} |h_i|^2$, in which $h_i = c_{i,j,1} \prod_{k=1}^{K} \beta_{j,l,k,k+1} b_{K,l} (d_{\text{B},1}^{-\frac{\alpha}{2}} \prod_{k=1}^{K} d_{k,k+1}^{-\frac{\alpha}{2}} d_{K,D}^{-\frac{\alpha}{2}})$ $e^{j\phi_{i,j,1} - \sum_{k=1}^{K} \theta_{k,j} + \xi_{j,l,k,k+1} + \psi_{K,l}}$. To achieve maximum signal power, the RIS phase shifts are adjusted to cancel out the channel phases [4], i.e., $\theta_{k,n} = \phi_{i,n,k} + \psi_{K,n} + \xi_{j,l,k,k+1}$, $\forall n \in \{j, l\}$ and $k = 1, \cdots, K$. Hence, $|h_i|^2 = \mathcal{S}_1 \left(\sum_{j=1,l=1,j \neq l}^{N_k} c_{i,j,1} \prod_{k=1}^{K} \beta_{j,l,k,k+1} b_{K,l} \right)^2 = \mathcal{S}_1 \left(\sum_{j=1,l=1,j \neq l}^{N_k} Y_{j,l} \right)^2$, where $\mathcal{S}_1 = d_{\text{B},1}^{-\alpha} \prod_{k=1}^{K} d_{k,k+1}^{-\alpha} d_{K,D}^{-\alpha}$. We assume that the distances $d_{\text{B},1}$ and $d_{k,k+1}$ for $k = 1, \cdots, K$, are known, whereas $d_{K,D}$ is a random variable.

Distributed RISs

In this deployment, the received signal at the typical harvesting device D can be expressed as

$$y = \sum_{k=1}^{K} \left(\mathbf{h}_{k,D}^{\text{H}} \boldsymbol{\Theta}_k \mathbf{H}_{\text{B},k}^{\text{H}} \right) \mathbf{f}_k s + z, \tag{4.6}$$

where $\mathbf{f}_k \in \mathbb{C}^{M_t \times 1}$ denotes the energy beamforming vector at node B, and where s and z are as defined after Eq. (4.2). Hence, the received signal power at the typical device can be calculated as

$$P_{\text{in}} = \left| \sum_{k=1}^{K} \left(\mathbf{h}_{k,\text{D}}^{\text{H}} \boldsymbol{\Theta}_k \mathbf{H}_{\text{B},k}^{\text{H}} \right) \mathbf{f}_k \right|^2. \tag{4.7}$$

In this model, any B-RIS$_k$-D link, $k = 1, \cdots, K$, is modeled as the concatenation of three components, namely, the B-RIS$_k$ link, the phase-shift matrix of RIS$_k$, and the RIS$_k$-D link, and is characterized by the random vector $\mathbf{h}_k \triangleq \mathbf{h}_{k,\text{D}}^{H} \boldsymbol{\Theta}_k \mathbf{H}_{\text{B},k}^{\text{H}}$. The optimal solution for the active beamforming vector $\mathbf{f}_k$ is the MRT beamforming vector, which can be expressed as $\mathbf{f}_k = \sqrt{P_t} \frac{\mathbf{h}_k^{\text{H}}}{\|\mathbf{h}_k\|^2}$. By substituting this beamforming vector into (4.7), while assuming no harvesting from the AWGN, the received power at the harvesting device can then be obtained as $P_{\text{EH}} = \eta P_t \sum_{k=1}^{K} \left\| \mathbf{h}_{k,\text{D}}^{\text{H}} \boldsymbol{\Theta}_k \mathbf{H}_{\text{B},k}^{\text{H}} \right\|^2$. Here also, we assume that the RIS phase shifts are adjusted to cancel the channel phases so as to achieve maximum received power. As such, we have $P_{\text{EH}} = \eta P_t \sum_{k=1}^{K} \sum_{i=1}^{M_t} |h_{k,i}|^2$, in which $|h_{k,i}|^2 = d_{\text{B},k}^{-\alpha} d_{k,\text{D}}^{-\alpha} \left(\sum_{n=1}^{N_k} c_{i,n,k} b_{k,n} \right)^2 = d_{\text{B},k}^{-\alpha} d_{k,\text{D}}^{-\alpha} \left(\sum_{n=1}^{N_k} Y_{k,i,n} \right)^2$. Further, it is assumed that the distances $d_{\text{B},k}$, $k = 1, \cdots, K$, are known at the power beacon, while $d_{k,\text{D}}$ is a random variable.

4.3   Wireless Power Coverage

4.3.1   Necessary Statistics

Our main goal is to evaluate the system performance in terms of the wireless power coverage. Hereafter, we consider the cooperation schemes with $K = 2$ RISs. Before proceeding with the calculation of this performance metric, several statistics pertaining to the distances between the typical device and RISs, as well as to the channels' gains, are needed.

Distance Distributions

For the coverage analysis, the probability density function (PDF) of the distance between the harvesting device and the last-hop RIS(s) intervening in the WPT towards it, is needed. In the distributed configuration, each of the two RISs create a separate last-hop towards device D. In the cascaded configuration, the PDF is similar to the above with $k = 2$, i.e., the index of the last RIS

in the chain of cascaded RISs between the beacon and the device. Hence, the PDF of the distance between D and RIS_k, $k = 1, 2$, is given by [56]

$$f_{d_{k,\text{D}}}(d) = 2\pi\lambda_{\text{RIS}} \ d \ e^{-\pi\lambda_{\text{RIS}}d^2}, \tag{4.8}$$

Channel Gain Distributions in Cascaded RISs

To obtain the PDF of $|h_i|^2$, we need the PDF of the amplitude of the B-RIS_1-RIS_2-D link, i.e., $\sum_{j=1,l=1,j\neq l}^{N_k} Y_{j,l}$. Note that $Y_{j,l}$ is the product of three Nakagami-m distributed random variables with parameters (m_1, Ω_1), (m_2, Ω_2) and (m_3, Ω_3), respectively, , with m_i and Ω_i are as defined after Eq. (4.1). The MGF of $Y_{j,l}$ can be expressed as follows [89]:

$$M_{Y_{j,l}}(s) = \frac{\frac{1}{\sqrt{\pi}}}{\prod_{i=1}^3 \Gamma(m_i)} G_{2,3}^{3,2} \left(\begin{array}{c} \frac{1}{2}, 1 \\ m_1, m_2, m_3 \end{array} \middle| \frac{4}{s^2} \prod_{i=1}^3 \frac{m_i}{\Omega_i} \right). \tag{4.9}$$

Let us now determine the distribution of $Y = \left(\sum_{j=1,l=1,j\neq l}^{N_k} Y_{j,l} \right)^2$. According to [90, Sec.2.2.2], and by applying the approximation of the first term of the Laguerre series, the PDF of Y is found as

$$f_Y(z) = \frac{z^v}{w^{v+1}\Gamma(v+1)} \exp\left(-\frac{z}{w}\right), \tag{4.10}$$

where v and w are related to the mean and variance of Y. That is, $v = \frac{(E(Y))^2}{\text{Var}(Y)} - 1$ and $w = \frac{\text{Var}(Y)}{E(Y)}$, in which $E(Y) = N_1 N_2 E(Y_{j,l})$ and $\text{Var}(Y) = N_1 N_2 \text{Var}(Y_{j,l})$, with $E(Y_{j,l}) = \frac{\Gamma(m_1+\frac{1}{2})\Gamma(m_2+\frac{1}{2})\Gamma(m_3+\frac{1}{2})}{\sqrt{\frac{m_1}{\Omega_1}}\Gamma(m_1)\sqrt{\frac{m_2}{\Omega_2}}\Gamma(m_2)\sqrt{\frac{m_3}{\Omega_3}}\Gamma(m_3)}$ and $\text{Var}(Y_{j,l}) = \Omega_1\Omega_2\Omega_3\left(1 - \frac{\Gamma(m_1+\frac{1}{2})^2\Gamma(m_2+\frac{1}{2})^2\Gamma(m_3+\frac{1}{2})^2}{\Gamma(m_1)^2\Gamma(m_2)^2\Gamma(m_3)^2}\right)$.

Channel Gain Distributions in Distributed RISs

Here, to obtain the PDF of $|h_{k,i}|^2$, we need the PDF of the amplitude of links B-RIS_k-D, for $k = 1, 2$. We follow similar steps as in the case with cascaded RISs. Based on [89], the PDF of $Y_{k,i,n}$, which is the product of two Nakagami-m random variables with parameters (m_1, Ω_1), and (m_2, Ω_2),

respectively, with m_i and Ω_i are as defined after Eq. (4.1), can be expressed as follows:

$$f_{Y_{k,i,n}}(x) = \frac{\frac{2}{x}}{\prod_{i=1}^{2}\Gamma(m_i)} G_{0,2}^{2,0}\left(\begin{array}{c} - \\ m_1, m_2 \end{array} \middle| x^2 \prod_{i=1}^{2}\frac{m_i}{\Omega_i}\right). \tag{4.11}$$

Therefore, the distribution of $Y_k = \left(\sum_{n=1}^{N_k} Y_{k,i,n}\right)^2$ can be obtained by using the approximation of the first term of the Laguerre series to yield

$$f_{Y_k}(z) = \frac{z^p}{q^{p+1}\Gamma(p+1)}\exp\left(-\frac{z}{q}\right), \tag{4.12}$$

where p and q are related to the mean and variance of Y_k. Specifically, $p = \frac{(E(Y_k))^2}{\text{Var}(Y_k)} - 1$ and $q = \frac{\text{Var}(Y_k)}{E(Y_k)}$, in which $E(Y_k) = N_k E(Y_{k,i,n})$ and $\text{Var}(Y_k) = N_k \text{Var}(Y_{k,i,n})$, with $E(Y_{k,i,n}) = \frac{\Gamma\left(m_1+\frac{1}{2}\right)\Gamma\left(m_2+\frac{1}{2}\right)}{\sqrt{\frac{m_1}{\Omega_1}}\Gamma(m_1)\sqrt{\frac{m_2}{\Omega_2}}\Gamma(m_2)}$ and $\text{Var}(Y_{k,i,n}) = \Omega_1\Omega_2\left(1 - \frac{\Gamma\left(m_1+\frac{1}{2}\right)^2\Gamma\left(m_2+\frac{1}{2}\right)^2}{\Gamma(m_1)^2\Gamma(m_2)^2}\right)$.

4.3.2 Analysis

Having the necessary statistics at hand, we now analyze the wireless power coverage of the system in different configurations.

Cascaded RISs

Interpreted as the complementary cumulative distribution function of the harvested power, the coverage probability in this case can be expressed as $P_{\text{cov}} = 1 - \mathbb{P}\left(\eta P_{\text{t}}\sum_{i=1}^{M_{\text{t}}}|h_i|^2 < \gamma_{\text{th}}\right)$. Since P_{EH} is the sum of M_{t} random variables involving the fast-fading channel coefficients and the random distance between the device and the last-hop RIS, direct computation of P_{cov} is not possible. Thus, we adopt the MGF-based approach to calculate P_{cov}. The MGF of the harvested power is given by $\mathcal{M}_{P_{\text{EH}}}(s) = \prod_{i=1}^{M_{\text{t}}}\mathcal{M}_{P_i}(s)$, where $\mathcal{M}_{P_i}(s)$ is the MGF of ith element of the random vector $\mathbf{h}_i$, which

is given by

$$
\begin{aligned}
\mathcal{M}_{P_i}(s) &= \mathbb{E}_{z,d}\left[\exp\left(-s\eta P_{\mathrm{t}}|h_i|^2\right)\right] \\
&= 2\pi\lambda_{\mathrm{RIS}}\int_{z=0}^{+\infty}\int_{d=0}^{+\infty}\exp\left(-s\eta P_{\mathrm{t}}d_{\mathrm{B},1}^{-\alpha}d_{1,2}^{-\alpha}dz\right)\frac{z^v}{w^{v+1}\Gamma(v+1)}\exp\left(-\frac{z}{w}\right)d\exp\left(-\pi\lambda_{\mathrm{RIS}}d^2\right)\mathrm{d}z\mathrm{d}d \\
&= \frac{2\pi\lambda_{\mathrm{RIS}}}{w^{v+1}\Gamma(v+1)}\left(\frac{\Gamma(\frac{1}{2})}{2\sqrt{\pi\lambda_{\mathrm{RIS}}}} - \frac{(1+v)(ws\eta P_{\mathrm{t}}d_{\mathrm{B},1}^{-\alpha}d_{1,2}^{-\alpha})\Gamma(\frac{3}{2})}{2(\pi\lambda_{\mathrm{RIS}})^{\frac{3}{2}}}\right).
\end{aligned}
\tag{4.13}
$$

The wireless power coverage at a typical device D is calculated as $P_{\mathrm{cov}} = 1 - \int_{-\infty}^{\gamma_{\mathrm{th}}} f_{P_{\mathrm{EH}}}(x)\mathrm{d}x$, where $f_{P_{\mathrm{EH}}}(x)$ is the PDF of the harvested power, which can be evaluated using the MGF as follows: $f_{P_{\mathrm{EH}}}(x) = \frac{1}{2\pi}\int_{-\infty}^{\infty}\mathcal{M}_{P_{\mathrm{EH}}}(js)\exp(-jsx)\mathrm{d}s$. After getting the MGF, and with further mathematical manipulations, the PDF of the harvested energy is expressed as

$$
\begin{aligned}
f_{P_{\mathrm{EH}}}(x) = &\frac{1}{2(\pi)^{\frac{3}{2}}}\left(\frac{2\pi\lambda_{\mathrm{RIS}}}{w^{v+1}\Gamma(v+1)}\right)^{M_{\mathrm{t}}} \\
&\left(G_{0,0:1,1:1,1}^{0,0:1,1:1,1}\left(\frac{x}{2},\frac{1}{2}\middle|\begin{array}{c}1,2\\2,\frac{5}{2}\end{array}\right) - \frac{M_{\mathrm{t}}\pi^2\lambda_{\mathrm{RIS}}}{2(\pi\lambda_{\mathrm{RIS}})^{\frac{3}{2}}}(1+v)(w\eta P_{\mathrm{t}}d_{\mathrm{B},1}^{-\alpha}d_{1,2}^{-\alpha})G_{0,0:1,1:1,1}^{0,0:1,1:1,1}\left(\frac{x}{2},\frac{1}{2}\middle|\begin{array}{c}1,2\\2,\frac{5}{2}\end{array}\right)\right).
\end{aligned}
\tag{4.14}
$$

Therefore, the coverage probability of the harvested energy at a typical device D is found as

$$
\begin{aligned}
P_{\mathrm{cov}} = 1 - &\frac{1}{2(\pi)^{\frac{3}{2}}}\left(\frac{2\pi\lambda_{\mathrm{RIS}}}{w^{v+1}\Gamma(v+1)}\right)^{M_{\mathrm{t}}} \\
&\left(G_{0,0:2,1:1,1}^{0,0:1,2:0,0}\left(\frac{\gamma_{\mathrm{th}}}{2},\frac{1}{2}\middle|\begin{array}{c}1,2,3\\3,\frac{7}{2}\end{array}\right) - \frac{M_{\mathrm{t}}\pi^2\lambda_{\mathrm{RIS}}}{2(\pi\lambda_{\mathrm{RIS}})^{\frac{3}{2}}}(1+v)(w\eta P_{\mathrm{t}}d_{\mathrm{B},1}^{-\alpha}d_{1,2}^{-\alpha})G_{0,0:2,1:1,1}^{0,0:1,2:0,0}\left(\frac{\gamma_{\mathrm{th}}}{2},\frac{1}{2}\middle|\begin{array}{c}1,2,3\\3,\frac{7}{2}\end{array}\right)\right),
\end{aligned}
\tag{4.15}
$$

where v and w are as defined after Eq. (4.10).

Distributed RISs

Assuming that the distances from the power beacon to RIS_k, $k = 1, 2$, are known, the MGF of the harvested energy from the WPT via the kth RIS is given by

$$\mathcal{M}_{P_{k,i}}(s) = \frac{2\pi\lambda_{\mathrm{RIS}}}{q^{p+1}\Gamma(p+1)} \left(\frac{\Gamma(\frac{1}{2})}{2\sqrt{\pi\lambda_{\mathrm{RIS}}}} - \frac{(1+p)(qs\eta P_{\mathrm{t}}d_{\mathrm{B},k}^{-\alpha})\Gamma(\frac{3}{2})}{2(\pi\lambda_{\mathrm{RIS}})^{\frac{3}{2}}} \right), \tag{4.16}$$

where p and q are as defined after Eq. (4.12). The MGF of the harvested energy is expressed as

$$\begin{aligned}
\mathcal{M}_{P_{\mathrm{EH}}}(s) &= \prod_{k=1}^{2} \prod_{i=1}^{M_{\mathrm{t}}} \mathcal{M}_{P_{k,i}}(s) \\
&= \left(\frac{2\pi\lambda_{\mathrm{RIS}}}{q^{p+1}\Gamma(p+1)} \right)^{2M_{\mathrm{t}}} \left(\frac{\Gamma(\frac{1}{2})}{2\sqrt{\pi\lambda_{\mathrm{RIS}}}} - \frac{(1+p)(qs\eta P_{\mathrm{t}}d_{\mathrm{B},k}^{-\alpha})\Gamma(\frac{3}{2})}{2(\pi\lambda_{\mathrm{RIS}})^{\frac{3}{2}}} \right)^{2M_{\mathrm{t}}}. \tag{4.17}
\end{aligned}$$

Therefore, the PDF of the harvested energy is given by

$$\begin{aligned}
f_{P_{\mathrm{EH}}}(x) = \frac{1}{2\pi} &\left(\frac{2\pi\lambda_{\mathrm{RIS}}}{q^{p+1}\Gamma(p+1)} \right)^{2M_{\mathrm{t}}} \\
&\left(G_{0,0:1,1:1,1}^{0,0:1,1:1,1} \left(\frac{x}{2}, \frac{1}{2} \middle| \begin{matrix} 1,2 \\ 2,\frac{5}{2} \end{matrix} \right) - \frac{M_{\mathrm{t}}\pi^2\lambda_{\mathrm{RIS}}}{(\pi\lambda_{\mathrm{RIS}})^{\frac{3}{2}}}(1+p)(q\eta P_{\mathrm{t}}d_{\mathrm{B},k}^{-\alpha}) G_{0,0:1,1:1,1}^{0,0:1,1:1,1} \left(\frac{x}{2}, \frac{1}{2} \middle| \begin{matrix} 1,2 \\ 2,\frac{5}{2} \end{matrix} \right) \right). \tag{4.18}
\end{aligned}$$

Finally, the coverage probability in this case is found as

$$\begin{aligned}
P_{\mathrm{cov}} = 1 - \frac{1}{2(\pi)^{\frac{3}{2}}} &\left(\frac{2\pi\lambda_{\mathrm{RIS}}}{q^{p+1}\Gamma(p+1)} \right)^{2M_{\mathrm{t}}} \\
&\left(G_{0,0:2,1:1,1}^{0,0:1,2:0,0} \left(\frac{\gamma_{\mathrm{th}}}{2}, \frac{1}{2} \middle| \begin{matrix} 1,2,3 \\ 3,\frac{7}{2} \end{matrix} \right) - \frac{M_{\mathrm{t}}\pi^2\lambda_{\mathrm{RIS}}}{(\pi\lambda_{\mathrm{RIS}})^{\frac{3}{2}}}(1+p)(q\eta P_{\mathrm{t}}d_{\mathrm{B},k}^{-\alpha}) G_{0,0:2,1:1,1}^{0,0:1,2:0,0} \left(\frac{\gamma_{\mathrm{th}}}{2}, \frac{1}{2} \middle| \begin{matrix} 1,2,3 \\ 3,\frac{7}{2} \end{matrix} \right) \right), \tag{4.19}
\end{aligned}$$

Single RIS

For comparison purposes, we also consider the case when only one RIS, with index 1, is involved in the WPT. In this case, the coverage probability is given by

$$P_{\text{cov}} = 1 - \frac{1}{2(\pi)^{\frac{3}{2}}} \left(\frac{2\pi\lambda_{\text{RIS}}}{\epsilon^{\delta+1}\Gamma(\delta+1)} \right)^{M_{\text{t}}}$$

$$\left(G_{0,0:2,1:1,1}^{0,0:1,2:0,0} \left(\frac{\gamma_{\text{th}}}{2}, \frac{1}{2} \middle| \begin{array}{c} 1,2,3 \\ 3,\frac{7}{2} \end{array} \right) - \frac{M_{\text{t}}\pi^2\lambda_{\text{RIS}}}{2(\pi\lambda_{\text{RIS}})^{\frac{3}{2}}} (1+\delta)(\epsilon\eta P_{\text{t}}d_{\text{B},1}^{-\alpha}) G_{0,0:2,1:1,1}^{0,0:1,2:0,0} \left(\frac{\gamma_{\text{th}}}{2}, \frac{1}{2} \middle| \begin{array}{c} 1,2,3 \\ 3,\frac{7}{2} \end{array} \right) \right),$$

$$\tag{4.20}$$

where δ and ϵ are related to the mean and variance of $Y_1 = \left(\sum_{n=1}^{N_1} Y_{1,i,n} \right)^2$, in which $Y_{1,i,n}$ being the amplitudes of the B-RIS-D channel which is the product of two nakagami-m distributed random variables with parameters (m_1, Ω_1) and (m_2, Ω_2). That is, $\delta = \frac{(E(Y_1))^2}{\text{Var}(Y_1)} - 1$ and $\epsilon = \frac{\text{Var}(Y_1)}{E(Y_1)}$, in which $E(Y_1) = N_1 E(Y_{1,i,n})$ and $\text{Var}(Y_1) = N_1 \text{Var}(Y_{1,i,n})$, with $E(Y_{1,i,n}) = \frac{\Gamma(m_1+\frac{1}{2})\Gamma(m_2+\frac{1}{2})}{\sqrt{\frac{m_1}{\Omega_1}}\Gamma(m_1)\sqrt{\frac{m_2}{\Omega_2}}\Gamma(m_2)}$ and $\text{Var}(Y_{1,i,n}) = \Omega_1\Omega_2 \left(1 - \frac{\Gamma(m_1+\frac{1}{2})^2\Gamma(m_2+\frac{1}{2})^2}{\Gamma(m_1)^2\Gamma(m_2)^2} \right)$.

4.4 Performance Evaluation

Now, we numerically evaluate the coverage probability expressions obtained above, and compare the results pertaining to the three WPT schemes. Unless otherwise stated, the simulation parameters are as follows: $P_{\text{t}} = 40$ dBm, $M_{\text{t}} = 8$, $\eta = 0.85$, $f = 2.5$ GHz, $\lambda_{\text{RIS}} = 1/100^2$ m^{-2}, $\gamma_{\text{th}} = 20$ dBm, and the number of elements in each RIS is $N = 16$. We assume that the nakagami-m paramaters are the same for all the channel realisations, i.e., $m_i = 3$ and $\Omega_i = 1$. The results are also compared to Monte-Carlo results obtained by up to 10^6 simulation realizations.

In Fig. 4.2, the coverage probability is plotted as a function of the power threshold. The three WPT schemes are compared, i.e., via single RIS, via distributed RISs, and via cascaded RISs. Results corresponding to the analytical expressions and the Monte-Carlo simulations (referred to as Theo and Sim in Fig. 4.2) are compared. The correctness of the closed-form expressions obtained in Eqs. (4.15), (4.19) and (4.20), is confirmed as they overlap with the simulation results for all the values. As observed, using cooperative RIS enhances the coverage probability of the system, as
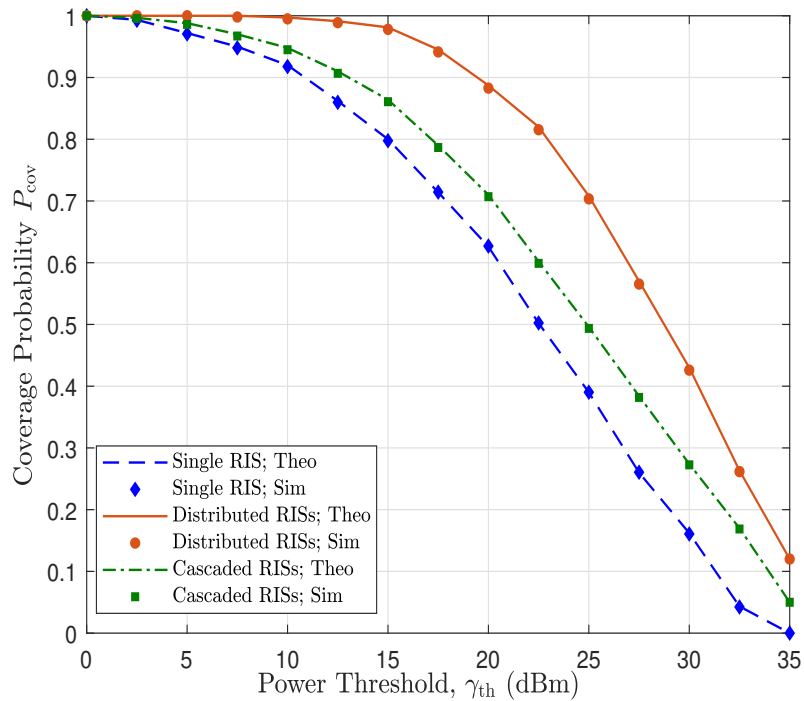
Figure 4.2: Coverage probability versus the power threshold.

it strengthens the received signal at the end device, thereby improving the harvested energy and leading to higher coverage. As such, for $\gamma_{\mathrm{th}} = 20$ dBm, gains of 10% and 30% can be obtained by doubling the number of RISs involved in the WPT, in the cascaded scheme and the distributed scheme, respectively. Also, we notice that the distributed configuration outperforms the cascaded scheme, which can be explained by the increased diversity in the latter scheme.

Figure 4.3 illustrates the coverage probability versus the number of RIS reflecting elements for the three schemes, considering different values for the RIS density. The figure demonstrates the superior improvement that can be achieved by utilizing more cooperating RISs or when integrating more reflecting elements at each RIS. Particularly, a gain of 20% can be obtained by doubling the number of RISs that aid the WPT, and 70% by increasing the number of RIS elements from 2 to 64. By using more reflecting elements at each RIS, the performance of the cascaded system becomes quite similar to the one of the distributed scheme. Moreover, as the RIS density increases, the distances between the nodes of the WPT link, i.e., power beacon to RIS(s), consecutive RISs, and last-hop RIS(s) to the harvesting device, gets shortened, thereby reducing the path loss severity and increasing the harvested energy, which results in better wireless power coverage.
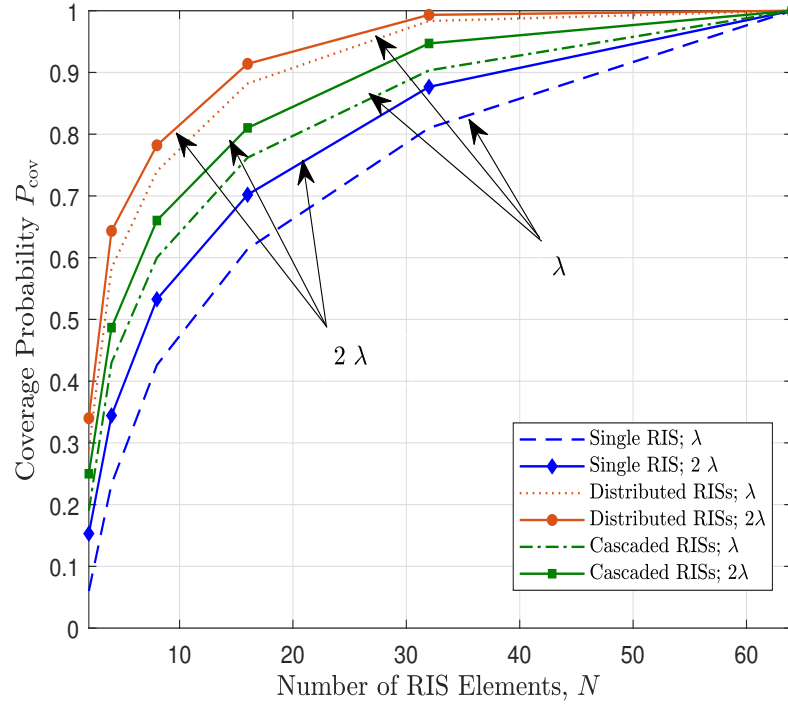
Figure 4.3: Coverage probability versus the number of RIS elements.
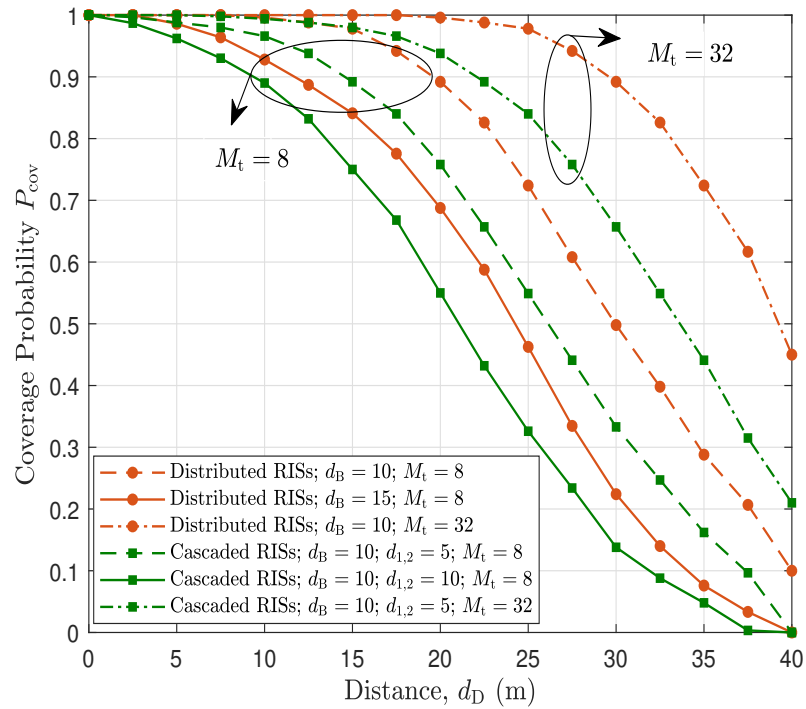
Figure 4.4: Effect of the distance between the device and the closest serving RIS on the coverage probability.

Figure 4.4 shows the coverage probability as a function of the distance between the device and its closest serving RIS(s), denoted here as d_{D}. In the cascaded configuration, the closest RIS is RIS_2, hence $d_{\mathrm{D}} = d_{2,\mathrm{D}}$. In the distributed configuration, the two serving RISs are assumed at the same distance from the device, i.e., $d_{\mathrm{D}} = d_{1,\mathrm{D}} = d_{2,\mathrm{D}}$. As expected, for given transmit power, power threshold, and RIS size, when the device is farther away from the serving RISs, i.e., d_{D} increases, the average harvested power decreases; leading to reduced coverage. For example, the coverage probability decreases from 1 to 0 as d_{D} increases from 5 m to 40 m. In the figure, we study the effect of the number of antennas at the power beacon (M_{t}), and the distance d_{B} of the latter from the first-hop RIS(s), i.e., RIS_1 in the cascaded configuration ($d_{\mathrm{B}} = d_{\mathrm{B},1}$) and the two RISs in the distributed configuration ($d_{\mathrm{B}} = d_{\mathrm{B},1} = d_{\mathrm{B},2}$). As d_{B} decreases, or that the distance $d_{1,2}$ between the RISs in the cascaded configuration decreases, the transmission loss can be counterbalanced by the cooperative gains that can be achieved. Moreover, increasing M_{t} increases the gain of the active beamforming at the beacon, thereby enhancing the harvested energy and the coverage probability.

4.5   Concluding Remarks

This contribution presented a theoretical framework for the performance evaluation of RIS-assisted WPT in terms of coverage when the power transfer is aided by multiple RISs according to different deployments, namely, cascaded and distributed. The distributions of the channels gains and the distances between the nodes of the WPT links, were obtained, and used in a moment generating function based approach to find the closed-form expressions for the coverage probability of the RIS-aided cooperative WPT.

Part II

RIS-Aided Wireless Information Transfer

The second part focuses on the design of RIS-aided WIT with the objective of maximizing the energy efficiency of the cell edge users. two deployment scenarios are considered single service or unicast (downlink in chapter 5 and uplink in chapter 6) and multiple services or the joint Unicast-broadcast transmission (chapter 7).

Chapter 5

Energy-Efficient Downlink RIS-Aided Communication

5.1 Introduction

Recall that the main objective of this part is to design a RIS-aided communication to serve the starved users, i.e., the cell-edge users or users in dead-zone with high EE. This chapter proposes to leverage aerial RIS, i.e., RIS mounted on UAV to improve the efficiency of the transmission, since UAV-assisted communications provide several advantages such as good connectivity conditions, improved capacity, better coverage area and flexible deployment. Therefore, a question arises here as to the gains that can be achieved if RIS technology is used in conjunction with UAV-assisted communications in terms of EE. Taking this question as a starting point, the EE maximization problem of a communication system in which the BS is called to send independent data streams to K single antenna ground users at a far distance from the BS. The downlink communication is assisted with a UAV equipped with RIS, a.k.a., aerial RIS. The optimization problem at hand requires jointly designing the active and passive beamforming matrix under the quality of service constraints. For such, the limiting case where the maximum ratio transmission (MRT) technique is used to design the active beamforming vectors is considered, and an efficient iterative algorithm that jointly designs the optimal power allocation matrix for the UEs and the RIS phase-shift matrix is proposed to solve the formulated optimization problem.

---

[0]The contents of this chapter are extracted from [91].
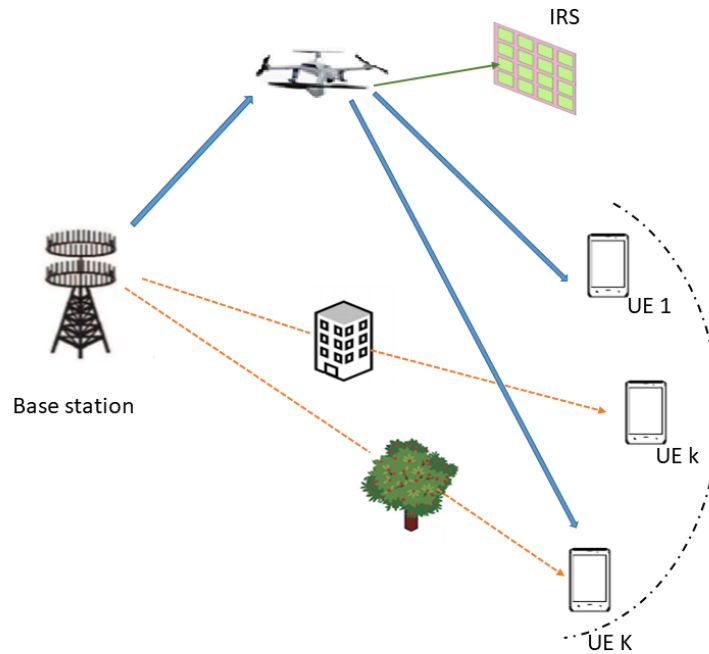
Figure 5.1: The aerial RIS aided communication system.

The organization of the chapter is as follows. The system model is detailed in Section 5.2. Then, in Section 5.3, the problem formulation and the proposed solution are presented. Through extensive simulations in Section 5.4, two communication systems, namely, the proposed aerial-RIS-based design and the conventional UAV-amplify-and-forward relaying, are compared in terms of the EE. Finally, Section 5.5 summarizes the chapter.

5.2 The RIS-UAV Aided Communication System

The system under consideration consists of a BS equipped with M antennas, and K single-antenna ground UEs awaiting service on the downlink as shown in Fig. 5.1. The UEs are in far distance from the servicing BS, i.e., at the edge of the coverage area. The downlink communication is assisted by a UAV which hovers at an intermediate position between the BS and the UEs. The UAV is equipped with N passive reflecting elements able to apply phase shifting on the impinging electromagnetic signal towards the UEs.

Let us denote the channel between the BS and the kth UE, and that between the RIS-UAV and the UE, by $\mathbf{h}_{\text{BS}-k} \in \mathbb{C}^{M \times 1}$ and $\mathbf{h}_{\text{UAV}-k} \in \mathbb{C}^{N \times 1}$, respectively. Further, let $\mathbf{H}_{\text{BS}-\text{UAV}} \in \mathbb{C}^{N \times M}$ denote the channel between the BS and the RIS-UAV. Channels follow the block-fading model, and are assumed to be independent from each others.[1] Due to the nature of the transceivers, terrestrial and aerial, we have two types of channels: the air-to-ground (A2G) for $\mathbf{h}_{\text{UAV}-k}$ and $\mathbf{H}_{\text{BS}-\text{UAV}}$, and the ground-to-ground (G2G) for $\mathbf{h}_{\text{BS}-k}$. The channel gains include the path loss and the fast fading effects, and expressed as $\mathbf{h}_{Q-k} = \sqrt{\mathbf{D}}\tilde{\mathbf{h}}$, where $Q \in \{\text{BS}, \text{UAV}\}$, $\mathbf{D}$ is diagonal matrix modeling the path loss effect, with elements $[\mathbf{D}]_{k,k} = d_{Q-k}^{-\alpha}$, $k \in \{1, 2, \dots, K\}$, in which $\alpha > 2$ is the path-loss exponent, $d_{Q,k}$ is the Euclidean distance separating transmitter Q and the kth UE, and $\tilde{\mathbf{h}}$ is the fast fading component modeled as a Rician distribution of two components: $\tilde{\mathbf{h}}^{\text{LoS}}$ represents the LoS component and $\tilde{\mathbf{h}}^{\text{NLoS}}$ is the NLoS fading component. Therefore, the channel can be expressed as

$$\mathbf{h}_{Q-k} = \sqrt{\frac{R\mathbf{D}}{R+1}}\tilde{\mathbf{h}}^{\text{LoS}} + \sqrt{\frac{\mathbf{D}}{R+1}}\tilde{\mathbf{h}}^{\text{NLoS}}, \tag{5.1}$$

where $Q \in \{\text{BS}, \text{UAV}\}$, and R is the Rician factor which determines the ratio between the Rician and the scattered components. As known, $R = 0$ results in a Rayleigh fading model, and $R \longrightarrow \infty$ results in LoS channel model. Here, $R = 0$ will be adopted for modeling the channel between the BS and the kth UE. The channel between the BS and the RIS-UAV can be explicitly written as

$$\mathbf{H}_{\text{BS}-\text{UAV}} = \tilde{\mathbf{H}}\mathbf{D}^{\frac{1}{2}}, \tag{5.2}$$

where $\tilde{\mathbf{H}} \in \mathcal{C}^{N \times M}$ represents the fast fading between the BS and the N reflecting elements of the RIS, and $\mathbf{D}$ is the $N \times N$ diagonal matrix modeling the path loss as defined before. We assume that the RIS mounted on the UAV is planar. The received baseband signal at the kth UE can be expressed as

$$y_k = \left(\mathbf{h}_{\text{UAV}-k}^{H}\mathbf{\Phi}\mathbf{H}_{\text{BS}-\text{UAV}}^{H} + \mathbf{h}_{\text{BS}-k}^{H}\right)\mathbf{g}_k x_k + n_k, \tag{5.3}$$

where x_k denotes the baseband transmitted signal from the BS to the kth UE, with $\mathbb{E}\{x_k\} = 1$; $\mathbf{\Phi} \triangleq diag(\phi_1, \dots, \phi_N)$ is a diagonal matrix composed of the phase shift values of the RIS elements, with $\phi_n \triangleq e^{j\theta_n}$ in which j is the imaginary unit and $\theta_n \in [0, 2\pi)$ is the phase shift of the nth unit cell applied to the incident signal; and where $\mathbf{g}_k \in \mathcal{C}^{M \times 1}$ denotes the transmit beamforming vector; and n_k is the complex additive white Gaussian noise with zero mean and variance σ^2. The SINR

---

[1]We assume full knowledge of the CSI, and leave investigations of cases with partial and imperfect CSI for future work.

at the kth UE is given by

$$\gamma_k = \frac{\left|\left(\mathbf{h}^H_{\text{UAV}-k}\boldsymbol{\Phi}\mathbf{H}^H_{\text{BS}-\text{UAV}} + \mathbf{h}^H_{\text{BS}-k}\right)\mathbf{g_k}\right|^2}{\sum\limits_{i=1,i\neq k}^{K}\left|\left(\mathbf{h}^H_{\text{UAV}-k}\boldsymbol{\Phi}\mathbf{H}^H_{\text{BS}-\text{UAV}} + \mathbf{h}^H_{\text{BS}-k}\right)\mathbf{g_i}\right|^2 + \sigma^2}. \tag{5.4}$$

Thus, the system sum-rate, in bits/s/Hz, can be written as

$$\mathcal{R} = \sum_{k=1}^{K}\log_2\left(1 + \gamma_k\right). \tag{5.5}$$

Now, we present the power consumption model for the RIS-UAV assisted communication system. The total dissipated power consists of the transmit power $P = \sum_{k=1}^{K}p_k$ at the BS, the hardware-related power that is consumed in the BS equipment, P_{BS}, the RIS power consumption, P_{RIS}, and the UAV power consumption, P_{UAV}. Hence, the total consumed power is given by

$$\mathcal{P}_\Sigma = P + P_{\text{BS}} + P_{\text{RIS}} + P_{\text{UAV}}. \tag{5.6}$$

The RIS power consumption depends on the nature and the resolution of the reflecting elements that effectively perform phase shifting on the incident signal. Assuming that each element is a phase shifter, the power consumed by an intelligent surface composed of N reflecting elements is given by $P_{\text{RIS}} = NP_n(b)$, where $P_n(b)$, $n = 1, \cdots, N$, denotes the power consumed by the circuitry required for adaptive phase-shifting having b-bit resolution. Typical values are provided in [22]. P_{UAV} consists in the power consumed by the UAV for its movement and hovering. We assume that the UAV is fixed-wing,[2] so the power can be expressed as $P_{\text{UAV}} = a_1 V^3 + \frac{a_2}{V}$, where a_1 and a_2 are constants that depend on several factors such as the UAV's weight, wing area, and air density [46], and where V is the UAV's constant velocity. Hence, the minimum power consumption of the UAV is given by $P_{\text{UAV}}^{\min} \triangleq \left(3^{-3/4} + 3^{1/4}\right)a_1^{1/4}a_2^{3/4}$ [46].

---

[2]Stable flight and positioning are assumed for the UAV. The effects of the UAV speed and trajectory on the LoS and the beamforming precision are left for future work.

5.3 Problem Formulation and Proposed Solution

Energy efficiency of the system under study is defined as the ratio of the achievable SE and the total consumed power, $\psi_{\text{EE}} = \frac{B\mathcal{R}}{\mathcal{P}_\Sigma}$, where B denotes the transmission bandwidth and $\mathcal{P}_\Sigma$ is the total power consumption shown in (5.6). The EE, in bits/Joule, is expressed as

$$\psi_{\text{EE}} = \frac{\sum\limits_{k=1}^{K} B \log_2 \left(1 + \gamma_k\right)}{\mathcal{P}_\Sigma}. \tag{5.7}$$

Our design aims at maximizing the EE of the communication system by jointly optimizing the BS beamforming matrix $\mathbf{G} = [\mathbf{g}_1, \mathbf{g}_2, \cdots, \mathbf{g}_K] \in \mathbb{C}^{M \times K}$, and the RIS phase shift matrix $\mathbf{\Phi}$. The optimization problem is formulated as

$$\begin{aligned}
\mathcal{P}_1 \ : \ &\underset{\mathbf{G}, \mathbf{\Phi}}{\text{maximize}} \ \psi_{\text{EE}} \\
&\text{s.t.} \quad \sum_{k=1}^{K} \|\mathbf{g}_k\|^2 \leq P_{\max}, \\
&\qquad \log_2(1 + \gamma_k) \geq R_{\min,k}, \ \forall k = 1, \cdots, K, \\
&\qquad \mathbf{\Phi} = diag(e^{j\theta_1}, \cdots, e^{j\theta_N}), \\
&\qquad 0 \leq \theta_n \leq 2\pi, \ \forall n = 1, \cdots, N,
\end{aligned} \tag{5.8}$$

where $P_{\max}$ is the maximum transmit power at the BS. The second constraint in (5.8) ensures the minimum required rate of each UE. Due to the non-convex nature of the user's rate and the fractional form of the EE objective function, the considered problem is difficult to tackle.

Recalling that our goal is to assess the limiting performance gains when the UAV is equipped with RIS, and that perfect CSI is assumed to be available at both the BS and the RIS, we make use of the asymptotic optimality of MRT when the number of antennas at the BS grows large [92, 93]. Therefore, for a given phase shift value θ_n and a transmit power level p_k, the beamforming vector $\mathbf{g}_k$ is expressed as

$$\mathbf{g}_k = \sqrt{p_k} \frac{\mathbf{H}_{\text{BS–UAV}} \mathbf{\Phi} \mathbf{h}_{\text{UAV}-k} + \mathbf{h}_{\text{BS}-k}}{\left\| \mathbf{h}_{\text{UAV}-k}^H \mathbf{\Phi} \mathbf{H}_{\text{BS–UAV}}^H + \mathbf{h}_{\text{BS}-k}^H \right\|}. \tag{5.9}$$

By substituting (5.9) into Eq. (5.7), the EE is written as

$$\psi_{EE} = \frac{\sum_{k=1}^{K} B \log_2 \left(1 + \frac{p_\text{k} \|\mathbf{h}_k\|^2}{\sum_{i=1,i\neq k}^{K} p_\text{i} \|\mathbf{h}_k\|^2 + \sigma^2} \right)}{P + P_\text{BS} + P_\text{RIS} + P_\text{UAV}}, \tag{5.10}$$

where $\mathbf{h}_k = \mathbf{h}_{\text{UAV}-k}^{H} \mathbf{\Phi} \mathbf{H}_{\text{BS}-\text{UAV}}^{H} + \mathbf{h}_{\text{BS}-k}^{H}$. The optimization problem $\mathcal{P}_1$ reduces to problem $\mathcal{P}_2$ shown below.

$$
\begin{aligned}
\mathcal{P}_2 \ : \ &\underset{\mathbf{\Phi},\mathbf{p}}{\text{maximize}} \ \psi_\text{EE} \\
&\text{s.t.} \ \sum_{k=1}^{K} p_k \leq P_\text{max}, \\
&\quad \log_2(1 + \gamma_k) \geq R_{\text{min},k}, \ \forall k = 1, \cdots, K, \\
&\quad \mathbf{\Phi} = diag(e^{j\theta_1}, \cdots, e^{j\theta_N}), \\
&\quad 0 \leq \theta_n \leq 2\pi, \ \forall n = 1, \cdots, N.
\end{aligned}
\tag{5.11}
$$

The problem in $\mathcal{P}_2$ is turned into finding the power allocation $\mathbf{p} = [p_1, \cdots, p_\text{K}]^T \in \mathbb{R}^{K \times 1}$, and the phase shift matrix for maximizing EE under the constraints of minimum users' data rates ($R_{\text{min},k}$). We omitted the bandwidth B in the formulations as it is constant, but will take it into account in the simulations. The objective function in $\mathcal{P}_2$ is non-convex. Making use of [94, Theorem 1], the objective function in $\mathcal{P}_2$ can be transformed into the following functional:

$$W(\mathbf{p}, \mathbf{\Phi}, \psi_\text{EE}) = \mathcal{R}(\mathbf{p}, \mathbf{\Phi}) - \psi_\text{EE} \mathcal{P}_{\sum}(\mathbf{p}). \tag{5.12}$$

Hence, the optimization problem $\mathcal{P}_2$ can be transformed into an equivalent problem:

$$
\begin{aligned}
\mathcal{P}_3 \ : \ &\underset{\mathbf{\Phi},\mathbf{p}}{\text{maximize}} \ W(\mathbf{p}, \mathbf{\Phi}, \psi_\text{EE}) \\
&\text{s.t.} \ \sum_{k=1}^{K} p_k \leq P_\text{max}, \\
&\quad \frac{p_k \|\mathbf{h}_k\|^2}{\sum_{i=1,i\neq k}^{K} p_i \|\mathbf{h}_k\|^2 + \sigma^2} \geq 2^{R_{\text{min},k}} - 1, \ \forall k = 1, \cdots, K, \\
&\quad \mathbf{\Phi} = diag(e^{j\theta_1}, \cdots, e^{j\theta_N}), \\
&\quad 0 \leq \theta_n \leq 2\pi, \ \forall n = 1, \cdots, N.
\end{aligned}
\tag{5.13}
$$

The optimal EE, ψ_EE^*, can be obtained by using the Dinkelbach method [95], through an effective iterative algorithm which updates ψ_EE at each iteration until it converges to ψ_EE^* or that the

---

Algorithm 5.1 Iterative algorithm for EE maximization in $\mathcal{P}_2$

Require: $s_{\max}, \epsilon_1, \mathbf{H}_{\mathrm{BS-UAV}}, \mathbf{h}_{\mathrm{BS}-k}, \mathbf{h}_{\mathrm{UAV}-k}, \psi_{\mathrm{EE}}^1 = 0$
1: The BS sets the beamforming vector as per Eq. (5.9).
2: Set $s = 1$
3: **repeat**
4: Solve the inner-loop problem $\mathcal{P}_3$ for a given ψ_{EE}^s to obtain $\mathbf{p}^s$ and $\mathbf{\Phi}^s$.
5: Set $\psi_{\mathrm{EE}}^s = \frac{\mathcal{R}(\mathbf{p}^s, \mathbf{\Phi}^s)}{\mathcal{P}_{\sum}(\mathbf{p}^s)}$
6: $s = s + 1$
7: **until** $\left| W(\mathbf{p}^{s-1}, \mathbf{\Phi}^{s-1}, \psi_{\mathrm{EE}}^{s-1}) - W(\mathbf{p}^s, \mathbf{\Phi}^s, \psi_{\mathrm{EE}}^s) \right| < \epsilon_1$ or $s > s_{\max}$.
Ensure: $\mathbf{p}^* = \mathbf{p}^{s-1}, \mathbf{\Phi}^* = \mathbf{\Phi}^{s-1}, \psi_{\mathrm{EE}}^* = \psi_{\mathrm{EE}}^{s-1}$

---

maximum number of iterations is reached. The procedure is summarized in Algorithm 5.1. As shown in Algorithm 5.1, we need to solve the following optimization problem for a given parameter ψ_{EE}^s, in each iteration s.

$$
\begin{aligned}
\mathcal{P}_4 \ : \ &\underset{\mathbf{p}, \mathbf{\Phi}}{\text{maximize}} \ \{W(\mathbf{p}, \mathbf{\Phi}, \psi_{\mathrm{EE}}^s) = \mathcal{R}(\mathbf{p}, \mathbf{\Phi}) - \psi_{\mathrm{EE}}^s \mathcal{P}_{\Sigma}(\mathbf{p})\} \\
&\text{s.t.} \ \sum_{k=1}^{K} p_k \leq P_{\max}, \\
&\qquad \frac{p_k \|\mathbf{h}_k\|^2}{\sum\limits_{i=1,i\neq k}^{K} p_i \|\mathbf{h}_k\|^2 + \sigma^2} \geq 2^{R_{\min,k}} - 1, \ \forall k = 1, \cdots, K, \\
&\qquad \mathbf{\Phi} = diag(e^{j\theta_1}, \cdots, e^{j\theta_N}), \\
&\qquad 0 \leq \theta_n \leq 2\pi, \ \forall n = 1, \cdots, N.
\end{aligned}
\tag{5.14}
$$

In order to solve the optimization problem $\mathcal{P}_4$, we adopt the alternating optimization technique. For a given phase shift matrix $\mathbf{\Phi}$, the objective function is optimized with respect to (w.r.t.) $\mathbf{p}$. Specifically, we focus on solving the following problem:

$$
\begin{aligned}
\mathcal{P}_5 \ : \ &\underset{\mathbf{p}}{\text{maximize}} \ \{W(\mathbf{p}, \mathbf{\Phi}, \psi_{\mathrm{EE}}^s) = \mathcal{R}(\mathbf{p}, \mathbf{\Phi}) - \psi_{\mathrm{EE}}^s \mathcal{P}_{\Sigma}(\mathbf{p})\} \\
&\text{s.t.} \ \frac{p_k \|\mathbf{h}_k\|^2}{\sum\limits_{i=1,i\neq k}^{K} p_i \|\mathbf{h}_k\|^2 + \sigma^2} \geq 2^{R_{\min,k}} - 1, \forall k = 1, \cdots, K, \\
&\qquad \sum_{k=1}^{K} p_k \leq P_{\max}.
\end{aligned}
\tag{5.15}
$$

We further transform the above into an approximately equivalent form. Based on [94, Eq. (11)-(13)], the objective function in $\mathcal{P}_5$ can be recast as

$$
V(\mathbf{p}) = f(\mathbf{p}) - l(\mathbf{p}), \tag{5.16}
$$

where $f(\mathbf{p}) = \sum_{k=1}^{K} \log_2(1 + \sum_{i=1}^{K} p_i \frac{\|\mathbf{h}_k\|^2}{\sigma^2}) - \psi_{\text{EE}}^s \mathcal{P}_\Sigma(\mathbf{p})$, and $l(\mathbf{p}) = \sum_{k=1}^{K} \log_2(1 + \sum_{i=1,i\neq k}^{K} p_i \frac{\|\mathbf{h}_k\|^2}{\sigma^2})$. Thus, $V(\mathbf{p})$ is the difference of two concave functions and, as such, the objective function is concave.

The function $l(\mathbf{p})$ can be approximated by its first-order Taylor expansion at $\mathbf{p}^j$, i.e., $l(\mathbf{p}^j) + \nabla l^T(\mathbf{p}^j)(\mathbf{p} - \mathbf{p}^j)$ in each iteration j, with $\nabla l^T(\mathbf{p}^j)$ being the gradient of $l(\mathbf{p})$ at $\mathbf{p}^j$.

The first constraint in problem $\mathcal{P}_5$ can be rewritten as

$$p_k \|\mathbf{h}_k\|^2 + (1 - 2^{R_{\min,k}}) \sum_{i=1,i\neq k}^{K} p_i \|\mathbf{h}_k\|^2 + \sigma^2 \geq 0, \ k = 1, \cdots, K. \tag{5.17}$$

Therefore, the problem in $\mathcal{P}_5$ is transformed to

$$\mathcal{P}_6 \ : \ \underset{\mathbf{p}}{\text{maximize}} \ \left\{ f(\mathbf{p}) - l(\mathbf{p}^j) - \nabla l^T(\mathbf{p}^j)(\mathbf{p} - \mathbf{p}^j) \right\}$$
$$\text{s.t.} \ \ (5.17), \tag{5.18}$$
$$\sum_{k=1}^{K} p_k \leq P_{\max}, \ \forall k = 1, \cdots, K.$$

The gradient of the function $l(\mathbf{p})$ at each $\mathbf{p}^j$ is given by

$$\nabla l(\mathbf{p}^j) = \sum_{k=1}^{K} \frac{1}{\sigma^2 + \sum_{i=1,i\neq k}^{K} \|\mathbf{h}\|^2 p_i} \mathbf{e}_k, \tag{5.19}$$

where $\mathbf{e}_k \in \mathbb{R}^K$ is a vector that can be written as

$$\mathbf{e}_k(i) = \begin{cases} 0, & \text{for } i = k \\ \frac{\|\mathbf{h}_k\|^2}{\ln 2} & \text{for } i \neq k. \end{cases} \tag{5.20}$$

The problem in (5.18) is a standard convex optimization problem, which can be effectively solved by the interior point method. The proposed power allocation algorithm is presented in Algorithm 2.

Algorithm 5.2 Iterative power allocation based on DC programming.

Require: $j_{\max}, \epsilon_2, j = 0, \Phi, \mathbf{p}^0$

    Calculate $V(\mathbf{p}^0) = f(\mathbf{p}^0) - l(\mathbf{p}^0)$

2: **repeat**

    Solve problem $\mathcal{P}_6$ by the interior point method to obtain $\mathbf{p}^{\mathrm{opt}}$ for a given $\mathbf{\Phi}$ and ψ_{EE}^s.

4: $j = j + 1$

    Set $\mathbf{p}^j = \mathbf{p}^{\mathrm{opt}}$ and calculate $V(\mathbf{p}^j) = f(\mathbf{p}^j) - l(\mathbf{p}^j)$.

6: **until** $j > j_{\max}$ or $|V(\mathbf{p}^j) - V(\mathbf{p}^{j-1})| < \epsilon_2$.

Ensure: $\mathbf{p}^s = \mathbf{p}^j$

Now, we focus on finding the optimal $\mathbf{\Phi}$ for a given transmit power $\mathbf{p}^s$ and EE value ψ_{EE}^s at each iteration s. The optimization problem $\mathcal{P}_4$ can be transformed to

$$
\mathcal{P}_7 : \underset{\mathbf{\Phi}}{\operatorname{maximize}} \ \{W\left(\mathbf{p}^s, \mathbf{\Phi}, \psi_{\mathrm{EE}}^s\right) = \mathcal{R}(\mathbf{p}^s, \mathbf{\Phi}) - \psi_{\mathrm{EE}}^s \mathcal{P}_\Sigma(\mathbf{p}^s)\}
$$

$$
\text{s.t.} \quad (5.17),
$$

$$
\mathbf{\Phi} = diag(e^{j\theta_1}, \cdots, e^{j\theta_N}),
$$

$$
0 \le \theta_n \le 2\pi, \forall n = 1, \cdots, N.
$$

(5.21)

The optimization problem $\mathcal{P}_7$ can be reduced to

$$
\mathcal{P}_8 \ : \ \underset{\mathbf{\Phi}}{\operatorname{maximize}} \ \sum_{k=1}^{K} \log_2 \left(1 + \frac{p_k \|\mathbf{h}_k\|^2}{\sum_{i=1, i\neq k}^{K} p_i \|\mathbf{h}_k\|^2 + \sigma^2} \right)
$$

$$
\text{s.t.} \quad (5.17),
$$

$$
\mathbf{\Phi} = diag(e^{j\theta_1}, \cdots, e^{j\theta_N}),
$$

$$
0 \le \theta_n \le 2\pi, \ \forall n = 1, \cdots, N.
$$

(5.22)

where $\mathbf{h}_k = \mathbf{h}_{\mathrm{UAV}-k}^H \mathbf{\Phi} \mathbf{H}_{\mathrm{BS-UAV}}^H + \mathbf{h}_{\mathrm{BS}-k}^H$. We proceed as in the case of optimization w.r.t. $\mathbf{p}$. The objective function can be recast as the difference of two concave functions $V_1(\mathbf{\Phi}) = f_1(\mathbf{\Phi}) - l_1(\mathbf{\Phi})$ with linear constraints, where $f_1(\mathbf{\Phi}) = \sum_{k=1}^{K} \log_2(\sigma^2 + \sum_{i=1}^{K} p_i \|\mathbf{h}_i\|^2)$ and $l_1(\mathbf{\Phi}) = \sum_{k=1}^{K} \log_2(\sigma^2 + \sum_{i=1, i\neq k}^{K} p_k \|\mathbf{h}_k\|^2)$. Thereafter, the problem can be efficiently solved by numerical optimization methods, such as the interior point or quasi-Newton methods.

5.4   Performance Evaluation

Simulation results are provided to validate the formulation and analysis of the proposed RIS-UAV assisted communication in comparison with the case of conventional AF relaying. For fair comparisons, the set-up in terms of the UEs' positions w.r.t. the BS is the same. We assume that the AF-UAV relay deploys a complex diagonal AF matrix $\mathbf{S}$ containing the amplifying factors. The system sum-rate is obtained using Eq. (5.5), with γ_k calculated as in [96]. The EE is calculated as per Eq. (5.7). Unlike the RIS case, the AF-UAV consumes power to amplify the incoming signal. Then, we maximize the EE w.r.t. $\mathbf{p}$ and $\mathbf{S}$ using the same proposed solution. Unless otherwise stated; we assume that the convergence parameters $\epsilon_1 = \epsilon_2 = 10^{-6}$ (cf. Algorithms 1 and 2), $B = 1$ MHz, the UE's minimum required rate is expressed as a function of a nominal rate $R_{\mathrm{n}} = 2\mathrm{bps/Hz}$, $\sigma^2 = -80$ dBm, $K = 16$, $P_{\max} = 30$ dBm, $P_n(b) = 0.01$ dBm, $P_{\mathrm{BS}} = 10$ dBm, $P_{\mathrm{UAV}} = 40$ dBm, and $P_{\mathrm{AF}} = 10$ dBm. The UAV's 2D position can vary, but the altitude is set to 50 m.
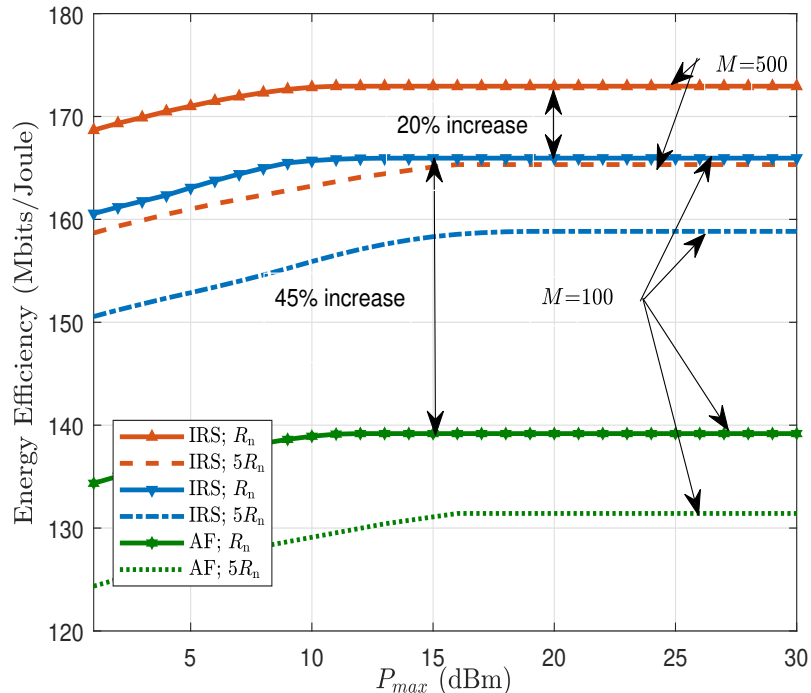
Figure 5.2: Energy efficiency versus BS's transmit power.

Figure 5.2 illustrates the achieved EE as a function of the maximum transmit power at the BS. Plots show that EE increases with the $P_{\max}$. It is also clear that leveraging the RIS-UAV to communicate with the UEs yields higher EE as compared to the scenario with conventional AF

relaying. In particular, for a BS power of $P_{\mathrm{max}} = 40$ dBm, the achieved EE in the RIS-UAV system is 45 % more than the AF-UAV based system. This is the consequence of the AF relay being an active equipment, thus having higher energy consumption compared to the RIS. At the BS side, on the other hand, increasing the number of antennas clearly yields higher EE. For instance, a gain of about 20 % is obtained when M is increased from 100 to 500 antennas. The figure also illustrates the impact of the UE's rate requirement on the achieved EE. Results are shown for $R_{min,k} = R_{\mathrm{n}}$ and $5R_{\mathrm{n}}$. As expected, an increase in the rate requirements reduces the achievable EE as the BS will need higher transmit power to meet the UEs' demands.
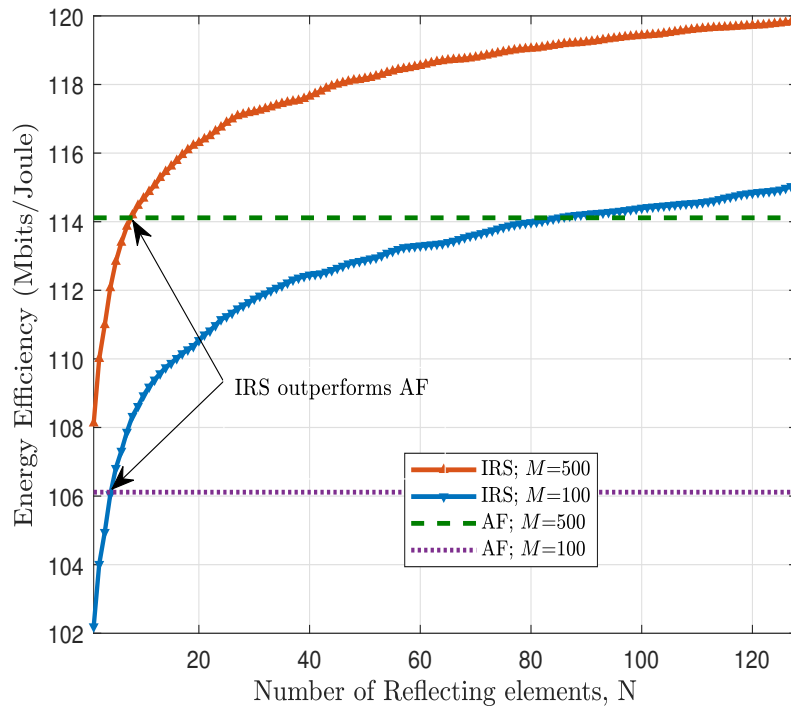
Figure 5.3: Energy efficiency versus the number of reflecting elements at the RIS-UAV, $M = 100$.

In Fig. 5.3, the achieved EE for different values of the number of reflecting elements is shown. As expected, the EE varies with the size of the RIS. When N is very small, say the extreme case of $N = 1$, the achieved EE is equal to 102 Mbits/Joule, a value that can be improved to 115 Mbits/Joule when using $N = 128$, thus resulting in an EE gain of 13 Mbits/Joule. As observed, when the number of reflecting elements $N < 4$ for the case with $M = 100$ or $N < 8$ for $M = 500$, the EE of the RIS-UAV based system is outperformed by the AF-UAV case. In practice, the number of reflecting elements at the RIS is much higher. The figure confirms that as N increases, the RIS outperforms the AF with a gain of more than 50% when $N = 128$. Such performance gain is due to

the fact that increasing N enables higher array gain, and the fact that using passive elements leads to important gains in terms of power consumption.
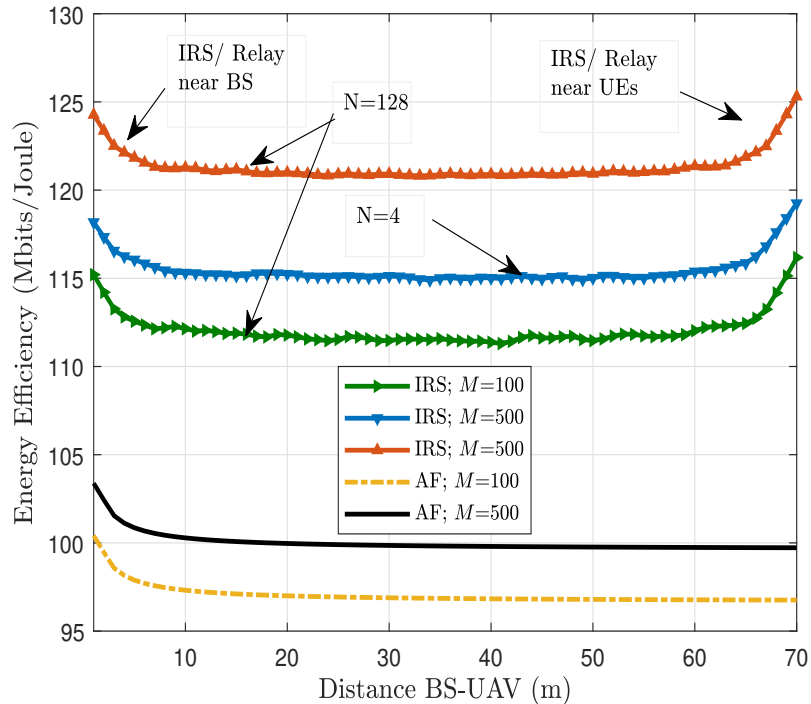
Figure 5.4: Energy efficiency versus the position of the RIS-UAV.

The effect of UAV position is investigated in Fig. 5.4. As before, the UEs are at equal distances from the BS, 70 m. We observe that if the RIS is closer to the BS, high EE can be achieved due to the strong LoS link in this case, which leads to a strong reflected signal at the RIS-UAV. The same behavior is observed when the UAV is closer to the UEs due to the virtual antenna array created. When the RIS-UAV is in between the BS and the UE, the EE decreases since the NLoS link becomes dominant and the reflected signal becomes weaker. In particular, a gain of more than 15% in EE is observed when the RIS-UAV is close to the BS, and a gain of 18% is achieved when the UAV is close to the UEs. Therefore, the RIS-UAV can be used in practice to serve cell-edge UEs with high energy efficiency. In the AF-UAV case, on the other hand, when the relaying node is far from the BSs the achieved EE decreases significantly, whereas a gain of 15% is obtained when the AF-UAV relay is closer to the BS. As the location of the RIS-UAV has an impact on the EE gain, the optimal deployment of this element in the 3D space must be studied.
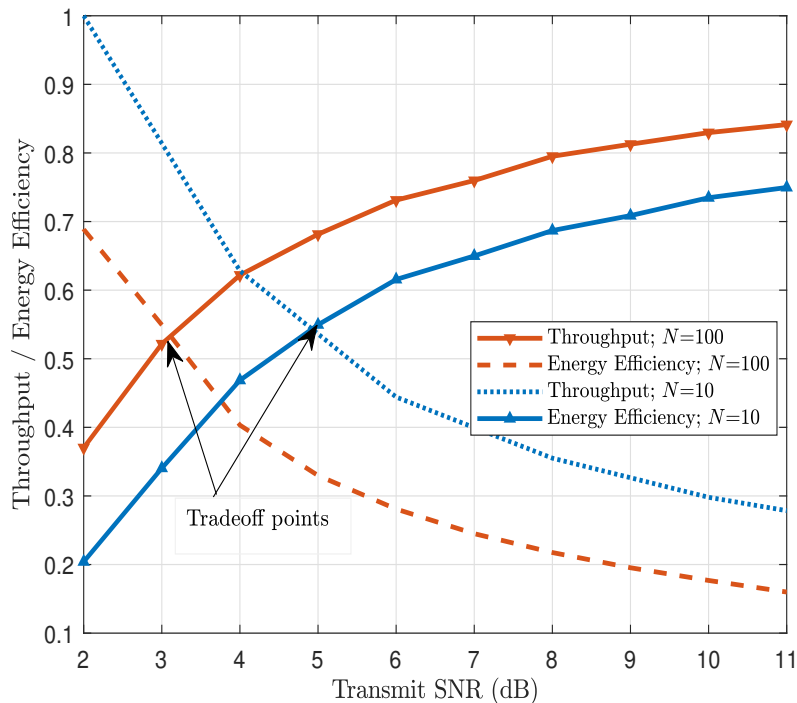
Figure 5.5: Normalized system throughput and energy efficiency versus the transmit SNR.

Figure 5.5 illustrates the tradeoff between the system throughput (sum-rate) and achieved EE for different values of transmit SNR, i.e., $\mathbb{E}\left[P_{\max}\|\mathbf{h}_k\|^2/\sigma^2\right]$. Normalized results are shown. We consider two extreme cases for the number of reflecting elements, $N = 100$ and $N = 10$, to assess the ensuing impact on the throughput-EE tradeoff point. The simulation set-up is the same as in the previous experiments, and we consider $M = 100$ antennas at the BS, and varying transmit power therein. The RIS-UAV is positioned at equal distance between the BS and the UEs. In the figure, the results are obtained by applying the power allocation algorithm and optimization algorithm described in Section III. As expected, the system throughput decreases when the SNR increases. Since maximizing EE will lead to a throughput decrease, which will affect the system performance, further investigations on the UAV positioning are required to adapt to the operating scenario and assist the BS in meeting the UEs rate demands with high EE.

5.5   Concluding Remarks

This chapter systematically considered a multi-user communication system where the base station leverages a UAV equipped with RIS to service its cell-edge UEs. Aiming at investigating the gains of the proposed deployment, we assumed the limiting case with maximum ratio transmission, and developed an efficient iterative algorithm that jointly optimizes the power allocation and the RIS phase shift matrix, with the goal of maximizing the overall EE. The performance of the proposed system was analyzed in comparison with the case when conventional AF relaying is used at the UAV. Comparative results were provided by analyzing the effects of the main system parameters on performance, and revealed that the RIS-UAV assisted communication can achieve significant gains compared to the AF-based system.

Chapter 6

Energy-Efficient Uplink Aerial-RIS Communication

6.1   Inroduction

Most of the existing works (cf. Chapter 1 Section 1.1.3) use RIS to assist the communication on the downlink. Motivated by this fact and the EE gains achieved by aerial-RIS while considering the limiting case and the cell-edge users (cf. Chapter 2), and that the UAV-aided communications are considered very promising for the next generation of wireless systems, to provide good connectivity conditions, capacity enhancement, better coverage area, and flexible deployment, a question arises about the gains that can be achieved when both technologies are jointly leveraged in the design of communication systems. In this chapter, we address the above question by considering a multi-cell system in which the uplink communication is performed via NOMA while assisted with aerial RIS, and assessing the merits of such design. The main objective is to maximize the EE of the system under individual power and rate constraints. The problem at hand requires to jointly optimize the UEs' transmit powers, the beamforming vectors at the BSs, and the phase shifts at the aerial RIS. The formulated EE maximization problem is a highly intractable non-convex problem. Herein, an iterative solution is proposed, based on the minimum mean square error (MMSE), and the semi-definite relaxation (SDR) techniques.

---

[0]The contents of this chapter are extracted from [97].

The organization of the chapter is as follows. The system model is detailed in Section 6.2. Then, in Section 6.3, the problem formulation and the proposed solution are presented. Simulations are conducted in Section 6.4 to verify the accuracy of the proposed solutions and to analyze the effect of the main system parameters on the EE of the two systems (the proposed aerial-RIS-based design and the conventional amplify-and-forward relaying at the UAV). Finally, Section 6.5 summarizes the chapter.

6.2 The RIS-UAV Aided Uplink Communication System
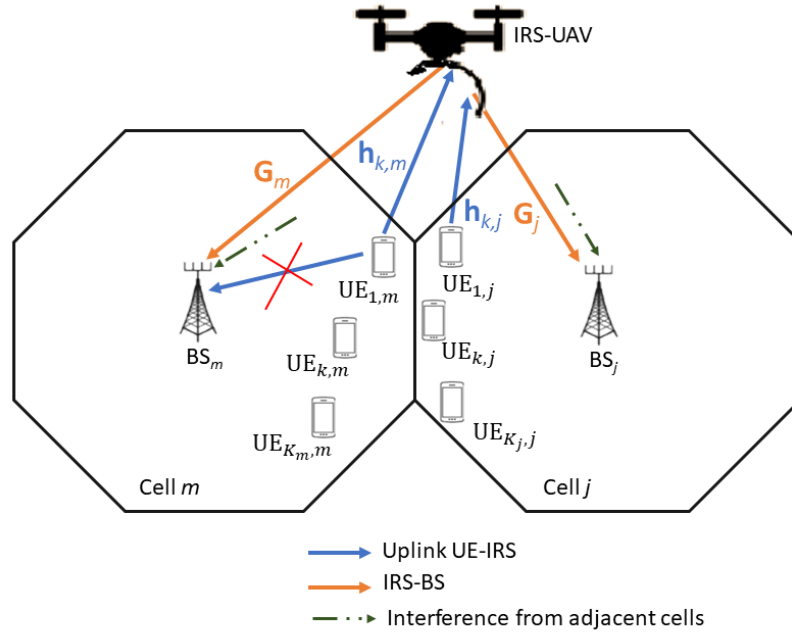
Figure 6.1: Uplink aerial RIS aided multi-cell communication system.

As illustrated in Fig. 6.1, we consider an aerial RIS-aided multi-cell uplink communication model constituted by M cells, each of which has a single BS equipped with $M_t > 1$ antennas, and K_m single-antenna UEs. The total number of UEs is then $K = \sum_{m=1}^{M} K_m$. Hereafter, these UEs are considered to be the cell-edge UEs. Indeed, such UEs being in far distance from the BS to which they are associated, suffer from poor channels conditions that can lead to service starvation, especially when the network is overloaded. The UAV, which is equipped with an RIS of N reflecting elements, is dedicated to assist the communication with such UEs in between adjacent cells. It is assumed that the UAV hovers at a fixed altitude A above the ground.

Let $\mathbf{G}_m \in \mathbb{C}^{N \times M_t}$ and $\mathbf{h}_{k,m} \in \mathbb{C}^{N \times 1}$ respectively denote the complex-equivalent baseband channels between the RIS and BS m, and between the RIS and the kth UE of cell m. Also, let $P_{k,m}$ denote the transmit power of UE k in cell m. We assume that the channel state information (CSI) of all channels is assumed to be perfectly known at the BS and the RIS [33], and all channels are assumed to experience block fading and to be independent from each other [91]. The channel gains include the effects of the path loss and the fast fading, and are expressed as $\mathbf{h}_{k,m} = \sqrt{\mathrm{D}}\tilde{\mathbf{h}}$, where $\mathbf{D}$ is a diagonal matrix modeling the path loss effect, with elements $[\mathbf{D}]_{k,k} = d_{k,m}^{-\alpha}, k \in \{1, 2, \ldots, K_m\}$, in which α is the path-loss exponent, $d_{k,m}$ is the Euclidian distance between the RIS-UAV and the kth UE of cell m, and $\tilde{\mathbf{h}}$ is the fast fading component modeled as a Rician distribution composed of two components: $\tilde{\mathbf{h}}^{\text{LoS}}$ represents the LoS component, and $\tilde{\mathbf{h}}^{\text{NLoS}}$ pertains to the NLoS fading. Hence, the channel between the kth UE of cell m and the RIS can be expressed as

$$\mathbf{h}_{k,m} = \sqrt{\frac{\mu \mathbf{D}}{\mu + 1}}\tilde{\mathbf{h}}^{\text{LoS}} + \sqrt{\frac{\mathbf{D}}{\mu + 1}}\tilde{\mathbf{h}}^{\text{NLoS}}, \tag{6.1}$$

where the Rician factor μ determines the ratio between the Rician and the scattered components. The channel between the RIS and the mth BS can be written as

$$\mathbf{G}_m = \tilde{\mathbf{G}}_m \mathbf{D}_m^{\frac{1}{2}}, \tag{6.2}$$

where $\tilde{\mathbf{G}}_m$ represents the fast fading between the mth BS and the RIS, and where $\mathbf{D}_m$ is the diagonal matrix modeling the path loss between the BS m and the RIS as defined before.

Within each cell m, the corresponding BS accommodates multiple UEs via NOMA. Without loss of generality, we assume that the UEs are arranged in descending order w.r.t. their effective channels, namely,

$$\left|\mathbf{G}_m^H \mathbf{h}_{1,m}\right| \geq \cdots \geq \left|\mathbf{G}_m^H \mathbf{h}_{K_m,m}\right|. \tag{6.3}$$

We consider universal frequency reuse among the cells and, thus, each BS receives interference from the active UEs in other cells. To mitigate interference, the successive interference cancelation (SIC) technique is used at the BSs. The SIC decoding order is based on the channel gains. Hence, the signal corresponding to the UE with the strongest channel gain is decoded first. The received signal

at the mth BS after applying the beamforming vector $\mathbf{w}_m \in \mathbb{C}^{M_{\text{t}} \times 1}$ can be expressed as

$$y_m = \sum_{k=1}^{K_m} \sqrt{P_{k,m}} \mathbf{w}_m^H \mathbf{G}_m^H \boldsymbol{\Theta} \mathbf{h}_{k,m} s_{k,m} + \sum_{j \neq m}^{M} \sum_{k=1}^{K_m} \sqrt{P_{k,j}} \mathbf{w}_m^H \mathbf{G}_j^H \boldsymbol{\Theta} \mathbf{h}_{k,j} s_{k,j} + n_m, \qquad (6.4)$$

where $\boldsymbol{\Theta} = \operatorname{diag}\left(e^{j\theta_1}, e^{j\theta_2}, \cdots, e^{j\theta_N}\right)$ is the matrix of the RIS phase shift elements, $s_{k,m}$ is the received signal from UE k of cell m, with $\mathbb{E}\left[|s_{k,m}|^2\right] = 1, \forall k \in \{1, \cdots, K_m\}$ and $m \in \{1, \cdots, M\}$, and where n_m is the additive white Gaussian noise at BS m, assumed of zero mean and variance σ_m^2.

At BS m, the SINR of UE k can be calculated as

$$\gamma_{k,m} = \frac{P_{k,m} \left|\mathbf{w}_m^H \mathbf{G}_m^H \boldsymbol{\Theta} \mathbf{h}_{k,m}\right|^2}{\sum_{i=k+1}^{K_m} P_{i,m} \left|\mathbf{w}_m^H \mathbf{G}_m^H \boldsymbol{\Theta} \mathbf{h}_{i,m}\right|^2 + \sum_{j \neq m}^{M} \sum_{k=1}^{K_m} P_{k,j} \left|\mathbf{w}_m^H \mathbf{G}_j^H \boldsymbol{\Theta} \mathbf{h}_{k,j}\right|^2 + \sigma_m^2}, \qquad (6.5)$$

Therefore, the system's achievable sum-rate, in bits/s/Hz, can be written as

$$R = B \sum_{m=1}^{M} \sum_{k=1}^{K_m} \log_2 \left(1 + \gamma_{k,m}\right), \qquad (6.6)$$

where B is the total bandwidth in Hz. For notational convenience, we set B to unity in the rest of this chapter.

Now, we present the power consumption model for the aerial RIS assisted uplink communication system:

$$P_\Sigma = P + P_{\text{c}} + P_{\text{RIS}} + P_{\text{UAV}}, \qquad (6.7)$$

where $P = \sum_{m=1}^{M} \sum_{k=1}^{K_m} P_{k,m}$ is the total transmit power of the UEs, $P_{\text{c}} = K P_{\text{UE}}$ is the power dissipated by the circuitry of the UEs, and P_{RIS} is the power consumed by the N reflecting elements of the RIS and expressed as $P_{\text{RIS}} = N P_{\text{n}}$, in which P_{n} denotes the power consumption of each element of the RIS for controlling the phase of the reflected signal when it is active. Besides, P_{UAV} is the flight power consumption of the UAV, which is finite and plays a crucial role in UAV-based communications due to the limited battery capacity of the UAV. In the system under consideration, similar to [91] we assume that the UAV is fixed-wing, and express its flight consumption power as $P_{\text{UAV}} = a_1 V^3 + \frac{a_2}{V}$.

The EE of the uplink communication system assisted by the UAV-RIS is the ratio of the achievable sum-rate shown in (6.6) and the total consumed power given in (6.7). Hence, we have

$$\psi_{\text{EE}} = \frac{\sum_{m=1}^{M} \sum_{k=1}^{K_m} \log_2 \left(1 + \gamma_{k,m}\right)}{P_{\Sigma}}. \tag{6.8}$$

6.3 Problem Formulation and Proposed Solution

Our design goal is to maximize the EE of the system under study by optimizing the phase shift matrix $\boldsymbol{\Theta}$ of the aerial RIS, the beamforming matrix $\mathbf{W} = [\mathbf{w}_1, \cdots, \mathbf{w}_M]$, and the power matrix $\mathbf{P} = [\mathbf{p}_1, \cdots, \mathbf{p}_M]$, with $\mathbf{p}_m = [P_{1,m} \cdots, P_{K_m,m}]^{\text{T}}$ denoting the power vector in cell m. The optimization problem is formulated as

$$\begin{aligned}
\mathcal{P}1 \ : \underset{\boldsymbol{\Theta},\mathbf{P},\mathbf{W}}{\text{maximize}} \ & \psi_{\text{EE}} \\
\text{s.t.:} \ & \\
& \text{C.1} \quad P_{k,m} \leq P_{k,m}^{\max}, \ \forall k \ \& \ \forall m, \\
& \text{C.2} \quad \|\mathbf{w}_m\|^2 = 1, \ \forall m, \\
& \text{C.3} \quad \log_2(1 + \gamma_{k,m}) \geq R_{k,m}^{\min}, \ \forall k \ \& \ \forall m, \\
& \text{C.4} \quad \boldsymbol{\Theta} = diag(e^{j\theta_1}, \cdots, e^{j\theta_N}), \\
& \qquad \ \ 0 \leq \theta_n \leq 2\pi; \ n = 1, \cdots, N,
\end{aligned} \tag{6.9}$$

where C.1 reflects the constraint on the maximum transmit power, C.2 denotes the amplitude constraint of each row in the active beamforming matrix, C.3 ensures the minimum required rate of each UE, and C.4 ensures the unit modulus constraint for the passive beamforming at the RIS.

Clearly, directly solving problem $\mathcal{P}1$ is difficult, due to the fact that the optimization variables are entangled with each other and the problem is non-convex and may not be converted to a convex problem with simple manipulations. As a solution, we adopt the alternating optimization approach to solve the non-convex EE maximization problem $\mathcal{P}1$. Therefore, the three-variable optimization problem is divided into two sub-problems and can be solved iteratively to achieve a suboptimal solution. The first sub-problem optimizes the power allocation, while the second one jointly optimizes the BS active beamforming matrix and the passive beamforming matrix, i.e., the phase-shift matrix.

For the first stage, the power allocation problem with fixed active and passive beamforming matrices, $\mathbf{W}$ and $\boldsymbol{\Theta}$, is expressed as

$$
\begin{aligned}
\mathcal{P}2 \ : & \underset{\mathbf{P}}{\text{maximize}} \ \psi_{\text{EE}} \\
& \text{s.t.:} \\
& \text{C.1} \quad P_{k,m} \leq P_{k,m}^{\max}, \ \forall k \ \& \ \forall m, \\
& \text{C.3} \quad \log_2(1 + \gamma_{k,m}) \geq R_{k,m}^{\min}, \ \forall k \ \& \ \forall m.
\end{aligned}
\tag{6.10}
$$

It is clear that (6.10) is a fractional problem. The latter can be transformed into a series of parametric subtractive-form subproblems as follows:

$$
\begin{aligned}
\mathcal{P}3 \ : & \underset{\mathbf{P}}{\text{maximize}} \ \sum_{m=1}^{M} \sum_{k=1}^{K_m} \log_2 \left(1 + \gamma_{k,m}\right) - \lambda^{(t-1)} \mathcal{P}_{\Sigma} \\
& \text{s.t.:} \ \text{C.1 and C.3,}
\end{aligned}
\tag{6.11}
$$

where t is the iteration index, and $\lambda^{(t-1)}$ is a non-negative parameter. Starting from $\lambda^{(0)} = 0$, $\lambda^{(t)}$ can be updated according to $\lambda^{(t)} = \frac{\sum_{m=1}^{M} \sum_{k=1}^{k_m} \log_2(1+\gamma_{k,m}^{(t)})}{P^{(t)}+P_{\text{c}}+P_{\text{RIS}}+P_{\text{UAV}}}$, where $P^{(t)}$ and $\gamma_{k,m}^{(t)}$ are the updated power and SINR after solving (6.11). Moreover, the maximum value of the objective function in (6.11) is calculated using $S_1^{(t)} = \sum_{m=1}^{M} \sum_{k=1}^{K_m} \log_2(1+\gamma_{k,m}^{(t)}) - \lambda^{(t-1)}(P^{(t)} + P_{\text{c}} + P_{\text{RIS}} + P_{\text{UAV}})$. When t increases, $\lambda^{(t)}$ keeps growing while $S_1^{(t)}$ decreases. When $S_1^{(t)} = 0$, $\lambda^{(t)}$ is maximized, which is also the maximum EE value of (6.10), as per the optimization theory described in [95].

Now the question is how to solve (6.11) for a given λ. Since the objective function is non-convex, the optimization problem is non-convex. After simple mathematical manipulation, the objective function in (6.11) can be re-written as

$$
f(\mathbf{P}) = \underbrace{- \sum_{m=1}^{M} \sum_{k=1}^{K_m} \log_2 \left(1 + I_1\right)}_{f_1(\mathbf{P})} - \lambda \, \mathcal{P}_{\Sigma} \underbrace{\sum_{m=1}^{M} \sum_{k=1}^{K_m} \log_2 \left(1 + I_2\right)}_{f_2(\mathbf{P})},
\tag{6.12}
$$

where $I_1 = \sum_{i=k+1}^{K_m} P_{i,m} v_{i,m} + \sum_{j \neq m}^{M} \sum_{k=1}^{K_m} P_{k,j} v_{k,j}$ and $I_2 = \sum_{i=k+1}^{K_m} P_{i,m} v_{i,m} + \sum_{j \neq m}^{M} \sum_{k=1}^{K_m} P_{k,j} v_{k,j}$, in which the variable $v_{p,q} = \left| \mathbf{w}_m^H \mathbf{G}_q^H \boldsymbol{\Theta} \mathbf{h}_{p,q} \right|^2 / \sigma_m^2$. Also, the constraint C.3 can be reformulated as

$$
P_{k,m} v_{k,m} \geq \left(2^{R_{k,m}^{\min}} - 1 \right) \left(1 + I_2\right), \ \forall k \ \& \ \forall m.
\tag{6.13}
$$

In the functional (6.12), both $f_1(\mathbf{P})$ and $f_2(\mathbf{P})$ are concave functions. Thus, the objective function $f(\mathbf{P})$ is the difference of two concave functions. For $k \in \{1, \cdots, K_m\}$ and $m \in \{1, \cdots, M\}$, let us define the vector $\mathbf{e}_{k,m}$, satisfying $\mathbf{e}_{k,m} = 0$ and $\mathbf{e}_{k,m}(i) = \frac{v_{k,m}}{ln2}$, $i \neq k$. The gradient of $f_2(\mathbf{P})$ can then be found as

$$\nabla f_2(\mathbf{P}) = \sum_{m=1}^{M} \sum_{k=1}^{K_m} \frac{\mathbf{e}_{k,m}}{1 + I_2}, \tag{6.14}$$

where I_2 is defined after (6.12). Here, we will generate a sequence $\{\mathbf{P}^{(t)}\}$ of feasible solutions. $\{\mathbf{P}^{(t)}\}$ is the optimal solution to the following convex optimization problem at the tth iteration

$$
\begin{aligned}
\mathcal{P}4 \ : \underset{\mathbf{P}}{\text{maximize}} \ & f_1(\mathbf{P}) - f_2\left(\mathbf{P}^{(t-1)}\right) - \langle \mathbf{J}_1, \mathbf{J}_2 \rangle \\
\text{s.t.: } & \text{C.1 and (6.13)},
\end{aligned}
\tag{6.15}
$$

where $\mathbf{J}_1 = \nabla f_2\left(\mathbf{P}^{(t-1)}\right)$ and $\mathbf{J}_2 = \mathbf{P} - \mathbf{P}^{(t-1)}$. Therefore, problem $\mathcal{P}4$ can be efficiently solved using the convex software package CVX [98].

For the second stage, with fixed power allocation matrix $\mathbf{P}$, the optimization problem $\mathcal{P}1$ can be simplified as follows:

$$
\begin{aligned}
\mathcal{P}5 \ : \underset{\mathbf{W}, \mathbf{\Theta}}{\text{maximize}} \ & \psi_{\text{EE}} \\
\text{s.t.: } & \\
\text{C.2} \quad & \|\mathbf{w}_m\|^2 = 1, \ \forall m, \\
\text{C.3} \quad & \log_2(1 + \gamma_{k,m}) \geq R_{k,m}^{\min}, \ \forall k \ \& \ \forall m, \\
\text{C.4} \quad & \mathbf{\Theta} = diag(e^{j\theta_1}, \cdots, e^{j\theta_N}), \\
& 0 \leq \theta_n \leq 2\pi, \ \forall n = 1, \cdots, N.
\end{aligned}
\tag{6.16}
$$

First, we focus on designing the optimal active beamforming matrix $\mathbf{W}$ for fixed $\mathbf{\Theta}$. Here, the objective function depends only on the SINRs, i.e., the $\gamma_{k,m}$'s, which depend on $\mathbf{w}_m$. The optimal beamforming vector that can balance interference and noise is the MMSE [99], expressed as

$$\mathbf{w}_m = \left(\sigma_m^2 \mathbf{I}_{M_t} + \sum_{i \neq k} P_{i,m} \bar{\mathbf{h}}_{i,m} \bar{\mathbf{h}}_{i,m}^H \right)^{-1} \bar{\mathbf{h}}_{k,m}, \tag{6.17}$$

where $\bar{\mathbf{h}}_{p,m} = \mathbf{G}_m^H \mathbf{\Theta} \mathbf{h}_{p,m}$ and $\mathbf{I}_{M_t}$ is the identity matrix.

Now, we focus on designing the passive beamforming matrix $\boldsymbol{\Theta}$ under the assumption that we have fixed $\mathbf{W}$ and $\mathbf{P}$. The optimization problem $\mathcal{P}1$ can be re-written as

$$\mathcal{P}6 \ : \underset{\boldsymbol{\Theta}}{\text{maximize}} \ \psi_{\text{EE}}$$

$$\text{s.t.:}$$
$$\text{C.3} \quad \log_2(1 + \gamma_{k,m}) \geq R_{k,m}^{\min}, \ \forall k \ \& \ \forall m, \tag{6.18}$$
$$\text{C.4} \quad \boldsymbol{\Theta} = diag(e^{j\theta_1}, \cdots, e^{j\theta_N}),$$
$$0 \leq \theta_n \leq 2\pi, \ \forall n = 1, \cdots, N.$$

We first re-arrange the diagonal matrix $\boldsymbol{\Theta}$ into a vector $\phi \in C^{N \times 1}$ to handle the term $\left|\mathbf{w}_m^H \mathbf{G}_m^H \boldsymbol{\Theta} \mathbf{h}_{k,m}\right|^2$ in the SINR. Then, we introduce an auxiliary vector $\tilde{\mathbf{h}}_{k,m} = \mathbf{w}_m^H \mathbf{G}_m^H \circ \mathbf{h}_{k,m}$. Hereafter, we obtain $\left|\mathbf{w}_m^H \mathbf{G}_m^H \boldsymbol{\Theta} \mathbf{h}_{k,m}\right|^2 = \left|\phi^H \tilde{\mathbf{h}}_{k,m}\right|^2$. We also reformulate $\left|\phi^H \tilde{\mathbf{h}}_{k,m}\right|^2 P_{k,m}$ as

$$\left|\phi^H \tilde{\mathbf{h}}_{k,m}\right|^2 P_{k,m} = \phi^H P_{k,m} \tilde{\mathbf{h}}_{k,m} \tilde{\mathbf{h}}_{k,m}^H \phi$$
$$= \text{Tr}\left(P_{k,m} \tilde{\mathbf{h}}_{k,m} \tilde{\mathbf{h}}_{k,m}^H \phi \phi^H\right). \tag{6.19}$$

Let us denote by $\tilde{\mathbf{H}}_{k,m} = P_{k,m} \tilde{\mathbf{h}}_{k,m} \tilde{\mathbf{h}}_{k,m}^H$ and $\boldsymbol{\Phi} = \phi \phi^H$ two auxiliary matrices. The constraint C.3 in the optimization problem $\mathcal{P}6$ can be also linearized as (6.13). As such, we obtain

$$\text{Tr}\left(\boldsymbol{\Phi} \tilde{\mathbf{H}}_{k,m}\right) \geq \left(2^{R_{k,m}^{\min}} - 1\right)\left(I_3(\boldsymbol{\Phi}) + \sigma_m^2\right), \ \forall k \ \& \ \forall m, \tag{6.20}$$

where $I_3(\boldsymbol{\Phi}) = \sum_{i=k+1}^{K_m} \text{Tr}\left(\mathbf{V}_{i,m}\right) + \sum_{j \neq m}^{M} \sum_{k=1}^{K_m} \text{Tr}\left(\mathbf{V}_{k,j}\right)$, in which $\mathbf{V}_{p,q} = \boldsymbol{\Phi} \tilde{\mathbf{H}}_{p,q}$. Therefore, problem $\mathcal{P}6$ can be re-written as

$$\mathcal{P}7 \ : \underset{\boldsymbol{\Phi}}{\text{maximize}} \ \sum_{m=1}^{M} \sum_{k=1}^{K_m} \log_2\left(1 + \frac{\text{Tr}\left(\mathbf{V}_{k,m}\right)}{I_3(\boldsymbol{\Phi}) + \sigma_m^2}\right)$$

$$\text{s.t.:}$$
$$\text{Eq. (6.20),}$$
$$\text{diag}\left(\boldsymbol{\Phi}\right) = 1, \tag{6.21}$$
$$\boldsymbol{\Phi} \succeq \mathbf{0},$$
$$\text{rank}(\boldsymbol{\Phi}) = 1,$$

where $\text{diag}\left(\boldsymbol{\Phi}\right)$ returns the diagonal elements of $\boldsymbol{\Phi}$.

The problem $\mathcal{P}7$ is still non-convex due to the objective function and the rank-one constraint. The rank-one constraint can be replaced with a convex positive semi-definite constraint $\boldsymbol{\Phi} - \bar{\phi}\bar{\phi}^H \geq 0$, with $\bar{\phi}$ an auxiliary variable. The objective function of problem $\mathcal{P}7$ can be recast as a difference of two concave functions, expressed as

$$S_3(\boldsymbol{\Phi}) = -\underbrace{\sum_{m=1}^{M}\sum_{k=1}^{K_m} \log_2\left(\sum_{k=1}^{K_m}\mathrm{Tr}\left(\mathbf{V}_{k,m}\right) + \sigma_m^2\right)}_{f_3(\boldsymbol{\Phi})} + \underbrace{\sum_{m=1}^{M}\sum_{k=1}^{K_m}\log_2\left(I_3(\boldsymbol{\Phi}) + \sigma_m^2\right)}_{f_4(\boldsymbol{\Phi})}, \qquad (6.22)$$

where $S_3(\boldsymbol{\Phi}) = \sum_{m=1}^{M}\sum_{k=1}^{K_m}\log_2\left(1 + \frac{\mathrm{Tr}\left(\mathbf{V}_{k,m}\right)}{I_3(\boldsymbol{\Phi})+\sigma_m^2}\right)$. Since $\boldsymbol{\Phi}$ is a complex matrix, we need to calculate the derivatives of $f_4(\boldsymbol{\Phi})$ over both the real and imaginary parts. As we need only the diagonal elements of $\boldsymbol{\Phi}$, we calculate the derivatives of only $\boldsymbol{\Phi}(n,l), \forall n \in \{1, \cdots, N\}$ and $l < n$. In so doing, we obtain

$$\frac{\partial f_4(\boldsymbol{\Phi})}{\partial \Re(\boldsymbol{\Phi}(n,l))} = \frac{-1}{\ln 2}\sum_{m=1}^{M}\sum_{k=1}^{K_m}\frac{E_1}{E_2},$$

and

$$\frac{\partial f_4(\boldsymbol{\Phi})}{\partial \Im(\boldsymbol{\Phi}(n,l))} = \frac{-i}{\ln 2}\sum_{m=1}^{M}\sum_{k=1}^{K_m}\frac{E_3}{E_4},$$

where $E_1 = \sum_{i=k+1}^{K_m}\mathbf{Z}_{i,m}(n,l) + \sum_{j\neq m}^{M}\sum_{k=1}^{K_m}\mathbf{Z}_{k,j}(n,l)$, $E_2 = \mathrm{Tr}\left(\boldsymbol{\Phi}\sum_{i=k+1}^{K_m}\tilde{\mathbf{H}}_{i,m}\right) + \mathrm{Tr}\left(\boldsymbol{\Phi}\sum_{j\neq m}^{M}\sum_{k=1}^{K_m}\tilde{\mathbf{H}}_{k,j}\right) + \sigma_m^2$, $E_3 = \sum_{i=k+1}^{K_m}\mathbf{U}_{i,m}(n,l) + \sum_{j\neq m}^{M}\sum_{k=1}^{K_m}\mathbf{U}_{k,j}(n,l)$ and $E_4 = \mathrm{Tr}\left(\boldsymbol{\Phi}\sum_{i=k+1}^{K_m}\tilde{\mathbf{H}}_{i,m}\right) + \mathrm{Tr}\left(\boldsymbol{\Phi}\sum_{j\neq m}^{M}\sum_{k=1}^{K_m}\tilde{\mathbf{H}}_{k,j}\right) + \sigma_m^2$, in which $\mathbf{Z}_{p,q}(n,l) = \tilde{\mathbf{H}}_{p,q}(n,l) + \tilde{\mathbf{H}}_{p,q}^H(n,l)$ and $\mathbf{U}_{p,q}(n,l) = \tilde{\mathbf{H}}_{p,q}(n,l) - \tilde{\mathbf{H}}_{p,q}^H(n,l)$.

Finally, the optimization problem reduces to

$$\mathcal{P}8 \; : \underset{\boldsymbol{\Phi},\bar{\phi}}{\text{maximize}}\; f_3(\boldsymbol{\Phi}) - f_4\left(\boldsymbol{\Phi}^{(t-1)}\right) - f_5(\boldsymbol{\Phi})$$

$$\text{s.t.:}$$

$$\text{Eq. (6.20)}, \qquad\qquad\qquad (6.23)$$

$$\boldsymbol{\Phi} \succeq \mathbf{0},$$

$$\boldsymbol{\Phi} - \bar{\phi}\bar{\phi}^H \geq 0,$$

where $f_5(\boldsymbol{\Phi}) = \sum_{n=1}^{N}\sum_{l=1}^{n-1}\Re\left(\boldsymbol{\Phi}(n,l) - \boldsymbol{\Phi}(n,l)^{(t-1)}\right)\frac{\partial f_4}{\partial \Im\left(\boldsymbol{\Phi}(n,l)^{(t-1)}\right)}$. At iteration t, problem $\mathcal{P}8$ is a convex semidefinite programming (SDP) optimization problem. Therefore, the optimal solution can be obtained using standard convex optimization methods such as the interior-point method.

6.4 Performance Evaluation

In this section, numerical results are presented to evaluate the performance of the proposed system design in terms of EE. We focus on two adjacent cells, i.e., $M = 2$, with the RIS-UAV hovering above the boundary of the adjacent cells at an altitude $A = 100$ m. The BSs of said cells, denoted BS_1 and BS_2, are separated by distance $D = 100$ m. In the comparisons, we consider two communication scenarios: (i) the proposed design with aerial RIS, referred to as A-RIS and (ii) the system with amplify-and-forward (AF) relaying at the UAV, referred to as aerial relay (A-Relay), in which signals received from the UEs at the UAV are transmitted to their target BS after amplification. For the A-Relay system, the uplink sum-rate is obtained using (6.6), where $\gamma_{k,m}$ is calculated as per [100, (6)]; the total power consumption is calculated with (6.7) after replacement of P_{RIS} with the relaying power P_{Relay}; and the achievable EE is calculated via (6.8). The AF amplification factors are stored in $\mathbf{G}_{\mathrm{AF}}$. The joint power allocation and $\mathbf{G}_{\mathrm{AF}}$ designs are also conducted using the same approach (MMSE and the SDR) as in the A-RIS system.

Unless otherwise stated, the default simulation parameters are: $\sigma_m^2 = -174$ dBm/Hz, $K_m = 2$, $M_{\mathrm{t}} = 4$, $\alpha = 4$, $\mu = 5$, $P_{\mathrm{c}} = 17$ dBm, $P_n = -20$ dBm, $R_{\min} = 1$ bit/s, $P_{\mathrm{UAV}} = 40$ dBm, and $P_{\mathrm{Relay}} = 10$ dBm. Figure 6.2 compares the achievable EE of the A-RIS and A-Relay systems as a function of the UEs' maximum transmit powers, for different values of the required rate. Here, we consider the maximum allowable transmit power and the minimum required rate for all UEs to be identical, i.e, $P_{k,m}^{\max} = P_{\max}$, $R_{k,m}^{\min} = R_{\min}$, $\forall k$ & $\forall m$.

The results validate that the EE first increases with the UE's maximum transmit power, and then saturates. This can be explained by the concavity of the log-function of the rate, and that each UE is constrained by its uplink maximum transmit power. For a given value of $P_{\max}$, leveraging an aerial RIS results in higher EE compared to the case with AF relaying at the UAV. For instance, a gain of 66% can be achieved with $P_{\max} = 24$ dBm and $N = 64$ RIS elements. The RIS reflecting elements being passive, equipping the UAV with larger meta-surfaces is energy efficient since the RIS does not require active radio-frequency chains and power amplifiers as in conventional transmitters. We also note that the higher the UEs' required rates, the lower the achievable EE. Indeed, transmitting more data requires more transmit power and, thus, higher energy consumption. Collectively, the results demonstrate the performance advantages of aerial RIS compared to the relaying benchmark.
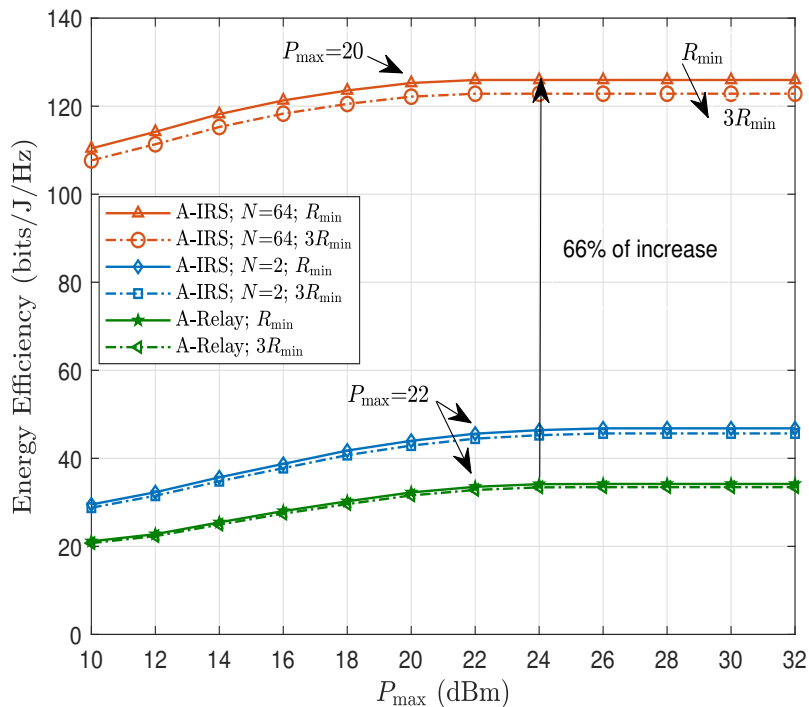
Figure 6.2: Energy efficiency versus the UEs' maximum transmit power.

Figure 6.3(a) plots the EE versus the number of reflecting elements at the RIS. For comparison purposes, the EE pertaining to the system with UAV relaying, i.e., A-Relay, is also shown. It is clear that the EE of the A-RIS system increases with the number of RIS elements, showing the effectiveness of deploying more reflectors at the RIS. For instance, a gain of 68% can be achieved when the number of elements increases from $N = 2$ to $N = 64$. We note that the A-RIS system always outperforms its A-Relay counterpart. In particular, an EE gain of 74% can be attained with a high number of reflecting elements, i.e., $N = 64$. Indeed, the signal power received at the RIS can be enhanced by increasing N, leading to a higher array gain, especially when recalling that the RIS elements are affecting both, the channel between the BS and the RIS and those between the RIS and the UEs. In contrast, the antennas at the BS only affect the channel between the BS and the RIS. On the other hand, for high values of N, the design of the power allocation and the phase shift coefficients for EE maximization becomes more flexible, thus leading to higher gains.

In Fig. 6.3(b), we study the impact of the position of the UAV w.r.t. the two BSs on the achievable EE. Denote the Euclidean distance between BS_1 and the UAV (A-RIS or A-Relay) by d. Plots show that the closer the A-RIS is to the cell-edge UEs, the higher the EE, due to the strong
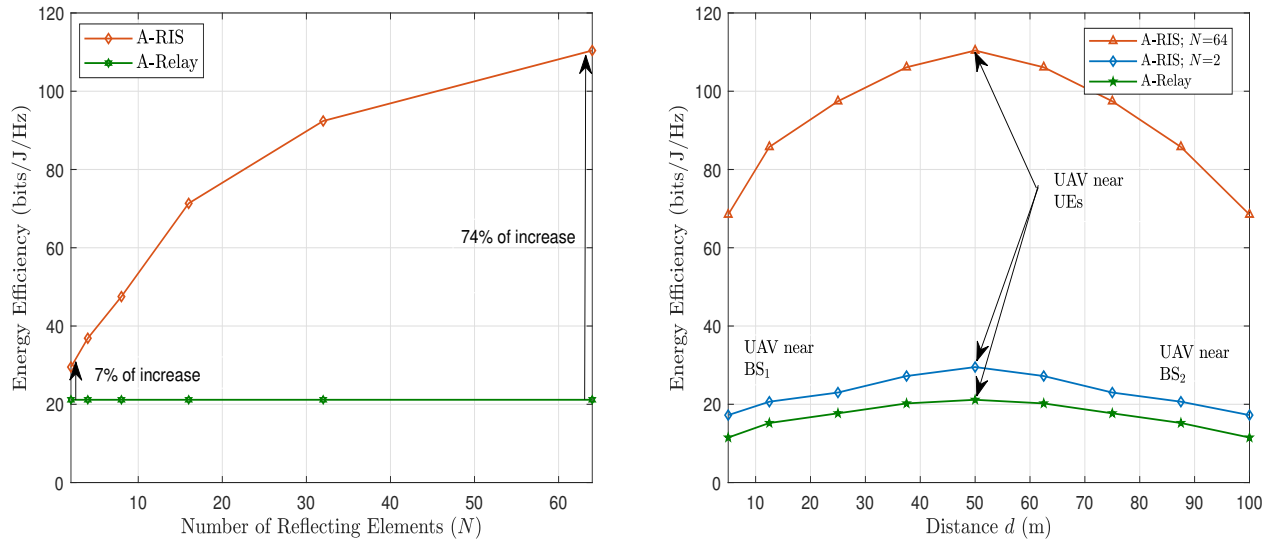
Figure 6.3: **(a) Energy efficiency versus the number of reflecting elements at the aerial RIS. (b) Energy efficiency versus the distance between the BS$_1$ and the UAV (aerial RIS or aerial relay). With $P_{\max}$=10 dBm for both sub-plots.**

LoS, which result in a reduction of the UEs' transmit powers and, hence, energy savings. On the other hand, the EE decreases when the UAV gets closer to either of the BSs. This can be explained by the fact that the distance between the cell-edge UEs and the UAV increases, and the path loss effects become higher. Therefore, the received signal gets attenuated and the EE performance gets deteriorated. Moreover, by choosing the appropriate UAV's location guaranteeing favorable BS-RIS and RIS-UEs links, the phase shifts can be smartly controlled to enable constructive addition at target BS or UEs, and achieve high beamforming gains, thereby making aerial RIS a promising solution to improve the EE performance of multi-cell communication networks, especially for cell-edge UEs.

6.5   Concluding Remarks

In this chapter, we studied the EE maximization for a multi-cell uplink system assisted with aerial RIS. Three different variables, namely, the transmit power at the UEs, the phase shifts at the RIS, and the BS beamforming matrix, need to be jointly optimized. An alternating solution based on the minimum mean square error (MMSE) and the semidefinite relaxation (SDR) techniques was proposed. Numerical results showed that the proposed system design yields significant performance

gains over the conventional counterpart in which the system operates with amplify-and-forward relaying at the UAV. In the state-of-the-art, the design and deployment of wireless communication systems with aerial RIS are in the early stage of investigations; challenges such as the stability, vibrations, fluctuations, mobility and controllability of the UAV(s), deserve further investigations.

Chapter 7

Energy-Efficient Aerial RIS Aided Joint Broadcast-Unicast Communications

7.1 Introduction

Motivated by the favorable characteristics of RIS, extensive research efforts have been devoted to exploit the new degrees-of-freedom that they introduce with the prospect of mitigating a wide range of challenges encountered in wireless networks, such as the reduction of the power consumption [11] and the enhancement of the spectral and energy efficiencies [22, 91]. Such potentials have been demonstrated for various models and set-ups of RIS-assisted systems, but mainly for single type of services. In many use cases and applications, however, different types of services need to be delivered concurrently [102]. The simultaneous support of multiple services via RIS remains an open problem, faced with many research issues that concern not only the modeling but also the design as well as the deployment and operation.

Generally speaking, three kinds of traffic patterns can be distinguished: multicasting, broadcasting, and unicasting. In the context of RIS-assisted communications, the main focus of prior research work was on either unicasting [4, 91], broadcasting [103], or multicasting [104, 105]. For the

---

simultaneous transmission of different traffic patterns, prior works considered conventional transmissions, in which the resources are not necessarily used with high efficiency. To accommodate the joint transmission of different kinds of traffic patterns, several techniques have been proposed, such as spatial multiplexing [106], superposition coding [92], layered-division multiplexing [102], and polarization [107].

Recently, polarization techniques have been leveraged to carry out different traffic patterns in an energy-efficient manner while keeping the communication rates and the transmission reliability at the target levels. Whether in RF, optical fiber, radar, or satellite communications, polarization has been demonstrated to be appealing in enhancing performance, e.g., w.r.t. channel capacity [108]. In the context of RIS, multiple polarization states of the EM waves can be realized by properly configuring the orientation and the structure of the RIS elements [109–111].

To deal with the demand for extremely high data rates and the coexistence of different services, leveraging polarization in RIS-assisted wireless communications was considered in [109, 111]. Specifically, [111] proposed a dual-polarized RIS to realize polarization manipulation of the EM waves. In [109], the authors proposed a dual-polarized RIS to alleviate the imperfect successive interference cancelation of massive MIMO communication with non-orthogonal multiple access. In [110], the performance of a dual-polarized RIS-assisted communication system is conducted while assuming imperfect polarization. From an implementation viewpoint, a dual-polarized RIS is constituted of two single-polarized RISs with orthogonal polarization, such that each element can reflect the incident signals in a given polarization state [112]. Such implementation still maintains the low-cost and low-power consumption advantages of the RIS technology, and is a promising solution for the high energy efficiency requirements of future wireless systems.

Motivated by the advantages of the aerial RIS technology and polarization, and aiming at multi-service communications with high energy efficiency, we propose an energy-efficient framework for joint broadcast-unicast communication via dual-polarized aerial RIS. In so doing, the key contributions of this research work consist in:

- Proposing a dual-polarized aerial-RIS assisted system model for the simultaneous transmission of unicast and broadcast signals to different groups of user equipments (UE). An energy-efficiency maximization problem is formulated, where the goal is to jointly design the unicast and broadcast beamformers at the BS, and the phase shifting at the dual-polarized RIS-UAV,

while considering operation constraints on the BS's maximum transmit power and the rate requirements in the unicast and broadcast services.

- Solving the highly non-convex energy-efficiency maximization problem. First, the fractional objective function of the optimization problem is transformed into an equivalent subtractive form, and then a two-stage iterative solution is developed. The RIS passive beamforming matrix is designed in the first stage. In the second stage, the active beamforming at the BS is designed based on a dual-structured beamforming approach. Specifically, the prebeamforming matrix, which is designed to eliminate the interference between the group of users, is obtained based on the interior point method. Then, a low-complexity zero forcing (ZF) technique based on the singular value decomposition (SVD) is developed to design the beamforming matrix pertaining to unicasting, and an iterative algorithm based on successive convex approximation Taylor series expansion is used to obtain the beamforming vector pertaining to the broadcasting.

- Assessing the energy efficiency of the proposed communication system with the proposed optimization algorithm in comparison to an equivalent system but operating with layered division multiplexing (LDM) [113], and the system counterpart in which polarization is ideal.

The organization of the chapter is as follows. The system model is detailed in Section 7.2. Then, in Section 7.3, the problem formulation and the proposed solution are presented. Through extensive simulations in Section 7.4, the proposed aerial-RIS-based design is compared to ideal polarization-based RIS-UAV assisted communication and the LDM-based one in terms of the EE. Finally, Section 7.5 summarizes the chapter.

7.2   The Dual-Polarized RIS-UAV Aided Communication System

The RIS-assisted multi-user aerial-terrestrial communication system is depicted in Fig. 7.1. In this system, a dual-polarized RIS is attached to a hovering UAV to assist the downlink data transmissions from the BS, equipped with $M_{\rm t}$ pairs of dual-polarized antennas organized in a uniform linear array (ULA), to K UEs, each having a single polarized antenna with either vertical or horizontal polarization. Two groups of UEs are considered, each associated with one service type: unicast or broadcast. Let $\mathcal{K}_{\rm u} = \{1, \cdots, K_{\rm u}\}$ be the set of UEs receiving the unicasting service via vertical po-

larization, and $\mathcal{K}_\mathrm{b} = \{1, \cdots, K_\mathrm{b}\}$ be the set of UEs receiving the broadcasting service via horizontal polarization. Assuming that each UE can only receive one type of traffic, it can only belong to one of the said sets. That is, $\mathcal{K}_\mathrm{b} \cap \mathcal{K}_\mathrm{u} = \emptyset$.
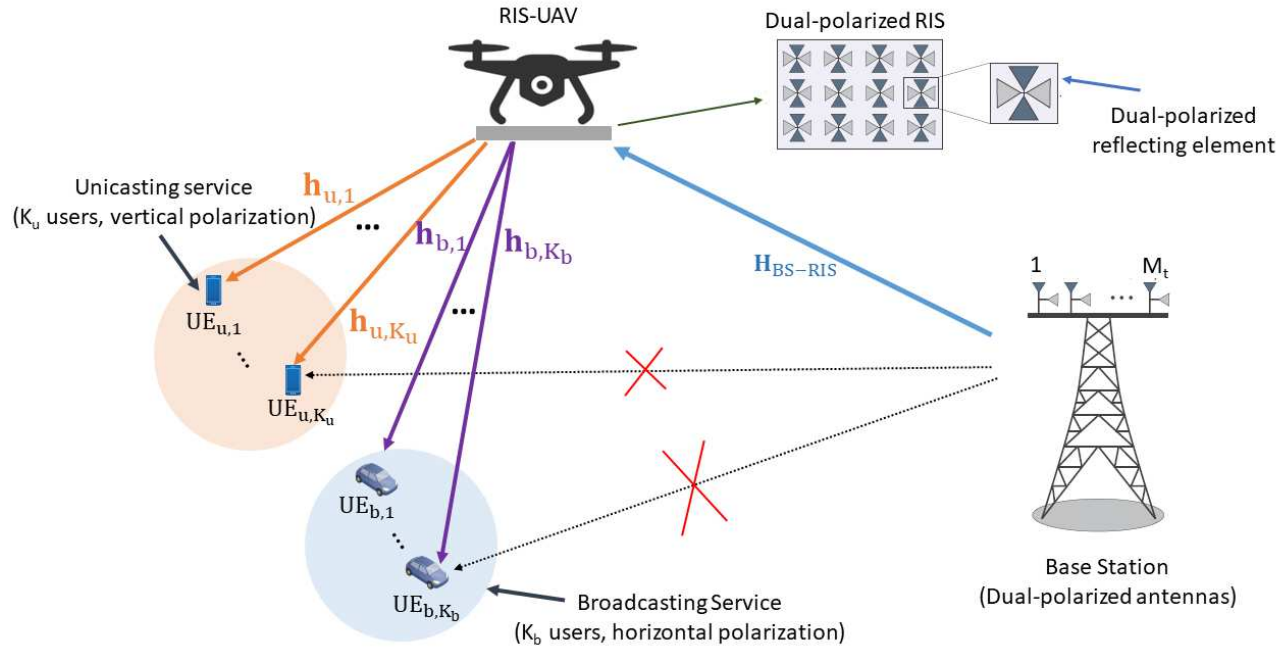
Figure 7.1: The dual-polarized aerial RIS aided joint broadcast-unicast communication system.

The RIS-UAV is equipped with N dual-polarized unit cells, organized in a uniform planar array (UPA), each of which can modulate the amplitude and phase of the reflected EM waves in either the vertical polarization or the horizontal polarization. Each unit cell of the RIS consists of the substrate, two pairs of mutually perpendicular rectangular metal patches to manipulate the EM waves, two varactor diodes connected across the metal patches to manipulate the resonant frequency, and microstrip lines. Two separate bias voltages are applied to the two varactor diodes through the two separate pairs of metal patches for a particular unit cell. With two separate varactor diodes, one controls the phase of the reflected wave in the vertical polarization, and the other controls the phase of the reflected wave in the horizontal polarization [112]. The polarization states are denoted by v and h, where v stands for vertical and h for horizontal.

The phase shifting matrix of the dual-polarized RIS-UAV is defined as

$$\mathbf{\Phi} = \begin{bmatrix} \mathbf{\Phi}^{\mathrm{v}} & \mathbf{\Phi}^{\mathrm{hv}} \\ \mathbf{\Phi}^{\mathrm{vh}} & \mathbf{\Phi}^{\mathrm{h}} \end{bmatrix}, \tag{7.1}$$

where $\mathbf{\Phi}^{\mathrm{v}} = \mathrm{diag}\left(\phi_1^{\mathrm{v}} \cdots, \phi_N^{\mathrm{v}}\right)$ is the vertical-polarization phase-shift component and $\mathbf{\Phi}^{\mathrm{h}} = \mathrm{diag}\left(\phi_1^{\mathrm{h}} \cdots, \phi_N^{\mathrm{h}}\right)$ is the horizontal-polarization phase-shift component, and where $\phi_n^p = a_n^p \exp(j\theta_n^p)$ in which a_n^p and $\theta_n^p \in [0, 2\pi)$ denote the amplitude reflection coefficient and the phase shift of the nth unit cell applied to the incident waves in polarization state $p \in \{\mathrm{v}, \mathrm{h}\}$. $\mathbf{\Phi}^{\mathrm{vh}} = \mathrm{diag}\left(\phi_1^{\mathrm{vh}} \cdots, \phi_N^{\mathrm{vh}}\right)$ and $\mathbf{\Phi}^{\mathrm{hv}} = \mathrm{diag}\left(\phi_1^{\mathrm{hv}} \cdots, \phi_N^{\mathrm{hv}}\right)$ indicate the phase shifts of the cross-polarized components, where $\phi_n^q = a_n^q \exp(j\theta_n^q)$, in which a_n^q and $\theta_n^q \in [0, 2\pi)$ are the amplitude reflection coefficient and the phase shift applied by the nth unit cell to the incident waves in the cross-polarized state $q \in \{\mathrm{vh}, \mathrm{hv}\}$.

Let $\mathbf{H}_{\mathrm{BS-RIS}} \in \mathbb{C}^{2M_{\mathrm{t}} \times 2N}$, $\mathbf{H}_{\mathrm{u}} \in \mathbb{C}^{2N \times K_{\mathrm{u}}}$ and $\mathbf{H}_{\mathrm{b}} \in \mathbb{C}^{2N \times K_{\mathrm{b}}}$ respectively denote the channel from the BS to the dual-polarized RIS-UAV, the channel from the RIS-UAV to the set of UEs $\mathcal{K}_{\mathrm{u}}$, and the channel from the RIS-UAV to the set $\mathcal{K}_{\mathrm{b}}$ of UEs. All channels are assumed to experience block fading and to be independent from each other. The channel gains include the effects of the path loss and the fast fading. The Rician fading model is considered for the BS-RIS and RIS-UE links [91]. The channel gain matrix of the BS-RIS link is given by

$$\mathbf{H}_{\mathrm{BS-RIS}} = \mathbf{D}^{\frac{1}{2}} \left(\sqrt{\frac{\mu}{1+\mu}} \overline{\mathbf{H}} + \sqrt{\frac{1}{1+\mu}} \hat{\mathbf{H}} \right), \tag{7.2}$$

where μ is the Rice factor, $\overline{\mathbf{H}} = \begin{bmatrix} \overline{\mathbf{H}}^{\mathrm{v}} & \overline{\mathbf{H}}^{\mathrm{hv}} \\ \overline{\mathbf{H}}^{\mathrm{vh}} & \overline{\mathbf{H}}^{\mathrm{h}} \end{bmatrix}$ is the LoS component matrix, with $\overline{\mathbf{H}}^p$ denoting the LoS component matrix between the BS antennas and the RIS in polarization $p \in \{\mathrm{v}, \mathrm{h}\}$ and $\overline{\mathbf{H}}^q$ denoting the LoS component matrix of the cross-polarized channel between the BS the RIS-UAV in polarization $q \in \{\mathrm{vh}, \mathrm{hv}\}$. Further, $\hat{\mathbf{H}} = \begin{bmatrix} \hat{\mathbf{H}}^{\mathrm{v}} & \hat{\mathbf{H}}^{\mathrm{hv}} \\ \hat{\mathbf{H}}^{\mathrm{vh}} & \hat{\mathbf{H}}^{\mathrm{h}} \end{bmatrix}$ is the non line-of-sight (NLoS) component matrix, where $\hat{\mathbf{H}}^p$ is the NLoS component matrix between the BS and the RIS-UAV in polarization $p \in \{\mathrm{v}, \mathrm{h}\}$, and $\hat{\mathbf{H}}^q$ is the NLoS component matrix of the cross-polarized channel between the BS and the RIS-UAV in polarization $q \in \{\mathrm{vh}, \mathrm{hv}\}$, the elements of which are i.i.d. complex Gaussian random variables having zero mean and unit variance. Matrix $\mathbf{D}$ in (7.2) is diagonal, where each

element $[\mathbf{D}]_{k,k} = d^{-\alpha}$, with d being the Euclidean distance between the BS and the RIS-UAV, and $\alpha \geq 2$ denoting the path-loss exponent. The LoS component is given by $\overline{\mathbf{H}} = \mathbf{a}_{M_t}(\psi)\,\mathbf{a}_N^H(\vartheta^a, \vartheta^e) \in \mathbb{C}^{2M_t \times 2N}$. Here, $\mathbf{a}_{M_t}(\psi) = \left[1, e^{j2\pi\frac{\Delta_1}{\lambda}\sin\psi}, \ldots, e^{j2\pi\frac{\Delta_1}{\lambda}(2M_t-1)\sin\psi}\right]^T \in \mathbb{C}^{2M_t \times 1}$ is the normalized steering vector of the $2M_t$-element ULA and ψ is the angle of departure (AoD) of the BS's signal. $\mathbf{a}_N(\vartheta^a, \vartheta^e) = \left[1, e^{j\xi_1(\sin\vartheta^a\sin\vartheta^e + \cos\vartheta^e)}, \cdots, e^{j\xi_{2N-1}(\sin\vartheta^a\sin\vartheta^e + \cos\vartheta^e)}\right]^T \in \mathbb{C}^{2N \times 1}$ is the normalized steering vector of the $2N$-element UPA of the RIS-UAV, in which $\xi_n = 2n\pi\frac{\Delta_2}{\lambda}, \forall n = 1, \cdots, 2N - 1$, ϑ^a is the angle of arrival (AoA) and ϑ^e is the AoD, where λ is the wavelength, and where Δ_1 is the antenna spacing and Δ_2 is the RIS element spacing taken as $\Delta_1 = \frac{\lambda}{2}$ and $\Delta_2 = \frac{\lambda}{8}$.

For the unicasting, the channel matrix $\mathbf{H}_u = \begin{bmatrix} \mathbf{H}_u^v & \mathbf{H}_u^{hv} \\ \mathbf{H}_u^{vh} & \mathbf{H}_u^h \end{bmatrix} = [\mathbf{h}_{u,1}, \cdots, \mathbf{h}_{u,K_u}]^T$, where $\mathbf{h}_{u,j} \in \mathbb{C}^{2N \times 1}$, $j \in \mathcal{K}_u$, is the random vector of the link between the RIS and UE$_{u,j}$, given by

$$\mathbf{h}_{u,j} = \sqrt{d_{u,j}^{-\beta}} \left(\sqrt{\frac{\mu_u}{1 + \mu_u}}\overline{\mathbf{h}}_{u,j} + \sqrt{\frac{1}{1 + \mu_u}}\hat{\mathbf{h}}_{u,j} \right), \tag{7.3}$$

where μ_u is the Rice factor, $\overline{\mathbf{h}}_{u,j}$ is the LoS component vector, given by $\overline{\mathbf{h}}_{u,j} = \mathbf{a}_N(\vartheta^a, \vartheta^e) \in \mathbb{C}^{2N \times 1}$ where $\mathbf{a}_N$ is as defined after (7.2), $\hat{\mathbf{h}}_{u,j}$ is the NLoS component vector whose elements are i.i.d. complex Gaussian random variables with zero mean and unit variance, $d_{u,j}$ is the Euclidean distance between the RIS and the jth UE in set $\mathcal{K}_u$, and $\beta \geq 2$ is the path-loss exponent.

With regard to the broadcasting, the channel matrix $\mathbf{H}_b = \begin{bmatrix} \mathbf{H}_b^v & \mathbf{H}_b^{hv} \\ \mathbf{H}_b^{vh} & \mathbf{H}_b^h \end{bmatrix} = [\mathbf{h}_{b,1}, \cdots, \mathbf{h}_{b,K_b}]^T$, where $\mathbf{h}_{b,k} \in \mathbb{C}^{2N \times 1}$, $k \in \mathcal{K}_b$, is the complex channel vector of the link between the RIS-UAV and UE$_{b,k}$, which is given by

$$\mathbf{h}_{b,k} = \sqrt{d_{b,k}^{-\beta}} \left(\sqrt{\frac{\mu_b}{1 + \mu_b}}\overline{\mathbf{h}}_{b,k} + \sqrt{\frac{1}{1 + \mu_b}}\hat{\mathbf{h}}_{b,k} \right), \tag{7.4}$$

where μ_b is the Rice factor, $\overline{\mathbf{h}}_{b,k}$ is the LoS component vector, given by $\overline{\mathbf{h}}_{b,k} = \mathbf{a}_N(\vartheta^a, \vartheta^e) \in \mathbb{C}^{2N \times 1}$ where $\mathbf{a}_N$ is as defined after Eq. (7.2), $\hat{\mathbf{h}}_{b,k}$ is the NLoS component vector whose elements are i.i.d. complex Gaussian random variables with zero mean and unit variance, and $d_{b,k}$ is the Euclidean distance between the RIS and the kth UE in set $\mathcal{K}_b$.

Let us denote by $\mathbf{H}_g$, with $g \in \{u, b\}$, the channel between the RIS-UAV and the gth group of UEs. The composite dual-polarized channel matrix is denoted as,[1]

$$\tilde{\mathbf{H}}_g = \mathbf{H}_g^{\text{H}} \mathbf{\Phi} \mathbf{H}_{\text{BS-RIS}}^{\text{H}} = \begin{bmatrix} \tilde{\mathbf{h}}_g^{\text{v}} & \tilde{\mathbf{h}}_g^{\text{hv}} \\ \tilde{\mathbf{h}}_g^{\text{vh}} & \tilde{\mathbf{h}}_g^{\text{h}} \end{bmatrix}, \tag{7.5}$$

where $\tilde{\mathbf{h}}_g^p$ is the complex channel vector in polarization $p \in \{h, v\}$, $\tilde{\mathbf{h}}_g^q = \sqrt{\chi}\tilde{\mathbf{h}}_g^q$, with $q \in \{vh, hv\}$, is the cross-polarized channel vector, and $0 < \chi \leq 1$ is the inverse of the cross-polar discrimination (iXPD) parameter. The XPD parameter describes the channel's ability to discriminate two polarizations, with $0 < \text{XPD} < \infty$. For notation simplicity, the iXPD is absorbed in the corresponding channel vector. [2] The superposition technique is applied to the data intended for the UEs within a group. Thus, the signal transmitted from the dual-polarized antennas of the BS can be expressed as

$$\mathbf{x} = \tilde{\mathbf{P}}\tilde{\mathbf{x}} = \begin{bmatrix} \mathbf{P}^{\text{v}} & \mathbf{0} \\ \mathbf{0} & \mathbf{P}^{\text{h}} \end{bmatrix} \begin{bmatrix} \mathbf{V} \\ \mathbf{w} \end{bmatrix} \begin{bmatrix} \mathbf{s}^{\text{v}} \\ \mathbf{s}^{\text{h}} \end{bmatrix}, \tag{7.6}$$

where $\tilde{\mathbf{P}} \in \mathbb{C}^{2M_t \times 2N}$ is designed based on the dual-structured beamforming approach [116, 117]. Specifically, $\mathbf{P} = \begin{bmatrix} \mathbf{P}^{\text{v}} & \mathbf{0} \\ \mathbf{0} & \mathbf{P}^{\text{h}} \end{bmatrix}$ is the prebeamforming matrix designed to eliminate the interferences between the groups of UEs, $\mathbf{V} = [\mathbf{v}_1, \cdots, \mathbf{v}_{K_u}]^{\text{T}} \in \mathbb{C}^{M_t \times K_u}$ is the beamforming matrix applied at the BS for transmission of the encoded unicasting symbols $\mathbf{s}^{\text{v}} = [s_1, \cdots, s_{K_u}]^{\text{T}}$ intended to the UEs in set $\mathcal{K}_u$, and $\mathbf{w} \in \mathbb{C}^{M_t \times 1}$ is the beamforming vector for the transmission of the common data symbol $\mathbf{s}^{\text{h}} = s$ intended for the UEs in set $\mathcal{K}_b$. The received signal at the gth group of UEs, $g \in \{u, b\}$, can be expressed in vector form as

$$\begin{aligned} \mathbf{y}_g = \begin{bmatrix} \mathbf{y}_g^{\text{v}} \\ \mathbf{y}_g^{\text{h}} \end{bmatrix} &= \tilde{\mathbf{H}}_g \mathbf{x} + \mathbf{n}_g \\ &= \begin{bmatrix} \tilde{\mathbf{h}}_g^{\text{v}} & \tilde{\mathbf{h}}_g^{\text{hv}} \\ \tilde{\mathbf{h}}_g^{\text{vh}} & \tilde{\mathbf{h}}_g^{\text{h}} \end{bmatrix} \begin{bmatrix} \mathbf{P}^{\text{v}} & \mathbf{0} \\ \mathbf{0} & \mathbf{P}^{\text{h}} \end{bmatrix} \begin{bmatrix} \mathbf{V} \\ \mathbf{w} \end{bmatrix} \begin{bmatrix} \mathbf{s}^{\text{v}} \\ \mathbf{s}^{\text{h}} \end{bmatrix}, \end{aligned} \tag{7.7}$$

---

[1] We assume that the channel state information (CSI) is available at the BS. Channel estimation methods, see e.g. [2, 33, 34], can be applied to acquire the CSI of the UEs independently.

[2] The Rice factor and the iXPD value are intertwined [114, 115]. Good channel orthogonality can be achieved in LoS scenarios, i.e., when the iXPD is close to 0. In non-LoS scenarios, where strong Rician fading is mainly attributed to dominant scattering objects that cause strong polarization coupling, the iXPD is close to 1, which reduces the system performance.

where $\mathbf{y}_g^{\mathrm{v}}$ and $\mathbf{y}_g^{\mathrm{h}}$ are the received signals with vertical and horizontal polarizations, respectively, and $\mathbf{n}_g = \begin{bmatrix} \mathbf{n}_g^{\mathrm{v}} \\ \mathbf{n}_g^{\mathrm{h}} \end{bmatrix}$ is the additive white Gaussian noise (AWGN) vector, the elements of which obey a Gaussian distribution with zero mean and variance σ^2. Without loss of generality, we assume equal noise powers at all UEs, i.e., $\sigma^2 = N_0 B, \forall k \in \{1, \cdots, K\}$, with N_0 denoting the noise power over the total transmission bandwidth B.

Based on the above, the received signal at the gth group of UEs, $g \in \{\mathrm{u}, \mathrm{b}\}$, is re-written as

$$\mathbf{y}_g = \begin{bmatrix} \tilde{\mathbf{h}}_g^{\mathrm{v}} \mathbf{P}^{\mathrm{v}} \mathbf{V} \mathbf{s}^{\mathrm{v}} + \tilde{\mathbf{h}}_g^{\mathrm{hv}} \mathbf{P}^{\mathrm{h}} \mathbf{w} \mathbf{s}^{\mathrm{h}} \\ \tilde{\mathbf{h}}_g^{\mathrm{vh}} \mathbf{P}^{\mathrm{v}} \mathbf{V} \mathbf{s}^{\mathrm{v}} + \tilde{\mathbf{h}}_g^{\mathrm{h}} \mathbf{P}^{\mathrm{h}} \mathbf{w} \mathbf{s}^{\mathrm{h}} \end{bmatrix} + \begin{bmatrix} \mathbf{n}_g^{\mathrm{v}} \\ \mathbf{n}_g^{\mathrm{h}} \end{bmatrix}, \tag{7.8}$$

where $\tilde{\mathbf{h}}_g^{\mathrm{v}}$, $\tilde{\mathbf{h}}_g^{\mathrm{h}}$, $\tilde{\mathbf{h}}_g^{\mathrm{vh}}$ and $\tilde{\mathbf{h}}_g^{\mathrm{hv}}$ are expressed as

$$\tilde{\mathbf{h}}_g^{\mathrm{v}} = (\mathbf{H}_g^{\mathrm{v}})^{\mathrm{H}} \boldsymbol{\Phi}^{\mathrm{v}} (\mathbf{H}_{\mathrm{BS-RIS}}^{\mathrm{hv}})^{\mathrm{H}} + (\mathbf{H}_g^{\mathrm{hv}})^{\mathrm{H}} \boldsymbol{\Phi}^{\mathrm{vh}} (\mathbf{H}_{\mathrm{BS-RIS}}^{\mathrm{v}})^{\mathrm{H}} + (\mathbf{H}_g^{\mathrm{v}})^{\mathrm{H}} \boldsymbol{\Phi}^{\mathrm{hv}} (\mathbf{H}_{\mathrm{BS-RIS}}^{\mathrm{vh}})^{\mathrm{H}} + (\mathbf{H}_g^{\mathrm{hv}})^{\mathrm{H}} \boldsymbol{\Phi}^{\mathrm{h}} (\mathbf{H}_{\mathrm{BS-RIS}}^{\mathrm{vh}})^{\mathrm{H}},$$

$$\tilde{\mathbf{h}}_g^{\mathrm{vh}} = (\mathbf{H}_g^{\mathrm{vh}})^{\mathrm{H}} \boldsymbol{\Phi}^{\mathrm{v}} (\mathbf{H}_{\mathrm{BS-RIS}}^{\mathrm{hv}})^{\mathrm{H}} + (\mathbf{H}_g^{\mathrm{h}})^{\mathrm{H}} \boldsymbol{\Phi}^{\mathrm{vh}} (\mathbf{H}_{\mathrm{BS-RIS}}^{\mathrm{v}})^{\mathrm{H}} + (\mathbf{H}_g^{\mathrm{vh}})^{\mathrm{H}} \boldsymbol{\Phi}^{\mathrm{hv}} (\mathbf{H}_{\mathrm{BS-RIS}}^{\mathrm{vh}})^{\mathrm{H}} + (\mathbf{H}_g^{\mathrm{h}})^{\mathrm{H}} \boldsymbol{\Phi}^{\mathrm{h}} (\mathbf{H}_{\mathrm{BS-RIS}}^{\mathrm{vh}})^{\mathrm{H}},$$

$$\tilde{\mathbf{h}}_g^{\mathrm{hv}} = (\mathbf{H}_g^{\mathrm{v}})^{\mathrm{H}} \boldsymbol{\Phi}^{\mathrm{v}} (\mathbf{H}_{\mathrm{BS-RIS}}^{\mathrm{hv}})^{\mathrm{H}} + (\mathbf{H}_g^{\mathrm{hv}})^{\mathrm{H}} \boldsymbol{\Phi}^{\mathrm{vh}} (\mathbf{H}_{\mathrm{BS-RIS}}^{\mathrm{hv}})^{\mathrm{H}} + (\mathbf{H}_g^{\mathrm{v}})^{\mathrm{H}} \boldsymbol{\Phi}^{\mathrm{hv}} (\mathbf{H}_{\mathrm{BS-RIS}}^{\mathrm{h}})^{\mathrm{H}} + (\mathbf{H}_g^{\mathrm{hv}})^{\mathrm{H}} \boldsymbol{\Phi}^{\mathrm{h}} (\mathbf{H}_{\mathrm{BS-RIS}}^{\mathrm{h}})^{\mathrm{H}},$$

$$\tilde{\mathbf{h}}_g^{\mathrm{h}} = (\mathbf{H}_g^{\mathrm{vh}})^{\mathrm{H}} \boldsymbol{\Phi}^{\mathrm{v}} (\mathbf{H}_{\mathrm{BS-RIS}}^{\mathrm{hv}})^{\mathrm{H}} + (\mathbf{H}_g^{\mathrm{h}})^{\mathrm{H}} \boldsymbol{\Phi}^{\mathrm{vh}} (\mathbf{H}_{\mathrm{BS-RIS}}^{\mathrm{h}})^{\mathrm{H}} + (\mathbf{H}_g^{\mathrm{vh}})^{\mathrm{H}} \boldsymbol{\Phi}^{\mathrm{hv}} (\mathbf{H}_{\mathrm{BS-RIS}}^{\mathrm{hv}})^{\mathrm{H}} + (\mathbf{H}_g^{\mathrm{h}})^{\mathrm{H}} \boldsymbol{\Phi}^{\mathrm{h}} (\mathbf{H}_{\mathrm{BS-RIS}}^{\mathrm{h}})^{\mathrm{H}}. \tag{7.9}$$

Let us recall that the UEs in the unicasting group receive their signals in the vertical polarization, based on (7.7). Hence, the received signal at $\mathrm{UE}_{\mathrm{u},j}$ in set $\mathcal{K}_{\mathrm{u}}$ can be expressed as

$$\begin{aligned} y_{\mathrm{u},j}^{\mathrm{v}} = &\Big((\mathbf{h}_{\mathrm{u},j}^{\mathrm{v}})^{\mathrm{H}} \boldsymbol{\Phi}^{\mathrm{v}} (\mathbf{H}_{\mathrm{BS-RIS}}^{\mathrm{hv}})^{\mathrm{H}} + (\mathbf{h}_{\mathrm{u},j}^{\mathrm{hv}})^{\mathrm{H}} \boldsymbol{\Phi}^{\mathrm{vh}} (\mathbf{H}_{\mathrm{BS-RIS}}^{\mathrm{v}})^{\mathrm{H}} + (\mathbf{h}_{\mathrm{u},j}^{\mathrm{v}})^{\mathrm{H}} \boldsymbol{\Phi}^{\mathrm{hv}} (\mathbf{H}_{\mathrm{BS-RIS}}^{\mathrm{vh}})^{\mathrm{H}} \\ &+ (\mathbf{h}_{\mathrm{u},j}^{\mathrm{hv}})^{\mathrm{H}} \boldsymbol{\Phi}^{\mathrm{h}} (\mathbf{H}_{\mathrm{BS-RIS}}^{\mathrm{vh}})^{\mathrm{H}} \Big) \mathbf{p}_j^{\mathrm{v}} \mathbf{v}_j s_j + \sum_{i=1, i \neq j}^{K_{\mathrm{u}}} \Big((\mathbf{h}_{\mathrm{u},j}^{\mathrm{v}})^{\mathrm{H}} \boldsymbol{\Phi}^{\mathrm{v}} (\mathbf{H}_{\mathrm{BS-RIS}}^{\mathrm{hv}})^{\mathrm{H}} + (\mathbf{h}_{\mathrm{u},j}^{\mathrm{hv}})^{\mathrm{H}} \boldsymbol{\Phi}^{\mathrm{vh}} (\mathbf{H}_{\mathrm{BS-RIS}}^{\mathrm{v}})^{\mathrm{H}} \\ &+ (\mathbf{h}_{\mathrm{u},j}^{\mathrm{v}})^{\mathrm{H}} \boldsymbol{\Phi}^{\mathrm{hv}} (\mathbf{H}_{\mathrm{BS-RIS}}^{\mathrm{vh}})^{\mathrm{H}} + (\mathbf{h}_{\mathrm{u},j}^{\mathrm{hv}})^{\mathrm{H}} \boldsymbol{\Phi}^{\mathrm{h}} (\mathbf{H}_{\mathrm{BS-RIS}}^{\mathrm{vh}})^{\mathrm{H}} \Big) \mathbf{p}_i^{\mathrm{v}} \mathbf{v}_i s_i \\ &+ \Big((\mathbf{h}_{\mathrm{u},j}^{\mathrm{v}})^{\mathrm{H}} \boldsymbol{\Phi}^{\mathrm{v}} (\mathbf{H}_{\mathrm{BS-RIS}}^{\mathrm{hv}})^{\mathrm{H}} + (\mathbf{h}_{\mathrm{u},j}^{\mathrm{hv}})^{\mathrm{H}} \boldsymbol{\Phi}^{\mathrm{vh}} (\mathbf{H}_{\mathrm{BS-RIS}}^{\mathrm{hv}})^{\mathrm{H}} + (\mathbf{h}_{\mathrm{u},j}^{\mathrm{v}})^{\mathrm{H}} \boldsymbol{\Phi}^{\mathrm{hv}} (\mathbf{H}_{\mathrm{BS-RIS}}^{\mathrm{h}})^{\mathrm{H}} \\ &+ (\mathbf{h}_{\mathrm{u},j}^{\mathrm{hv}})^{\mathrm{H}} \boldsymbol{\Phi}^{\mathrm{h}} (\mathbf{H}_{\mathrm{BS-RIS}}^{\mathrm{h}})^{\mathrm{H}} \Big) \mathbf{P}^{\mathrm{h}} \mathbf{w} s + n_{\mathrm{u},j}^{\mathrm{v}}. \end{aligned} \tag{7.10}$$

The UEs in the broadcasting service receive their signals at the horizontal polarization. Thus, the received signal at $\text{UE}_{\text{b},k}$ in set $\mathcal{K}_\text{b}$ can be expressed as

$$
\begin{aligned}
y_{\text{b},k}^{\text{h}} = {}& \Big((\mathbf{h}_{\text{b},k}^{\text{vh}})^{\text{H}} \boldsymbol{\Phi}^{\text{v}} (\mathbf{H}_{\text{BS}-\text{RIS}}^{\text{v}})^{\text{H}} + (\mathbf{h}_{\text{b},k}^{\text{h}})^{\text{H}} \boldsymbol{\Phi}^{\text{vh}} (\mathbf{H}_{\text{BS}-\text{RIS}}^{\text{v}})^{\text{H}} + (\mathbf{h}_{\text{b},k}^{\text{vh}})^{\text{H}} \boldsymbol{\Phi}^{\text{hv}} (\mathbf{H}_{\text{BS}-\text{RIS}}^{\text{vh}})^{\text{H}} \\
& + (\mathbf{h}_{\text{b},k}^{\text{h}})^{\text{H}} \boldsymbol{\Phi}^{\text{h}} (\mathbf{H}_{\text{BS}-\text{RIS}}^{\text{vh}})^{\text{H}} \Big) \mathbf{P}^{\text{v}} \sum_{j=1}^{K_\text{u}} \mathbf{v}_j s_j + \Big((\mathbf{h}_{\text{b},k}^{\text{vh}})^{\text{H}} \boldsymbol{\Phi}^{\text{v}} (\mathbf{H}_{\text{BS}-\text{RIS}}^{\text{hv}})^{\text{H}} + (\mathbf{h}_{\text{b},k}^{\text{h}})^{\text{H}} \boldsymbol{\Phi}^{\text{vh}} (\mathbf{H}_{\text{BS}-\text{RIS}}^{\text{h}})^{\text{H}} \\
& + (\mathbf{h}_{\text{b},k}^{\text{vh}})^{\text{H}} \boldsymbol{\Phi}^{\text{hv}} (\mathbf{H}_{\text{BS}-\text{RIS}}^{\text{hv}})^{\text{H}} + (\mathbf{h}_{\text{b},k}^{\text{h}})^{\text{H}} \boldsymbol{\Phi}^{\text{h}} (\mathbf{H}_{\text{BS}-\text{RIS}}^{\text{h}})^{\text{H}} \Big) \mathbf{p}_k^{\text{h}} \mathbf{w} s \\
& + \sum_{i=1,i\neq k}^{K_\text{b}} \Big((\mathbf{h}_{\text{b},k}^{\text{vh}})^{\text{H}} \boldsymbol{\Phi}^{\text{v}} (\mathbf{H}_{\text{BS}-\text{RIS}}^{\text{hv}})^{\text{H}} + (\mathbf{h}_{\text{b},k}^{\text{h}})^{\text{H}} \boldsymbol{\Phi}^{\text{vh}} (\mathbf{H}_{\text{BS}-\text{RIS}}^{\text{h}})^{\text{H}} + (\mathbf{h}_{\text{b},k}^{\text{vh}})^{\text{H}} \boldsymbol{\Phi}^{\text{hv}} (\mathbf{H}_{\text{BS}-\text{RIS}}^{\text{hv}})^{\text{H}} \\
& + (\mathbf{h}_{\text{b},k}^{\text{h}})^{\text{H}} \boldsymbol{\Phi}^{\text{h}} (\mathbf{H}_{\text{BS}-\text{RIS}}^{\text{h}})^{\text{H}} \Big) \mathbf{p}_i^{\text{h}} \mathbf{w} s + n_{\text{b},k}^{\text{h}}.
\end{aligned}
\tag{7.11}
$$

Each $\text{UE}_{\text{u},j}$ in set $\mathcal{K}_\text{u}$ decodes its target signal while considering the signals of the other users in the same group as interference and the broadcasting signal as polarization interference. The SINR of $\text{UE}_{\text{u},j}$ in the unicasting service is expressed as

$$
\begin{aligned}
\gamma_{\text{u},j} = {}& \frac{1}{\mathcal{I}_\text{u} + \sigma^2} \times \Big| \Big((\mathbf{h}_{\text{u},j}^{\text{v}})^{\text{H}} \boldsymbol{\Phi}^{\text{v}} (\mathbf{H}_{\text{BS}-\text{RIS}}^{\text{hv}})^{\text{H}} + (\mathbf{h}_{\text{u},j}^{\text{hv}})^{\text{H}} \boldsymbol{\Phi}^{\text{vh}} (\mathbf{H}_{\text{BS}-\text{RIS}}^{\text{v}})^{\text{H}} \\
& + (\mathbf{h}_{\text{u},j}^{\text{v}})^{\text{H}} \boldsymbol{\Phi}^{\text{hv}} (\mathbf{H}_{\text{BS}-\text{RIS}}^{\text{vh}})^{\text{H}} + (\mathbf{h}_{\text{u},j}^{\text{hv}})^{\text{H}} \boldsymbol{\Phi}^{\text{h}} (\mathbf{H}_{\text{BS}-\text{RIS}}^{\text{vh}})^{\text{H}} \Big) \mathbf{p}_j^{\text{v}} \mathbf{v}_j \Big|^2,
\end{aligned}
\tag{7.12}
$$

where $\mathcal{I}_\text{u}$ represents the interference at $\text{UE}_{\text{u},j}$, given by

$$
\begin{aligned}
\mathcal{I}_\text{u} = {}& \sum_{i\in\mathcal{K}_\text{u}, i\neq j} \Big| \Big((\mathbf{h}_{\text{u},j}^{\text{v}})^{\text{H}} \boldsymbol{\Phi}^{\text{v}} (\mathbf{H}_{\text{BS}-\text{RIS}}^{\text{hv}})^{\text{H}} + (\mathbf{h}_{\text{u},j}^{\text{hv}})^{\text{H}} \boldsymbol{\Phi}^{\text{vh}} (\mathbf{H}_{\text{BS}-\text{RIS}}^{\text{v}})^{\text{H}} \\
& + (\mathbf{h}_{\text{u},j}^{\text{v}})^{\text{H}} \boldsymbol{\Phi}^{\text{hv}} (\mathbf{H}_{\text{BS}-\text{RIS}}^{\text{vh}})^{\text{H}} + (\mathbf{h}_{\text{u},j}^{\text{hv}})^{\text{H}} \boldsymbol{\Phi}^{\text{h}} (\mathbf{H}_{\text{BS}-\text{RIS}}^{\text{vh}})^{\text{H}} \Big) \mathbf{p}_i^{\text{v}} \mathbf{v}_i \Big|^2 \\
& + \Big| \Big((\mathbf{h}_{\text{u},j}^{\text{v}})^{\text{H}} \boldsymbol{\Phi}^{\text{v}} (\mathbf{H}_{\text{BS}-\text{RIS}}^{\text{hv}})^{\text{H}} + (\mathbf{h}_{\text{u},j}^{\text{hv}})^{\text{H}} \boldsymbol{\Phi}^{\text{vh}} (\mathbf{H}_{\text{BS}-\text{RIS}}^{\text{hv}})^{\text{H}} \\
& + (\mathbf{h}_{\text{u},j}^{\text{v}})^{\text{H}} \boldsymbol{\Phi}^{\text{hv}} (\mathbf{H}_{\text{BS}-\text{RIS}}^{\text{h}})^{\text{H}} + (\mathbf{h}_{\text{u},j}^{\text{hv}})^{\text{H}} \boldsymbol{\Phi}^{\text{h}} (\mathbf{H}_{\text{BS}-\text{RIS}}^{\text{h}})^{\text{H}} \Big) \mathbf{P}^{\text{h}} \mathbf{w} \Big|^2.
\end{aligned}
\tag{7.13}
$$

With regard to the broadcasting, each $\text{UE}_{\text{b},k}$ in set $\mathcal{K}_\text{b}$ decodes its desired signal while considering the unicasting signals as polarization interference. Therefore, the SINR for $\text{UE}_{\text{b},k}$ is

$$
\begin{aligned}
\gamma_{\text{b},k} = {}& \frac{1}{\mathcal{I}_\text{b} + \sigma^2} \times \Big| \Big(\mathbf{h}_{\text{b},k}^{\text{vh}})^{\text{H}} \boldsymbol{\Phi}^{\text{v}} (\mathbf{H}_{\text{BS}-\text{RIS}}^{\text{hv}})^{\text{H}} + (\mathbf{h}_{\text{b},k}^{\text{h}})^{\text{H}} \boldsymbol{\Phi}^{\text{vh}} (\mathbf{H}_{\text{BS}-\text{RIS}}^{\text{h}})^{\text{H}} \\
& + (\mathbf{h}_{\text{b},k}^{\text{vh}})^{\text{H}} \boldsymbol{\Phi}^{\text{hv}} (\mathbf{H}_{\text{BS}-\text{RIS}}^{\text{hv}})^{\text{H}} + (\mathbf{h}_{\text{b},k}^{\text{h}})^{\text{H}} \boldsymbol{\Phi}^{\text{h}} (\mathbf{H}_{\text{BS}-\text{RIS}}^{\text{h}})^{\text{H}} \Big) \mathbf{p}_k^{\text{h}} \mathbf{w} \Big|^2,
\end{aligned}
\tag{7.14}
$$

where $\mathcal{I}_b$ is the interference at $UE_{b,k}$, given by

$$
\begin{aligned}
\mathcal{I}_b = \Bigg| \Big((\mathbf{h}_{b,k}^{vh})^H \mathbf{\Phi}^v (\mathbf{H}_{BS-RIS}^v)^H + (\mathbf{h}_{b,k}^h)^H \mathbf{\Phi}^{vh} (\mathbf{H}_{BS-RIS}^v)^H \\
+ (\mathbf{h}_{b,k}^{vh})^H \mathbf{\Phi}^{hv} (\mathbf{H}_{BS-RIS}^{vh})^H + (\mathbf{h}_{b,k}^h)^H \mathbf{\Phi}^h (\mathbf{H}_{BS-RIS}^{vh})^H \Big) \mathbf{P}^v \sum_{j=1}^{K_u} \mathbf{v}_j \Bigg|^2 \\
+ \sum_{i=1,i\neq k}^{K_b} \Bigg| \Big((\mathbf{h}_{b,k}^{vh})^H \mathbf{\Phi}^v (\mathbf{H}_{BS-RIS}^{hv})^H + (\mathbf{h}_{b,k}^h)^H \mathbf{\Phi}^{vh} (\mathbf{H}_{BS-RIS}^{hv})^H \\
+ (\mathbf{h}_{b,k}^{vh})^H \mathbf{\Phi}^{hv} (\mathbf{H}_{BS-RIS}^{hv})^H + (\mathbf{h}_{b,k}^h)^H \mathbf{\Phi}^h (\mathbf{H}_{BS-RIS}^h)^H \Big) \mathbf{p}_i^h \mathbf{w} \Bigg|^2 .
\end{aligned}
\tag{7.15}
$$

7.3 Problem Formulation and Proposed Solution

Our objective is to jointly optimize the reflection coefficient matrix of the dual-polarized RIS and the active beamforming matrix at the BS to maximize the EE under constraints on the users' minimum required rates and the BS's maximum transmit power. For such, we need first to compute the EE of the proposed dual-polarized aerial RIS-assisted joint broadcast-unicast communication system. Therefore, the sum-rates obtained at the two sets of UEs and the power consumption in the system are required. The sum-rates of the unicast and broadcast services, in bps/Hz, are respectively defined as

$$
R_u = \sum_{j \in \mathcal{K}_u} R_{u,j}, \qquad R_b = \sum_{k \in \mathcal{K}_b} R_{b,k},
\tag{7.16}
$$

where $R_{u,j} = B \log_2 (1 + \gamma_{u,j})$ and $R_{b,k} = B \log_2 (1 + \gamma_{b,k})$ respectively represent the rate of a UE in the unicast service group and in the broadcast service group.

The power consumption of the RIS-UAV-assisted communication system is constituted of three major parts: (i) the transmit power, (ii) the static hardware power, and (iii) the RIS-UAV power consumption, and is given in Watts (W) by

$$
P_\Sigma = P + P_{BS} + K P_{UE} + P_{RIS} + P_{UAV},
\tag{7.17}
$$

where P is the BS's transmit power, P_{UE} is the hardware-dissipated power at the UE, with $P_{UE} = P_{0,UE} + P_{RF}$ in which $P_{0,UE}$ is the static hardware power consumption and P_{RF} is the power consumption of an active RF chain [118], P_{BS} is the hardware-dissipated power at the BS, $P_{RIS} = 2NP_n$

is the hardware-dissipated power at the RIS, with P_n denoting the contribution of each reflecting element [119], and P_{UAV} is the power consumption of the UAV for the hovering.

Therefore, the expression of system's energy efficiency (EE), in bit/Joule, can be found by substituting (7.16) and (7.17) in the following

$$\eta_{\text{EE}} = \frac{\text{Total Throughput}}{\text{Total Consumed Energy}} = \frac{R_{\text{u}} + R_{\text{b}}}{P_{\Sigma}}. \tag{7.18}$$

The EE maximization problem is therefore formulated as

$$
\begin{aligned}
(\mathcal{P}1) \quad & \underset{\mathbf{P},\mathbf{V},\mathbf{w},\boldsymbol{\Phi}}{\text{maximize}} \; \eta_{\text{EE}} \\
& \text{subject to:} \\
& \text{(C1)} \quad \boldsymbol{\Phi}^q = \text{diag}\,(\phi_1^q, \cdots, \phi_N^q), \; \forall q \in \{\text{vh}, \text{hv}\} \\
& \text{(C2)} \quad \phi_n^q = a_n^q \exp(j\theta_n^q), \quad \theta_n^q \in [0, 2\pi), \; \forall n \in \{1, \cdots, N\} \; \& \; \forall q \in \{\text{vh}, \text{hv}\}, \\
& \text{(C3)} \quad |a_n^q|^2 \leq 1, \; \forall n \in \{1, \cdots, N\} \; \& \; \forall q \in \{\text{vh}, \text{hv}\} \\
& \text{(C4)} \quad \boldsymbol{\Phi}^p = \text{diag}\,(\phi_1^p, \cdots, \phi_N^p), \; \forall p \in \{\text{v}, \text{h}\} \\
& \text{(C5)} \quad \phi_n^p = a_n^p \exp(j\theta_n^p), \quad \theta_n^p \in [0, 2\pi), \; \forall n \in \{1, \cdots, N\} \; \& \; \forall p \in \{\text{v}, \text{h}\}, \\
& \text{(C6)} \quad |a_n^p|^2 \leq 1, \; \forall n \in \{1, \cdots, N\} \; \& \; \forall p \in \{\text{v}, \text{h}\} \\
& \text{(C7)} \quad \log_2\,(1 + \gamma_{\text{u},j}) \geq R_{\text{u,min}}, \; \forall j \in \mathcal{K}_{\text{u}} \\
& \text{(C8)} \quad \log_2\,(1 + \gamma_{\text{b},k}) \geq R_{\text{b,min}}, \; \forall k \in \mathcal{K}_{\text{b}} \\
& \text{(C9)} \quad \|\mathbf{P}\|^2 + \sum_{j=1}^{K_{\text{u}}} \|\mathbf{v}_j\|^2 + \|\mathbf{w}\|^2 \leq P_{\text{max}},
\end{aligned}
\tag{7.19}
$$

where P_{max} is the BS's power budget.

The constraints (C1)–(C6) ensure that each reflecting element in the dual-polarized RIS-UAV does not change the amplitude of the incident signal, indicating full reflection efficiency.[3] The inequalities in (C7) and (C8) constitute the minimum required service rates in the unicasting and broadcasting, respectively, where $R_{\text{u,min}}$ is the required rate by the UEs in the set $\mathcal{K}_{\text{u}}$ and $R_{\text{b,min}}$ is the required rate by the the UEs in the set $\mathcal{K}_{\text{b}}$. (C9) is the constraint on the active beamforming, meaning that the total transmit power is limited. We assume that this optimization problem is

---

[3]The elements of the optimal matrix $\boldsymbol{\Phi}$ are discrete values. Since the solution to the case with discrete phase shifts can be obtained from the case of continuous phase shifts via quantization [22], here the focus will be on the continuous phase shift case.

solved at the BS which has knowledge of the CSI of all involved links and other parameters such as $P_{\max}$, $R_{\mathrm{u,min}}$ and $R_{\mathrm{b,min}}$.

The EE maximization is a non-convex fractional problem, which is hard to tackle due to the non-convexity of the objective function and the bi-quadratic constraints (C7) and (C8), where the beamforming components at the BS and the RIS-UAV phase-shift matrix are coupled. To make the problem ($\mathcal{P}1$) tractable, we solve it by using the block coordinate descent (BCD) method. The BCD algorithm decouples the optimization variables, thus resulting in a two-stage approach. Specifically, we propose an iterative algorithm to solve problem (7.19) suboptimally with low complexity. In the first stage, the focus is on the design of the optimal passive beamforming matrix $\boldsymbol{\Phi}$ subject to the optimization constraints, i.e., (C1)–(C8). In the second stage, we tackle the problem of designing the active beamforming components, i.e., $\mathbf{P}$, $\mathbf{V}$ and $\mathbf{w}$.

Now, we investigate the passive beamforming design. Given the set of active beamforming components, i.e., $\mathbf{P}$, $\mathbf{V}$ and $\mathbf{w}$, the optimization problem reduces to

$$
\begin{aligned}
(\mathcal{P}2) \quad & \underset{\boldsymbol{\Phi}^{\mathrm{v}}, \boldsymbol{\Phi}^{\mathrm{h}}, \boldsymbol{\Phi}^{\mathrm{vh}}, \boldsymbol{\Phi}^{\mathrm{hv}}}{\text{maximize}} \quad R_{\mathrm{u}} + R_{\mathrm{b}} \\
& \text{subject to:} \\
& \text{(C1)} \quad \boldsymbol{\Phi}^q = \operatorname{diag}\left(\phi_1^q, \cdots, \phi_N^q\right), \ \forall q \in \{\mathrm{vh, hv}\} \\
& \text{(C2)} \quad \phi_n^q = a_n^q \exp(j\theta_n^q), \quad \theta_n^q \in [0, 2\pi), \ \forall n \in \{1, \cdots, N\} \ \& \ \forall q \in \{\mathrm{vh, hv}\}, \\
& \text{(C3)} \quad |a_n^q|^2 \leq 1, \ \forall n \in \{1, \cdots, N\} \ \& \ \forall q \in \{\mathrm{vh, hv}\} \\
& \text{(C4)} \quad \boldsymbol{\Phi}^p = \operatorname{diag}\left(\phi_1^p, \cdots, \phi_N^p\right), \ \forall p \in \{\mathrm{v, h}\} \\
& \text{(C5)} \quad \phi_n^p = a_n^p \exp(j\theta_n^p), \quad \theta_n^p \in [0, 2\pi), \ \forall n \in \{1, \cdots, N\} \ \& \ \forall p \in \{\mathrm{v, h}\} \\
& \text{(C6)} \quad |a_n^p|^2 \leq 1, \ \forall n \in \{1, \cdots, N\} \ \& \ \forall p \in \{\mathrm{v, h}\} \\
& \text{(C7)} \quad \log_2\left(1 + \gamma_{\mathrm{u},j}\right) \geq R_{\mathrm{u,min}} \ , \ \forall j \in \mathcal{K}_{\mathrm{u}} \\
& \text{(C8)} \quad \log_2\left(1 + \gamma_{\mathrm{b},k}\right) \geq R_{\mathrm{b,min}} \ , \ \forall k \in \mathcal{K}_{\mathrm{b}}.
\end{aligned}
\tag{7.20}
$$

The constraints (C7) and (C8) on the minimum required rates can be rewritten as follows:

$$
\left|\mathbf{h}_{\mathrm{u},j}^{\mathrm{eq}} \mathbf{p}_j^{\mathrm{v}} \mathbf{v}_j\right|^2 - \left(2^{R_{\mathrm{u,min}}} - 1\right)\left(\sum_{i=1, i \neq k}^{K_{\mathrm{u}}} \left|\mathbf{h}_{\mathrm{u},j}^{\mathrm{eq}} \mathbf{p}_i^{\mathrm{v}} \mathbf{v}_i\right|^2 + \left|\mathbf{h}_{\mathrm{u},j}^{\mathrm{eq}} \mathbf{P}^{\mathrm{h}} \mathbf{w}\right|^2 + \sigma^2\right) \geq 0, \ \forall j \in \mathcal{K}_{\mathrm{u}},
\tag{7.21}
$$

$$
\left|\mathbf{h}_{\mathrm{b},k}^{\mathrm{eq}} \mathbf{p}_k^{\mathrm{h}} \mathbf{w}\right|^2 - \left(2^{R_{\mathrm{b,min}}} - 1\right)\left(\left|\mathbf{h}_{\mathrm{b},k}^{\mathrm{eq}} \mathbf{P}^{\mathrm{v}} \sum_{j=1}^{K_{\mathrm{u}}} \mathbf{v}_j\right|^2 + \left|\mathbf{h}_{\mathrm{b},k}^{\mathrm{eq}} \mathbf{p}_i^{\mathrm{h}} \mathbf{w}\right|^2 + \sigma^2\right) \geq 0, \ \forall k \in \mathcal{K}_{\mathrm{b}},
\tag{7.22}
$$

where $\mathbf{h}_{\mathrm{b},k}^{\mathrm{eq}}$ and $\mathbf{h}_{\mathrm{u},j}^{\mathrm{eq}}$ are expressed as:

$$\mathbf{h}_{\mathrm{b},k}^{\mathrm{eq}} = (\mathbf{h}_{\mathrm{b},k}^{\mathrm{vh}})^{\mathrm{H}}\boldsymbol{\Phi}^{\mathrm{v}}(\mathbf{H}_{\mathrm{BS-RIS}}^{\mathrm{hv}})^{\mathrm{H}} + (\mathbf{h}_{\mathrm{b},k}^{\mathrm{h}})^{\mathrm{H}}\boldsymbol{\Phi}^{\mathrm{vh}}(\mathbf{H}_{\mathrm{BS-RIS}}^{\mathrm{h}})^{\mathrm{H}} + (\mathbf{h}_{\mathrm{b},k}^{\mathrm{vh}})^{\mathrm{H}}\boldsymbol{\Phi}^{\mathrm{hv}}(\mathbf{H}_{\mathrm{BS-RIS}}^{\mathrm{hv}})^{\mathrm{H}} + (\mathbf{h}_{\mathrm{b},k}^{\mathrm{h}})^{\mathrm{H}}\boldsymbol{\Phi}^{\mathrm{h}}(\mathbf{H}_{\mathrm{BS-RIS}}^{\mathrm{h}})^{\mathrm{H}},$$

$$\mathbf{h}_{\mathrm{u},j}^{\mathrm{eq}} = (\mathbf{h}_{\mathrm{u},j}^{\mathrm{v}})^{\mathrm{H}}\boldsymbol{\Phi}^{\mathrm{v}}(\mathbf{H}_{\mathrm{BS-RIS}}^{\mathrm{hv}})^{\mathrm{H}} + (\mathbf{h}_{\mathrm{u},j}^{\mathrm{hv}})^{\mathrm{H}}\boldsymbol{\Phi}^{\mathrm{vh}}(\mathbf{H}_{\mathrm{BS-RIS}}^{\mathrm{v}})^{\mathrm{H}} + (\mathbf{h}_{\mathrm{u},j}^{\mathrm{v}})^{\mathrm{H}}\boldsymbol{\Phi}^{\mathrm{hv}}(\mathbf{H}_{\mathrm{BS-RIS}}^{\mathrm{vh}})^{\mathrm{H}} + (\mathbf{h}_{\mathrm{u},j}^{\mathrm{hv}})^{\mathrm{H}}\boldsymbol{\Phi}^{\mathrm{h}}(\mathbf{H}_{\mathrm{BS-RIS}}^{\mathrm{vh}})^{\mathrm{H}}.$$

The above optimization problem can be further transformed to

$$(\mathcal{P}3) \quad \underset{\substack{\boldsymbol{\Phi}^{\mathrm{hv}},\zeta_{\mathrm{b},k},\zeta_{\mathrm{u},j} \\ \boldsymbol{\Phi}^{\mathrm{v}},\boldsymbol{\Phi}^{\mathrm{h}}\boldsymbol{\Phi}^{\mathrm{vh}}}}{\operatorname{maximize}} \quad \sum_{j=1}^{K_{\mathrm{u}}} F_j\left(\zeta_{\mathrm{u},j},\gamma_{\mathrm{u},j}\right) + \sum_{k=1}^{K_{\mathrm{b}}} F_k\left(\zeta_{\mathrm{b},k},\gamma_{\mathrm{b},k}\right)$$

subject to:

(C1)　$\boldsymbol{\Phi}^q = \operatorname{diag}\left(\phi_1^q,\cdots,\phi_N^{p,q}\right),\ \forall q \in \{\mathrm{vh},\mathrm{hv}\}$

(C2)　$\phi_n^q = a_n^q\exp(j\theta_n^q),\quad \theta_n^q \in [0,2\pi),\ \forall n \in \{1,\cdots,N\}\ \&\ \forall q \in \{\mathrm{vh},\mathrm{hv}\}$

(C3)　$|a_n^q|^2 \leq 1,\ \forall n \in \{1,\cdots,N\}\ \&\ \forall q \in \{\mathrm{vh},\mathrm{hv}\}$ (7.23)

(C4)　$\boldsymbol{\Phi}^p = \operatorname{diag}\left(\phi_1^p,\cdots,\phi_N^p\right),\ \forall p \in \{\mathrm{v},\mathrm{h}\}$

(C5)　$\phi_n^p = a_n^p\exp(j\theta_n^p),\quad \theta_n^p \in [0,2\pi),\ \forall n \in \{1,\cdots,N\}\ \&\ \forall p \in \{\mathrm{v},\mathrm{h}\}$

(C6)　$|a_n^p|^2 \leq 1,\ \forall n \in \{1,\cdots,N\}\ \&\ \forall p \in \{\mathrm{v},\mathrm{h}\}$,

(C7)　(7.21) & (7.22),

where $F(\zeta,\gamma) = \log(1+\zeta) - \zeta + \frac{(1+\zeta)\gamma}{1+\gamma}$, and where $\zeta_{\mathrm{b},k}$ and $\zeta_{\mathrm{u},j}$ are auxiliary variables associated with $\gamma_{\mathrm{b},k}$ and $\gamma_{\mathrm{u},j}$, respectively.

For given $\{\zeta_{\mathrm{b},k}, \zeta_{\mathrm{u},j}\}$, optimizing ϕ_n^p, ϕ_n^q in problem $(\mathcal{P}3)$ becomes a multiple-ratio fractional programming (MRFP) problem:

$$(\mathcal{P}4) \quad \underset{\substack{\boldsymbol{\Phi}^{\mathrm{hv}},\zeta_{\mathrm{b},k},\zeta_{\mathrm{u},j} \\ \boldsymbol{\Phi}^{\mathrm{v}},\boldsymbol{\Phi}^{\mathrm{h}},\boldsymbol{\Phi}^{\mathrm{vh}}}}{\text{maximize}} \; \tilde{F}(\boldsymbol{\Phi}) = \sum_{j=1}^{K_{\mathrm{u}}} \frac{\tilde{\zeta}_{\mathrm{u},j}\gamma_{\mathrm{u},j}}{1+\gamma_{\mathrm{u},j}} + \sum_{k=1}^{K_{\mathrm{b}}} \frac{\tilde{\zeta}_{\mathrm{b},k}\gamma_{\mathrm{b},k}}{1+\gamma_{\mathrm{b},k}}$$

subject to:

$\quad$ (C1) $\quad \boldsymbol{\Phi}^q = \mathrm{diag}\,(\phi_1^q, \cdots, \phi_N^q), \; \forall q \in \{\mathrm{vh}, \mathrm{hv}\}$

$\quad$ (C2) $\quad \phi_n^q = a_n^q \exp(j\theta_n^q), \quad \theta_n^q \in [0, 2\pi), \; \forall n \in \{1, \cdots, N\} \; \& \; \forall q \in \{\mathrm{vh}, \mathrm{hv}\}$

$\quad$ (C3) $\quad |a_n^q|^2 \leq 1, \; \forall n \in \{1, \cdots, N\} \; \& \; \forall q \in \{\mathrm{vh}, \mathrm{hv}\}$ $\qquad\qquad$ (7.24)

$\quad$ (C4) $\quad \boldsymbol{\Phi}^p = \mathrm{diag}\,(\phi_1^p, \cdots, \phi_N^p), \; \forall p \in \{\mathrm{v}, \mathrm{h}\}$

$\quad$ (C5) $\quad \phi_n^p = a_n^p \exp(j\theta_n^p), \quad \theta_n^p \in [0, 2\pi), \; \forall n \in \{1, \cdots, N\} \; \& \; \forall p \in \{\mathrm{v}, \mathrm{h}\}$

$\quad$ (C6) $\quad |a_n^p|^2 \leq 1, \; \forall n \in \{1, \cdots, N\} \; \& \; \forall p \in \{\mathrm{v}, \mathrm{h}\}$,

$\quad$ (C7) $\quad$ (7.21) & (7.22),

where $\tilde{\zeta}_{\mathrm{u},j} = 1 + \zeta_{\mathrm{u},j}$ and $\tilde{\zeta}_{\mathrm{b},k} = 1 + \zeta_{\mathrm{b},k}$.

To solve this MRFP problem, we apply the quadratic transform [120] to the objective function of $(\mathcal{P}4)$. Then, $\tilde{F}(\boldsymbol{\Phi})$ can be rewritten as

$$\begin{aligned}
\tilde{F}(\boldsymbol{\Phi}, \boldsymbol{\zeta}_{\mathrm{u}}, \boldsymbol{\zeta}_{\mathrm{b}}) &= \sum_{j=1}^{K_{\mathrm{u}}} 2\sqrt{\tilde{\zeta}_{\mathrm{u},j}}\mathrm{Re}\left(\zeta_{\mathrm{u},j}^* \left|\mathbf{h}_{\mathrm{u},j}^{\mathrm{eq}}\mathbf{p}_j^{\mathrm{v}}\mathbf{v}_j\right|^2\right) - |\zeta_{\mathrm{u},j}|^2 \left(\sum_{i=1,i\neq j}^{K_{\mathrm{u}}} \left|\mathbf{h}_{\mathrm{u},j}^{\mathrm{eq}}\mathbf{p}_i^{\mathrm{v}}\mathbf{v}_i\right|^2 + \left|\mathbf{h}_{\mathrm{u},j}^{\mathrm{eq}}\mathbf{P}^{\mathrm{h}}\mathbf{w}\right|^2 + \sigma^2\right) \\
&\quad + \sum_{k=1}^{K_{\mathrm{b}}} 2\sqrt{\tilde{\zeta}_{\mathrm{b},k}}\mathrm{Re}\left(\zeta_{\mathrm{b},k}^* \left|\mathbf{h}_{\mathrm{b},k}^{\mathrm{eq}}\mathbf{p}_k^{\mathrm{h}}\mathbf{w}\right|^2\right) - |\zeta_{\mathrm{b},k}|^2 \left(\sum_{i=1,i\neq k}^{K_{\mathrm{b}}} \left|\mathbf{h}_{\mathrm{b},k}^{\mathrm{eq}}\mathbf{p}_i^{\mathrm{h}}\mathbf{w}\right|^2 + \left|\mathbf{h}_{\mathrm{b},k}^{\mathrm{eq}}\mathbf{P}^{\mathrm{h}}\sum_{j\in\mathcal{K}_{\mathrm{u}}}\mathbf{v}_j\right|^2 + \sigma^2\right),
\end{aligned}$$
$$(7.25)$$

where $\boldsymbol{\zeta}_{\mathrm{u}} = [\zeta_{\mathrm{u},1}, \cdots, \zeta_{\mathrm{u},K_{\mathrm{u}}}]^{\mathrm{T}}$ and $\boldsymbol{\zeta}_{\mathrm{b}} = \left[\zeta_{\mathrm{b},1}, \cdots, \zeta_{\mathrm{b},K_{\mathrm{b}}}\right]^{\mathrm{T}}$ are auxiliary variables introduced by the quadratic transform to the objective function of $(\mathcal{P}4)$. We optimize $\{\boldsymbol{\zeta}_{\mathrm{u}}, \boldsymbol{\zeta}_{\mathrm{b}}\}$ and $\boldsymbol{\Phi}$ in an alternating manner. The optimal $\zeta_{\mathrm{u},j}, \; \forall j = 1, \cdots, K_{\mathrm{u}}$, and $\zeta_{\mathrm{b},k}, \; \forall k = 1, \cdots, K_{\mathrm{b}}$, under a given $\boldsymbol{\Phi}$ can be computed by setting their first derivatives to zero, as given by

$$\begin{aligned}
\hat{\zeta}_{\mathrm{u},j} &= \frac{\sqrt{\tilde{\zeta}_{\mathrm{u},j}}\left|\mathbf{h}_{\mathrm{u},j}^{\mathrm{eq}}\mathbf{p}_j^{\mathrm{v}}\mathbf{v}_j\right|^2}{\sum_{i=1,i\neq j}^{K_{\mathrm{u}}}\left|\mathbf{h}_{\mathrm{u},j}^{\mathrm{eq}}\mathbf{p}_i^{\mathrm{v}}\mathbf{v}_i\right|^2 + \left|\mathbf{h}_{\mathrm{u},j}^{\mathrm{eq}}\mathbf{P}^{\mathrm{h}}\mathbf{w}\right|^2 + \sigma^2}, \\
\hat{\zeta}_{\mathrm{b},k} &= \frac{\sqrt{\tilde{\zeta}_{\mathrm{b},k}}\left|\mathbf{h}_{\mathrm{b},k}^{\mathrm{eq}}\mathbf{p}_k^{\mathrm{h}}\mathbf{w}\right|^2}{\sum_{i=1,i\neq k}^{K_{\mathrm{b}}}\left|\mathbf{h}_{\mathrm{b},k}^{\mathrm{eq}}\mathbf{p}_i^{\mathrm{h}}\mathbf{w}\right|^2 + \left|\mathbf{h}_{\mathrm{b},k}^{\mathrm{eq}}\mathbf{P}^{\mathrm{h}}\sum_{j\in\mathcal{K}_{\mathrm{u}}}\mathbf{v}_j\right|^2 + \sigma^2}.
\end{aligned}$$
$$(7.26)$$

With further manipulations on $\mathbf{h}^{\mathrm{eq}}_{\mathrm{u},j}$ and $\mathbf{h}^{\mathrm{eq}}_{\mathrm{b},k}$, we get $\mathbf{h}^{\mathrm{eq}}_{\mathrm{b},k} = (\phi^{\mathrm{v}})^{\mathrm{H}}\mathbf{z}_1 + (\phi^{\mathrm{vh}})^{\mathrm{H}}\mathbf{z}_2 + (\phi^{\mathrm{hv}})^{\mathrm{H}}\mathbf{z}_3 +$
$(\phi^{\mathrm{h}})^{\mathrm{H}}\mathbf{z}_4$, where $\mathbf{z}_1 = \mathrm{diag}\,\big((\mathbf{h}^{\mathrm{vh}}_{\mathrm{b},k})^{\mathrm{H}}\big)\big(\mathbf{H}^{\mathrm{hv}}_{\mathrm{BS-RIS}}\big)^{\mathrm{H}}$, $\mathbf{z}_2 = \mathrm{diag}\,\big((\mathbf{h}^{\mathrm{h}}_{\mathrm{b},k})^{\mathrm{H}}\big)\big(\mathbf{H}^{\mathrm{h}}_{\mathrm{BS-RIS}}\big)^{\mathrm{H}}$,
$\mathbf{z}_3 = \mathrm{diag}\,\big((\mathbf{h}^{\mathrm{vh}}_{\mathrm{b},k})^{\mathrm{H}}\big)\big(\mathbf{H}^{\mathrm{hv}}_{\mathrm{BS-RIS}}\big)^{\mathrm{H}}$ and $\mathbf{z}_4 = \mathrm{diag}\,\big((\mathbf{h}^{\mathrm{h}}_{\mathrm{b},k})^{\mathrm{H}}\big)\big(\mathbf{H}^{\mathrm{h}}_{\mathrm{BS-RIS}}\big)^{\mathrm{H}}$. The same operations are applied to $\mathbf{h}^{\mathrm{eq}}_{\mathrm{u},j} = (\phi^{\mathrm{v}})^{\mathrm{H}}\mathbf{q}_1 + (\phi^{\mathrm{vh}})^{\mathrm{H}}\mathbf{q}_2 + (\phi^{\mathrm{hv}})^{\mathrm{H}}\mathbf{q}_3 + (\phi^{\mathrm{h}})^{\mathrm{H}}\mathbf{q}_4$.

Now, we proceed to optimize $\phi^q = \mathrm{vecd}\,(\mathbf{\Phi}^q)$ and $\phi^p = \mathrm{vecd}\,(\mathbf{\Phi}^p)$ given $\{\zeta_{\mathrm{u}}, \zeta_{\mathrm{b}}\}$. Expanding the squared terms in (7.25), we can write

$$\tilde{F}(\phi^{\mathrm{v}}, \phi^{\mathrm{vh}}, \phi^{\mathrm{hv}}, \phi^{\mathrm{h}}) = -\Big((\phi^{\mathrm{v}})^{\mathrm{H}}\mathbf{\Upsilon}_1\phi^{\mathrm{v}} + (\phi^{\mathrm{vh}})^{\mathrm{H}}\mathbf{\Upsilon}_2\phi^{\mathrm{vh}} + (\phi^{\mathrm{hv}})^{\mathrm{H}}\mathbf{\Upsilon}_3\phi^{\mathrm{hv}} + (\phi^{\mathrm{h}})^{\mathrm{H}}\mathbf{\Upsilon}_4\phi^{\mathrm{h}}\Big)$$
$$+ 2\Big(\mathrm{Re}\left\{\mathbf{u}_1^{\mathrm{H}}\phi^{\mathrm{v}}\right\} + \mathrm{Re}\left\{\mathbf{u}_2^{\mathrm{H}}\phi^{\mathrm{vh}}\right\} + \mathrm{Re}\left\{\mathbf{u}_3^{\mathrm{H}}\phi^{\mathrm{hv}}\right\} + \mathrm{Re}\left\{\mathbf{u}_4^{\mathrm{H}}\phi^{\mathrm{h}}\right\}\Big), \qquad (7.27)$$

where

$$\mathbf{\Upsilon}_l = \sum_{j=1}^{K_{\mathrm{u}}}|\zeta_{\mathrm{u},j}|^2\left(\mathbf{a}_j\mathbf{a}_j^{\mathrm{H}} + \sum_{i=1,i\neq j}^{K_{\mathrm{u}}}\mathbf{b}_{i,j}\mathbf{b}_{i,j}^{\mathrm{H}} + \mathbf{c}_j\mathbf{c}_j^{\mathrm{H}}\right) + \sum_{k=1}^{K_{\mathrm{b}}}|\zeta_{\mathrm{b},k}|^2\left(\boldsymbol{\alpha}_k\boldsymbol{\alpha}_k^{\mathrm{H}} + \sum_{i=1,i\neq k}^{K_{\mathrm{b}}}\boldsymbol{\beta}_k\boldsymbol{\beta}_k^{\mathrm{H}} + \mathbf{r}_k\mathbf{r}_k^{\mathrm{H}}\right), \qquad (7.28)$$

$$\mathbf{u}_l = \sum_{j=1}^{K_{\mathrm{u}}}\sqrt{\tilde{\zeta}_{\mathrm{u},j}}\zeta_{\mathrm{u},j}\mathbf{a}_j - |\zeta_{\mathrm{u},j}|^2\left(\sum_{i=1,i\neq j}^{K_{\mathrm{u}}}|\mathbf{b}_{i,j}|^2 + |\mathbf{c}_j|^2\right) + \sum_{k=1}^{K_{\mathrm{b}}}\sqrt{\tilde{\zeta}_{\mathrm{b},k}}\zeta_{\mathrm{b},k}\boldsymbol{\alpha}_k - |\zeta_{\mathrm{u},k}|^2\left(\sum_{i=1,i\neq k}^{K_{\mathrm{b}}}|\boldsymbol{\beta}_k|^2 + |\mathbf{r}_k|^2\right),$$
$$\qquad (7.29)$$

in which $l = 1, \cdots, 4$, $\mathbf{a}_j = \mathbf{z}_j\mathbf{p}^{\mathrm{v}}_j\mathbf{v}_j$, $\mathbf{b}_{i,j} = \mathbf{z}_j\mathbf{p}^{\mathrm{v}}_i\mathbf{v}_i$, $\mathbf{c}_j = \mathbf{z}_j\mathbf{P}^{\mathrm{h}}\mathbf{w}$, $\alpha_k = \mathbf{q}_k\mathbf{p}^{\mathrm{h}}_k\mathbf{w}$, $\beta_k = \mathbf{q}_k\mathbf{p}^{\mathrm{h}}_i\mathbf{w}$, and
$\mathbf{r}_k = \mathbf{q}_k\mathbf{P}^{\mathrm{v}}\sum_{j=1}^{K_{\mathrm{u}}}\mathbf{v}_j$.

The optimization problem can be reformulated as

$(\mathcal{P}5) \quad \underset{\phi^{\mathrm{v}},\phi^{\mathrm{h}},\phi^{\mathrm{vh}},\phi^{\mathrm{hv}}}{\mathrm{maximize}} \;\; \tilde{F}(\phi^{\mathrm{v}}, \phi^{\mathrm{vh}}, \phi^{\mathrm{hv}}, \phi^{\mathrm{h}})$

     subject to:

       (C1) $\mathbf{\Phi}^q = \mathrm{diag}\,(\phi^q_1, \cdots, \phi^q_N), \; \forall q \in \{\mathrm{vh}, \mathrm{hv}\}$

       (C2) $\phi^q_n = a^q_n\exp(j\theta^q_n), \quad \theta^q_n \in [0, 2\pi), \; \forall n \in \{1, \cdots, N\} \;\&\; \forall q \in \{\mathrm{vh}, \mathrm{hv}\}$

       (C3) $|a^q_n|^2 \leq 1, \; \forall n \in \{1, \cdots, N\} \;\&\; \forall q \in \{\mathrm{vh}, \mathrm{hv}\}$ (7.30)

       (C4) $\mathbf{\Phi}^p = \mathrm{diag}\,(\phi^p_1, \cdots, \phi^p_N), \; \forall p \in \{\mathrm{v}, \mathrm{h}\}$

       (C5) $\phi^p_n = a^p_n\exp(j\theta^p_n), \quad \theta^p_n \in [0, 2\pi), \; \forall n \in \{1, \cdots, N\} \;\&\; \forall p \in \{\mathrm{v}, \mathrm{h}\}$

       (C6) $|a^p_n|^2 \leq 1, \; \forall n \in \{1, \cdots, N\} \;\&\; \forall p \in \{\mathrm{v}, \mathrm{h}\}$

       (C7)   (7.21) & (7.22).

Here, the alternating optimization technique will be adopted. The problem will be divided into sub-problems w.r.t. to the optimization variables $\phi^p, p \in \{h, v\}$ and $\phi^q, q \in \{vh, hv\}$. As such, two optimization problems are defined:

$$
(\mathcal{P}6) \ \underset{\phi^q}{\text{maximize}} \ = -(\phi^q)^H \boldsymbol{\Upsilon} \phi^q + 2 \left(\text{Re} \left\{ \mathbf{u}^H \phi^q \right\} \right)
$$

subject to:

(C1) $\boldsymbol{\Phi}^q = \text{diag} \left(\phi_1^q, \cdots, \phi_N^q \right), \ \forall q \in \{vh, hv\}$

(C2) $\phi_n^q = a_n^q \exp(j\theta_n^q), \quad \theta_n^q \in [0, 2\pi), \ \forall n \in \{1, \cdots, N\} \ \& \ \forall q \in \{vh, hv\}$

(C3) $|a_n^q|^2 \leq 1, \ \forall n \in \{1, \cdots, N\} \ \& \ \forall q \in \{vh, hv\}$

(C7)   (7.21) & (7.22). $\qquad (7.31)$

and

$$
(\mathcal{P}7) \ \underset{\phi^p}{\text{maximize}} \ = -(\phi^p)^H \boldsymbol{\Upsilon} \phi^p + 2 \left(\text{Re} \left\{ \mathbf{u}^H \phi^p \right\} \right)
$$

subject to:

(C4) $\boldsymbol{\Phi}^p = \text{diag} \left(\phi_1^p, \cdots, \phi_N^p \right), \ \forall p \in \{v, h\}$

(C5) $\phi_n^p = a_n^p \exp(j\theta_n^p), \quad \theta_n^p \in [0, 2\pi), \ \forall n \in \{1, \cdots, N\} \ \& \ \forall p \in \{v, h\}$

(C6) $|a_n^p|^2 \leq 1, \ \forall n \in \{1, \cdots, N\} \ \& \ \forall p \in \{v, h\}$

(C7)   (7.21) & (7.22). $\qquad (7.32)$

The problems $(\mathcal{P}6)$ and $(\mathcal{P}7)$ are of inhomogeneous QCQP type [121]. A popular method for solving such type of problems is the Gaussian randomization-based SDR [13], which relaxes the QCQP into a semi-definite program (SDP). The proposed procedure for the passive beamforming design is summarized in Algorithm 7.3.

Algorithm 7.3 Passive Beamforming Design.

Require: Given $\mathbf{V}$, $\mathbf{w}$ and $\mathbf{P}$.
 1: Calculate $\tilde{\zeta}_{u,j} = \gamma_{u,j}, \ j = 1, \cdots, K_u$, and $\tilde{\zeta}_{b,k} = \gamma_{b,k}, \ k = 1, \cdots, K_b$, by using (7.12) & (7.14).
 2: Given $\boldsymbol{\Phi}$, update $\{\boldsymbol{\zeta}_u, \boldsymbol{\zeta}_b\}$ by using (27) & (28).
 3: Given $\{\boldsymbol{\zeta}_u, \boldsymbol{\zeta}_b\}$
   Initialize: $l = 1, \{\boldsymbol{\Upsilon}_l, \mathbf{u}_l\}$
   Repeat
   1. Using SDR, solve $(\mathcal{P}6)$ and $(\mathcal{P}7)$ to obtain the optimal ϕ^q and ϕ^p.
   2. Update $\{\boldsymbol{\Upsilon}_l, \mathbf{u}_l\}$ by using (28) & (29).
   3. $l = l + 1$.
   Until: Convergence of the objective functions of $(\mathcal{P}6)$ and $(\mathcal{P}7)$ & $l = 4$.
Ensure: $\boldsymbol{\Phi}$.

Due to the constraint (C2) in ($\mathcal{P}6$), the solution values for θ_n^p and θ_n^q will be in $[0, 2\pi)$. Let us define the feasible set of discrete phase shifts as $\mathcal{F} = \{\exp(\frac{j2\pi n}{2^b})\}_{n=0}^{2^b-1}$, where b is the bit resolution and n is the phase-shift index. By seting $b = 1$, the feasible set will be reduced to $\mathcal{F} = \{0, \pi\}$, $\forall n = 1, 2, \ldots, 2N$. To discretize the solution according to the feasible set of phases $\mathcal{F}$, we set $\theta_n^q = 0$ when the solution to ($\mathcal{P}6$) is such that $\frac{3\pi}{2} \leq \theta_n^q < 2\pi$ and $0 \leq \theta_n^q < \frac{\pi}{2}$, and $\theta_n^q = \pi$ when the solution is such that $\frac{\pi}{2} \leq \theta_n^q < \pi$ or $\pi \leq \theta_n^q < \frac{3\pi}{2}$. The same steps are followed to discretize the solution of the problem ($\mathcal{P}7$).

Now, we investigate the active beamforming design. For fixed $\boldsymbol{\Phi}$, the optimization problem ($\mathcal{P}1$) is reduced to

$$(\mathcal{P}8) \quad \underset{\mathbf{P},\mathbf{V},\mathbf{w}}{\text{maximize}} \ \eta_{\text{EE}}$$

$$\text{subject to:}$$

$$(\text{C7}) \quad (7.21) \ \& \ (7.22)$$

$$(\text{C9}) \quad \|\mathbf{P}\|^2 + \sum_{j=1}^{K_u} \|\mathbf{v}_j\|^2 + \|\mathbf{w}\|^2 \leq P_{\max}. \tag{7.33}$$

To tackle the optimization problem ($\mathcal{P}8$) effectively, we first transform it into the following equivalent problem by utilizing the Dinkeblach's method [95].

$$(\mathcal{P}9) \quad \underset{\mathbf{P},\mathbf{V},\mathbf{w}}{\text{maximize}} \ (R_u + R_b) - \eta_{\text{EE}} P_\Sigma$$

$$\text{subject to:}$$

$$(\text{C7}) \quad (7.21) \ \& \ (7.22)$$

$$(\text{C9}) \quad \|\mathbf{P}\|^2 + \sum_{j=1}^{K_u} \|\mathbf{v}_j\|^2 + \|\mathbf{w}\|^2 \leq P_{\max}. \tag{7.34}$$

The objective function in ($\mathcal{P}9$) is a monotonically decreasing function w.r.t. η_{EE}. Here as well, we adopt the alternating optimization technique to design the active beamforming components, i.e., $\mathbf{P}$, $\mathbf{V}$ and $\mathbf{w}$. Firstly, we fix matrix $\mathbf{V}$ and vector $\mathbf{w}$, and design of the prebeamforming matrix $\mathbf{P}$ to maximize the EE. The optimization problem becomes

$$(\mathcal{P}10) \quad \underset{\mathbf{P}}{\text{maximize}} \ (R_u + R_b) - \eta_{\text{EE}} P_\Sigma$$

$$\text{subject to:}$$

$$(\text{C7}) \quad (7.21) \ \& \ (7.22)$$

$$(\text{C9}) \quad \|\mathbf{P}\|^2 + \sum_{j=1}^{K_u} \|\mathbf{v}_j\|^2 + \|\mathbf{w}\|^2 \leq P_{\max}. \tag{7.35}$$

Clearly, the optimization in ($\mathcal{P}10$) is a standard SDP problem w.r.t. $\mathbf{P}$, which can be solved with the interior point method.

Hereafter, we fix the prebeamforming matrix $\mathbf{P}$, and design the beamforming matrix $\mathbf{V}$ and vector $\mathbf{w}$. The optimization problem is as follows:

$$(\mathcal{P}11) \ \underset{\mathbf{V},\mathbf{w}}{\text{maximize}} \ (R_\text{u} + R_\text{b}) - \eta_\text{EE} P_\Sigma$$

subject to:

(C7) (7.21) & (7.22)

(C9) $\|\mathbf{P}\|^2 + \sum_{j=1}^{K_\text{u}} \|\mathbf{v}_j\|^2 + \|\mathbf{w}\|^2 \leq P_\text{max}.$

$$(7.36)$$

The alternating optimization techniques are also adopted to solve the above problem. First, we fix the broadcasting vector $\mathbf{w}$ and optimize w.r.t. the beamforming matrix $\mathbf{V}$. The optimization problem reduces to

$$(\mathcal{P}12) \ \underset{\mathbf{V}}{\text{maximize}} \ (R_\text{u} + R_\text{b}) - \eta_\text{EE} P_\Sigma$$

subject to:

(C7) (7.21) & (7.22)

(C9) $\|\mathbf{P}\|^2 + \sum_{j=1}^{K_\text{u}} \|\mathbf{v}_j\|^2 + \|\mathbf{w}\|^2 \leq P_\text{max},$

$$(7.37)$$

in which the optimal $\mathbf{V}$ can be obtained by simple ZF scheme that can achieve near-optimal performance [122].

Given the beamforming directions pertaining to the unicasting, it can be seen from (7.21) and (7.22) that the inter-user interference is removed from both types of SINRs. Therefore, the SINR constraints for the unicasting and broadcasting are expressed as

$$\left| \mathbf{h}_{\text{u},j}^{\text{eq}} \mathbf{p}_j^\text{v} \mathbf{v}_j \right|^2 - (2^{R_\text{u,min}} - 1)\left(\sigma^2 + \left| \mathbf{h}_{\text{u},j}^{\text{eq}} \mathbf{P}^\text{h} \mathbf{w} \right|^2 \right) \geq 0, \ \forall j \in \mathcal{K}_\text{b}, \tag{7.38}$$

$$\left| \mathbf{h}_{\text{b},k}^{\text{eq}} \mathbf{p}_k^\text{h} \mathbf{w} \right|^2 - (2^{R_\text{b,min}} - 1)\left(\left| \mathbf{h}_{\text{b},k}^{\text{eq}} \mathbf{P}^\text{v} \sum_{j=1}^{K_\text{u}} \mathbf{v}_j \right|^2 + \sum_{i=1,i\neq k}^{K_\text{b}} \left| \mathbf{h}_{\text{b},k}^{\text{eq}} \mathbf{p}_\text{i}^\text{h} \mathbf{w} \right|^2 + \sigma^2 \right) \geq 0, \ \forall k \in \mathcal{K}_\text{b}. \tag{7.39}$$

Accordingly, the optimization problem ($\mathcal{P}$12) can be recast as follows:

$$(\mathcal{P}13) \quad \underset{\mathbf{w}}{\text{maximize}} \ (R_\mathrm{u} + R_\mathrm{b}) - \eta_\mathrm{EE} P_\Sigma$$

$$\text{subject to:}$$

$$\text{(C7)} \quad \text{(7.38) \& (7.39)}$$

$$\text{(C9)} \quad \|\mathbf{P}\|^2 + \sum_{j=1}^{K_\mathrm{u}} \|\mathbf{v}_j\|^2 + \|\mathbf{w}\|^2 \leq P_\mathrm{max}. \tag{7.40}$$

Obviously, ($\mathcal{P}$13) is still a non-convex optimization problem due to the non-convex constraints (7.38) and (7.39). Initialized by a given $\mathbf{w}^0$ feasible for ($\mathcal{P}$13), the successive convex approximation (SCA) method can be used to solve the convex approximations of ($\mathcal{P}$5) successively. Let us denote the beamforming vector at the tth iteration by $\mathbf{w}^{(t)}$. The left-hand-side (LHS) of (7.38) is a quadratic-over-affine function, which is convex w.r.t. $\mathbf{w}^{(t)}$. Thus, for any fixed points $(e_{\mathrm{b},k}^{*(t)}, l_{\mathrm{b},k}^{*(t)})$ at iteration t, with $e_{\mathrm{b},k}^{*(0)} \geq 1$, and $l_{\mathrm{b},k}^{*(0)} \geq 0$, the LHS of (7.38) can be tightly approximated by its lower bound obtained from the first-order Taylor series expansion. Therefore, (7.38) reduces to:

$$2\frac{e_{\mathrm{u},j}^{*(t)} e_{\mathrm{u},j}^{(t)}}{l_{\mathrm{u},j}^{*(t)}} - \frac{\left|e_{\mathrm{u},j}^{*(t)}\right|^2}{\left(l_{\mathrm{u},j}^{*(t)}\right)^2} \, l_{\mathrm{u},j}^{(t)} \geq 2^{R_\mathrm{u,min}} - 1, \tag{7.41}$$

where $e_{\mathrm{u},j}^{(t)} \triangleq \mathbf{h}_{\mathrm{u},j}^\mathrm{eq} \mathbf{p}_j^\mathrm{v} \mathbf{v}_j$ and $l_{\mathrm{u},j}^{(t)} \triangleq \sigma^2 + \left|\mathbf{h}_{\mathrm{u},j}^\mathrm{eq} \mathbf{P}^\mathrm{h} \mathbf{w}^{(t)}\right|^2$. The same manipulations are applied to (7.39). Thus, we obtain

$$2\frac{e_{\mathrm{b},k}^{*(t)} e_{\mathrm{b},k}^{(t)}}{l_{\mathrm{b},k}^{*(t)}} - \frac{\left|e_{\mathrm{b},k}^{*(t)}\right|^2}{\left(l_{\mathrm{b},k}^{*(t)}\right)^2} \, l_{\mathrm{b},k}^{(t)} \geq 2^{R_\mathrm{b,min}} - 1, \tag{7.42}$$

where $e_{\mathrm{b},k}^{(t)} \triangleq \mathbf{h}_{\mathrm{b},k}^\mathrm{eq} \mathbf{p}_k^\mathrm{h} \mathbf{w}^{(t)}$ and $l_{\mathrm{b},k}^{(t)} \triangleq \left|\mathbf{h}_{\mathrm{b},k}^\mathrm{eq} \mathbf{P}^\mathrm{v} \sum_{j=1}^{K_\mathrm{u}} \mathbf{v}_j\right|^2 + \sigma^2$. Replacing (7.38) with (7.41) and (7.39) with (7.42) in ($\mathcal{P}$13), the problem becomes a tractable convex optimization problem, namely,

$$(\mathcal{P}14) \quad \underset{\mathbf{w}^{(t)}}{\text{maximize}} \ \left(R_\mathrm{u}^{(t)} + R_\mathrm{b}^{(t)}\right) - \eta_\mathrm{EE} \, P_\Sigma^{(t)}$$

$$\text{subject to:}$$

$$\text{(C7)} \quad \text{(7.41) \& (7.42)}$$

$$\text{(C9)} \quad \|\mathbf{P}\|^2 + \sum_{j=1}^{K_\mathrm{u}} \|\mathbf{v}_j\|^2 + \|\mathbf{w}\|^2 \leq P_\mathrm{max} \,, \tag{7.43}$$

which can be efficiently solved by existing convex solvers such as CVX. At each iteration, $(e_{\mathrm{b},k}^{*(t)}, l_{\mathrm{b},k}^{*(t)})$ are updated as $e_{\mathrm{b},k}^{*(t)} = e_{\mathrm{b},k}^{(t-1)}$ and $l_{\mathrm{b},k}^{*(t)} = l_{\mathrm{b},k}^{(t-1)}$, $(e_{\mathrm{u},j}^{*(t)}, l_{\mathrm{u},j}^{*(t)})$ are updated as $e_{\mathrm{u},j}^{*(t)} = e_{\mathrm{u},j}^{(t-1)}$ and $l_{\mathrm{u},j}^{*(t)} = l_{\mathrm{u},j}^{(t-1)}$, and the beamforming vector as $\mathbf{w}^{(t)} = \mathbf{w}^{(t-1)}$, until convergence is reached.

The proposed active beamforming design is summarized in Algorithm 7.4.

Algorithm 7.4 Active Beamforming Design.

Require: Phase-shift matrix $\boldsymbol{\Phi}$.

1: Calculate the prebeamforming matrix $\mathbf{P}$ based on the interior point method.

2: Calculate the beamforming matrix $\mathbf{V}$ using low-complexity ZF based on SVD.

Initialization: Set $t = 0$, and generate $\mathbf{w}^{(0)}$

Repeat

1. Solve (7.43) to obtain the optimal beamforming vector $\mathbf{w}^{\mathrm{opt}}$

2. Update $\mathbf{w}^{(t)} = \mathbf{w}^{\mathrm{opt}}$

3. $t = t + 1$.

Until the objective function in (7.43) with the obtained $\mathbf{w}^{(t)}$ reaches convergence.

Ensure: $\mathbf{P}$, $\mathbf{V}$ and $\mathbf{w}^{(t)}$.

7.2

Theorem 7.3. *The proposed two-stage iterative algorithm converges to a stationary point.*

The proof is provided in Appendix A.

It is clear that the computational complexity of our proposed two-stage solution mainly comes from solving three SDP problems related to the variables $\mathbf{P}$, $\mathbf{w}$ and $\boldsymbol{\Phi}$. Based on [123], the complexity of standard SDP programming is

$$O\left(M_{\mathrm{sdp}}N_{\mathrm{sdp}}^{3.5} + M_{\mathrm{sdp}}^2 N_{\mathrm{sdp}}^3 + M_{\mathrm{sdp}}N_{\mathrm{sdp}}^{0.5}\right)\log(\frac{1}{\epsilon_{\mathrm{sdp}}})$$

, where M_{sdp} is the number of semi-definite cone constraints, N_{sdp} is the dimension of semi-definite cones, and ϵ_{sdp} is the accuracy of the solution of the SDP problem. In our case, the number of semi-definite cone constraints is as follows: $M_{\mathrm{sdp}} = 4K$, in which K is the total number of UEs, w.r.t. the design of $\mathbf{P}$, $M_{\mathrm{sdp}} = 4K_{\mathrm{b}}$ w.r.t. the design of $\mathbf{w}$, and $M_{\mathrm{sdp}} = 8NK_{\mathrm{u}}K_{\mathrm{b}}$ when designing $\boldsymbol{\Phi}$. As for the semi-definite cone dimension, $N_{\mathrm{sdp}} = 1 + \frac{K_{\mathrm{u}}}{2} + \frac{M_{\mathrm{t}}}{2}$.

7.4 Performance Evaluation

The performance of the proposed polarization-based RIS-UAV-assisted joint broadcast-unicast communication system is now evaluated. Practical scenarios with imperfect polarization are investigated, and comparisons with the equivalent system but implementing LDM are provided. Herein, the following parameter setting is used, unless otherwise stated: $B = 10$ MHz, the noise power $BN_0 = -104$ dBm, $P_{\text{BS}} = 30$ dBm, $P_{\text{UE}} = 10$ dBm, $P_n = 10$ dBm, $P_{\text{UAV}} = 40$ dBm, $\alpha = 2.2$, $\beta = 2.8$, $\mu = \mu_{\text{b}} = \mu_{\text{u}} = 5$, $R_{\text{b,min}} = 3$ bps/Hz, and $R_{\text{u,min}} = 0.5$ bps/Hz. We consider a 3D coordinate system, in which the BS is located at the origin $(0, 0, 0)$, and the UEs pertaining to the unicast and boradcast services are randomly located in the areas $\{(x, y) \mid 70 \text{ m} < x < 100 \text{ m}, 0 < y < 50 \text{ m}\}$ and $\{(x, y) \mid 60 \text{ m} < x < 70 \text{ m}, 0 < y < 50 \text{ m}\}$, respectively. The RIS-UAV is hovering at $(\text{x}, 0, A_0)$, where $A_0 = 100$ m is the altitude. Results are obtained using up to 50 random channel realizations.

The LDM-based System

LDM is a power-based non-orthogonal multiplexing technique based on a layered structure, where different services can be transmitted simultaneously with different power levels and robustness [124]. For the LDM-based RIS-UAV-assisted system [113], a two-layered structure is adopted, where the broadcasting signal is sent on the core layer and the unicasting signals are sent on the enhanced layer. The received signal at the jth UE in set $\mathcal{K}_{\text{u}}$ is expressed as

$$y_{\text{u},j} = \mathbf{h}_{\text{u},j}^{\text{H}} \boldsymbol{\Phi} \mathbf{H}_{\text{BS-RIS}}^{\text{H}} \left(\mathbf{w}s + \sum_{j=1}^{K_{\text{u}}} \mathbf{v}_j s_j \right) + n_{\text{u},j}, \tag{7.44}$$

and the corresponding SINR is given by

$$\gamma_{\text{u},j} = \frac{\left| \mathbf{h}_{\text{u},j}^{\text{H}} \boldsymbol{\Phi} \mathbf{H}_{\text{BS-RIS}}^{\text{H}} \mathbf{v}_j \right|^2}{\sum_{i=1, i \neq j}^{K_{\text{u}}} \left| \mathbf{h}_{\text{u},j}^{\text{H}} \boldsymbol{\Phi} \mathbf{H}_{\text{BS-RIS}}^{\text{H}} \mathbf{v}_i \right|^2 + \sigma^2}. \tag{7.45}$$

For the broadcast service, the received signal at the kth UE in set $\mathcal{K}_{\text{b}}$ is expressed as

$$y_{\text{b},k} = \mathbf{h}_{\text{b},k}^{\text{H}} \boldsymbol{\Phi} \mathbf{H}_{\text{BS-RIS}}^{\text{H}} \left(\mathbf{w}s + \sum_{j=1}^{K_{\text{u}}} \mathbf{v}_j s_j \right) + n_{\text{b},k}, \tag{7.46}$$

and the corresponding SINR is given by

$$\gamma_{\mathrm{b},k} = \frac{\left| \mathbf{h}_{\mathrm{b},k}^{\mathrm{H}} \boldsymbol{\Phi} \mathbf{H}_{\mathrm{BS-RIS}}^{\mathrm{H}} \mathbf{w} \right|^2}{\sum_{j=1}^{K_{\mathrm{u}}} \left| \mathbf{h}_{\mathrm{b},k}^{\mathrm{H}} \boldsymbol{\Phi} \mathbf{H}_{\mathrm{BS-RIS}}^{\mathrm{H}} \mathbf{v}_j \right|^2 + \sigma^2}. \tag{7.47}$$

Ideal Polarization

In this case, $\chi = 0$ and the polarized signals are perfectly distinguished from each other. Therefore, the composite channel $\tilde{\mathbf{H}}_g$ will reduce to $\tilde{\mathbf{H}}_g = \begin{bmatrix} \tilde{\mathbf{h}}_g^{\mathrm{v}} & \mathbf{0} \\ \mathbf{0} & \tilde{\mathbf{h}}_g^{\mathrm{h}} \end{bmatrix}$, $g \in \{\mathrm{u}, \mathrm{b}\}$. The received signal at the jth UE in the unicast group is expressed as

$$y_{\mathrm{u},j}^{\mathrm{v}} = (\mathbf{h}_{\mathrm{u},j}^{\mathrm{v}})^{\mathrm{H}} \boldsymbol{\Phi}^{\mathrm{v}} (\mathbf{H}_{\mathrm{BS-RIS}}^{\mathrm{v}})^{\mathrm{H}} \mathbf{p}_j^{\mathrm{v}} \mathbf{v}_j s_j + (\mathbf{h}_{\mathrm{u},j}^{\mathrm{v}})^{\mathrm{H}} \boldsymbol{\Phi}^{\mathrm{v}} (\mathbf{H}_{\mathrm{BS-RIS}}^{\mathrm{v}})^{\mathrm{H}} \sum_{i=1,i\neq j}^{K_{\mathrm{u}}} \mathbf{p}_i^{\mathrm{v}} \mathbf{v}_i s_i + n_{\mathrm{u},j}^{\mathrm{v}}. \tag{7.48}$$

For the broadcasting service, the received signal at the kth UE is expressed as

$$\begin{aligned} y_{\mathrm{b},k}^{\mathrm{h}} &= (\mathbf{h}_{\mathrm{b},k}^{\mathrm{h}})^{\mathrm{H}} \boldsymbol{\Phi}^{\mathrm{h}} (\mathbf{H}_{\mathrm{BS-RIS}}^{\mathrm{h}})^{\mathrm{H}} \mathbf{P}^{\mathrm{h}} \mathbf{x}^{\mathrm{h}} + n_{\mathrm{b},k}^{\mathrm{h}} \\ &= (\mathbf{h}_{\mathrm{b},k}^{\mathrm{h}})^{\mathrm{H}} \boldsymbol{\Phi}^{\mathrm{h}} (\mathbf{H}_{\mathrm{BS-RIS}}^{\mathrm{h}})^{\mathrm{H}} \mathbf{p}_k^{\mathrm{h}} \mathbf{w} s + \sum_{i=1,i\neq k}^{K_{\mathrm{b}}} (\mathbf{h}_{\mathrm{b},k}^{\mathrm{h}})^{\mathrm{H}} \boldsymbol{\Phi}^{\mathrm{h}} (\mathbf{H}_{\mathrm{BS-RIS}}^{\mathrm{h}})^{\mathrm{H}} \mathbf{p}_i^{\mathrm{h}} \mathbf{w} s + n_{\mathrm{b},k}^{\mathrm{h}}. \end{aligned} \tag{7.49}$$

Therefore, the SINR at the jth UE in set $\mathcal{K}_{\mathrm{u}}$ is given by

$$\gamma_{\mathrm{u},j} = \frac{\left| (\mathbf{h}_{\mathrm{u},j}^{\mathrm{v}})^{\mathrm{H}} \boldsymbol{\Phi}^{\mathrm{v}} (\mathbf{H}_{\mathrm{BS-RIS}}^{\mathrm{v}})^{\mathrm{H}} \mathbf{p}_j^{\mathrm{v}} \mathbf{v}_j \right|^2}{\sum_{i=1,i\neq j}^{K_{\mathrm{u}}} \left| (\mathbf{h}_{\mathrm{u},j}^{\mathrm{v}})^{\mathrm{H}} \boldsymbol{\Phi}^{\mathrm{v}} (\mathbf{H}_{\mathrm{BS-RIS}}^{\mathrm{v}})^{\mathrm{H}} \mathbf{p}_i^{\mathrm{v}} \mathbf{v}_i \right|^2 + \sigma^2}. \tag{7.50}$$

and the SINR at the kth UE in set $\mathcal{K}_{\mathrm{b}}$ is defined as

$$\gamma_{\mathrm{b},k} = \frac{\left| (\mathbf{h}_{\mathrm{b},k}^{\mathrm{h}})^{\mathrm{H}} \boldsymbol{\Phi}^{\mathrm{h}} (\mathbf{H}_{\mathrm{BS-RIS}}^{\mathrm{h}})^{\mathrm{H}} \mathbf{p}_k^{\mathrm{v}} \mathbf{w} \right|^2}{\sum_{i=1,i\neq k}^{K_{\mathrm{b}}} \left| (\mathbf{h}_{\mathrm{b},k}^{\mathrm{h}})^{\mathrm{H}} \boldsymbol{\Phi}^{\mathrm{h}} (\mathbf{H}_{\mathrm{BS-RIS}}^{\mathrm{h}})^{\mathrm{H}} \mathbf{p}_i^{\mathrm{v}} \mathbf{w} \right|^2 + \sigma^2}. \tag{7.51}$$

For the above systems (i.e., the LDM-based and the one with ideal polarization), the sum-rates are calculated using (7.16), the power consumption is calculated with (7.17), and the EE is calculated via (7.18). The active beamforming design is done using Algorithm 2. For fair comparisons, the locations of the UEs are the same in all scenarios.
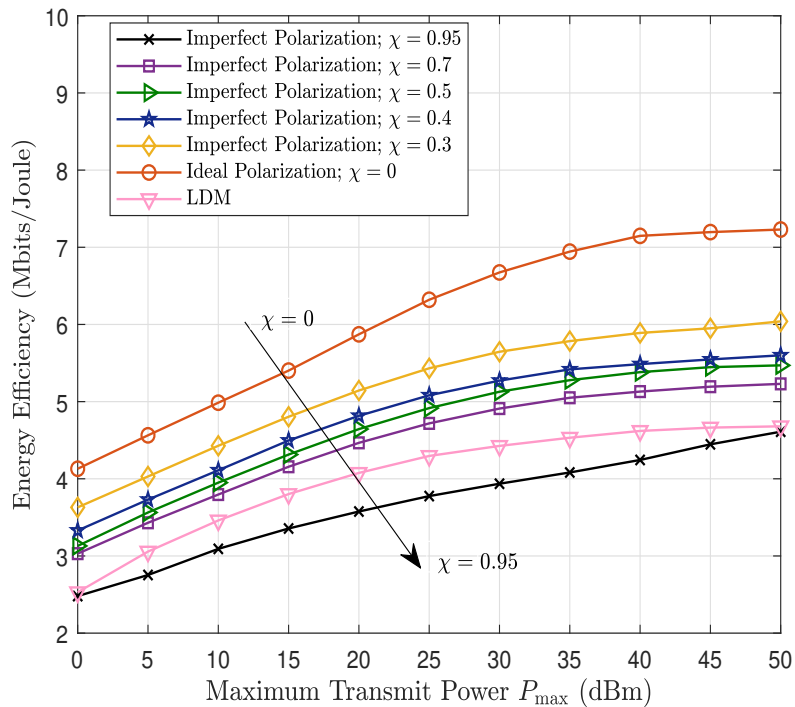
Figure 7.2: Energy efficiency versus the BS's maximum transmit power, with $2M_\text{t} = 16$ **and** $2N = 32$.

Figure 7.2 compares the EE of the three RIS-UAV-assisted systems (i.e, with imperfect polarization, ideal polarization, and LDM) versus the BS's maximum transmit power, for different values of the iXPD parameter χ, while considering fixed numbers of antennas and reflecting elements, i.e., $2N = 32$ and $2M_\text{t} = 16$, and $K_\text{u} = K_\text{b} = 5$ UEs per group. The EE of the systems under comparison increases and then stabilizes as the BS's power P_max increases. This is because EE is not a monotonically increasing function of the transmit power (cf. Eq. (7.18)). When the optimal transmit power is achieved, the excess of power is not used since it will decrease the EE gains. As expected, the system with ideal polarization is more energy efficient than the two others. Indeed, imperfect polarization results in additional interference which makes the signal weaker, hence deteriorating the EE. The plots also illustrate the effect of the level of cross-polar transmissions. The higher the iXPD, the worst are the EE gains. For instance, for $P_\text{max} = 25$ dBm, the EE decreases by 35% as compared to the case when $\chi = 0.95$.

In Fig. 7.3, we study the convergence of the proposed two-stage algorithm in the same three systems as above (i.e, with ideal polarization, imperfect polarization, and LDM). As observed, only few iterations are required for the two-stage algorithm to converge in the case of ideal polarization,
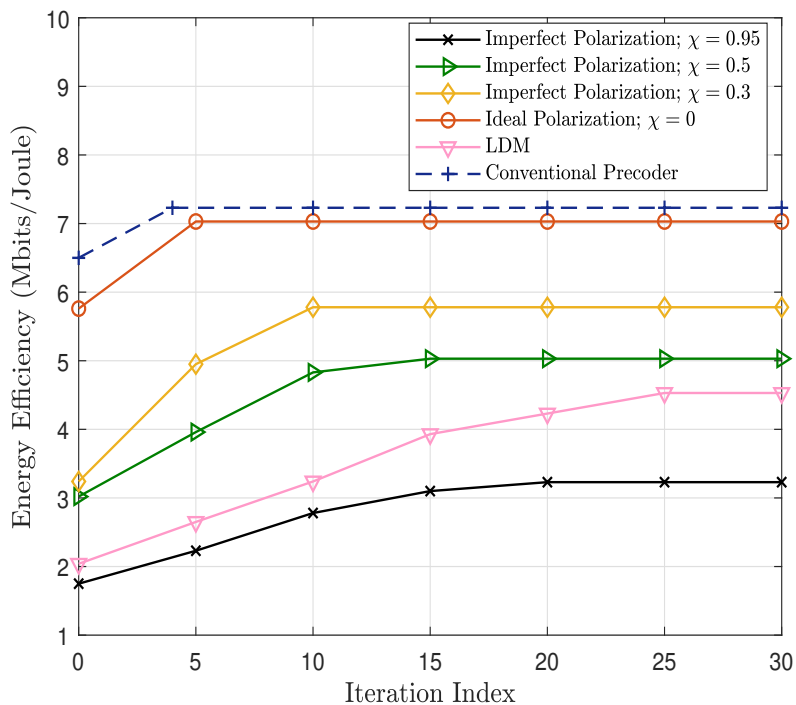
Figure 7.3: Convergence of the proposed algorithm for random channel realizations, with $P_{\max} = 25$ dBm and $2M_{\mathrm{t}} = 16$.

namely, 5 iterations. Although the LDM-based transmission achieves better EE compared to the system with imperfect polarization and $\chi = 0.95$, it requires more iterations to converge. In particular, 25 iterations are needed for the algorithm to converge compared to the case with $\chi = 0.95$ which requires only 20 iterations. This means that the LDM-based scheme is more time-consuming than the polarization-based one. For further comparisons, conventional percoding design based on [125], i.e., directly designing the active beamforming components as described by Algorithm 1 of [125], but with some modification to fit our system model, is added as a benchmark (the phase-shift matrix is designed based on our proposed Algorithm 1). As shown, the performance with the proposed two-stage algorithm under the ideal case is similar to the optimal one (cf. curves in blue and red in Fig. 7.3).

In Fig. 7.4, we investigate the impact of the number of RIS elements, N, on the EE of the three systems (imperfect polarization, ideal polarization, and LDM) for different numbers of BS antennas, namely, $2M_{\mathrm{t}} = 16$ in Fig. 7.4(a), and $2M_{\mathrm{t}} = 64$ in Fig. 7.4(b). Here, we consider $K_{\mathrm{u}} = K_{\mathrm{b}} = 5$ UEs per group. As expected, the EE of all the systems increases with N. In fact, using more RIS elements will enhance the signal strength with less transmit power at the BS, hence leading
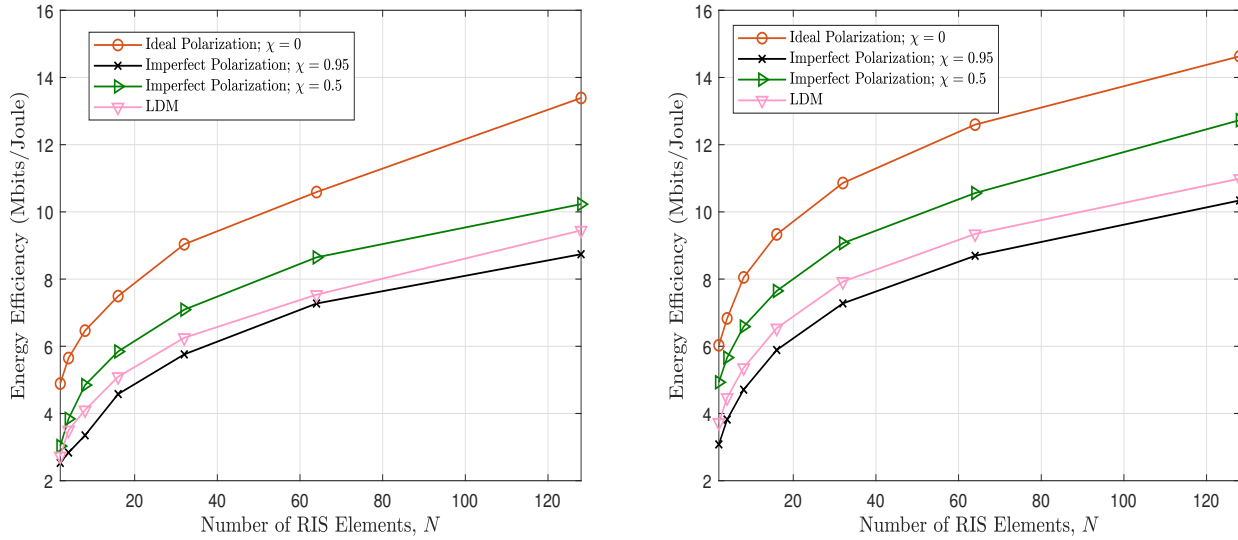
Figure 7.4: Energy efficiency versus the number of RIS elements, with $P_{\max} = 25$ dBm and (a) $2M_{\mathrm{t}} = 16$ **or (b)** $2M_{\mathrm{t}} = 64$**.**

to higher EE gains. Moreover, the simulation results validate that the ideal polarization system is more energy efficient than the two others. Besides, it is observed that the trend of the EE increases with the number of antennas at the BS. In particular, for $N = 64$, the EE gets increased by 15% when the number of antennas goes from $2M_{\mathrm{t}} = 16$ to $2M_{\mathrm{t}} = 64$ (cf. curves in green for the imperfect polarization case in the two figures). This can be explained by the fact that the achieved sum-rate is higher than the power consumption costs.
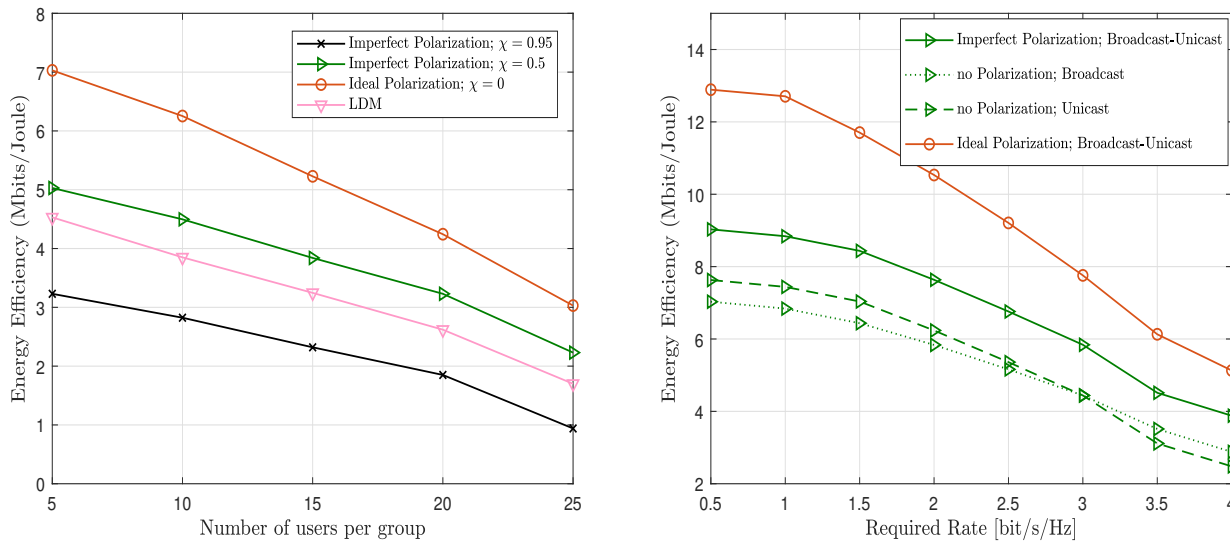
Figure 7.5: (a) Energy efficiency versus the number of users per group, $P_{\max} = 25$ **dBm,** $2M_{\mathrm{t}} = 16$**;** $N = 16$**; (b) Energy efficiency versus the minimum rate requirement of the services** $R_{\min}$**, with** $M_{\mathrm{t}} = 8$ **and** $P_{\max} = 25$**,** $N = 16$**,** $\chi = 0.5$**.**

In Fig. 7.5(a), the EE versus the number of UEs per group (note that here $K_u = K_b$) of the broadcast-unicast communication system with perfect or imperfect polarization is plotted. As expected, an increase in the number of UEs per group decreases the achievable EE. This can be explained by the fact that serving more UEs requires higher transmit power at the BS and that the UEs' hardware static powers become higher. Hence, the total power consumption increases and the EE will drastically decrease. The curves here also validate that the RIS-UAV system with ideal polarization outperforms the LDM-based system.

Finally, Fig. 7.5(b) illustrates the EE versus the rate requirement for different schemes, namely, joint broadcast-unicast with ideal or imperfect polarization, and special cases with a single service (unicast or broadcast). When the single service is unicast, then $R_{b,min} = 0$ bps/Hz, and when the broadcasting is the unique service, then $R_{u,min} = 0$ bps/Hz. For the joint broadcast-unicast system, the rate requirement pertaining to the unicast is set to $R_{u,min} = 0.5$ bps/Hz, and we vary the required rate in the broadcasting, i.e., $R_{b,min}$. In this case, high EE gains can be achieved when $R_{b,min}$ is low. Obviously, when the rate requirements are higher, the resources are consumed to satisfy the broadcasting constraints. Moreover, an increase in the rate requirements of the broadcasting service reduces the achievable EE, as the BS will need higher transmit power to meet the UEs' demands and, thus, higher power consumption will follow. We note that the polarization based system achieves higher gains compared to the single service case (cf. the green curves in Fig. 7.5(b)). Also, the curves validate that ideal polarization leads to more energy-efficient operation compared to the imperfect polarization case, even when the required rates are higher (cf. red and green curves in the figure).

7.5   Concluding Remarks

In conclusion, this chapter proposed a framework for polarization-based joint broadcast-unicast communications via aerial RIS. We focused on maximizing the energy efficiency of the system by properly designing the active and passive beamforming matrices. The energy-efficiency maximization problem being non-convex, a low-complexity two-stage algorithm based on alternating optimization was proposed. First, the passive beamforming matrix of the UAV-mounted dual-polarized RIS was designed. Then, the dual-structured beamforming approach was used to design the active beamforming at the BS. Particularly, the prebeamforming matrix was designed based on the interior

point method, and the beamforming matrices pertaining to the unicasting and broadcasting services were obtained based on zero-forcing technique and successive convex approximation, respectively. Numerical results were provided, with analysis of the effects of the main system parameters on the energy efficiency performance compared to communications based on layered division multiplexing (LDM). The polarization based RIS-UAV assisted communication can achieve significant gains compared to the LDM-based system.

Part III

RIS-Aided Simultaneous Wireless Information and Power Transfer

Unlike the previous parts that deal only with either power transfer or information transfer, this part focuses on the SWIPT system assisted with RIS. The main objective is to design a novel RIS-aided SWIPT system based on the null space.

Chapter 8

RIS Aided SWIPT: A Null Space Based Design

8.1 Introduction

The integration of RIS with SWIPT was first proposed in [51–53]. For instance, in [52], the weighted sum power maximization problem was studied for a RIS-aided SWIPT system, without additional dedicated energy-carrying signals. In [51], the minimum rates for the IRs maximization problem were formulated and solved under ideal and non-ideal channel conditions based on an iterative algorithm. In [53], the weighted sum rate is maximized under the maximum transmit power constraints of the APs and the minimum total energy harvesting power constraints of the ERs, by jointly optimizing the active beamforming matrices and the passive RIS reflection matrix for cell-free SWIPT MIMO system.

Although the above studies are beneficial for understanding the theoretical bounds of RIS-aided SWIPT systems, there are certain challenges when it comes to implementing SWIPT technology in practice. For instance, when the channel state information (CSI) to the energy receivers is unavailable at the base station/ access point, beamforming is impossible and the only way to benefit from multiple antennas is to use the excess degrees of freedom that are available; notably, to enhance SWIPT performance by transmitting energy signal in the channel null space.

It is worth noting that this work is different from the above prior works that investigated the joint active and passive beamforming in RIS-assisted SWIPT systems. Firstly, this contribution considers the multi-objective maximization of RIS-assisted SWIPT, in which the multi-antenna AP beamforms information signals to the IRs set and uses the null space of the channel between the AP and the IRs to transmit energy signal to the ERs. To the best of our knowledge, this is the first endeavor for exploiting the degree of freedom of the null space to send energy signals in RIS-aided SWIPT. The main contributions can be summarized as follows:

- We exploit the unused degree of freedom of the composite full channel matrix between the access point (AP) and the IRs to transmit the energy signal in the null space. For that, the singular value decomposition (SVD) is used to determine the null space of the matrix and the energy signal is chosen as the eigenvector corresponding to the largest eigenvalue of the projected version of the channel in the null space.

- We aim to study the balance between the harvested energy at the ERs and the total sum rate of the IRs. Therefore, we take advantage of the multi-objective optimization (MOO) framework and the weighted Tchebycheff approach to formulate the equivalent sum rates (ESR) maximization problem. A MOO problem is proposed to jointly design the active transmit information beamforming matrix at the AP and the passive beamforming matrix at the RIS, subject to the minimum required transmission rate constraints at the IRs, the minimum required EH values at the ERs, the maximum transmit power constraint at the AP, and the unit modulus phase-shift at the RIS. To solve the highly non-convex formulated maximization problem, an efficient two-layer algorithm based on alternating optimization techniques is proposed. In particular, the RIS passive beamforming matrix is designed in the first layer based on semi-definite relaxation (SDR) and random Gaussian randomization after transforming the non-convex QCQP problem to the convex semi-definite programming (SDP) form. In the second layer, the active beamforming at the AP is designed based on a low-complexity zero forcing (ZF) technique.

- Numerical results are conducted to evaluate the proposed design performance in comparison to an equivalent system but operating with conventional SWIPT with or without RIS, and other schemes with only information beamforming with RIS assistance. Our findings show that the proposed RIS-assisted SWIPT system with both information and energy signals achieves

significant performance gains over the benchmark schemes with or without RIS deployed and/or without dedicated energy signals used.

The remainder of this chapter is organized as follows. Section 8.2 presents the RIS-assisted SWIPT model. In Section 8.3, a non-convex MOO problem is formulated and a two-layer algorithm is proposed to tackle the problem. Section 8.4 presents the special case of total harvested energy maximization. The numerical results are presented in Section 8.5, followed by conclusions in Section 8.6.

8.2 The RIS-Aided SWIPT System

The RIS-aided downlik multi-user SWIPT system considered in this chapter is shown in Fig. 8.1, where an access point (AP) equipped with $M_{\mathrm{t}} \geq 1$ antennas is mandated to transmit information to K_{I} information receivers (IRs), and simultaneously transfer energy to K_{E} energy receivers (ERs), equipped with single antennas and operating over the same frequency band. A RIS composed of N reflecting elements is deployed to assist the information transmission and energy transfer in the SWIPT system.[1] The set of IRs is denoted by $\mathcal{K}_{\mathrm{I}} = \{1, \cdots, K_{\mathrm{I}}\}$ and $\mathcal{K}_{\mathrm{E}} = \{1, \cdots, K_{\mathrm{E}}\}$ is the index set of the ERs. We assume that a given receiver is not able to decode information and to harvest energy simultaneously. Therefore, $\mathcal{K}_{\mathrm{I}} \cap \mathcal{K}_{\mathrm{E}} = \emptyset$ and $K_{\mathrm{I}} + K_{\mathrm{E}} = K$.[2]

Let us denote by $\mathbf{H}_{\mathrm{AP-RIS}} \in \mathbb{C}^{M_{\mathrm{t}} \times N}$, $\mathbf{H}_{\mathrm{I}} \in \mathbb{C}^{N \times K_{\mathrm{I}}}$ and $\mathbf{H}_{\mathrm{E}} \in \mathbb{C}^{N \times K_{\mathrm{E}}}$, the channel spanning from the AP to the RIS, the channel from the RIS to the set of IRs $\mathcal{K}_{\mathrm{I}}$, and the channel from the RIS to the set of ERs $\mathcal{K}_{\mathrm{E}}$, respectively. We assume that all channels experience block fading and are independent from each other. The channel gains include the effects of the path loss and the fast fading. The Rician fading channel model is considered for the AP-RIS and RIS-device links [91].

The channel gain matrix of the AP-RIS link is given by

$$\mathbf{H}_{\mathrm{AP-RIS}} = \mathbf{D}^{\frac{1}{2}} \left(\sqrt{\frac{\mu}{1+\mu}} \overline{\mathbf{H}} + \sqrt{\frac{1}{1+\mu}} \hat{\mathbf{H}} \right), \tag{8.1}$$

---

[1]A smart controller, which communicates with the AP to exchange information via a separate link, controls the phase shifts of the passive reflecting elements of the RIS.

[2]For simplicity of the formulation, we hereafter assume that a user belongs to either the harvesting set or the information set and that both sets are known and fixed.
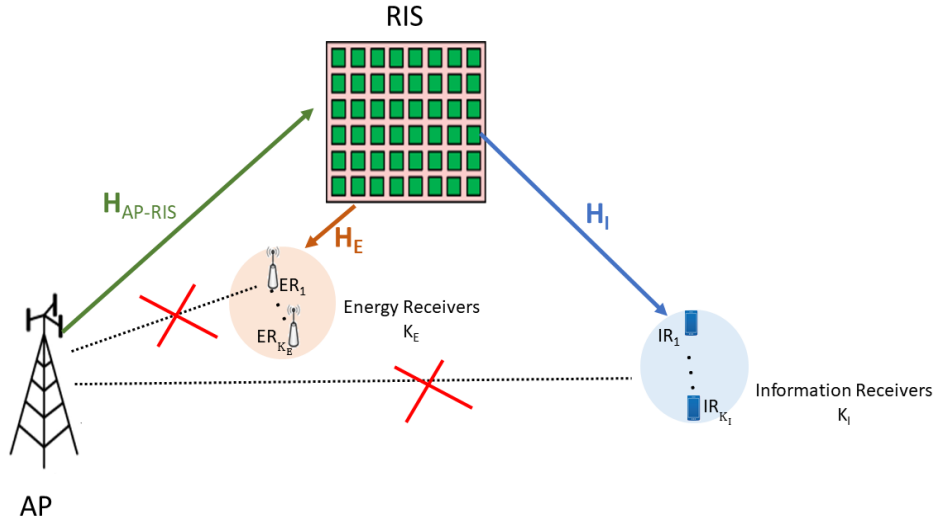
Figure 8.1: The RIS aided downlink multi-user MISO SWIPT system.

where μ is the Rice factor, $\overline{\mathbf{H}}$ is the line-of-sight (LoS) component matrix, and $\hat{\mathbf{H}}$ is the non line-of-sight (NLoS) component matrix, the elements of which are i.i.d. complex Gaussian random variables having zero mean and unit variance. Finally, matrix $\mathbf{D}$ in (8.1) is diagonal, where each element $[\mathbf{D}]_{k,k} = d^{-\alpha}$, with d indicating the Euclidean distance between the AP and the RIS, and α denoting the path-loss exponent [113].

The complex channel vector between the RIS and $\mathrm{IR}_{\mathrm{I},j}$ is given by

$$\mathbf{h}_{\mathrm{I},j} = \sqrt{d_{\mathrm{I},j}^{-\beta}} \left(\sqrt{\frac{\mu_{\mathrm{I}}}{1+\mu_{\mathrm{I}}}} \overline{\mathbf{h}}_{\mathrm{I},j} + \sqrt{\frac{1}{1+\mu_{\mathrm{I}}}} \hat{\mathbf{h}}_{\mathrm{I},j} \right), \tag{8.2}$$

where μ_{I} is the Rice factor, $\overline{\mathbf{h}}_{\mathrm{I},j}$ is the LoS component vector, and $\hat{\mathbf{h}}_{\mathrm{I},j}$ is NLoS component vector whose elements are i.i.d. complex Gaussian random variables with zero mean and unit variance. Parameter $d_{\mathrm{I},j}$ denotes the Euclidean distance between the RIS and the jth receiver in set $\mathcal{K}_{\mathrm{I}}$, and β is the path-loss exponent.

The complex channel vector between the RIS and $\mathrm{ER}_{\mathrm{E},k}$ is defined as

$$\mathbf{h}_{\mathrm{E},k} = \sqrt{d_{\mathrm{E},k}^{-\beta}} \left(\sqrt{\frac{\mu_{\mathrm{E}}}{1+\mu_{\mathrm{E}}}} \overline{\mathbf{h}}_{\mathrm{E},k} + \sqrt{\frac{1}{1+\mu_{\mathrm{E}}}} \hat{\mathbf{h}}_{\mathrm{E},k} \right), \tag{8.3}$$

where μ_E is the Rice factor, $\overline{\mathbf{h}}_{E,k}$ is the LoS component vector, $\hat{\mathbf{h}}_{E,k}$ is the NLoS component vector whose elements are i.i.d. complex Gaussian random variables with zero mean and unit variance. $d_{E,k}$ is the Euclidean distance between the RIS and the kth ER in set $\mathcal{K}_E$.

Let us denote by $\tilde{\mathbf{H}}_I$, the composite full channel matrix between the AP and the set of IRs.[3] The channel is expressed as

$$\tilde{\mathbf{H}}_I = \mathbf{H}_I^H \mathbf{\Phi} \mathbf{H}_{\text{AP}-\text{RIS}}^H, \tag{8.4}$$

where $\mathbf{\Phi}$ is a diagonal matrix accounting for the reflection matrix of the RIS and defined as $\mathbf{\Phi} = \text{diag}(\phi_1, \cdots, \phi_n)$, in which $\phi_n = a_n e^{j\theta_n}$, $\forall n = 1, \cdots, N$, with $\theta_n \in [0, 2\pi)$ and $a_n \in [0, 1]$ denote the phase shift and the amplitude reflection coefficient associated with the nth passive element of the RIS, respectively.[4]

We assume that the AP does not have CSI to these ERs, therefore, it cannot beamform to them. Therefore, the AP simultaneously transmits information signals to all K_I IRs via beamforming and transfers energy signal to the ERs using the null space of the composite channel between the AP-RIS-IRs noted as $\tilde{\mathbf{H}}_I$. The fundamental feature of massive MIMO that makes this possible is that with M_t antennas and beamforming to K_I devices, there are $M_t - K_I$ unused degrees of freedom. Here, the $M_t - K_I$ degrees of freedom are exploited to transmit the energy signal in a subspace orthogonal to the channel collectively seen by the K_I receivers [44]. Therefore, the part of the transmitted vector $\mathbf{x}$ which falls in the null space of the matrix $\tilde{\mathbf{H}}_I$ will be invisible by all IRs in the set $\mathcal{K}_I$. Hence, the AP may add energy signal to the ERs of the set $\mathcal{K}_E$. Let $\{\mathbf{u}\}$ be a sequence of M_t-vectors intended for the ERs. Therefore, the transmit signal at the AP is given by [44]

$$\mathbf{x} = \sum_{j=1}^{K_I} \mathbf{v}_j s_j^I + \mathbf{\Pi}_{\tilde{\mathbf{H}}_I}^{\perp} \mathbf{u}, \tag{8.5}$$

where $s_j^I \approx \mathcal{CN}(0, 1)$ denote the information signal and is independent and identically distributed (i.i.d) circularly symmetric complex Gaussian (CSCG) random variable with zero mean and unit variance. $\mathbf{v}_j$ is the information beamforming vector to the jth IR in $\mathcal{K}_I$. $\mathbf{\Pi}_{\tilde{\mathbf{H}}_I}^{\perp} = \mathbf{I} - \mathbf{\Pi}_{\tilde{\mathbf{H}}_I}$, where $\mathbf{\Pi}_{\tilde{\mathbf{H}}_I} = \tilde{\mathbf{H}}_I (\tilde{\mathbf{H}}_I^H \tilde{\mathbf{H}}_I)^{-1} \tilde{\mathbf{H}}_I^H$ denotes the projection onto the column space of $\tilde{\mathbf{H}}_I$ where $\mathbf{u}$ is normalized

---

[3] We assume that the channel state information (CSI) is available at the AP. Channel estimation methods, see e.g. [2], can be applied to acquire the CSI of the receivers independently.

[4] In practice, each element of the RIS is usually designed to maximize the signal reflection. Hereafter, we assume that $a_n = 1$, $\forall n = 1, \cdots, N$, for simplicity.

such that $\mathbb{E}[\|\mathbf{\Pi}_{\tilde{\mathbf{H}}_I}^{\perp}\mathbf{u}\|^2] = 1$. We note that the first term and the second term of (8.5) are statistically uncorrelated.

Construction of u

Recall that the energy signal lies in the null space of the composite channel AP-RIS-IRs. Threrefore, let us assume that $\mathbf{u} \in \mathbb{C}^{M' \times 1}$ is confined to a subspace of dimension M', with $M' \leq M_t - K_I$, and is generated at the AP as random sequence with zero mean and covariance $\mathbf{U} = \mathbb{E}[\mathbf{u}\mathbf{u}^H]$. Recall that $\mathbf{u}$ lies into the null space of $\tilde{\mathbf{H}}_I$, noted as $\tilde{\mathbf{H}}_{Null}$ and can be obtained by singular value decomposition (SVD) [5] of $\tilde{\mathbf{H}}_I$ as $\tilde{\mathbf{H}}_I = \mathbf{U}_L \mathbf{\Sigma} \mathbf{U}_R$. The null space $\tilde{\mathbf{H}}_{Null}$ is expressed as depends

$$\tilde{\mathbf{H}}_{Null} = \mathbf{U}_R \in \mathbb{C}^{M_t \times (M_t - (K_I - r + 2))}, \tag{8.6}$$

r show the number of available column vectors of the null space of the channel $\tilde{\mathbf{H}}_I \in \mathbb{C}^{M_t \times K_I}$. Initially, r is equal to K_I. Let us define $\mathbf{G}_N$, which is the projected version of $\tilde{\mathbf{H}}_E$ onto the null space of the composite channel to the information devices, as

$$\mathbf{G}_N = \tilde{\mathbf{H}}_E \tilde{\mathbf{H}}_{Null} \tilde{\mathbf{H}}_{Null}^H. \tag{8.7}$$

Therefore, $\mathbf{u}$ is obtained as the eigenvector corresponding to the largest eigenvalue of $\mathbf{G}_N \mathbf{G}_N^H$, i.e.,

$$\mathbf{u} = \text{eig}(\mathbf{G}_N \mathbf{G}_N^H), \tag{8.8}$$

As the AP has full knowledge of the channel state information of the jth IR in the set $\mathcal{K}_I$, and the energy signal lies in the null space which is a subspace orthogonal to the channel of the IRs, the signal will not be seen by the IRs, then

$$\mathbf{h}_{I,j}^H \mathbf{\Phi} \mathbf{H}_{AP-RIS}^H \mathbf{\Pi}_{\tilde{\mathbf{H}}_I}^{\perp} = 0. \tag{8.9}$$

Therefore, the received signal then at the jth IR is written as

$$y_j = \mathbf{h}_{I,j}^H \mathbf{\Phi} \mathbf{H}_{AP-RIS}^H \sum_{j=1}^{K_I} \mathbf{v}_j s_j^I + w_j, \tag{8.10}$$

---

[5]The null space of $\tilde{\mathbf{H}}_I$ can be obtained using Gram-Schmidt process or matrix decomposition methods. For simplicity, singular value decomposition is utilized.

where $w_j \approx \mathcal{CN}(0, \sigma_j^2)$, is the additive white Gaussian noise (AWGN) with zero mean and variance $\sigma_j^2 = N_0 B, \forall j \in \{1, \cdots, K_I\}$, with N_0 denoting the noise power over the total transmission bandwidth B.

We assume that the unintended data signals are treated as interference, the received SINR at the jth IR in $\mathcal{K}_I$ is given by

$$\gamma_j = \frac{|\mathbf{h}_{I,j}^H \mathbf{\Phi} \mathbf{H}_{AP-RIS}^H \mathbf{v}_j|^2}{\sum\limits_{i=1, i \neq j}^{K_I} |\mathbf{h}_{I,j}^H \mathbf{\Phi} \mathbf{H}_{AP-RIS}^H \mathbf{v}_i|^2 + \sigma_j^2}. \tag{8.11}$$

The achievable transmission rate for j^{th} IR can be expressed as

$$R_j^I = \log_2(1 + \gamma_j). \tag{8.12}$$

Therefore, the total transmission rate is given by

$$R^I = \sum_{j=1}^{K_I} R_j^I = \sum_{j=1}^{K_I} \log_2(1 + \gamma_j). \tag{8.13}$$

On the other hand, an ER will not see the effect of the projection $\mathbf{\Pi}_{\tilde{\mathbf{H}}_I}$ explicitly [44]. Instead, the ER will effectively see $\mathbf{u}$ transmitted over a channel with response $\mathbf{\Pi}_{\tilde{\mathbf{H}}_I}^{\perp} \tilde{\mathbf{h}}_{E,k}$. The vector $\tilde{\mathbf{h}}_{E,k}$ will be unknown to the AP anyway, and so will be considered as $\mathbf{\Pi}_{\tilde{\mathbf{H}}_I}^{\perp} \tilde{\mathbf{h}}_{E,k}$. As such, the received signal at the kth ER in the set $\mathcal{K}_E$ is given by

$$
\begin{aligned}
y_k &= \mathbf{h}_{E,k}^H \mathbf{\Phi} \mathbf{H}_{AP-RIS}^H \mathbf{\Pi}_{\tilde{\mathbf{H}}_I}^{\perp} \mathbf{u} + \mathbf{h}_{E,k}^H \mathbf{\Phi} \mathbf{H}_{AP-RIS}^H \sum_{j=1}^{K_I} \mathbf{v}_j s_j + w_k \\
&= \mathbf{h}_{E,k}^H \mathbf{\Phi} \mathbf{H}_{AP-RIS}^H \mathbf{u} + \mathbf{h}_{E,k}^H \mathbf{\Phi} \mathbf{H}_{AP-RIS}^H \sum_{j=1}^{K_I} \mathbf{v}_j s_j + w_k,
\end{aligned} \tag{8.14}
$$

where $w_k \approx \mathcal{CN}(0, \sigma_k^2)$ is the AWGN with zero mean and variance $\sigma_k^2 = N_0 B, \forall k \in \{1, \cdots, K_E\}$, with N_0 denoting the noise power over the total transmission bandwidth B.

The total transmit power at the AP is expressed as $\mathbb{E}[|\mathbf{x}|^2] = \sum_{j=1}^{K_I} \|\mathbf{v}_j\|^2 + \text{tr}(\mathbf{U})$. Nevertheless, thanks to the law of energy conservation, it can be assumed that the total harvested power the kth

ER in $\mathcal{K}_{\mathrm{E}}$, denoted by $Q_k(\mathbf{V}, \mathbf{U}, \boldsymbol{\Phi})$, is given as follows:

$$Q_k(\mathbf{V}, \mathbf{U}, \boldsymbol{\Phi}) = \eta \mathbb{E}[|\mathbf{h}_{\mathrm{E},k}^{\mathrm{H}} \boldsymbol{\Phi} \mathbf{H}_{\mathrm{AP-RIS}}^{\mathrm{H}} \mathbf{x}|^2]$$
$$= \eta \left(\left(\mathbf{h}_{\mathrm{E},k}^{\mathrm{H}} \boldsymbol{\Phi} \mathbf{H}_{\mathrm{AP-RIS}}^{\mathrm{H}} \right)^{\mathrm{H}} \mathbf{U} \left(\mathbf{h}_{\mathrm{E},k}^{\mathrm{H}} \boldsymbol{\Phi} \mathbf{H}_{\mathrm{AP-RIS}}^{\mathrm{H}} \right) + \sum_{j=1}^{K_{\mathrm{I}}} |\mathbf{h}_{\mathrm{E},k}^{\mathrm{H}} \boldsymbol{\Phi} \mathbf{H}_{\mathrm{AP-RIS}}^{\mathrm{H}} \mathbf{v}_j|^2 \right), \quad (8.15)$$

where $\mathbf{V} = [\mathbf{v}_1, \cdots, \mathbf{v}_{K_{\mathrm{I}}}]^{\mathrm{T}}$ is the beamforming matrix to the IRs, η is a constant that accounts for the loss in the energy transducer for converting the harvested energy to electrical energy to be stored, in this work, it is assumed that each ER_k, $k \in \mathcal{K}_{\mathrm{E}}$ has an identical energy conversion coefficient $0 < \eta < 1$. Recall that the covariance matrix $\mathbf{U} = \mathbb{E}[\mathbf{u}\mathbf{u}^{\mathrm{H}}]$ can be fixed by construction as the $\mathbf{u}$ is constructed to lie in the null space. Then, the total harvested power by all ERs is given by

$$Q = \sum_{k=1}^{K_{\mathrm{E}}} Q_k(\mathbf{V}, \boldsymbol{\Phi}). \quad (8.16)$$

8.3 Equivalent Sum-Rate Maximization

Our objective is to jointly optimize the reflection coefficient matrix of the RIS and the active beamforming vectors at the AP in order to maximize the total sum rate of the IRs and the total harvested energy at the ERs under constraints on the minimum required rates, the minimum harvested energy demands, and the AP's maximum transmit power. Therefore, the optimization problem is formulated as follows:

$$(P1) \quad \underset{\boldsymbol{\Phi}, \mathbf{V}}{\mathrm{maximize}} \ (Q, R^{\mathrm{I}})$$

$$\text{subject to:}$$

$$\begin{aligned}
(\mathrm{C}1) \quad & |\phi_n| = 1, \ \forall n \in \{1, \cdots, N\} \\
(\mathrm{C}2) \quad & \log_2 (1 + \gamma_j) \geq R_{\mathrm{I,min}}, \ \forall j \in \mathcal{K}_{\mathrm{I}} \\
(\mathrm{C}3) \quad & Q_k \geq Q_{\mathrm{th}}, \ \forall k \in \mathcal{K}_{\mathrm{E}}, \\
(\mathrm{C}4) \quad & \sum_{j=1}^{K_{\mathrm{I}}} \|\mathbf{v}_j\|^2 + \mathrm{tr}(\mathbf{U}) \leq P_{\mathrm{max}},
\end{aligned} \quad (8.17)$$

where P_{max} is the maximum transmit power at the AP. The constraint (C1) ensure that each reflecting element in the RIS does not change the amplitude of the incident signal, indicating full reflection efficiency [91]. The inequality in (C2) constitutes the minimum required rate for the IRs,

where $R_{\mathrm{I,min}}$ is the minimum required rate by the jth IR. The constraint (C3) ensure that the harvested power by each ER should be higher than a predefined threshold Q_{th}. (C4) is used to guarantee the maximum power budget. We assume that this optimization problem is solved at the AP which posses the knowledge of the CSI of the IRs' related links and other related parameters such as P_{max}, Q_{th} and $R_{\mathrm{I,min}}$.

The formulated problem is a constrained multi-objective optimization (MOO) problem, aiming at jointly maximizing two conflicting objective functions, i.e., Q and R^{I}. Therefore, it can be often solved by combining its multiple objectives into a single objective function as shown in [54, 126]. This approach is in general known as the weighted sum or Tchebycheff approach. Therefore, (8.17) can be converted to a single objective optimization problem. For that, the total achievable rate transformed from ER is expressed as

$$R^{\mathrm{E}} = \sum_{k=1}^{K_{\mathrm{E}}} R_k^{\mathrm{E}}, \tag{8.18}$$

where R_k^{E} represents the achievable rate that is transformed from the harvested energy that can be stored in the battery of device k and will be used to perform data transmission in the next time slots. It can be expressed as $R_k^{\mathrm{E}} = \log_2\left(1 + \frac{\xi Q_k}{\sigma_k^2}\right)$, with ξ denotes the efficiency converting from battery power to RF [126].

After applying this transformation and by adopting the weighted sum method, the objective function of our optimization problem is recast as

$$R = \nu_{\mathrm{I}} R^{\mathrm{I}} + \nu_{\mathrm{E}} R^{\mathrm{E}}. \tag{8.19}$$

where $\nu_{\mathrm{E}} > 0$ and $\nu_{\mathrm{I}} > 0$ are the weights of the two objective functions. The new objective function is called the "equivalent sum rate" (ESR) [54].

To further simplify the problem, we here normalize $\nu = \nu_{\mathrm{E}}/\nu_{\mathrm{I}}$. Therefore, the objective function is rewritten as $R = R^{\mathrm{I}} + \nu R^{\mathrm{E}}$. Without loss of generality, we consider ν as a constant in our optimization problem. As a result, the transformed optimization problem can be reformulated as

follows:

$$(P2) \quad \underset{\mathbf{\Phi}, \mathbf{V}}{\text{maximize}} \ R$$

$$\text{subject to:}$$

$$\begin{aligned}
&(\text{C1}) \quad |\phi_n| = 1, \ \forall n \in \{1, \cdots, N\} \\
&(\text{C2}) \quad \log_2\left(1 + \gamma_j\right) \geq R_{\text{I,min}}, \ \forall j \in \mathcal{K}_{\text{I}} \\
&(\text{C3}) \quad Q_k \geq Q_{\text{th}}, \ \forall k \in \mathcal{K}_{\text{E}} \\
&(\text{C4}) \quad \sum_{j=1}^{K_{\text{I}}} \|\mathbf{v}_j\|^2 + \text{tr}(\mathbf{U}) \leq P_{\text{max}}.
\end{aligned}$$

(8.20)

The considered ESR optimization problem is non-convex, since the objective function R is neither convex nor concave w.r.t. $\mathbf{V}$ and $\mathbf{\Phi}$. It should be noted that all the constraints are convex with respect to $\mathbf{V}$ but the (C1) is non-convex. Consequently, problem (P2) is a non-convex problem. In general, the solution is nontrivial and cannot be obtained directly. To solve this problem, we rely on the alternating optimization techniques [91]. As a result, an efficient iterative algorithm is developed by decomposing the optimization problem into two sub-problems and solving them iteratively. As such, we separate the active and passive beamforming design to facilitate possible implementation in practice. In the first layer, the focus will be on the design of the optimal passive beamforming matrix $\mathbf{\Phi}$ at the RIS. In the second layer, the problem of designing the active beamforming matrix $\mathbf{V}$ will be tackled.

The Passive Beamforming Design

For fixed active beamforming matrix at the AP, i.e., $\mathbf{V} = \mathbf{V}^{\text{opt}}$, we focus on optimizing the phase shift matrix $\mathbf{\Phi}$ at the RIS. By dropping the terms that are independent of $\mathbf{\Phi}$, and with further manipulation to the objective function and the constraint (C2) and (C3) such as $\mathbf{h}_{\text{E},k}^{\text{H}} \mathbf{\Phi} \mathbf{H}_{\text{AP}-\text{RIS}} \mathbf{u} = \phi^{\text{H}} \mathbf{a}_k$, $\mathbf{h}_{\text{E},k}^{\text{H}} \mathbf{\Phi} \mathbf{H}_{\text{AP}-\text{RIS}} \mathbf{v}_j^{\text{opt}} = \phi^{\text{H}} \mathbf{b}_j$, where $\phi = [\phi_1, \cdots, \phi_N]^{\text{H}}$, $\phi_n, \forall n = 1, \cdots, N$, $\mathbf{a}_k = \text{diag}(\mathbf{h}_{\text{E},k}^{\text{H}}) \mathbf{H}_{\text{AP}-\text{RIS}} \mathbf{u}$, $\mathbf{b}_{j,k} = \text{diag}(\mathbf{h}_{\text{E},k}^{\text{H}}) \mathbf{H}_{\text{AP}-\text{RIS}} \mathbf{v}_j^{\text{opt}}$, and $\mathbf{c}_j = \text{diag}(\mathbf{h}_{\text{I},j}^{\text{H}}) \mathbf{H}_{\text{AP}-\text{RIS}} \mathbf{v}_j^{\text{opt}}$. Since the $\log_2$ function is a mono-

tonic increasing one, maximizing R is reduced to maximize $\nu\xi\sum_{k=1}^{K_E} Q_k + \sum_{j=1}^{K_I} |\mathbf{h}_{I,j}^H \boldsymbol{\Phi}\mathbf{H}_{AP-RIS}\mathbf{v_j}^{opt}|^2$. Problem (8.20) is reduced to

$$
(P3) \ \underset{\phi}{\text{maximize}} \ \nu\xi\sum_{k=1}^{K_E}\left(\|\phi^H\mathbf{a}_k\|^2 + \sum_{j=1}^{K_I}|\phi^H\mathbf{b}_{j,k}|^2\right) + \sum_{j=1}^{K_I}|\phi^H\mathbf{c}_j|^2
$$

subject to:

    (C1) $|\phi_n| = 1,, \ \forall n \in \{1, \cdots, N\}$

    (C2) $\frac{\phi^H\mathbf{c}_j}{\sum_{i=1,i\neq j}^{K_I}|\phi^H\mathbf{c}_i|^2+\sigma_j^2} \geq 2^{R_{I,min}-1}, \ \forall j \in \mathcal{K}_I$

    (C3) $Q_k \geq Q_{th}, \ \forall k \in \mathcal{K}_E.$

$$(8.21)$$

It is obvious that the objective function of (8.21) is convex with respect to ϕ. However, the constraints (C1)–(C3) are non-convex. Since ϕ is involved in both the objective function and the constraints, the conventional successive convex approximation technique cannot be applied directly to the non-convex QCQP problem. Hence, further manipulations are required to transform the non-convex QCQP problem to the SDP form that can be solved by applying the semi-definite relaxation (SDR) techniques [97]. For that, let us denote by $\tilde{\phi} = \begin{bmatrix} \phi \\ t \end{bmatrix}$, $\mathbf{R}_E = \begin{bmatrix} \mathbf{a}_k\mathbf{a}_k^H & 0 \\ 0 & 0 \end{bmatrix}$; $\mathbf{R}_I = \begin{bmatrix} \mathbf{c}_j\mathbf{c}_j^H & 0 \\ 0 & 0 \end{bmatrix}$, $\mathbf{R} = \begin{bmatrix} \mathbf{b}_{j,k}\mathbf{b}_{j,k}^H & 0 \\ 0 & 0 \end{bmatrix}$, where t is an auxiliary optimization variable included here. It is noteworthy that $\tilde{\phi}^H\mathbf{R}_E\tilde{\phi} = \text{Tr}(\mathbf{R}_E\tilde{\phi}\tilde{\phi}^H)$ and $\tilde{\phi}^H\mathbf{R}_I\tilde{\phi} = \text{Tr}(\mathbf{R}_I\tilde{\phi}\tilde{\phi}^H)$. Let us define $\mathbf{W} = \tilde{\phi}\tilde{\phi}^H$, with $\mathbf{W}$ needs to satisfy the following conditions, i.e., $\mathbf{W} \geq 0$ and $\text{rank}(\mathbf{W}) = 1$. As the rank-one condition is non-convex, we drop this constraint and relax the problem (8.21) as

$$
(P4) \ \underset{\mathbf{W}}{\text{maximize}} \ \nu\xi\sum_{k=1}^{K_E}\left(\text{Tr}(\mathbf{R}_E\mathbf{W}) + \sum_{j=1}^{K_I}\text{Tr}(\mathbf{R}\mathbf{W})\right) + \sum_{j=1}^{K_I}\text{Tr}(\mathbf{R}_I\mathbf{W})
$$

subject to:

    (C1) $\mathbf{W}_{[n,n]} = 1, \forall n = 1, \cdots, N+1, \&\mathbf{W} \geq 0$

    (C2) $\text{Tr}(\mathbf{R}_I\mathbf{W}) \geq 2^{R_{I,min}-1}(\text{Tr}(\mathbf{R}_I\mathbf{W}) + \sigma_j^2), \ \forall j \in \mathcal{K}_I$

    (C3) $Q_k \geq Q_{th}, \ \forall k \in \mathcal{K}_E.$

$$(8.22)$$

The Problem (8.22) is a convex semi-definite program (SDP) that can be optimally solved by CVX [98]. However, it may not lead to a rank-one solution in general, i.e., $\text{rank}(\mathbf{W}) = 1$, which implies that the optimal value of the objective function of the problem (8.22) only serves an upper

bound of problem (8.17). In this case, Gaussian randomization can be used to recover a high-quality feasible solution of the problem (8.17) similarly as presented in [15]. In practice, the elements of the RIS phase-shift matrix would indeed be discrete. The solution to the case with discrete phase shifts can be obtained from the case of continuous phase shifts via quantization [15], until this level we considered continuous phase shifts as the solution values for θ_n will be in $[0, 2\pi)$. Now, to discretize the solution, let us define the feasible set of discrete phase shifts as $\mathcal{F} = \{\exp(\frac{j2\pi n}{2^b})\}_{n=0}^{2^{b-1}}$, where b is the bit resolution and n is the phase-shift index. By seting $b = 1$, the feasible set will be reduced to $\mathcal{F} = \{0, \pi\}$, $\forall n = 1, \cdots, N$. To discretize the solution according to the feasible set of phases $\mathcal{F}$, we set $\theta_n = 0$ when the solution to (8.22) is such that $\frac{3\pi}{2} \leq \theta_n < 2\pi$ and $0 \leq \theta_n < \frac{\pi}{2}$, and $\theta_n = \pi$ when the solution is such that $\frac{\pi}{2} \leq \theta_n < \pi$ or $\pi \leq \theta_n < \frac{3\pi}{2}$ [113].

The Active Beamforming Design

For fixed phase shift matrix $\mathbf{\Phi} = \mathbf{\Phi}^{\text{opt}}$, and by dropping the constraints that not depend on $\mathbf{V}$, the problem (8.17) is reduced to:

$$(P5) \quad \underset{\mathbf{V}}{\text{maximize}} \ R$$

$$\text{subject to:}$$

$$\text{(C2)} \quad \log_2 (1 + \gamma_j) \geq R_{\text{I,min}}, \ \forall j \in \mathcal{K}_{\text{I}} \tag{8.23}$$

$$\text{(C3)} \quad Q_k \geq Q_{\text{th}}, \ \forall k \in \mathcal{K}_{\text{E}}$$

$$\text{(C4)} \quad \sum_{j=1}^{K_{\text{I}}} \|\mathbf{v}_j\|^2 + \text{tr}(\mathbf{U}) \leq P_{\text{max}}.$$

The problem (8.23) reduces to maximizing the ESR while satisfying the IRs' minimum transmission rate constraints and the ERs' minimum harvested energy. It is true that the interference is a degrading factor for all IRs. However, interference is beneficial to all ERs since they can harvest energy from the surrounding environment. In particular, the beamforming vector for the IR$_j$, $\mathbf{v}_j$ can be designed based on the Zero-forcing (ZF) beamforming strategy [127]. Thus, ZF beamforming is used here to remove the inter-user interference for the IRs. After applying the ZF processing the interference term $\sum_{i=1, i \neq j}^{K_{\text{I}}} |\mathbf{h}_{\text{I},j}^{\text{H}} \mathbf{\Phi} \mathbf{H}_{\text{AP-RIS}}^{\text{H}} \mathbf{v}_i|^2$ is canceled from the SINR expression (cf. Eq. (8.11)) and from the constraint (C2).

The proposed solution is summarized in the following algorithm.

Algorithm 8.5 Proposed solution: two-layer algorithm.

Require: $\mathbf{H}_{\mathrm{AP-RIS}}$, K_{E}, K_{I}, N, $\epsilon_{\mathrm{sdp}} = 10^{-3}$

1: **Initialization:** Set $r = K_{\mathrm{I}}$,

      Repeat:

        Construct the null space of $\tilde{\mathbf{H}}_{\mathrm{I}}$ based on the SVD.

        Generate $\tilde{\mathbf{H}}_{\mathrm{N}}$, based on (8.6)

        Calculate $\mathbf{G}_{\mathrm{N}}$ based on (8.7)

        The optimal energy vector $\mathbf{u} = \mathrm{eig}(\mathbf{G}_{\mathrm{N}}\mathbf{G}_{\mathrm{N}}^{\mathrm{H}})$, $\mathbf{U} = \mathbb{E}[\mathbf{u}\mathbf{u}^{\mathrm{H}}]$, $r = r - 1$.

      Until: $r = 0$

2: **Given V**

    Solve the SDP problem (8.22) using CVX.

    Applying Gaussian randomization method to derive ϕ.

    Discretize the obtained θ_n as described above.

3: **Given $\boldsymbol{\Phi}$**

    Calculate the information beamforming vectors $\{\mathbf{v}_j\}_{j=1}^{K_{\mathrm{I}}}$ using ZF techniques.

Ensure: $\boldsymbol{\Phi}$, $\mathbf{V}$ and $\mathbf{U}$.

Complexity Analysis

Here, the computational complexity of our proposed two-layer solution is analyzed. It is trivial that the complexity of the optimal solution depends on the optimization technique used, the number of optimization variables and the number of constraints.

For the passive beamforming design, the complexity comes essentially from solving the SDP problem related to the variable $\boldsymbol{\Phi}$. Following [123], the complexity of standard SDP programming is given by

$$O\left(M_{\mathrm{sdp}}N_{\mathrm{sdp}}^{3.5} + M_{\mathrm{sdp}}^2 N_{\mathrm{sdp}}^3 + M_{\mathrm{sdp}}N_{\mathrm{sdp}}^{0.5}\right)\log(\frac{1}{\epsilon_{\mathrm{sdp}}}), \tag{8.24}$$

where M_{sdp} is the number of semi-definite cone constraints, N_{sdp} is the dimension of semi-definite cones, and ϵ_{sdp} is the accuracy of the solution of the SDP problem, with $M_{\mathrm{sdp}} = 4NK_{\mathrm{I}}$, and $N_{\mathrm{sdp}} = 1 + \frac{K_{\mathrm{I}}+M_{\mathrm{t}}}{2}$.

For the active beamforming layer, based on [128], we note the complexity of eigenvalue decomposition and matrix inversion operations by $O(n^3)$ with n is the dimension of the matrix and by $O(n)$ the complexity of the other operations such as summation, multiplication, etc. Therefore, the total complexity is given by

$$O\left(M_{\mathrm{t}}^3 + M_{\mathrm{t}}^3 K_{\mathrm{I}}^2 + M_{\mathrm{t}}^3 K_{\mathrm{I}}\right). \tag{8.25}$$

8.4 Total Harvested Power Maximization

In this part, we tackle the special case of the maximization of the total harvested power to the ERs. Accordingly, $\nu_{\mathrm{I}} = 0$. Therefore, the objective function of the problem (8.20) is reduced to R^{E}, which is equivalent to maximize the total harvested power while satisfying the minimum required rates at the IRs, the minimum harvested power at the ERs, the maximum transmit power at the AP and the unit modulus of the phase shift values at the RIS. Hereafter, the total harvested power maximization problem for the RIS-aided SWIPT system is formulated as

$$
\begin{aligned}
(P6) \quad & \underset{\mathbf{V}, \boldsymbol{\Phi}}{\text{maximize}} \; Q = \sum_{k=1}^{K_{\mathrm{E}}} Q_k(\mathbf{V}, \boldsymbol{\Phi}) \\
& \text{subject to:} \\
& (\mathrm{C1}) \quad |\phi_n| = 1, \; \forall n \in \{1, \cdots, N\} \\
& (\mathrm{C2}) \quad \log_2(1 + \gamma_j) \geq R_{\mathrm{I,min}}, \; \forall j \in \mathcal{K}_{\mathrm{I}} \\
& (\mathrm{C3}) \quad Q_k \geq Q_{\mathrm{th}}, \; \forall k \in \mathcal{K}_{\mathrm{E}} \\
& (\mathrm{C4}) \quad \sum_{j=1}^{K_{\mathrm{I}}} \|\mathbf{v}_j\|^2 + \mathrm{tr}(\mathbf{U}) \leq P_{\max}.
\end{aligned}
\tag{8.26}
$$

We note that the problem (8.26) is non-convex due to the non-concave nature of the objective function with respect to $\boldsymbol{\Phi}$ and $\mathbf{V}$, and the non-convex condition (C1). Here, also, we adopt the alternating optimization technique to solve the problem. In the sequel, the proposed solution is presented.

The Passive Beamforming Design

For fixed active beamforming matrix at the AP, i.e., $\mathbf{V} = \mathbf{V}^{\mathrm{opt}}$, we focus on optimizing the phase shift matrix $\boldsymbol{\Phi}$ at the RIS. By dropping the terms that are independent of $\boldsymbol{\Phi}$, and after applying

the mathematical transformation as described in the Section 8.3, the optimization problem (8.26) is reduced to

$$
\begin{aligned}
(P7) \quad &\underset{\mathbf{W}}{\text{maximize}} \quad \sum_{k=1}^{K_{\mathrm{E}}} \left(\mathrm{Tr}(\mathbf{R}_{\mathrm{E}}\mathbf{W}) + \sum_{j=1}^{K_{\mathrm{I}}} \mathrm{Tr}(\mathbf{R}\mathbf{W}) \right) \\
&\text{subject to:} \\
&\quad (\mathrm{C1}) \quad \mathbf{W}_{[n,n]} = 1, \forall n = 1, \cdots, N+1, \& \mathbf{W} \geq 0 \\
&\quad (\mathrm{C2}) \quad \mathrm{Tr}(\mathbf{R}_{\mathrm{I}}\mathbf{W}) \geq 2^{R_{\mathrm{I,min}}-1}(\mathrm{Tr}(\mathbf{R}_{\mathrm{I}}\mathbf{W}) + \sigma_j^2), \ \forall j \in \mathcal{K}_{\mathrm{I}} \\
&\quad (\mathrm{C3}) \quad Q_k \geq Q_{\mathrm{th}}, \ \forall k \in \mathcal{K}_{\mathrm{E}}.
\end{aligned}
\tag{8.27}
$$

By combining the condition (C3) and the objective function, the problem (8.27) can be reduced to maximize the minimum harvested power by all the ERs. Therefore, the optimization problem is expressed as

$$
\begin{aligned}
(P8) \quad &\underset{\mathbf{W}}{\text{maximize}} \ \min \ \left(\mathrm{Tr}(\mathbf{R}_{\mathrm{E}}\mathbf{W}) + \sum_{j=1}^{K_{\mathrm{I}}} \mathrm{Tr}(\mathbf{R}\mathbf{W}) \right) \\
&\text{subject to:} \\
&\quad (\mathrm{C1}) \quad \mathbf{W}_{[n,n]} = 1, \forall n = 1, \cdots, N+1, \& \mathbf{W} \geq 0 \\
&\quad (\mathrm{C2}) \quad \mathrm{Tr}(\mathbf{R}_{\mathrm{I}}\mathbf{W}) \geq 2^{R_{\mathrm{I,min}}-1}(\mathrm{Tr}(\mathbf{R}_{\mathrm{I}}\mathbf{W}) + \sigma_j^2), \ \forall j \in \mathcal{K}_{\mathrm{I}}.
\end{aligned}
\tag{8.28}
$$

which is a convex SDP that can be optimally solved by standard tools such as CVX [98]. Here also, to satisfy the rank one condition, the Gaussian randomization can be used to recover a high-quality feasible solution of the problem (8.26). The elements of the RIS phase shift matrix would indeed be discrete. The obtained solution can also be discretized as described above (cf. Section 8.3).

The Active Beamforming Design

For fixed phase shift matrix $\mathbf{\Phi} = \mathbf{\Phi}^{\mathrm{opt}}$, the problem (8.26) is reduced to:

$$(P9) \quad \underset{\mathbf{V}}{\mathrm{maximize}} \; Q = \sum_{k=1}^{K_{\mathrm{E}}} Q_k(\mathbf{V}, \mathbf{\Phi}^{\mathrm{opt}})$$

$$\text{subject to:}$$

$$(\mathrm{C2}) \quad \log_2\left(1 + \gamma_j\right) \geq R_{\mathrm{I,min}}, \; \forall j \in \mathcal{K}_{\mathrm{I}} \tag{8.29}$$

$$(\mathrm{C3}) \quad Q_k \geq Q_{\mathrm{th}}, \; \forall k \in \mathcal{K}_{\mathrm{E}}$$

$$(\mathrm{C4}) \quad \sum_{j=1}^{K_{\mathrm{I}}} \|\mathbf{v}_j\|^2 + \mathrm{tr}(\mathbf{U}) \leq P_{\mathrm{max}}.$$

The problem (8.29) reduces to maximizing the total harvested energy while satisfying the IRs' minimum transmission rate constraints. It can be solved with ZF beamforming as described in [52, 127].

8.5   Performance Evaluation

In this section, simulation and numerical results are provided to validate the performance of the proposed RIS-aided SWIPT design. In the simulations, the following parameter setting is used, unless otherwise stated: $\eta = 1$, ξ is set to 10% , $\nu = 1$ [54]. $P_{\mathrm{max}} = 25$ dBm, $\sigma_k^2 = \sigma_j^2 = \sigma^2 = -50$ dBm, $M_{\mathrm{t}} = 8$, $K_{\mathrm{E}} = K_{\mathrm{I}} = 2$, $N = 32$, $\mu = \mu_{\mathrm{E}} = \mu_{\mathrm{I}} = 3$, $Q_{\mathrm{th}} = 0.1$ W and $\alpha = \beta = 2.2$. The simulation results are obtained by using up to 50 random channel realizations.

We consider a two-dimensional coordinate system, where a uniform linear array at the AP and a uniform planar array at the RIS are deployed. The antenna spacing is half the wavelength and the reference (center) antennas at the AP and the RIS are respectively located at (0,0) and (d_0, d_1). The devices pertaining to the energy receivers and the information receivers sets are randomly located in the areas $\{(x, y) \mid 0 \text{ m} < x < d_0 \text{ m}, 0 < y < 20 \text{ m}\}$ and $\{(x, y) \mid d_1 \text{ m} < x < 50 \text{ m}, 0 < y < 30 \text{ m}\}$, respectively. The channel model is reduced to the LoS model when $\mu = \mu_{\mathrm{I}} = \mu_{\mathrm{E}} \to \infty$. The signal attenuation at a reference distance of 1 m is set as 30 dB for all channels.

Next, we compare the performance of the proposed SWIPT scheme versus the following benchmark schemes with/without RIS deployed and/or without dedicated energy signals used.

Information Beamforming with RIS

In this scheme, the AP sends information beams only. The transmit signal is formulated as $\sum_{j=1}^{K_I} \mathbf{v}_j s_j^I$. Accordingly, $\mathbf{u} = 0$ in this case. The ERs users harvest energy from the information signals. After obtaining the optimal phase shifting $\mathbf{\Phi}$ as described Section 8.3, the problem of maximizing the ESR subject to the constraints on the minimum required rates can be formulated as shown in (8.23), and it can be solved with the same algorithm (cf. Section 8.3).

Conventional SWIPT Design with RIS

Here, the AP transmits both information and energy beams for SWIPT. The transmit signal is formulated as $\sum_{j=1}^{K_I} \mathbf{v}_j s_j^I + \sum_{k=1}^{K_E} \mathbf{w}_k s_k^E$, where $\mathbf{v}_j$ and s_j^I are the beamforming vector and the information symbol intended to the jth IR respectively, $\mathbf{w}_k$ is the energy beamforming vector to user k and s_k^E is the energy signal for ER_k [52]. The optimization problem can be formulated as Problem (P1) in [52], but with three optimization variables, namely, $\mathbf{W} = [\mathbf{w}_1, \cdots, \mathbf{K}_E]^T$, $\mathbf{V}$ and $\mathbf{\Phi}$, which can be solved by the alternating optimization technique [52]. After solving the passive beamforming problem as described in Section 8.3 the problem is reduced to design $\mathbf{V}$ and $\mathbf{W}$. The solution to this problem can be obtained by using the SDR technique and the Gaussian randomization, as described in [129].

For comparison reasons, we also study the computational complexity of the proposed solution, which is based on the SDP for finding beamforming matrices. Therefore, the complexity is given by $3O\left(M_{\text{sdp}}N_{\text{sdp}}^{3.5} + M_{\text{sdp}}^2 N_{\text{sdp}}^3 + M_{\text{sdp}}N_{\text{sdp}}^{0.5}\right) \log(\frac{1}{\epsilon_{\text{sdp}}})$, where M_{sdp} is the number of semi-definite cone constraints, N_{sdp} is the dimension of semi-definite cones, and ϵ_{sdp} is the accuracy of the solution of the SDP problem as shown in [123]. In this case, the number of semi-definite cone constraints is as follows $M_{\text{sdp}} = 4K_I$, w.r.t. the design of $\mathbf{V} = [\mathbf{v}_1, \cdots, \mathbf{v}_{K_I}]^T$, $M_{\text{sdp}} = 4K_E$ w.r.t. the design of $\mathbf{W} = [\mathbf{w}_1, \cdots, \mathbf{w}_{K_E}]^T$, and $M_{\text{sdp}} = 4NK_IK_E$ when designing $\mathbf{\Phi}$. As for the semi-definite cone dimension, $N_{\text{sdp}} = 1 + \frac{K+M_t}{2}$, with $K = K_I + K_E$.

Conventional SWIPT design without RIS

In this scheme, the AP transmits both information and energy beams. The transmit signal is formulated as $\sum_{j=1}^{K_I} \mathbf{v}_j s_j^I + \sum_{k=1}^{K_E} \mathbf{w}_k s_k^E$, where $\mathbf{v}_j$ and s_j^I, $\mathbf{w}_k$, and s_k^E are as defined above (cf.

Section 8.5). The ESR optimization problem is reduced to design the active beamforming that satisfy the minimum required rates and minimum harvested energies and the total transmit power budget. However, no RIS is deployed to assist the SWIPT, hence, $\mathbf{\Phi}$, which can be solved by using the SDR technique together with Gaussian randomization, as shown in [129].
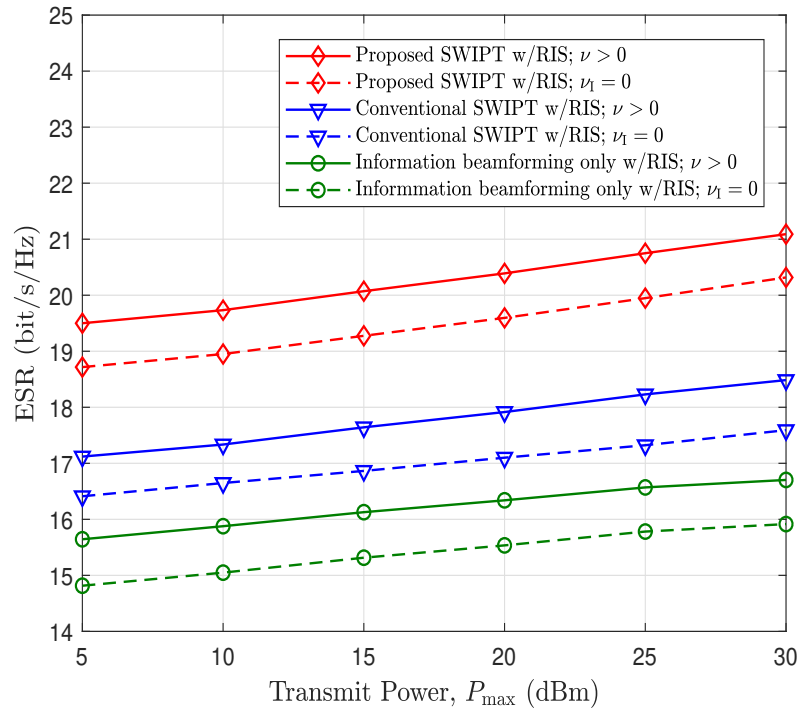

Figure 8.2: The equivalent sum rates (ESR) versus total transmit power.

Figure 8.2 shows the ESR versus the transmit power at the AP. We compare the proposed RIS-aided SWIPT design referred here as Proposed SWIPT to the benchmarks described above, i.e., the conventional SWIPT and the information beamforming aided with RIS. As expected, the ESR is increasing with the increase in the transmit power at AP for all schemes. This is due to the fact that increasing the transmit power will improve the signal strength and therefore the harvested power and the beamforming gains and hence, the transmission rates. Furthermore, the figure shows that the proposed RIS-aided SWIPT design achieves significant performance gains over the other benchmark schemes. This can be explained by the fact that sending additional energy beams leads to a significant enhancement of the total harvested power, since it is considered as additional beneficial interference at the ERs and thus enhances the ESR gains. Moreover, we compare the proposed MOO model to the single objective optimization one which consists on maximizing the total harvested

energy for the ERs under the same constraints (i.e., $\nu_\mathrm{I} = 0$), to highlight the performance gain that can be achieved when using the MOO framework. It is observed that the results with MOO are always better than the used benchmark. For instance, a gain of 10% of the achieved ESR can be obtained when using the MOO model compared to its counterpart with the harvested energy maximization only (cf. red curves in the figure).
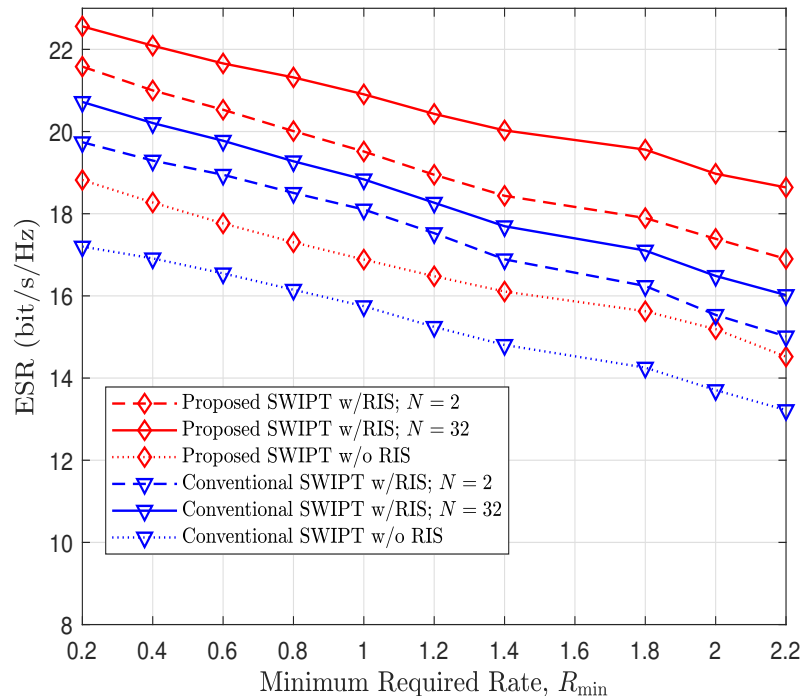

Figure 8.3: ESR versus minimum transmission rate requirement with different number of RIS elements, $P_\mathrm{max} = 25$ **dBm,** $K_\mathrm{I} = K_\mathrm{E} = 2$**,** $Q_\mathrm{th} = 0.1$ **W and** $M_\mathrm{t} = 8$**.**

In Fig. 8.3, we study the impact of the minimum transmission rate R_min of the IRs on the ESR gains of the proposed SWIPT system based on the null space compared to the conventional SWIPT with and without RIS assistance, and with different RIS element numbers, i.e., $N = 2$ and $N = 32$. As it can be seen from the curves that, with fixed number of RIS elements, the ESR decreases with the increase of the minimum transmission rate of the IRs for all the schemes. This can be explained by the fact that more resource are needed to be allocated to the IRs to meet the increasing rate requirements, thus degrades the overall performance of the system. On the other hand, we observe that by deploying the RIS, the ESR gains are higher than the counterpart without RIS (cf. curves in blue in the figure). Now, we explore the variation of the number of RIS element and study its effect on the achieved ESR. We notice that the ESR is increasing with the number of

RIS elements, N, under the same requirements $(R_{\mathrm{min,I}}, Q_{\mathrm{th}})$, as expected. For instance, using more RIS elements will enhance the signal strength with less transmit power at the AP, hence leading to higher gains. In particular, gains of 10% and 13% are achieved when increasing N from 2 to 32 for the conventional and the proposed SWIPT designs, respectively. As a conclusion, the fact of sending a dedicated energy signal in the null space, deploying RIS and using the high number of RIS elements, N, results on transmit power savings at the AP, since the AP will need less power to steer its beam direction and guarantee the balance of service between the IRs and ERs. The curves also validate that the proposed design with RIS outperforms the other benchmark schemes.
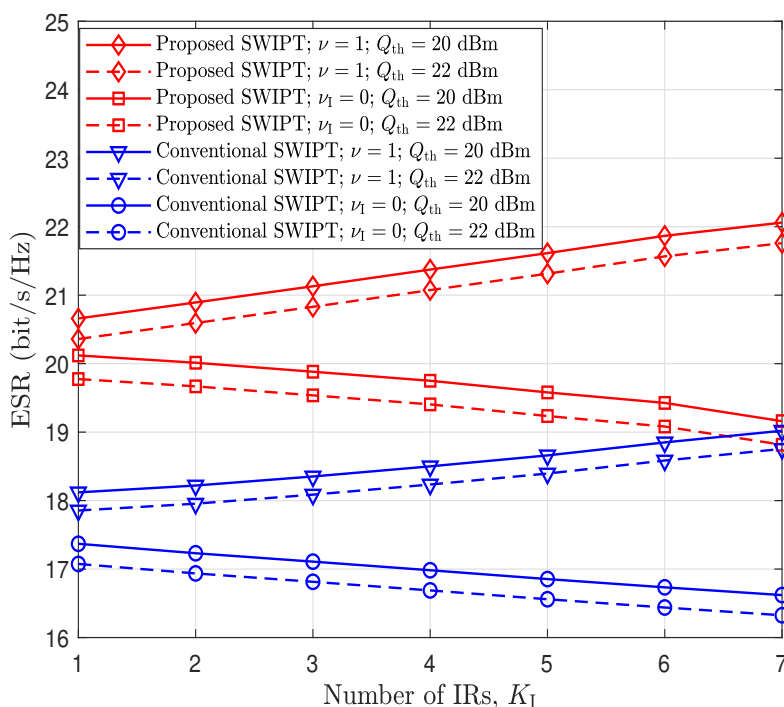
Figure 8.4: The ESR versus the number of IRs, K_{I}.

Figure 8.4 plots the achieved ESR versus the number of IRs, K_{I}, with different minimum required harvested energy values at the ERs, Q_{th}, for the proposed RIS-aided SWIPT based on the null space and the RIS-aided conventional SWIPT. First, it is observed that increasing the number of IRs (K_{I}) increases the achieved ESR for both the proposed and the conventional SWIPT designs, due to the increase of information beamforming gains, hence, the information sum rates (cf. curves in blue and red in the figure). On the other hand, as expected, increasing the required harvested energy at the ERs will reduce the ESR as it will require higher transmit power at the AP. Second, we consider the special case of maximizing the harvested energy, i.e., $\nu_{\mathrm{I}} = 0$. It is shown that the increase in the

number of IRs results in a decrease of the harvested power and thus a decrease of the equivalent transmitted rate. This can be explained by the fact at a low value of K_I, a high number of degree of freedom that can be used to transmit energy signals, $M_\mathrm{t} - K_\mathrm{I}$ dimensional free space, which results on a high achieved amounts of harvested energy. However, increasing K_I reduces the dimension of the subspace and the degree of freedom, hence, decreasing the achieved harvested power and therefore, the achieved ESR. This observation demonstrates the effectiveness of using the null space to transmit the energy signals.
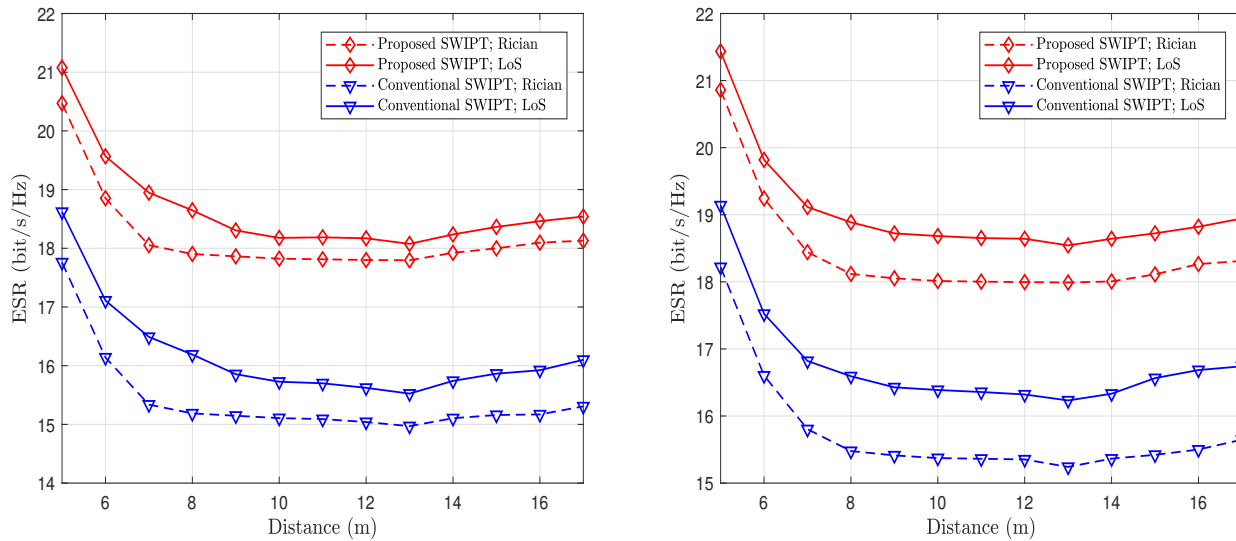
Figure 8.5: The ESR versus the AP-RIS distance (a)$M_\mathrm{t} = 8$**, (b)** $M_\mathrm{t} = 16$**; In both sub-plots,** $K_\mathrm{I} = 2$**,** $K_\mathrm{E} = 4$**,** $N = 32$**.**

In Fig. 8.5, we plot the ESR versus the distance between the AP and the RIS of the proposed RIS-aided SWIPT design and the conventional RIS-aided SWIPT, for different values of the number of antennas at the AP, namely, $M_\mathrm{t} = 8$ (cf. 8.5 (a)) and $M_\mathrm{t} = 16$ (cf. 8.5 (b)), and different channel configurations. Here we assume that $d_0 = d_1 = 20$ m. As expected, the achievable ESR decreases as the RIS is positioned away from the AP, i.e., the distance increases. This can be explained by the fact that the received signal power at the RIS gets smaller when the RIS is farther away from the source, hence the reflected signal power is weaker. However, a slight increase is observed when the RIS is deployed near the devices. Indeed, the RIS creates a virtual array around the devices which will strengthen the reflected signals and hence, the achieved rates. For further analysis, we also consider different channel configurations, i.e., when the AP-RIS channel is dominated by the LoS link and when the AP-RIS channel is following the Rician model. Typically, the achieved ESR when the channel is dominated by the LoS link is higher than its contrepart when the channel follows

the Rician model. Moreover, increasing the number of antennas at the AP leads to enhancement of the received signal power since it improves the transmit signal strength and increases the degree of freedom and so the null space, thus more energy signals can be sent (cf. Eq. (8.6)), which will improve the ESR of the system.
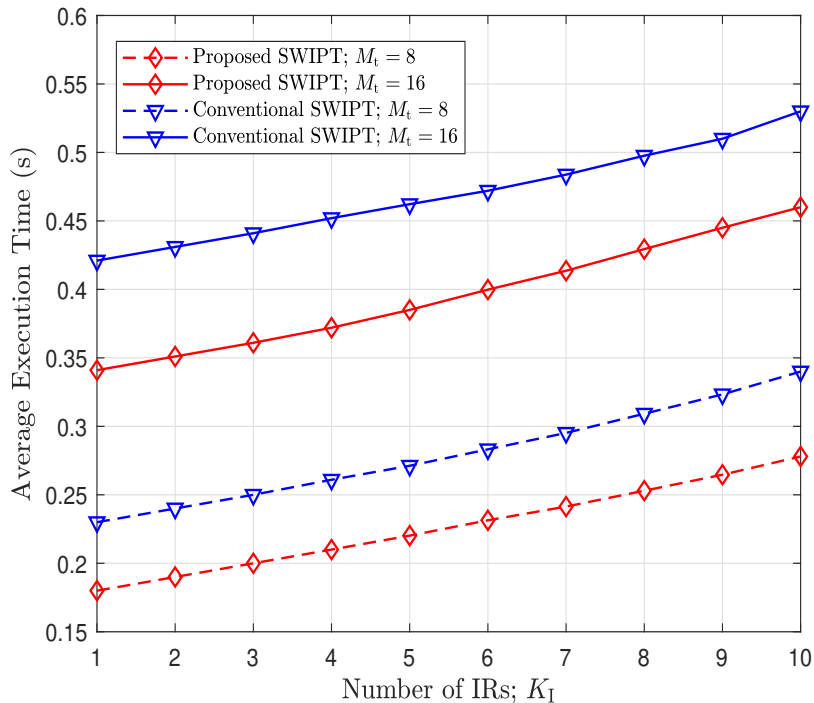

Figure 8.6: Average time complexity per optimization versus the number of IRs, K_I.

In order to highlight the proposed SWIPT design and the proposed algorithm compared to the conventional SWIPT scheme, we study the complexity performance of both systems. For that, the average time complexity versus the number of IRs, with different numbers of antennas, $M_\text{t} = 8$ and $M_\text{t} = 16$, is plotted in in Fig. 8.6. Clearly, the average execution time of the proposed algorithm (Algorithm 8.5) with RIS-aided SWIPT design is less than that of the conventional schemes (solution obtained with SDR techniques [98]). This is due to the high execution time of the SDR techniques to converge to the optimal solution. Moreover, increasing the number of IRs or the number of antennas results in an increase of the complexity, hence, the execution time (cf. Section 8.3 & Section 8.5).

8.6 Concluding Remarks

This chapter proposed a reconfigurable intelligent surface aided simultaneous information and power transfer system design based on the null space. Specifically, the degrees of freedom of the cascaded channel between the access point and the information receivers are used to construct the energy signal. The design goal is to maximize the equivalent sum rates subject to individual rate constraints at the information receivers, the minimum harvested power at the energy receivers, and the maximum transmit power at the access point. The formulated non-convex problem was relaxed to sub-problems, which can be solved based on two-layer algorithm. The first layer was devoted to designing the phase shifting at the RIS. The second layer, is allocated to designing the information beamforming vectors. Finally, simulation results are provided and confirmed the performance advantages of the proposed scheme compared to benchmark schemes.

Conclusion

Chapter 9

Conclusion

This dissertation addressed three main challenges/questions:

- How to enhance WPT/WIPT efficiency with/without RIS?

- How to enhance EE of different systems, i.e., WPT, WIT and SWIPT with/without RIS?

- How to serve starved users (cell-edge) with high quality of service?

9.1   Part I

This part designed a cooperative WPT and cooperative RIS-aided WPT systems and developed a framework for calculation and performance evaluation of WPT with/without RIS. In particular, stochastic geometry tools are leveraged to model the PPP distributed networks' nodes and to determine the closed-form expressions of the WPT coverage probability and the data transmission probability in two tessellations for different types of devices. The simulation results validated the correctness of the derivations as per this work's analysis and emphasize the importance of leveraging the cooperative beamforming and the cooperative RIS in the design of efficient WPT systems.

9.2 Part II

Part II of this dissertation designed an aerial RIS-aided WIT system for serving the cell-edge users with high EE and developed optimal/near optimal solutions for EE maximization in two deployment scenarios: single service or unicast and multiple services or joint broadcast-unicast. More specifically, chapter 5 and chapter 6 investigated the scenario of the single service transmission with the assistance of UAV equipped with RIS for downlink and uplink communication, respectively and chapter 7 considered the multi-services transmission scenario, where the communication is assisted with an aerial dual-polarized RIS. The main objective of part II is to jointly design the active beamforming at the base station and the passive beamforming at the RIS in order to maximize the energy efficiency of the communication system. Efficient low-complexity algorithms were proposed to solve the formulated optimization problems. Results showed the superiority of leveraging aerial RIS compared to the conventional AF relaying and the efficiency of using polarization for the joint transmission of different kinds of traffic patterns.

9.3 Part III

This part proposed a design for a RIS-aided SWIPT system based on the null space and developed a framework for a multi-objective function optimization and performance evaluation. What highlights this work, in comparison to the recent works on the integration of RIS with SWIPT systems, is the use of the degree of freedom of the channel between the IRs and the AP to send additional energy signals. To this end, first the SVD was used to determine the null space, then, the energy signal is chosen as the eigenvector corresponding to the largest eigenvalue of the projected version of the channel between ER and the AP in the null space. The main design goal is to achieve a balance between the sum-rate of the IRs and the harvested power at the ERs. For such, a multi-objective optimization problem subject to quality of services requirements constraints was formulated and solved through a two-layer iterative algorithm. The findings confirmed the performance advantages of the proposed scheme compared to benchmark schemes.

9.4   Future Works

Although, a substantial research work was carried out in this thesis regarding the RIS-aided WIPT, several works can be done in the future such as:

- Generalize the cooperative RIS-aided WPT framework to the SWIPT case.

- Tackle the RIS channel estimation problem.

- Consider the UAV trajectory in the design.

9.5   Publications

The findings of this thesis have already resulted in several published and submitted transactions and conference papers as listed in the following.

Journal Papers

- Z. Mohamed and S. Aïssa, "Reconfigurable Intelligent Surface Aided SWIPT: A Null Space Based Design," in *IEEE Trans. Wireless Commun., To be submitted (Apr. 2023).*

- Z. Mohamed and S. Aïssa, "Energy-Efficient Joint Broadcast-Unicast Communications via Dual-Polarized Aerial RIS," in *IEEE Trans. Wireless Commun.*, Sep. 2022.

- Z. Mohamed, A. Bhowal and S. Aïssa, "Distance Distributions and Coverage Probabilities in Poisson-Delaunay Triangular Cells with Application to Coordinated Multi-Point Wireless Power Transfer," in *IEEE Trans. Wireless Commun.*, May 2022.

Conference Papers

- Z. Mohamed, and S. Aïssa, "Energy-Efficient Joint Broadcast-Unicast Communications via Aerial RIS," *in Proc. IEEE Wireless Commun. Net. Conf. (WCNC)*,Glasgow, Scotland, UK, Mar., 2023.

164

- Z. Mohamed, and S. Aïssa, "Wireless Power Transfer Aided With Reconfigurable Intelligent Surfaces: Design, and Coverage Analysis," *in Proc. IEEE Int. Symp. Personal Indoor Mobile Radio Commun. (PIMRC)*, Tokyo, Japan, Sep., 2022.

- Z. Mohamed and S. Aïssa, "Resource Allocation for Energy-Efficient Cellular Communications via Aerial IRS," *in Proc. IEEE Wireless Commun. Net. Conf. (WCNC)*, Nanjing, China, Apr., 2021.

- Z. Mohamed and S. Aïssa, "Coordinated Energy Beamforming: Wireless Power Coverage and Transmission Probability," *in Proc. IEEE Wireless Commun. Net. Conf. (WCNC)*, Nanjing, China, Apr. 2021.

- Z. Mohamed and S. Aïssa, "Leveraging UAVs with Intelligent Reflecting Surfaces for Energy-Efficient Communications with Cell-Edge Users," *in Proc. IEEE Int. Conf. on Commun. (ICC)* Dublin, Ireland, June, 2020, pp. 1-6.

Other Publications

These publications are out of the scope of this dissertation.

- Z. Mohamed, M. Amjad, L. Musavian, and S. Aïssa, "Non-Orthogonal Multiple Access with Finite Blocklength for Low-Latency Communications: Effective Capacity Analysis," *in IEEE Trans. Commun, to be submitted (Apr. 2023)*.

- Z. Mohamed, C. Chen, and S. Aïssa, "SLNR-Based Precoding for Multi-User Communications Assisted with Reconfigurable Surfaces," *in Proc. IEEE Int. Wireless Commun. Mobile Comp. Conf. (IWCMC)*, Harbin, China, June, 2021. (Best Paper Award)

References

[1] W. Saad, M. Bennis, and M. Chen, "A vision of 6G wireless systems: Applications, trends, technologies, and open research problems," *IEEE Net.*, vol. 34, no. 3, pp. 134–142, May 2020.

[2] J. Zhang, E. Björnson, M. Matthaiou, D. Ng, H. Yang, and D. Love, "Prospective multiple antenna technologies for beyond 5G," *IEEE J. Sel. Areas Commun.*, vol. 38, no. 8, pp. 1637–1660, Aug. 2020.

[3] M. Di Renzo, K. Ntontin, J. Song, F. Danufane, X. Qian, F. Lazarakis, J. De Rosny, D. Phan-Huy, O. Simeone, R. Zhang, M. Debbah, G. Lerosey, M. Fink, S. Tretyakov, and S. Shamai, "Reconfigurable intelligent surfaces vs. relaying: Differences, similarities, and performance comparison," *IEEE Open J. Commun. Soc.*, vol. 1, pp. 798–807, June 2020.

[4] E. Basar, M. Di Renzo, J. De Rosny, M. Debbah, M. Alouini, and R. Zhang, "Wireless communications through reconfigurable intelligent surfaces," *IEEE Access*, vol. 7, pp. 116 753–116 773, Aug. 2019.

[5] M. Di Renzo, A. Zappone, M. Debbah, M. Alouini, C. Yuen, J. de Rosny, and S. Tretyakov, "Smart radio environments empowered by reconfigurable intelligent surfaces: How it Works, State of Research, and the road ahead," *IEEE J. Sel. Areas Commun.*, vol. 38, no. 11, pp. 2450–2525, Nov. 2020.

[6] L. Subrt and P. Pechac, "Intelligent walls as autonomous parts of smart indoor environments," *IET Commun.*, vol. 6, pp. 1004–1010, May 2012.

[7] C. Liaskos, S. Nie, A. Tsioliaridou, A. Pitsillides, S. Ioannidis, and I. Akyildiz, "A new wireless communication paradigm through software-controlled metasurfaces," *IEEE Commun. Mag.*, vol. 56, no. 9, pp. 162–169, Sep. 2018.

[8] M. Giordani, M. Polese, M. Mezzavilla, S. Rangan, and M. Zorzi, "Toward 6G networks: Use cases and technologies," *IEEE Commun. Mag.*, vol. 58, no. 3, pp. 55–61, Mar. 2020.

[9] K. Achouri, M. Salem, and C. Caloz, "General metasurface synthesis based on susceptibility tensors," *IEEE Trans. Antennas Prop.*, vol. 63, no. 7, pp. 2977–2991, July 2015.

[10] M. Patzold, "It's time to go big with 5G mobile radio," *IEEE Veh. Tech. Mag.*, vol. 13, no. 4, pp. 4–10, Dec. 2018.

[11] Q. Wu, S. Zhang, B. Zheng, C. You, and R. Zhang, "Intelligent reflecting surface aided wireless communications: A tutorial," *IEEE Trans. Commun.*, vol. 69, no. 5, pp. 1–1, May 2021.

[12] L. Zhao, Z. Wang, and X. Wang, "Wireless power transfer empowered by reconfigurable intelligent surfaces," *IEEE Sys. J.*, vol. 15, no. 2, pp. 2121–2124, Apr. 2021.

[13] Q. Wu and R. Zhang, "Towards smart and reconfigurable environment: intelligent reflecting surface aided wireless network," *IEEE Commun. Mag.*, vol. 58, no. 1, pp. 106–112, Jan. 2020.

[14] S. Kumar and N. Nagarajan, "Analysis of transparent and non-transparent relay modes in IEEE 802.16j mobile multi-hop relay networks," *J. Discrete Mathematical Sciences and Cryptography*, vol. 15, 02 2012.

[15] Q. Wu and R. Zhang, "Intelligent reflecting surface enhanced wireless network via joint active and passive beamforming," *IEEE Trans. Wireless. Commun.*, vol. 18, no. 11, pp. 5394–5409, Nov. 2019.

[16] D. Wang, L. Yin, T. Huang, F. Han, Z. Zhang, Y. Tan, and P. Liu, "Design of a 1 bit broadband space-time-coding digital metasurface element," *IEEE Antennas Wireless Prop. Lets.*, vol. 19, no. 4, pp. 611–615, Apr. 2020.

[17] M. Trampler, R. Lovato, and X. Gong, "Dual-resonance continuously beam-scanning X-band reflectarray antenna," *IEEE Trans. Antennas Prop.*, vol. 68, no. 8, pp. 6080–6087, Aug. 2020.

[18] X. Yang, S. Xu, F. Yang, and M. Li, "Design of a 2-bit reconfigurable reflectarray element using two MEMS switches," in *Proc. IEEE Int. Symp. Antennas Prop. USNC/URSI Nat. Radio Science Meeting*, July 2015, pp. 2167–2168.

[19] G. Perez-Palomino, P. Baine, R. Dickie, M. Bain, J. Encinar, R. Cahill, M. Barba, and G. Toso, "Design and experimental validation of liquid crystal-based reconfigurable reflectarray elements with improved bandwidth in F-band," *IEEE Trans. Antennas Prop.*, vol. 61, no. 4, pp. 1704–1713, Apr. 2013.

[20] S. Hu, F. Rusek, and O. Edfors, "Beyond massive MIMO: the potential of data transmission with large intelligent surfaces," *IEEE Trans. Signal Process.*, vol. 66, no. 10, pp. 2746–2758, May 2018.

[21] M. Jung, W. Saad, Y. Jang, G. Kong, and S. Choi, "Performance analysis of large intelligence surfaces (LISs): asymptotic data rate and channel hardening effects," *IEEE Trans. Wireless Commun.*, vol. 19, no. 3, pp. 2052–2065, Mar. 2020.

[22] C. Huang, A. Zappone, G. Alexandropoulos, M. Debbah, and C. Yuen, "Reconfigurable intelligent surfaces for energy efficiency in wireless communication," *IEEE Trans. Wireless Commun.*, vol. 18, no. 8, pp. 4157–4170, June 2019.

[23] M. Fu, Y. Zhou, and Y. Shi, "Intelligent reflecting surface for downlink non-orthogonal multiple access networks," in *Proc. IEEE Globecom Workshops (GC Wkshps)*, Mar. 2019, pp. 1–6.

[24] Q. Nadeem, A. Kammoun, A. Chaaban, M. Debbah, and M. Alouini, "Asymptotic Max-Min SINR analysis of reconfigurable intelligent surface assisted MISO systems," *IEEE Trans. Wireless Commun.*, vol. 19, no. 12, pp. 7748–7764, Dec. 2020.

[25] Z. He and X. Yuan, "Cascaded channel estimation for large intelligent metasurface assisted massive MIMO," *IEEE Wireless Commun. Lets.*, vol. 9, no. 2, pp. 210–214, Feb. 2020.

[26] S. Abeywickrama, R. Zhang, Q. Wu, and C. Yuen, "Intelligent reflecting surface: Practical phase shift model and beamforming optimization," *IEEE Trans. Commun.*, vol. 68, no. 9, pp. 5849–5863, Sep. 2020.

[27] C. Liaskos, A. Tsioliaridou, S. Nie, A. Pitsillides, S. Ioannidis, and I. Akyildiz, "An interpretable neural network for configuring programmable wireless environments," in *Proc. IEEE Int. Sig. Process. Advances Wireless Commun. (SPAWC)*, 2019, pp. 1–5.

[28] A. Taha, M. Alrabeiah, and A. Alkhateeb, "Deep learning for large intelligent surfaces in millimeter wave and massive MIMO systems," in *Proc. IEEE Global Commun. Conf. (GLOBECOM)*, Dec. 2019, pp. 1–6.

[29] F. Mismar, B. Evans, and A. Alkhateeb, "Deep reinforcement learning for 5G networks: Joint beamforming, power control, and interference coordination," *IEEE Trans. Commun.*, vol. 68, no. 3, pp. 1581–1592, Mar. 2020.

[30] R. Shafin, H. Chen, Y. Nam, S. Hur, J. Park, J. Zhang, J. Reed, and L. Liu, "Self-tuning sectorization: Deep reinforcement learning meets broadcast beam optimization," pp. 1–1, Mar. 2019.

[31] C. Huang, R. Mo, and C. Yuen, "Reconfigurable intelligent surface assisted multiuser MISO systems exploiting deep reinforcement learning," *IEEE J. Sel. Areas Commun.*, vol. 38, no. 8, pp. 1839–1850, Aug. 2020.

[32] H. Wu, X. Tao, N. Zhang, D. Wang, S. Zhang, and X. Shen, "On base station coordination in cache- and energy harvesting-enabled HetNets: a stochastic geometry study," *IEEE Trans. Commun.*, vol. 66, no. 7, pp. 3079–3091, July 2018.

[33] L. Wei, C. Huang, G. Alexandropoulos, C. Yuen, Z. Zhang, and M. Debbah, "Channel estimation for RIS-empowered multi-user MISO wireless communications," *IEEE Trans. Commun.*, vol. 69, no. 6, pp. 4144–4157, June 2021.

[34] X. Wei, D. Shen, and L. Dai, "Channel estimation for RIS assisted wireless communications—part i: Fundamentals, solutions, and future opportunities," *IEEE Commun. Letts.*, vol. 25, no. 5, pp. 1398–1402, May 2021.

[35] D. Mishra and H. Johansson, "Channel estimation and low-complexity beamforming design for passive intelligent surface assisted MISO wireless energy transfer," in *Proc. IEEE Int. Conf. Acoust. Speech Sig. Process. (ICASSP)*, May 2019, pp. 4659–4663.

[36] T. Jensen and E. De Carvalho, "An optimal channel estimation scheme for intelligent reflecting surfaces based on a minimum variance unbiased estimator," in *Proc. IEEE Int. Conf. Acou. Speech Signal Process. (ICASSP)*, May 2020, pp. 5000–5004.

[37] B. Zheng and R. Zhang, "Intelligent reflecting surface-enhanced OFDM: Channel estimation and reflection optimization," *IEEE Wireless Commun. Letts.*, vol. 9, no. 4, pp. 518–522, Apr. 2020.

[38] J. Zuo, Y. Liu, Z. Ding, and L. Songg, "Simultaneously transmitting and reflecting (STAR) RIS assisted NOMA systems," in *Proc. IEEE Global Commun. Conf. (GLOBECOM)*, Dec. 2021, pp. 1–6.

[39] X. Lu, P. Wang, D. Niyato, D. Kim, and Z. Han, "Wireless networks with RF energy harvesting: A contemporary survey," *IEEE Commun. Surv. Tuts.*, vol. 17, no. 2, pp. 757–789, Nov. 2015.

[40] B. Clerckx, R. Zhang, R. Schober, D. Ng, D. Kim, and H. Poor, "Fundamentals of wireless information and power transfer: From RF energy harvester models to signal and system designs," *IEEE J. Sel. Areas Commun.*, vol. 37, no. 1, p. 4–33, Jan. 2019.

[41] K. Choi, A. Aziz, D. Setiawan, N. Tran, L. Ginting, and D. Kim, "Distributed wireless power transfer system for internet of things devices," *IEEE Int. Things J.*, vol. 5, no. 4, pp. 2657–2671, Aug. 2018.

[42] A. Bayat and S. Aïssa, "Deep learning based auction-driven beamforming for wireless information and power transfer," *IEEE Trans. Wireless Commun.*, vol. 21, no. 2, pp. 781–793, Feb. 2022.

[43] T. Ponnimbaduge Perera, D. Jayakody, S. Sharma, S. Chatzinotas, and J. Li, "Simultaneous wireless information and power transfer (SWIPT): Recent advances and future challenges," *IEEE Commun. Surv. Tuts.*, vol. 20, no. 1, pp. 264–302, Dec. 2018.

[44] E. Larsson and H. Poor, "Joint beamforming and broadcasting in massive MIMO," *IEEE Trans. Wireless Commun.*, vol. 15, no. 4, pp. 3058–3070, Jan. 2016.

[45] K. Xu, Z. Shen, Y. Wang, and X. Xia, "Resource allocation for hybrid TS and PS SWIPT in massive MIMO system," *Physical Communication*, vol. 28, pp. 201–213, 2018.

[46] Y. Zeng and R. Zhang, "Energy-efficient UAV communication with trajectory optimization," *IEEE Trans. Wireless Commun.*, vol. 16, no. 6, pp. 3747–3760, June 2017.

[47] B. Li, Y. Dai, Z. Dong, E. Panayirci, H. Jiang, and H. Jiang, "Energy-efficient resources allocation with millimeter-wave massive MIMO in ultra dense HetNets by SWIPT and CoMP," *IEEE Trans. Wireless Commun.*, pp. 1–1, Feb. 2021.

[48] J. Tang, D. So, A. Shojaeifard, and K. Wong, "Energy-efficient resource allocation in CoMP-SWIPT heterogeneous networks," in *Proc. IEEE Int. Conf. Commun. China (ICCC)*, Apr. 2017, pp. 1–6.

[49] I. Krikidis, S. Timotheou, S. Nikolaou, G. Zheng, D. Ng, and R. Schober, "Simultaneous wireless information and power transfer in modern communication systems," *IEEE Commun. Mag.*, vol. 52, no. 11, pp. 104–110, Nov. 2014.

[50] X. Chen, Z. Zhang, H. Chen, and H. Zhang, "Enhancing wireless information and power transfer by exploiting multi-antenna techniques," *IEEE Commun. Mag.*, vol. 53, no. 4, pp. 133–141, Apr. 2015.

[51] C. Pan, H. Ren, K. Wang, M. Elkashlan, A. Nallanathan, J. Wang, and L. Hanzo, "Intelligent reflecting surface aided MIMO broadcasting for simultaneous wireless information and power transfer," *IEEE J. Sel. Areas Commun.*, vol. 38, no. 8, pp. 1719–1734, Aug. 2020.

[52] Q. Wu and R. Zhang, "Joint active and passive beamforming optimization for intelligent reflecting surface assisted SWIPT under QoS constraints," *IEEE J. Sel. Areas Commun.*, vol. 38, no. 8, pp. 1735–1748, Aug. 2020.

[53] H. Yang, X. Yuan, J. Fang, and Y. Liang, "Reconfigurable intelligent surface aided constant-envelope wireless power transfer," *IEEE Trans. Sig. Process.*, vol. 69, pp. 1347–1361, Feb. 2021.

[54] Y. Tang, G. Ma, H. Xie, J. Xu, and X. Han, "Joint transmit and reflective beamforming design for IRS-assisted multiuser MISO SWIPT systems," in *Proc. IEEE Int. Conf. Commun. (ICC)*, June 2020, pp. 1–6.

[55] W. Shi, X. Zhou, L. Jia, Y. Wu, F. Shu, and J. Wang, "Enhanced secure wireless information and power transfer via intelligent reflecting surface," *IEEE Commun. Letts.*, pp. 1–1, Dec. 2020.

[56] Z. Mohamed and S. Aïssa, "Coordinated energy beamforming: Wireless power coverage and transmission probability," in *Proc. IEEE Wireless Commun. Net. Conf. (WCNC)*, Apr. 2021, pp. 1–6.

[57] S. Jung, H. Lee, and S. Kim, "Worst-case user analysis in poisson voronoi cells," *IEEE Commun. Letts.*, vol. 17, no. 8, pp. 1580–1583, Aug. 2013.

[58] J. Guo, X. Zhou, and S. Durrani, "Wireless power transfer via mmwave power beacons with directional beamforming," *IEEE Wireless Commun. Letts*, vol. 8, no. 1, pp. 17–20, Feb. 2019.

[59] G. Kamga and S. Aïssa, "Wireless power transfer in mmWave massive MIMO systems with/without rain attenuation," *IEEE Trans. Commun.*, vol. 67, no. 1, pp. 176–189, Jan. 2019.

[60] L. Shi, L. Zhao, K. Liang, X. Chu, G. Wu, and H. Chen, "Profit maximization in wireless powered communications with improved non-linear energy conversion and storage efficiencies," in *Proc. IEEE Int. Conf. Commun. (ICC)*, July 2017, pp. 1–6.

[61] M. Xia and S. Aïssa, "On the efficiency of far-field wireless power transfer," *IEEE Trans. Sig. Proc.*, vol. 63, no. 11, pp. 2835–2847, June 2015.

[62] C. Chen and X. Zhao, "Cell boundary user performance in multi-user MIMO poisson voronoi cell," *IEEE Commun. Letts.*, vol. 22, no. 4, pp. 772–775, Apr. 2018.

[63] J. Filho and M. Yacoub, "Nakagami-m approximation to the sum of M non-identical independent nakagami-m variates," *Elec. Letts.*, vol. 40, no. 15, pp. 951–952, Aug. 2004.

[64] A.Mathai, "A handbook of generalized special functions for statistical and physical sciences," *Oxford University Press*, Mar. 1993.

[65] E. Chen, M. Xia, and S. Aïssa, "Coverage probability of hierarchical wireless networks with hybrid powering/relaying nodes (invited paper)," in *Proc. Int. Symp. Wireless Commun. Systems (ISWCS)*, Oct. 2018, pp. 1–6.

[66] Z. Mohamed, A. Bhowal, and S. Aïssa, "Distance distributions and coverage probabilities in poisson-delaunay triangular cells with application to coordinated multi-point wireless power transfer," *IEEE Trans. Wireless Commun.*, pp. 1–1, May 2022.

[67] D. Taylor, H. Dhillon, T. Novlan, and J. Andrews, "Pairwise interaction processes for modeling cellular network topology," in *Proc. IEEE Global Commun. Conf. (GLOBECOM)*, Dec. 2012, pp. 4524–4529.

[68] K. Baltzis, "Hexagonal vs circular cell shape: A comparative analysis and evaluation of the two popular modeling approximations," in *Cellular Networks - Positioning, Performance Analysis, Reliability.* IntechOpen, Apr. 2011.

[69] Y. Li, M. Xia, and S. Aïssa, "Coordinated multi-point transmission: A poisson-delaunay triangulation based approach," *IEEE Trans. Wireless Commun.*, vol. 19, no. 5, pp. 2946–2959, May 2020.

[70] M. Haenggi, "Stochastic geometry for wireless networks." Cambridge University Press, Nov. 2012.

[71] M. Haenggi, J. Andrews, F. Baccelli, O. Dousse, and M. Franceschetti, "Stochastic geometry and random graphs for the analysis and design of wireless networks," *IEEE J. Sel. Areas Commun.*, vol. 27, no. 7, pp. 1029–1046, Sep. 2009.

[72] X. Liu, "Closed-form coverage probability in cellular networks with poisson point process," *IEEE Trans. Veh. Tech.*, vol. 68, no. 8, pp. 8206–8209, Aug. 2019.

[73] F. Baccelli and A. Giovanidis, "A stochastic geometry framework for analyzing pairwise-cooperative cellular networks," *IEEE Trans. Wireless Commun.*, vol. 14, no. 2, pp. 794–808, Feb. 2015.

[74] C. Guo, J. Xin, L. Zhao, and X. Chu, "Performance analysis of cooperative NOMA with energy harvesting in multi-cell networks," *China Commun.*, vol. 16, no. 11, pp. 120–129, Nov. 2019.

[75] K. Choi, L. Ginting, D. Setiawan, A. Aziz, and D. Kim, "Coverage probability of distributed wireless power transfer system," in *Proc. IEEE Int. Conf. Ubiquitous Future Nets (ICUFN)*, July 2017, pp. 691–696.

[76] S. Srinivasa and M. Haenggi, "Distance distributions in finite uniformly random networks: Theory and applications," *IEEE Trans. Veh. Tech.*, vol. 59, no. 2, pp. 940–949, Feb. 2010.

[77] F. Fabbri and R. Verdone, "A statistical model for the connectivity of nodes in a multi-sink wireless sensor network over a bounded region," in *Proc. IEEE European Wireless Conf.*, June 2008, pp. 1–6.

[78] J. Guo, S. Durrani, and X. Zhou, "Outage probability in arbitrarily-shaped finite wireless networks," *IEEE Trans. Commun.*, vol. 62, no. 2, pp. 699–712, Feb. 2014.

[79] M. Ahmadi and J. Pan, "Random distances associated with arbitrary triangles: a recursive approach with an arbitrary reference point," *UVicSpace*, pp. 1–13, Jan. 2014.

[80] G. Mao and B. Anderson, "Towards a better understanding of large-scale network models," *IEEE Trans. Net.*, vol. 20, no. 2, pp. 408–421, Apr. 2012.

[81] N. Cressie and M. Borkent, "The moment generating function has its moments," *J. Stat. Planning Inference*, vol. 13, pp. 337–344, 1986.

[82] M. Duz, "On an application of laplace transforms," *New Trends in Mathematical Science*, vol. 2, pp. 193–198, July 2017.

[83] L. Muche, "The poisson voronoi tessellation III. miles' formula," *Mathematische Nachrichten*, vol. 191, no. 1, pp. 247–267, 1998.

[84] J. Zhang, M. Matthaiou, G. Karagiannidis, and L. Dai, "On the multivariate Gamma–Gamma distribution with arbitrary correlation and applications in wireless communications," *IEEE Trans. Veh. Tech.*, vol. 65, no. 5, pp. 3834–3840, May 2016.

[85] V. Adamchik and O. Marichev, "The algorithm for calculating integrals of hypergeometric type functions and its realization in REDUCE system," in *Proc. Int. Symp. Symbo. Alg. Comp. (ISSAC)*, July 1990, p. 212–224.

[86] Z. Mohamed and S. Aïssa, "Wireless power transfer aided with reconfigurable intelligent surfaces: Design, and coverage analysis," *Proc. IEEE Int. Symp. Personal Indoor Mobile Radio Commun. (PIMRC)*, Sep. 2022.

[87] C. Psomas, H. Suraweera, and I. Krikidis, "On the association with intelligent reflecting surfaces in spatially random networks," in *Proc. IEEE Int. Conf. Commun.(ICC)*, June 2021, pp. 1–6.

[88] W. Mei and R. Zhang, "Cooperative beam routing for multi-IRS aided communication," *IEEE Wireless Commun. Lets.*, vol. 10, no. 2, pp. 426–430, Feb. 2021.

[89] G. Karagiannidis, N. Sagias, and T. Mathiopoulos, "The N* nakagami fading channel model," in *Proc. IEEE Int. Symp. Wireless Commun. Sys.*, Dec. 2005, pp. 185–189.

[90] S. Primak, V. Kontorovich, and V. Lyandres, *Random Variables and Their Description.*   John Wiley and Sons, Ltd, 2004, ch. 2, pp. 7–58.

[91] Z. Mohamed and S. Aïssa, "Leveraging UAVs with intelligent reflecting surfaces for energy-efficient communications with cell-edge users," in *Proc. IEEE Int. Conf. Commun. (ICC)*, June 2020, pp. 1–6.

[92] L. Zhao, X. Wang, and K. Zheng, "Downlink hybrid information and energy transfer with massive MIMO," *IEEE Trans. Wireless Commun.*, vol. 15, no. 2, pp. 1309–1322, Feb. 2016.

[93] T. Marzetta, "Noncooperative cellular wireless with unlimited numbers of base station antennas," *IEEE Trans. Wireless Commun.*, vol. 9, no. 11, pp. 3590–3600, Nov. 2010.

[94] Y. Li, M. Sheng, C. Yang, and X. Wang, "Energy efficiency and spectral efficiency tradeoff in interference-limited wireless networks," *IEEE Commun. Letts.*, vol. 17, no. 10, pp. 1924–1927, Oct. 2013.

[95] W. Dinkelbach, "On nonlinear fractional programming," *Management Science*, vol. 13, no. 7, pp. 492–498, 1967.

[96] D. B. da Costa and S. Aïssa, "Capacity analysis of cooperative systems with relay selection in nakagami-m fading," *IEEE Commun. Lets.*, vol. 13, no. 9, pp. 637–639, Sep. 2009.

[97] Z. Mohamed and S. Aïssa, "Resource allocation for energy-efficient cellular communications via aerial IRS," in *Proc. IEEE Wireless Commun. Net. Conf. (WCNC)*, Apr. 2021.

[98] M. Grant and S. Boyd, "CVX: Matlab software for disciplined convex programming, version 2.1," http://cvxr.com/cvx, Mar. 2014.

[99] B. Wang, Y. Chang, and D. Yang, "On the SINR in massive MIMO networks with MMSE receivers," *IEEE Commun. Letts.*, vol. 18, no. 11, pp. 1979–1982, Nov. 2014.

[100] S. Zhang, H. Zhang, Q. He, K. Bian, and L. Song, "Joint trajectory and power optimization for UAV relay networks," *IEEE Commun. Letts.*, vol. 22, no. 1, pp. 161–164, Oct. 2018.

[101] Z. Mohamed and S. Aïssa, "Energy-efficient joint broadcast-unicast communications via dual-polarized aerial RIS," *IEEE Trans. Wireless Commun.*, pp. 1–1, Sep. 2022.

[102] A. Qiaochu, S. Yuanming, and Z. Yong, "Reconfigurable intelligent surface assisted non-orthogonal unicast and broadcast transmission," in *Proc. IEEE Veh. Tech. Conf. (VTC-Spring)*, May 2020, pp. 1–5.

[103] H. Han, J. Zhao, D. Niyato, M. Di Renzo, and Q. Pham, "Intelligent reflecting surface aided network: Power control for physical-layer broadcasting," in *Proc. IEEE Int. Conf. Commun. (ICC)*, June 2020, pp. 1–7.

[104] O. Tervo, L. Trant, S. Chatzinotas, B. Ottersten, and M. Juntti, "Multigroup multicast beamforming and antenna selection with rate-splitting in multicell systems," in *Proc. IEEE SPAWC*, Dec. 2018, pp. 1–5.

[105] G. Zhou, C. Pan, H. Ren, K. Wang, and A. Nallanathan, "Intelligent reflecting surface aided multigroup multicast MISO communication systems," *IEEE Trans. Signal Process.*, vol. 68, pp. 3236–3251, Apr. 2020.

[106] O. Özdogan, E. Björnson, and E. Larsson, "Using intelligent reflecting surfaces for rank improvement in MIMO communications," in *Proc. IEEE Int. Conf. Acou. Speech Sig. Process. (ICASSP)*, May 2020, pp. 9160–9164.

[107] Y. Guo, S. Yin, and J. Hao, "Joint placement and resources optimization for multi-user UAV-relaying systems with underlaid cellular networks," *IEEE Trans. Veh. Tech.*, vol. 69, no. 10, pp. 12 374–12 377, Aug. 2020.

[108] J. Park and B. Clerckx, "Multi-user linear precoding for multi-polarized massive MIMO system under imperfect CSIT," *IEEE Trans. Wireless Commun.*, vol. 14, pp. 2532–2547, May 2015.

[109] A. de Sena, P. Nardelli, D. da Costa, F. Lima, L. Yang, P. Popovski, Z. Ding, and C. Papadias, "IRS-assisted massive MIMO-NOMA networks: Exploiting wave polarization," *IEEE Trans. Wireless Commun.*, vol. 20, no. 11, pp. 7166–7183, Nov. 2021.

[110] Y. Han, X. Li, W. Tang, S. Jin, Q. Cheng, and T. Cui, "Dual-polarized RIS-assisted mobile communications," *IEEE Trans. Wireless Commun.*, vol. 21, no. 1, pp. 591–606, July 2021.

[111] J. Ke, J. Dai, M. Chen, L. Wang, C. Zhang, W. Tang, J. Yang, W. Liu, X. Li, Y. Lu, Q. Cheng, S. Jin, and T. Cui, "Linear and nonlinear polarization syntheses and their programmable controls based on anisotropic time-domain digital coding metasurface," *Small Structures*, vol. 2, no. 1, p. 2000060, 2021.

[112] X. Chen, J. Ke, W. Tang, M. Chen, J. Dai, E. Basar, S. Jin, Q. Cheng, and T. Cui, "Design and implementation of MIMO transmission based on dual-polarized reconfigurable intelligent surface," *IEEE Wireless Commun. Letts.*, pp. 1–1, July 2021.

[113] Z. Mohamed and S. Aïssa, "Energy-efficient joint broadcast-unicast communications via aerial RIS," *IEEE Wireless Commun. Net. Conf. (WCNC)*, Mar. 2023.

[114] F. Quitin, C. Oestges, F. Horlin, and P. De Doncker, "Small-scale variations of cross-polar discrimination in polarized MIMO systems," in *Proc. European Conf. Antennas and Propagation (EUCAP)*, Mar. 2009, pp. 1011–1015.

[115] G. Zafari, M. Koca, and H. Sari, "Dual-polarized spatial modulation over correlated fading channels," *IEEE Trans. Commun.*, vol. 65, no. 3, pp. 1336–1352, Mar. 2017.

[116] S. Gong, C. Xing, S. Chen, N. Yang, and Y. Zhou, "Robust energy-efficient precoding optimization for dual-polarized multiuser MIMO downlink," in *Proc. IEEE Int. Conf. Commun. China (ICCC)*, Apr. 2017, pp. 1–6.

[117] A. Sousa de Sena, D. Benevides da Costa, Z. Ding, and P. Nardelli, "Massive MIMO–NOMA networks with multi-polarized antennas," *IEEE Trans. Wireless Commun.*, vol. 18, no. 12, pp. 5630–5642, Dec. 2019.

[118] O. Tervo, L. Tran, S. Chatzinotas, M. Juntti, and B. Ottersten, "Energy-efficient joint unicast and multicast beamforming with multi-antenna user terminals," in *Proc. IEEE SPAWC*, Dec. 2017, pp. 1–5.

[119] C. Huang, A. Zappone, M. Debbah, and C. Yuen, "Achievable rate maximization by passive intelligent mirrors," in *in Proc. IEEE Int. Conf. Acoust. Speech Sig. Process. (ICASSP)*, Apr. 2018, pp. 3714–3718.

[120] K. Shen and W. Yu, "Fractional programming for communication systems—part I: Power control and beamforming," *IEEE Trans. Sig. Process.*, vol. 66, no. 10, pp. 2616–2630, Mar. 2018.

[121] Z. Luo, W. Ma, A. So, Y. Ye, and S. Zhang, "Semidefinite relaxation of quadratic optimization problems," *IEEE Sig. Process. Mag.*, vol. 27, no. 3, pp. 20–34, May 2010.

[122] A. Li and C. Masouros, "Hybrid analog-digital millimeter-wave MU-MIMO transmission with virtual path selection," *IEEE Commun. Letts.*, vol. 21, no. 2, pp. 438–441, Feb. 2017.

[123] A. Lewis, "Lectures on modern convex optimization: Analysis, algorithms, and engineering applications," *SIAM Review*, vol. 44, no. 4, pp. 731–734, 2002.

[124] L. Zhang, W. Li, Y. Wu, X. Wang, S. Park, H. Kim, J. Lee, P. Angueira, and J. Montalban, "Layered-division-multiplexing: Theory and practice," *IEEE Trans. Broad.*, vol. 62, no. 1, pp. 216–232, Mar. 2016.

[125] X. Yin, S. Gong, S. Wang, and Z. Zhang, "Two timescale robust energy-efficient precoding for dual-polarized MIMO systems," *IEEE Trans. Commun.*, vol. 68, no. 9, pp. 5575–5589, Sep. 2020.

[126] J. Tang, D. So, E. Alsusa, and K. Hamdi, "Resource efficiency: A new paradigm on energy efficiency and spectral efficiency tradeoff," *IEEE Trans. Wireless Commun.*, vol. 13, no. 8, pp. 4656–4669, Aug. 2014.

[127] J. Tang, A. Shojaeifard, D. So, K. Wong, and N. Zhao, "Energy efficiency optimization for CoMP-SWIPT heterogeneous networks," *IEEE Trans. Commun.*, vol. 66, no. 12, pp. 6368–6383, Dec. 2018.

[128] L. Van, F. Charles, and G. Golub, "Matrix computations (johns hopkins studies in mathematical sciences)," *Matrix Computations*, 1996.

[129] J. Xu, L. Liu, and R. Zhang, "Multiuser MISO beamforming for simultaneous wireless information and power transfer," *IEEE Trans. Sig. Process.*, vol. 62, no. 18, pp. 4798–4810, Sep. 2014.

[130] A. Aubry, V. Carotenuto, and A. Maio, "New results on generalized fractional programming problems with toeplitz quadratics," *IEEE Signal Process. Letts.*, vol. 23, no. 6, pp. 848–852, June 2016.

[131] R. Beals and J. Szmigielski, "Meijer G–functions: A gentle introduction," *Notices of the American Mathematical Society*, vol. 60, Aug. 2013.

[132] J. Moller, *Lectures on Random Voronoi Tessellations*, ser. Lecture Notes in Statistics. Springer New York, 2012.

Part IV

Résumé en Français

Transmission éco-énergétique de l'information et de puissance assistée par surfaces intelligentes reconfigurables

par

Zina Mohamed

Synthèse en français

Récemment, les surfaces intelligentes reconfigurables (SIR) ont attiré l'attention de l'industrie et du milieu universitaire en tant que solution potentielle aux effets de perte de chemin, d'ombrage et de trajets multiples et en tant que technologie prometteuse pour améliorer les performances des futurs réseaux. Les RIS sont des réseaux plans, constitués d'éléments réfléchissants presque passifs et à faible coût, qui contrôlent l'environnement de propagation en réfléchissant le signal incident dans une direction spéciale en concevant et en ajustant correctement les valeurs de déphasage des éléments réfléchissants. Cette thèse vise à concevoir un cadre pour le transfert d'information et de puissance sans fil assisté par RIS. Nous nous concentrons sur l'évaluation, la conception et l'amélioration de l'efficacité énergétique (EE) et de la fiabilité de différents types de systèmes : transfert d'énergie sans fil (WPT), transfert d'informations sans fil (WIT) et transfert simultané d'informations et d'énergie sans fil (SWIPT). En particulier, dans la première partie de ce travail, nous visons à concevoir un WPT coopératif assisté par RIS à haut rendement. À cette fin, la conception d'un WPT coopératif est considérée comme un point de départ. Plus précisément, nous nous concentrons sur l'amélioration de l'efficacité de la transmission en abordant les mesures les plus importantes caractérisant les performances du système, à savoir la probabilité de couverture WPT et la probabilité de transmission de données. Le cadre et la conception développés sont ensuite étendus au cas de plusieurs systèmes WPT assistés par RIS. Ensuite, dans la deuxième partie de ce travail, nous nous concentrons sur la conception d'un système WIT assisté par RIS économe en énergie pour les utilisateurs de la périphérie cellulaire. En particulier, deux scénarios sont envisagés : le service unique ou monodiffusion et les services multiples la diffusion monodiffusion conjointe. Enfin, la troisième partie de cette thèse se concentre sur la conception d'un système SWIPT assisté par RIS basé sur l'espace nul. L'objectif principal de cette partie est d'atteindre un équilibre entre l'énergie récupérée au niveau des récepteurs d'énergie et le débit total des récepteurs d'informations. Un cadre pour optimiser une fonction multi-objectif est proposé.

Le chapitre 1 présente l'état de l'art de la technologie SIR en se concentrant sur les comparaisons avec la technologie de relais, les travaux orientés vers l'optimisation, l'estimation des canaux, la conception des SIR, ainsi que les limites et les défis. D'autre part, le concept et les défis du transfert d'information et de puissance sans fil sont également présentés.

La première partie de cette thèse porte sur la conception d'un WPT coopératif assisté par SIR. En particulier, des outils de géométrie stochastique pour modéliser les nœuds de réseau distribué du processus ponctuel de Poisson (PPP) (points d'accès (AP), appareil, SIR) et pour déterminer les expressions sous forme fermée de la probabilité de couverture WPT et de la probabilité de transmission de données pour différents types des appareils sont exploités. Les expressions obtenues sont une fonction de la fonction de MeijerG multivariée généralisée étendue (EGMMGF). Une nouvelle implémentation de l'EGMMGF est également présentée. Les formules proposées dans

cette partie évitent la plupart des problèmes de complexité et de consommation de temps déjà dans la littérature. Les résultats fournissent une ligne directrice pour dériver des formules traitables similaires pour différents modèles de système.

La deuxième partie de cette thèse porte sur la conception d'un WIT assisté par RIS économe en énergie pour les utilisateurs de la périphérie cellulaire pour deux scénarios de déploiement : le service unique (unicast) et le multiservice (diffusion-unicast conjointe). En particulier, un drone équipé d'un RIS est mis à profit pour faciliter la communication en liaison descendante et en liaison montante. L'objectif principal est de maximiser l'efficacité énergétique (EE) des utilisateurs de bord de cellule en concevant correctement les matrices de formation de faisceau actives et passives. Des solutions optimales pour résoudre les problèmes d'optimisation sont présentées. Les résultats numériques montrent que des améliorations significatives des performances sont obtenues par le SIR-UAV par rapport à son homologue, mais avec des techniques de relais standard et valident que le SIR-UAV peut être exploité pour servir les utilisateurs en périphérie de cellule avec un EE élevé. De plus, une conception de cadre pour une communication conjointe en liaison descendante monodiffusion-diffusion assistée par un SIR aérien à double polarisation est proposée. Les résultats montrent la supériorité de l'exploitation de la polarisation pour la transmission conjointe de différents types de modèles de trafic.

Contrairement aux parties I et II qui ne traitent que des systèmes WPT ou WIT, les systèmes SWIPT sont explorés dans la partie III de cette thèse. Plus précisément, une conception de cadre pour le SWIPT assisté par RIS basée sur le degré de liberté fourni par l'espace nul de la matrice de canal composite entre l'AP et les récepteurs d'informations est proposée pour envoyer un signal d'énergie supplémentaire. L'objectif principal est d'atteindre un équilibre entre l'énergie récupérée au niveau des récepteurs d'énergie (ER) et le débit total des récepteurs d'informations (IR). Sur la base du cadre d'optimisation multi-objectifs (MOO) et de l'approche pondérée de Tchebycheff, le problème de maximisation du taux de somme équivalent est formulé en premier. Ensuite, un algorithme efficace à deux couches est proposé pour concevoir les vecteurs de formation de faisceaux d'informations actives au point d'accès (AP) et la matrice de formation de faisceaux passive au SIR. Les résultats de cette partie sont nouveaux et soulignent l'importance d'intégrer le RIS et d'exploiter l'espace nul lors de la conception des systèmes SWIPT.

Enfin, le chapitre 9 conclut cette thèse et propose les travaux futurs.

Chapter 10

Résumé

10.1 Introduction

10.1.1 Introduction du SIR

De nos jours, les réseaux sans fil de nouvelles générations de communications apporteront de nombreuses applications et commodités pour rendre la vie plus facile, plus fluide et plus confortable avec une meilleure qualité de service (QoS), des coûts et une complexité réduits [1]. Les recherches montrent que les communications 6Gs sont destinées à fournir une connectivité massive, une couverture plus large, un débit élevé, une capacité améliorée, une fiabilité élevée et une faible latence grâce à ses cas d'utilisation telque les communications de type machine, les communications ultra-fiable et à faible latence (uRLLC), les communications à très faible puissance et les communications longue distance et à haute mobilité.

Pour répondre aux exigences strictes de la connectivité des appareils qui devrait être supérieure à 107 appareils/Km^2; la fiabilité qui est censée être supérieure à 99,9999%, la latence qui est censée être inférieure à 0,1 ms; le débit qui sera supérieur à 1 Tb/s et l'efficacité énergétique qui devrait être 10 à 100 fois supérieure à celle de la 5G [1–3], les recherches se sont multipliées. En particulier, l'accent a été mis sur les interruptions de connectivité causées par le caractère aléatoire de l'environnement de communication, c'est-à-dire les canaux sans fil, la perte de trajet, les effets d'ombrage et le blocage (obstacles). Comme solution, le déploiement de plus de stations de base (BS), de plus d'antennes au niveau de la BS ou l'utilisation de plus de spectre ont été proposés pour faire face à ces limitations. Cependant, ces techniques entraînent une forte consommation d'énergie, des coûts de déploiement et de maintenance élevés et une grande complexité de traitement du signal. Par conséquent, l'objectif principal de la recherche a été tourné vers la conception de techniques sophistiquées au niveau de l'émetteur et du récepteur pour compenser les effets de la propagation et pour transformer l'environnement de propagation lui-même en une variable d'optimisation, c'est-à-dire la création d'un environnement radio intelligent. Parmi les techniques émergents rentables, les surfaces intelligentes reconfigurables (SIR) ont suscité un large intérêt de la part de l'industrie et du milieu universitaire en tant que technologie prometteuse pour les communications à faible coût, agiles et intelligents [4].

6

10.1.2 Transfert de l'Information et de Puissance Sans Fil

Ces dernières années, la récupération d'énergie (EH) est devenue une technologie habilitante pour relever le défi clé de la durabilité dans les réseaux de communication en croissance constante. En particulier, pour faire face aux énormes demandes énergétiques des appareils sans fil, les radiofréquences (RF) ont été considérées comme fournissant une source d'énergie stable et contrôlable [39, 40] et constituaient une solution prometteuse pour améliorer les futurs réseaux sans fil en prolongeant leur durée de vie. EH a reçu une grande attention de la part de la communauté de la recherche et de l'industrie et a été intégré dans de nombreuses applications, y compris les réseaux de capteurs sans fil, les industries de la maison intelligente et l'Internet des objets (IoT) en général [41]. En conséquence, l'intégration de la capacité EH dans les systèmes de communication sans fil traditionnels est récemment apparue comme une orientation de recherche importante, à savoir les réseaux de communication sans fil, où le transfert de puissance sans fil (WPT) est effectuée sur la liaison descendante et la transmission d'informations sans fil (WIT) a lieu sur la liaison montante. Dans une tentative d'exploiter la double utilisation des signaux RF pour transférer conjointement l'information et l'énergie, les chercheurs se sont concentrés sur l'unification des processus de transmission de l'information et de l'énergie. Cette unification mène à une nouvelle technologie appelée le transfert simultané d'information et de puissance sans fil (SWIPT), où le décodage d'information (ID) et EH sont effectués simultanément. SWIPT est devenu une technologie attrayante et a suscité un intérêt généralisé en tant que solution prometteuse aux contraintes de puissance des systèmes de communication sans fil émergents en prolongeant la durée de vie du réseau sans avoir besoin de recharger la batterie et/ou de la remplacer, qui entraînent des coûts élevés. De plus, l'exploitation de l'énergie de l'environnement est une technologie prometteuse pour améliorer l'efficacité énergétique des réseaux sans fil. SWIPT a reçu un large intérêt en tant que solution prometteuse au problème de l'efficacité limitée, qui est d'une importance primordiale et l'un des aspects de conception les plus difficiles des systèmes de communication sans fil émergents. Sans être interrompu par l'épuisement de l'énergie dû à l'utilisation des communications, SWIPT devrait améliorer l'expérience et la commodité de l'utilisateur, avec des performances de débit plus élevées et plus durables par rapport aux systèmes de communication conventionnels alimentés par batterie. Plusieurs travaux de recherche ont été menés dans la littérature pour étudier le SWIPT du point de vue de la conception, de l'évaluation des performances et de l'optimisation. Par exemple, une étude complète de l'état de l'art de SWIPT et des idées connexes telles que les architectures d'émetteurs-récepteurs pratiques, les modèles SWIPT et l'exploitation des interférences est fournie dans [43]. De plus, le compromis débit et énergie (R-E) est étudié dans plusieurs travaux, par exemple, [40, 44–46]. Motivés par les potentiels de la transmission multipoint coordonnée (CoMP) et de la formation de faisceaux multi-antennes pour améliorer la puissance du signal et l'efficacité de la transmission, les systèmes CoMP-SWIPT ont été étudiés dans [47, 48].

10.1.3 WIPT Assisté par SIR

Rappelons que l'objectif principal des systèmes de communication sans fil de nouvelle génération est d'améliorer la connectivité en augmentant les débits de données, la couverture, les bandes passantes et la fiabilité tout en réduisant la consommation d'énergie. En réponse à ces exigences majeures, le développement de la communication verte et l'amélioration de l'EE deviennent une nécessité.À cette fin, l'une des solutions prometteuses qui a récemment attiré l'attention des chercheurs, est de tirer parti des avantages des SIRS pour aider les systèmes SWIPT. Ce domaine de recherche est encore

balbutiant et peu de travaux de recherche sont récemment apparus dans la littérature [51–53]. Par exemple, dans [52], le problème de maximisation de la somme de puissance pondérée a été étudié pour un système SWIPT assisté par SIR, sans signaux porteurs d'énergie dédiés. Dans [51], le problème de maximisation du débit minimum a été formulé et résolu dans des conditions de canal idéales et non idéales sur la base d'un algorithme itératif. Dans [53], le taux de somme pondéré est maximisé sous les contraintes de QoS, en optimisant conjointement les matrices de formation de faisceau actives et la matrice de réflexion au niveau des SIR pour le système SWIPT.

Récemment, des travaux de recherche se sont concentrés sur l'amélioration de l'efficacité de la puissance sans fil et la réduction de la puissance de transmission, ainsi que sur la fourniture de plus de flexibilité et de degré de liberté pour la conception de la formation de faisceaux pour l'énergie et l'information, améliorant ainsi à la fois le débit total et la quantité d'énergie récoltée dans les systèmes SWIPT [2,52]. En général, la conception de la formation de faisceaux devient plus difficile en raison du compromis et des objectifs de conception contradictoires pour les transferts d'informations et de puissance. Cela motive la nécessité de repenser en profondeur aux techniques de formation de faisceaux existantes. Afin d'adapter la solution proposée aux objectifs contradictoires ci-dessus, un problème d'optimisation avec des contraintes non convexes a été proposé et résolu dans [51, 54, 55].

Notez que les études mentionnées au dessus étaient basées sur des techniques d'optimisation conventionnelles pour concevoir les vecteurs de formation de faisceaux d'énergie et d'information des systèmes SWIPT assistés par SIR.

10.2 Objectifs de Recherche

L'objectif de cette thèse est de concevoir un cadre pour le transfert d'information et de puissance sans fil assisté par SIR, en mettant l'accent sur l'évaluation, l'optimisation et l'amélioration de l'efficacité énergétique et de la fiabilité de la transmission sans fil. À cette fin, différentes formes de systèmes sont envisagées telles que WPT, WIT et SWIPT. Les objectifs spécifiques découlant de l'objectif ultime se résument comme suit:

- Concevoir un WPT coopératif assisté par SIR avec un rendement élevé. Comme point de départ, la conception d'un WPT coopératif est considérée. L'objectif principal de ce travail est d'améliorer l'efficacité de la transmission en abordant les métriques les plus importantes caractérisant les performances du système, à savoir la probabilité de couverture WPT et la probabilité de transmission de données. Ensuite, le cadre et la conception développés seront étendus pour couvrir le cas de plusieurs SIR coopérant pour le WPT afin d'atteindre l'objectif principal de cette partie.

- Concevoir un WIT assisté par SIR économe en énergie pour les utilisateurs en périphérie de cellule. Deux scénarios de déploiement sont étudiés dans cette partie : le service unique ou monodiffusion (communication descendante et montante) et les services multiples (la transmission conjointe monodiffusion-diffusion).

- Concevoir un système SWIPT assisté par SIR efficace basé sur le degré de liberté fourni par l'espace nul du canal composite entre l'AP et les IRs. L'objectif principal de cette partie est d'atteindre un équilibre entre le débit total des IRs et la puissance récupérée aux ERs.

10.3   Méthodologie

10.3.1   Partie I: WPT assisté par SIR

L'objectif de la première partie de cette thèse est d'améliorer l'efficacité du système WPT, d'augmenter la puissance du signal au niveau des dispositifs de collecte, et donc la couverture énergétique et l'énergie pour la transmission de données. À cette fin, ce travail propose d'exploiter la formation de faisceaux d'énergie coopérative.

Le premier chapitre de cette partie considère un réseau de communication sans fil, où plusieurs points d'accès, distribués selon PPP, collaborent pour transférer l'alimentation sans fil aux appareils sur la liaison descendante, qui est ensuite utilisée pour la transmission de données sur la liaison montante. L'objectif principal de ce chapitre est de dériver la probabilité de couverture WPT et la probabilité de transmission de données dans leurs expressions de forme fermée, et de fournir une étude comparative du mécanisme coopératif avec le schéma non coopératif conventionnel. En particulier, la tessellation de Poisson-Voronoi est prise en compte et chaque appareil est desservi par le ou les points d'accès actifs les plus proches. Cela motive la catégorisation des dispositifs en trois types : cellule interne, bord de cellule et cellule vertex. En exploitant des outils de géométrie stochastique et en se basant sur l'approche de la fonction génératrice de moment (MGF), les expressions pour les trois types d'appareils sont fournies et évaluées. De telles analyses souligneront l'importance d'exploiter les outils de formation de faisceaux coopératifs et de géométrie stochastique pour concevoir un système WPT à haut rendement.

Motivés par le fait que la formation de faisceaux d'énergie coopérative améliore l'efficacité de la transmission, les performances de la formation de faisceaux d'énergie multipoint coordonnée (CoMPe) dans un Poisson-Delaunay triangulaire sont étudiées dans le deuxième chapitre de la partie I. En particulier, les points d'accès sont distribués selon PPP et coopèrent ensemble pour répondre aux besoins énergétiques des appareils uniformément répartis dans la zone de couverture. L'appareil typique est desservi par trois points d'accès. En fonction de la distance entre le point d'accès de desserte et l'appareil cible, trois types d'appareils sont considérés ici. L'objectif principal est de fournir des formules fermées traitables pour la probabilité de couverture WPT et de mener une étude comparative avec un schéma WPT non coopératif. À cette fin, tout d'abord, les fonctions de densité de probabilité de distance (PDF) sont dérivées, car elles n'ont pas été explorées auparavant pour ce type de tessellation. Ensuite, les outils de géométrie stochastique, l'approche MGF et les PDF nouvellement dérivés sont utilisés pour dériver les expressions sous forme fermée de la probabilité de couverture WPT. Une comparaison avec la tessellation de Poisson-Voronoi est également présentée dans ce chapitre.

Malgré le gain obtenu avec CoMPe, certains appareils souffrent encore d'un faible rendement, notamment en présence d'obstacles ou lorsqu'ils sont situés à de grandes distances. Pour traiter cette question, le troisième chapitre de cette partie propose de tirer parti des SIF coopératifs pour assister le système WPT. En particulier, les équipements et les SIR sont répartis selon un PPP. Pour l'analyse, un dispositif typique D est considéré, qui est supposé être dans le champ lointain de la balise de puissance (PB) sans LoS direct entre les deux. Deux configurations de conceptions sont envisagées : (i) la configuration en cascade, où le signal transmis par le BP atteint l'équipement final via le canal en cascade entre K SIR, (ii) la configuration distribuée, où les SIR K relaient simultanément le signal du PB vers l'appareil final. L'objectif principal de ce chapitre est de présenter le cadre théorique pour la dérivation de la probabilité de couverture WPT basée sur des

outils de géométrie stochastique et l'approche MGF pour le système WPT assisté par SIR coopératif pour les deux configurations susmentionnées et de fournir une étude comparative avec un système WPT assisté par une seule SIR.

10.3.2 Partie II: WIT Assisté par SIR

La deuxième partie de cette thèse vise à concevoir un système WIT qui améliore les performances de communication des utilisateurs affamés (c'est-à-dire les utilisateurs en zone morte ou à la périphérie de la cellule). Ce travail propose de tirer parti du RIS aérien pour faciliter la communication puisque les UAV sont une solution très prometteuse qui offre de bonnes conditions de connectivité, une capacité de canal améliorée, une zone de couverture étendue et un déploiement flexible. Par conséquent, l'équité entre les utilisateurs est garantie et des gains de performances élevés sont obtenus au niveau des utilisateurs en périphérie de cellule. Motivés par cela, l'évaluation, la conception et l'amélioration de l'EE des systèmes WIT assistés par SIR aériens dans deux scénarios de déploiement, à savoir, service unique et multiservices, sont explorées.

Dans le premier chapitre de cette partie, le système à l'étude consiste en une BS avec une antenne M qui envoie des flux de données indépendants à des UE au sol à antenne unique K éloignés de la BS, c'est-à-dire des utilisateurs en périphérie de cellule. La communication descendante est assistée par un drone équipé d'éléments réfléchissants N. L'objectif de ce chapitre est de maximiser l'EE en concevant conjointement les matrices de formation de faisceau active et passive. À cette fin, le cas limite de la technique MRT est utilisé pour concevoir les vecteurs de formation de faisceaux à la BS. Ensuite, le problème d'optimisation est réduit à la recherche d'un algorithme d'allocation de puissance et d'une conception de matrice de déphasage efficaces. Comme solution, un algorithme itératif efficace basé sur des techniques d'optimisation alternées est proposé. En particulier, la matrice d'allocation de puissance est obtenue sur la base de la méthode du point intérieur, et la matrice de déphasage est obtenue sur la base du SDR.

Dans le deuxième chapitre de la partie II, la communication cellulaire montante assistée par RIS-UAV est étudiée. L'objectif principal est de concevoir conjointement les puissances d'émission des utilisateurs, la formation de faisceau active au niveau des stations de base et la formation de faisceau passive au SIR tout en satisfaisant aux exigences de qualité de service afin de maximiser l'EE pour les utilisateurs en périphérie de cellule. Pour traiter le problème non convexe hautement insoluble, une solution itérative basée sur des techniques d'optimisation alternées est proposée. En particulier, l'allocation de puissance est conçue sur la base de l'algorithme de Dinkelbach ; les vecteurs de formation de faisceaux sont obtenus sur la base de MMSE, et la matrice de déphasage est conçue sur la base de SDR.

Dans le troisième chapitre de la partie II, les avantages potentiels en termes de performances apportés par un SIR-UAV à double polarisation dans la transmission de deux types de modèles de trafic avec un EE élevé, à savoir les transmissions unicast et broadcast, sont étudiés. La communication de liaison descendante assistée par un SIR aérien à double polarisation, où la BS transmet simultanément des flux de données indépendants à un ensemble d'UE et diffuse un autre flux de données à un autre ensemble d'UE, à une grande distance de la BS. L'objectif principal de ce travail est de maximiser l'EE du système en concevant conjointement les formateurs de faisceaux au BS pour les messages unicast et broadcast et la matrice de déphasage au SIR aérien tout en tenant compte des exigences de QoS de tous les services et de la contraintes de module unitaire

au RIS aérien. À cette fin, un algorithme efficace à deux étapes de faible complexité est proposé pour résoudre le problème formulé. Dans la première étape, la matrice de formation de faisceau passive du SIR aérien à double polarisation est conçue sur la base de la méthode de randomisation gaussienne, qui détend le QCQP non convexe inhomogène en un programme semi-défini. Dans la deuxième étape, la formation de faisceaux active au niveau de la BS est conçue sur la base d'une approche de formation de faisceaux à double structure, dans laquelle la méthode du point intérieur est utilisée pour obtenir la matrice de pré-formation de faisceaux, et les matrices de formation de faisceaux relatives à l'unicasting et à la diffusion sont obtenues sur la base de forçage zéro de faible complexité et approximation convexe successive, respectivement.

10.3.3 Partie III: SWIPT assisté par SIR

Contrairement aux deux parties précédentes qui ne traitent que du transfert de puissance ou du transfert d'informations, la partie III de cette thèse se concentre sur le système SWIPT assisté par SIR. Un cadre de conception pour coordonner et équilibrer le taux de somme des IRs et l'énergie récoltée aux ERs est proposé. En particulier, les degrés de liberté du canal entre les IRS et l'AP sont utilisés pour construire le signal d'énergie. Tout d'abord, l'espace nul de la matrice est calculé sur la base du SVD. Deuxièmement, le signal d'énergie est choisi comme vecteur propre correspondant à la plus grande valeur propre de la version projetée du canal entre les ER et l'AP dans l'espace nul calculé. Troisièmement, un problème MOO est formulé et vise à concevoir conjointement la matrice de formation de faisceaux d'informations de transmission active au point d'accès et la matrice de formation de faisceaux passive au SIR tout en satisfaisant aux exigences de qualité de service. Enfin, pour résoudre le problème de maximisation formulé hautement non convexe, le cadre MOO et l'approche pondérée de Tchebycheff sont exploités pour formuler le problème de maximisation des taux de somme équivalente (ESR) qui peut être résolu avec un algorithme à deux couches basé sur les techniques d'optimisation alternées. En particulier, la formation de faisceau active au niveau de l'AP est conçue sur la base de techniques ZF à faible complexité dans la première couche, et la matrice de formation de faisceau passive au SIR est conçue sur la base de la méthode de randomisation gaussienne et du SDR.

Part V

Appendix

Appendix A

Proof of Theorem 7.3

Firstly, we prove the convergence of the active beamforming algorithm, i.e., Algorithm 7.4. For a given η_{EE}, the objective function is given by

$$\mathcal{J}(\mathbf{P}, \mathbf{V}, \mathbf{w}) = R - \eta_{\text{EE}} P_{\Sigma}. \tag{A.1}$$

Let the solution obtained in the tth iteration of Algorithm 2 be $\left\{\mathbf{P}^{(t)}, \mathbf{V}^{(t)}, \mathbf{w}^{(t)}\right\}$. At the $(t+1)^{\text{th}}$ iteration, we first obtain the optimal $\mathbf{P}^{(t+1)}$ for fixed $\mathbf{V}^{(t)}$ and $\mathbf{w}^{(t)}$, which clearly satisfies

$$\mathcal{J}\left(\mathbf{P}^{(t)}, \mathbf{V}^{(t)}, \mathbf{w}^{(t)}\right) \geq \mathcal{J}\left(\mathbf{P}^{(t+1)}, \mathbf{V}^{(t)}, \mathbf{w}^{(t)}\right), \tag{A.2}$$

because the optimization (7.34) is a standard convex problem. Given $\mathbf{P}^{(t)}$ and $\mathbf{w}^{(t)}$, at iteration $(t+1)$ we design $\mathbf{V}^{(t+1)}$ based on low-complexity ZF, which satisfies

$$\mathcal{J}\left(\mathbf{P}^{(t+1)}, \mathbf{V}^{(t)}, \mathbf{w}^{(t)}\right) \geq \mathcal{J}\left(\mathbf{P}^{(t+1)}, \mathbf{V}^{(t+1)}, \mathbf{w}^{(t)}\right). \tag{A.3}$$

Similarly, $\mathbf{w}^{(t+1)}$ obtained in the $(t+1)^{\text{th}}$ iteration, which is the solution of the SDP (7.40), satisfies

$$\mathcal{J}\left(\mathbf{P}^{(t+1)}, \mathbf{V}^{(t+1)}, \mathbf{w}^{(t)}\right) \geq \mathcal{J}\left(\mathbf{P}^{(t+1)}, \mathbf{V}^{(t+1)}, \mathbf{w}^{(t+1)}\right). \tag{A.4}$$

Combining (A.2) to (A.4), we obtain

$$\mathcal{J}\left(\mathbf{P}^{(0)}, \mathbf{V}^{(0)}, \mathbf{w}^{(0)}\right) \geq \mathcal{J}\left(\mathbf{P}^{(1)}, \mathbf{V}^{(1)}, \mathbf{w}^{(1)}\right) \geq \cdots \geq \mathcal{J}\left(\mathbf{P}^{(t)}, \mathbf{V}^{(t)}, \mathbf{w}^{(t)}\right), \tag{A.5}$$

which indicates that the functional $\mathcal{J}(\mathbf{P}, \mathbf{V}, \mathbf{w})$ is non-increasing as t increases. Next, we prove that the objective function in (7.34) is invariant to increase in t. Recalling the SINR definitions in (7.12) and (7.14), it is clear that upper bounds on these SINRs are given by

$$\gamma_{\text{u},j} \leq \left| \left((\mathbf{h}_{\text{u},j}^{\text{v}})^{\text{H}} \boldsymbol{\Phi}^{\text{v}} (\mathbf{H}_{\text{BS-RIS}}^{\text{hv}})^{\text{H}} + (\mathbf{h}_{\text{u},j}^{\text{hv}})^{\text{H}} \boldsymbol{\Phi}^{\text{vh}} (\mathbf{H}_{\text{BS-RIS}}^{\text{v}})^{\text{H}} \right. \right.$$
$$\left. \left. + (\mathbf{h}_{\text{u},j}^{\text{v}})^{\text{H}} \boldsymbol{\Phi}^{\text{hv}} (\mathbf{H}_{\text{BS-RIS}}^{\text{vh}})^{\text{H}} + (\mathbf{h}_{\text{u},j}^{\text{hv}})^{\text{H}} \boldsymbol{\Phi}^{\text{h}} (\mathbf{H}_{\text{BS-RIS}}^{\text{vh}})^{\text{H}} \right) \mathbf{p}_j^{\text{v}} \mathbf{v}_j \right|^2, \tag{A.6}$$

$$\gamma_{\mathrm{b},k} \leq \left| \left(\mathbf{h}_{\mathrm{b},k}^{\mathrm{vh}} \right)^{\mathrm{H}} \boldsymbol{\Phi}^{\mathrm{v}} (\mathbf{H}_{\mathrm{BS-RIS}}^{\mathrm{hv}})^{\mathrm{H}} + (\mathbf{h}_{\mathrm{b},k}^{\mathrm{h}})^{\mathrm{H}} \boldsymbol{\Phi}^{\mathrm{vh}} (\mathbf{H}_{\mathrm{BS-RIS}}^{\mathrm{h}})^{\mathrm{H}} \right. $$

$$\left. + (\mathbf{h}_{\mathrm{b},k}^{\mathrm{vh}})^{\mathrm{H}} \boldsymbol{\Phi}^{\mathrm{hv}} (\mathbf{H}_{\mathrm{BS-RIS}}^{\mathrm{hv}})^{\mathrm{H}} + (\mathbf{h}_{\mathrm{b},k}^{\mathrm{h}})^{\mathrm{H}} \boldsymbol{\Phi}^{\mathrm{h}} (\mathbf{H}_{\mathrm{BS-RIS}}^{\mathrm{h}})^{\mathrm{H}} \right) \mathbf{p}_k^{\mathrm{h}} \mathbf{w} \right|^2 . \tag{A.7}$$

Substituting the SINRs with their upper bounds (A.6) and (A.7) in the objective function of (A.1), we obtain a lower bound on the said function. Combining the non-increasing and lower bounded characteristics of the objective function $\mathcal{J}(\mathbf{P}, \mathbf{V}, \mathbf{w})$, we can conclude that the iterative procedure of Algorithm 7.4 converges. As the procedure for updating η_{EE} is performed with bisection, which is a convergent method, the convergence of Algorithm 7.4 is guaranteed to local optimal solution. Assume that Algorithm 7.4 converges to the solution $\mathbf{Q}^* = \{\mathbf{P}^*, \mathbf{V}^*, \mathbf{w}^*\}$. By considering an arbitrary point $\mathbf{Q}$ at the neighboring of $\mathbf{Q}^*$ and with further manipulations, it is easy to show that Algorithm 7.4 converges to a stationary point (for further details please refer to [130]). Now, w.r.t. the convergence of the passive beamforming algorithm, i.e., Algorithm 7.3, the phase-shift values are obtained based on SDP, which is guaranteed to converge to a local optimal solution. Therefore, the proposed two-stage algorithm converges to a stationary point.

Appendix B

Meijer-G function

B.1 Definition of the MeijerG Function

The Meijer G-function is a very general function defined by

$$G_{p,q}^{n,m}\left(\begin{array}{c} a_m,...,a_p \\ b_n,...,b_q \end{array} \middle| z\right) = \frac{-1}{(2\pi j)} \int_{\mathcal{R}} \frac{\prod_{j=1}^{m} \Gamma\left(b_j - s\right) \prod_{j=1}^{n} \Gamma\left(1 - a_j + s\right)}{\prod_{j=n+1}^{p} \Gamma\left(a_j - s\right) \prod_{j=m+1}^{q} \Gamma\left(1 - b_j + s\right)} z^s \mathrm{d}s, \tag{B.1}$$

where $\Gamma(s)$ is the gamma function. The integral representation is called Mellin–Barnes representation, and may be viewed as an inverse Mellin transform.

The definition holds under the following assumptions:

- $0 \le m \le q$ and $0 \le n \le p$, where m, n, p and q are integer numbers

- $a_k - b_j \neq 1, 2, 3, \cdots$ for $k = 1, 2, \cdots, n$ and $j = 1, 2, \cdots, m$, which implies that no pole of any $\Gamma(b_j - s), j = 1, 2, \cdots, m$, coincides with any pole of any $\Gamma(1 - a_k + s), k = 1, 2, \cdots, n$

- $z \neq 0$.

The MeijerG can be reduced to simpler special functions (for more details [85, 131]).

B.2 Main Properties of the Meijer-G Function

B.2.1 Transformations and Argument Simplifications

Laplace Transform

$$\int_0^\infty \exp(-wx) x^{-\alpha} G_{p,q}^{n,m} \left(\begin{array}{c} \mathbf{a}_p \\ \mathbf{b}_q \end{array} \middle| \nu x \right) \mathrm{d}x = w^{\alpha-1} G_{p,q+1}^{n,m+1} \left(\begin{array}{c} \alpha, \mathbf{a}_p \\ \mathbf{b}_q \end{array} \middle| \frac{\nu}{w} \right),$$

(B.2)

where $\mathrm{Re}(w) > 0$.

Argument Simplifications

$$z^\alpha G_{p,q}^{n,m} \left(\begin{array}{c} \mathbf{a}_p \\ \mathbf{b}_q \end{array} \middle| z \right) = G_{p,q}^{n,m} \left(\begin{array}{c} \mathbf{a}_p + \alpha \\ \mathbf{b}_q + \alpha \end{array} \middle| z \right).$$

(B.3)

$$G_{p,q}^{n,m} \left(\begin{array}{c} \mathbf{a}_p \\ \mathbf{b}_q \end{array} \middle| z^{-1} \right) = G_{p,q}^{n,m} \left(\begin{array}{c} 1 - \mathbf{a}_p \\ 1 - \mathbf{b}_q \end{array} \middle| z \right).$$

(B.4)

B.2.2 Product, Differentiation and Integration

Product

$$G_{p_1,q_1}^{n_1,m_1} \left(\begin{array}{c} \mathbf{a}_{p_1} \\ \mathbf{b}_{q_1} \end{array} \middle| z \right) G_{p_2,q_2}^{n_2,m_2} \left(\begin{array}{c} \mathbf{a}_{p_2} \\ \mathbf{b}_{q_2} \end{array} \middle| w \right) = G_{0,0:p_1,q_1:p_2,q_2}^{0,0:n_1,m_1:n_2,m_2} \left(\begin{array}{c} \mathbf{a}_{p_1} \\ \mathbf{b}_{q_1} \end{array} \middle| \begin{array}{c} \mathbf{a}_{p_2} \\ \mathbf{b}_{q_2} \end{array} \middle| z, w \right).$$

(B.5)

Differentiation

$$\frac{\mathrm{d} G_{p,q}^{n,m} \left(\begin{array}{c} \mathbf{a}_p \\ \mathbf{b}_q \end{array} \middle| z \right)}{\mathrm{d}z} = G_{p+1,q+1}^{n,m+1} \left(\begin{array}{c} -1, \mathbf{a}_p - 1 \\ \mathbf{b}_q - 1 \end{array} \middle| z \right).$$

(B.6)

Integration

$$\int G_{p,q}^{n,m} \left(\begin{array}{c} \mathbf{a}_p \\ \mathbf{b}_q \end{array} \middle| z \right) \mathrm{d}z = G_{p+1,q+1}^{n,m+1} \left(\begin{array}{c} 1, \mathbf{a}_p + 1 \\ \mathbf{b}_n + 1, 0, b_{n+1} + 1, \cdots, b_q + 1 \end{array} \middle| z \right).$$

(B.7)

$$\int z^{\alpha-1} G_{p,q}^{n,m} \left(\begin{array}{c} \mathbf{a}_p \\ \mathbf{b}_q \end{array} \middle| z \right) \mathrm{d}z = G_{p+1,q+1}^{n,m+1} \left(\begin{array}{c} 1, \mathbf{a}_p + \alpha \\ \mathbf{b}_n + \alpha, 0, b_{n+1} + \alpha, \cdots, b_q + \alpha \end{array} \middle| z \right). \tag{B.8}$$

$$\int_0^\infty t^{\alpha-1} G_{p,q}^{n,m} \left(\begin{array}{c} \mathbf{a}_p \\ \mathbf{b}_q \end{array} \middle| tz \right) \mathrm{d}t = \frac{\prod_{k=1}^n \Gamma(\alpha + b_k) \prod_{k=1}^m \Gamma(1 - \alpha - a_k)}{\prod_{k=m+1}^p \Gamma(\alpha + a_k) \prod_{k=n+1}^q \Gamma(1 - \alpha - b_k)} z^{-\alpha}. \tag{B.9}$$

$$\int_0^\infty \tau^{\alpha-1} G_{p_1,q_1}^{n_1,m_1} \left(\begin{array}{c} \mathbf{c}_{p_1} \\ \mathbf{d}_{q_1} \end{array} \middle| \tau z \right) G_{p_2,q_2}^{n_2,m_2} \left(\begin{array}{c} \mathbf{a}_{p_2} \\ \mathbf{b}_{q_2} \end{array} \middle| \tau w \right) \mathrm{d}\tau =$$

$$w^{-\alpha} G_{q_1+p_2,p_1+q_2}^{m_1+n_2,m_2+n_1} \left(\begin{array}{c} \mathbf{a}_{m_2}, 1 - \alpha - \mathbf{d}_{q_1}, a_{m_1+1}, \cdots, a_{p_1} \\ \mathbf{b}_{n_2}, 1 - \alpha - \mathbf{c}_{p_1}, b_{n_2+1}, \cdots, b_{q_2} \end{array} \middle| \frac{z}{w} \right). \tag{B.10}$$

Appendix C

Distance Distributions

C.1 Proof of Theorem 3.1

We have $|A_0 A_1| = |A_0 A_2|$ and $\angle A_1 A_0 A_2 = 2\alpha$. According to the range of r, we have different cases to discuss.

Case 1: If $0 < r \leq h$, the CDF $F_r(r)$ is the area of a sector divided by the area $\triangle A_0 A_1 A_2$:

$$F_r(r) = \frac{\alpha r^2}{2\mathcal{A}}, \tag{C.1}$$

where $\alpha = \angle A_1 A_0 A_2$.

Case 2: If $h < r \leq |A_0 A_2|$, the CDF $F_r(r)$ will be the intersection area divided by $\mathcal{A}$. That is,

$$F_r(r) = \frac{1}{\mathcal{A}} \left(\beta r^2 + d_r h \right), \tag{C.2}$$

where d_r and β are related to r according to:

$$\beta = \angle H A_0 A_1 - \arccos \frac{h}{r}$$
$$d_r = \sqrt{r^2 - h^2}. \tag{C.3}$$

Case 3: If $r > |A_0 A_2|$, then the CDF is $F_r(r) = 1$.

CDF and PDF

The distance CDF is expressed as

$$F_r(r) = \begin{cases} 0, & r \leq 0 \\ \frac{1}{\mathcal{A}}\alpha r^2, & 0 < r \leq h \\ \frac{1}{\mathcal{A}}\left(\beta r^2 + d_r h\right), & h < r \leq |A_0 A_2| \\ 1, & r > |A_0 A_2|. \end{cases} \tag{C.4}$$

To obtain the PDF, we first calculate the derivative of $g(r) = \beta r^2 + d_r h$. The derivative is given by $g'(r) = 2\beta r + \beta' r^2 + d_r' h$, where $d_r' = \frac{r}{\sqrt{r^2 - h^2}}$ and $\beta' = \frac{-h}{r\sqrt{r^2 - h^2}}$. Therefore, the conditional PDF is expressed as

$$f(r \mid \alpha, \beta) = \begin{cases} \frac{2}{\mathcal{A}}\alpha r, & 0 < r \leq h \\ \frac{2}{\mathcal{A}}\beta r, & h < r \leq |A_0 A_2| \\ 0, & \text{otherwise.} \end{cases} \tag{C.5}$$

The joint PDF can be determined by applying the Bayes theorem, i.e., $f(r, \alpha, \beta) = f(r \mid \alpha, \beta) f_{\alpha,\beta}(\alpha, \beta)$. Therefore, we obtain

$$f(r, \alpha, \beta) = \begin{cases} \frac{4\alpha r}{3\pi \mathcal{A}} \sin\frac{\alpha}{2} \sin\frac{\beta}{2} \sin\frac{\alpha+\beta}{2}, & 0 < r \leq h \\ \frac{4\beta r}{3\pi \mathcal{A}} \sin\frac{\alpha}{2} \sin\frac{\beta}{2} \sin\frac{\alpha+\beta}{2}, & h < r \leq |A_0 A_2| \\ 0, & \text{otherwise.} \end{cases} \tag{C.6}$$

Finally, the PDF of r is obtained using $f_r(r) = \int_0^\pi \int_0^{2\pi-\alpha} f(r, \alpha, \beta) \mathrm{d}\alpha \mathrm{d}\beta$, and expressed as shown in (3.14).

C.2 Proof of Theorem 3.2

Without loss of generality, we assume that $|A_0 A_2| < |A_0 A_1|$. Here also, we have different cases to discuss according to the range of r.

Case 1: If $0 < r \leq h$, the CDF of the distance distribution is expressed as

$$F_r(r) = \frac{\alpha r^2}{2\mathcal{A}}, \tag{C.7}$$

where $\alpha = \angle A_1 A_0 A_2$.

Case 2: If $h < r \leq |A_0 A_2|$, the CDF is expressed as

$$F_r(r) = \frac{1}{\mathcal{A}} \left[\frac{\alpha r^2}{2} + \nu\left(\frac{1}{2}\left((\beta - \alpha) r^2 + d_r h\right)\right) \right], \tag{C.8}$$

where $\alpha = \angle A_2 A_0 A_1$, M is the intersection with the base $A_1 A_2$, $\beta = \angle M A_0 A_1$, $\beta - \alpha = \angle M A_0 A_2$, and $d_r = |HM|$ (cf. Fig. 3.3 (b)). Also, d_r and β are related to r as per

$$\beta = \angle H A_0 A_1 - \arccos \frac{h}{r}$$
$$d_r = \sqrt{r^2 - h^2}, \tag{C.9}$$

where ν is an indicator of the type of the triangle, i.e.,

$$\nu = \begin{cases} 2, & \text{Fig. 3.2 (a)}, \\ 0, & \text{Fig. 3.2 (b)}. \end{cases}$$

Case 3: When $|A_0 A_2| < r \le |A_0 A_1|$ (cf. Fig. 3.3 (c)), the CDF $F_r(r)$ is expressed as

$$F_r(r) = \frac{1}{2\mathcal{A}} \left(\beta r^2 + |M A_2| h \right), \tag{C.10}$$

where $|M A_2| = |A_1 A_2| - |A_1 M| = |A_1 A_2| - \left(\sqrt{|A_0 A_1|^2 - h^2} - d_r \right)$.

Case 4: If $r > |A_0 A_1|$ (cf. Fig. 3.3 (d)), then the CDF $F_r(r) = 1$.

CDF and PDF

In summary, the distance CDF is given by

$$F_r(r) = \begin{cases} 0, & r \le 0 \\ \frac{\alpha r^2}{2\mathcal{A}}, & 0 < r \le h \\ \frac{\alpha r^2 + \frac{\nu}{2} g(r)}{2\mathcal{A}}, & h < r \le |A_0 A_2| \\ \frac{\beta r^2 + |M A_2| h}{2\mathcal{A}}, & |A_0 A_2| < r \le |A_0 A_1| \\ 1, & r > |A_0 A_1| \end{cases} \tag{C.11}$$

To obtain the distance PDF, we first calculate the derivative of $g(r) = (\beta - \alpha) r^2 + d_r h$. The derivative is given by $g'(r) = \beta' r^2 + 2 (\beta - \alpha) r + d_r' h$, where $d_r' = \frac{r}{\sqrt{r^2 - h^2}}$, $\beta' = \frac{-h}{r\sqrt{r^2 - h^2}}$, and $|M A_2|' = \frac{r}{\sqrt{r^2 - h^2}}$. Consequently, the distance PDF is written as

$$f(r|\alpha, \beta) = \begin{cases} \frac{1}{\mathcal{A}} \alpha r, & 0 < r \le h \\ \frac{1}{\mathcal{A}} [\alpha + \eta(\beta - \alpha)] r, & h < r \le |A_0 A_2| \\ \frac{1}{\mathcal{A}} \beta r, & |A_0 A_2| < r \le |A_0 A_1| \\ 0, & \text{otherwise.} \end{cases} \tag{C.12}$$

Joint PDF

Parameter α is the angle between two edges of a triangle emanating from a nucleus; thus the density of α is defined as [132, Eq. (4.3.8)]

$$f_\alpha(\alpha) = \frac{4\sin\alpha}{3\pi}\left((\pi-\alpha)\cos\alpha + \sin\alpha\right), \ 0 < \alpha < \pi. \tag{C.13}$$

The PDF of β is expressed as

$$f_\beta(\beta) = \frac{2}{3\pi}\sin\frac{\beta}{2}\left[\left(\pi-\frac{\beta}{2}\right)\cos\frac{\beta}{2} + \sin\frac{\beta}{2}\right]. \tag{C.14}$$

Therefore, the joint PDF is expressed as

$$f_{\alpha,\beta}(\alpha,\beta) = \frac{2}{3\pi}\sin\frac{\alpha}{2}\sin\frac{\beta}{2}\sin\frac{\alpha+\beta}{2}, \tag{C.15}$$

with $0 \leq \beta < 2\pi - \alpha$. Here, the joint PDF can be determined as in Appendix **??**, yielding

$$f(r,\alpha,\beta) = \begin{cases} \frac{2\alpha r}{3\pi\mathcal{A}}\sin\frac{\alpha}{2}\sin\frac{\beta}{2}\sin\frac{\alpha+\beta}{2}, & 0 < r \leq h \\ \frac{2(\alpha+\nu(\beta-\alpha))r}{3\pi\mathcal{A}}\sin\frac{\alpha}{2}\sin\frac{\beta}{2}\sin\frac{\alpha+\beta}{2}, & h < r \leq e \\ \frac{2\beta r}{3\pi\mathcal{A}}\sin\frac{\alpha}{2}\sin\frac{\beta}{2}\sin\frac{\alpha+\beta}{2}, & e < r \leq d \\ 0, & \text{otherwise,} \end{cases} \tag{C.16}$$

where $e = |A_0 A_1|$ and $d = |A_0 A_2|$.

Finally, the PDF of r is obtained as shown in Eq. (3.16).

Appendix D

Implementation and Integrals Calculation

D.1 Implementation of the Extended Generalized Multivariate MeijerG Function

Algorithm D.6 is developed to obtain the numerical values of the EGMMGF defined in (D.1), with its inner function $F(x, y, z)$ explicitly defined in (D.2).

$$
G^{n_1,m_1:n_2,m_2:n_3,m_3:n_4,m_4}_{p_1,q_1:p_2,q_2:p_3,q_3:p_4,q_4} \left(\begin{array}{c|c|c|c} a_{m_1}, a_{p_1} & c_{m_2}, c_{p_2} & e_{m_3}, e_{p_3} & g_{m_4}, g_{p_4} \\ b_{n_1}, b_{q_1} & d_{n_2}, d_{q_2} & f_{n_3}, f_{p_3} & h_{n_4}, h_{q_4} \end{array} \middle| x, y, z \right)
$$

$$
= \frac{-1}{(2\pi j)^3} \int\limits_{c_s-jW}^{c_s+jW} \int\limits_{c_t-jW}^{c_t+jW} \int\limits_{c_r-jW}^{c_r+jW} F(x, y, z) \mathrm{d}x \mathrm{d}y \mathrm{d}z. \tag{D.1}
$$

$F(x, y, z) =$

$$
\frac{\Gamma(r_l + 1 - a_{m_1})\Gamma(b_{n_1} - r_l)\Gamma(r_l + 1 - c_{m_2})\Gamma(d_{n_2} - r_l)\Gamma(r_l + 1 - e_{m_3})\Gamma(f_{n_3} - r_l)}{\Gamma(a_{p_1} - r_l)\Gamma(1 - b_{q_1} + r_l)\Gamma(c_{p_2} - r_l)\Gamma(1 - d_{q_2} + r_l)\Gamma(e_{p_3} - r_l)\Gamma(1 - f_{q_3} + r_l)}
$$

$$
\times \frac{\Gamma(r_l + 1 - g_{m_4})\Gamma(h_{n_4} - r_l)}{\Gamma(g_{p_4} - r_l)\Gamma(1 - h_{q_4} + r_l)} x^{r_l} y^{r_l} z^{r_l}. \tag{D.2}
$$

Algorithm D.6 Numerical Evaluation of EGMMGF.

Require: c_s, a_{m_1}, a_{p_1}, b_{n_1}, b_{q_1}, c_{m_2}, c_{p_2}, d_{n_2}, d_{q_2}, e_{m_3}, e_{p_3}, f_{n_3}, f_{q_3}, g_{m_4}, h_{n_4}, g_{p_4}, h_{q_4}, x, y, z.

  1: Calculate the inner function $F(x, y, z)$ using (D.2);

  2: Set $Q_s = \min(d_{n_2}, d_{q_2})$, $U_s = -\max(1 - c_{m_2}, 1 - c_{p_2})$;

  3: Set $c_s = \frac{Q_s + U_s}{4}$;

  4: Set $Q_t = \min(f_{n_3}, f_{q_3})$, $U_t = \max(-a_{m_1} - c_s, e_{m_3} - 1)$;

  5: Set $c_t = Q_t - \frac{Q_t - U_t}{20}$;

  6: Set $Q_r = \min(h_{n_4}, h_{q_4})$, $U_r = \max(-a_{m_1} - c_s - c_t, g_{m_4} - 1)$;

  7: Set $c_r = Q_r - \frac{Q_r - U_r}{20}$.

  8: Set $W = 1$.

  9: Calculate
$$out = \frac{-1}{(2\pi j)^3} \int_{c_s - jW}^{c_s + jW} \int_{c_t - jW}^{c_t + jW} \int_{c_r - jW}^{c_r + jW} F(x, y, z)\mathrm{d}x\mathrm{d}y\mathrm{d}z.$$

Ensure: The EGMMGF value out

D.2 Integrals Calculation

To use (3.29), we need to determine the integrals I_2, I_3, I_4 and I_5, explicitly. To this end, the exponential is rewritten in the form of MeijerG function as $G_{0,1}^{1,0}\left(\begin{matrix} 0 \\ - \end{matrix} \middle| jsx\right)$, and the Mellin-Barnes contours integral form of the MeijerG function is explored. First, we have

$$
I_2 = \int_{-\infty}^{+\infty} (js)^{-3} G_{3,3}^{2,2}\left(\begin{matrix} 1, \frac{3}{2} + m, 1 \\ 1, \frac{3}{2}, m - 1 \end{matrix} \middle| \frac{js\eta P_{\mathrm{t}}\Omega}{e^4 m}\right)^3 \exp(-jsx)\mathrm{d}s
$$

$$
= \frac{1}{(2\pi j)^4} \int_{\mathcal{R}_1} \int_{\mathcal{R}_2} \int_{\mathcal{R}_3} \int_{\mathcal{R}_4} \prod_{i=1}^{3} \frac{\Gamma(r_i + \frac{3}{2})\Gamma(-r_i)\Gamma(\frac{-1}{2} - m - r_i)}{\Gamma(2 - m - r_i)}
$$

$$
\times \Gamma(1 - r_4) \int_{-\infty}^{+\infty} (js)^{-3} \left(\frac{js\eta P_{\mathrm{t}}\Omega}{e^4 m}\right)^{-r_i} (-jsx)^{-r_4} \mathrm{d}s\mathrm{d}r_1\mathrm{d}r_2\mathrm{d}r_3\mathrm{d}r_4
$$

$$
= x^2 G_{1,0:3,3:3,3:3,3}^{0,1:2,2:2,2:2,2}\left(\begin{matrix} 3 \\ - \end{matrix} \middle| \begin{matrix} \mathbf{b}_5 \\ \mathbf{b}_6 \end{matrix} \middle| \begin{matrix} \mathbf{b}_5 \\ \mathbf{b}_6 \end{matrix} \middle| \begin{matrix} \mathbf{b}_5 \\ \mathbf{b}_6 \end{matrix} \middle| \frac{-\gamma_1}{x}, \frac{-\gamma_1}{x}, \frac{-\gamma_1}{x}\right), \tag{D.3}
$$

where $\gamma_1 = \frac{\eta P_{\mathrm{t}}\Omega}{e^4 m}$, $\mathbf{b}_5 = [1, \frac{3}{2} + m, 1]$ and $\mathbf{b}_6 = [1, \frac{3}{2}, m - 1]$.

The integral I_3 is evaluated as

$$
I_3 = \int_{-\infty}^{+\infty} (js)^{-3} G_{3,3}^{2,2} \left(\begin{matrix} 1, \frac{3}{2}+m, 1 \\ 1, \frac{3}{2}, m-1 \end{matrix} \,\middle|\, \frac{js\eta P_t \Omega}{e^4 m} \right)^2 G_{3,3}^{2,2} \left(\begin{matrix} 1, \frac{3}{2}+m, 1 \\ 1, \frac{3}{2}, m-1 \end{matrix} \,\middle|\, \frac{js\eta P_t \Omega}{c^4 m} \right) \exp(-jsx) \mathrm{d}s
$$

$$
= \frac{1}{(2\pi j)^4} \int_{\mathcal{R}_1} \int_{\mathcal{R}_2} \int_{\mathcal{R}_3} \int_{\mathcal{R}_4} \prod_{i=1}^{3} \frac{\Gamma(r_i + \frac{3}{2})\Gamma(-r_i)\Gamma(\frac{-1}{2} - m - r_i)}{\Gamma(2 - m - r_i)}
$$

$$
\times \Gamma(1 - r_4) \int_{-\infty}^{+\infty} (js)^{-3} \prod_{i=1}^{2} \left(\frac{js\eta P_t \Omega}{e^4 m} \right)^{-r_i} \left(\frac{js\eta P_t \Omega}{c^4 m} \right)^{-r_3} (-jsx)^{-r_4} \, \mathrm{d}s\mathrm{d}r_1\mathrm{d}r_2\mathrm{d}r_3\mathrm{d}r_4
$$

$$
= x^2 G_{1,0:3,3:3,3:3,3}^{0,1:2,2:2,2:2,2} \left(\begin{matrix} 3 \\ - \end{matrix} \,\middle|\, \begin{matrix} \mathbf{b}_5 \\ \mathbf{b}_6 \end{matrix} \,\middle|\, \begin{matrix} \mathbf{b}_5 \\ \mathbf{b}_6 \end{matrix} \,\middle|\, \begin{matrix} \mathbf{b}_5 \\ \mathbf{b}_6 \end{matrix} \,\middle|\, \frac{-\gamma_1}{x}, \frac{-\gamma_1}{x}, \frac{-\gamma}{x} \right). \tag{D.4}
$$

where $\gamma = \frac{\eta P_t \Omega}{c^4 m}$.

The integral I_4 is obtained as follows

$$
I_4 = \int_{-\infty}^{+\infty} (js)^{-3} G_{3,3}^{2,2} \left(\begin{matrix} 1, \frac{3}{2}+m, 1 \\ 1, \frac{3}{2}, m-1 \end{matrix} \,\middle|\, \frac{js\eta P_t \Omega}{c^4 m} \right)^2 G_{3,3}^{2,2} \left(\begin{matrix} 1, \frac{3}{2}+m, 1 \\ 1, \frac{3}{2}, m-1 \end{matrix} \,\middle|\, \frac{js\eta P_t \Omega}{e^4 m} \right) \exp(-jsx) \mathrm{d}s
$$

$$
= \frac{1}{(2\pi j)^4} \int_{\mathcal{R}_1} \int_{\mathcal{R}_2} \int_{\mathcal{R}_3} \int_{\mathcal{R}_4} \prod_{i=1}^{3} \frac{\Gamma(r_i + \frac{3}{2})\Gamma(-r_i)\Gamma(\frac{-1}{2} - m - r_i)}{\Gamma(2 - m - r_i)}
$$

$$
\times \Gamma(1 - r_4) \int_{-\infty}^{+\infty} (js)^{-3} \prod_{i=1}^{2} \left(\frac{js\eta P_t \Omega}{c^4 m} \right)^{-r_i} \left(\frac{js\eta P_t \Omega}{e^4 m} \right)^{-r_3} (-jsx)^{-r_4} \, \mathrm{d}s\mathrm{d}r_1\mathrm{d}r_2\mathrm{d}r_3\mathrm{d}r_4
$$

$$
= x^2 G_{1,0:3,3:3,3:3,3}^{0,1:2,2:2,2:2,2} \left(\begin{matrix} 3 \\ - \end{matrix} \,\middle|\, \begin{matrix} \mathbf{b}_5 \\ \mathbf{b}_6 \end{matrix} \,\middle|\, \begin{matrix} \mathbf{b}_5 \\ \mathbf{b}_6 \end{matrix} \,\middle|\, \begin{matrix} \mathbf{b}_5 \\ \mathbf{b}_6 \end{matrix} \,\middle|\, \frac{-\gamma_1}{x}, \frac{-\gamma}{x}, \frac{-\gamma}{x} \right). \tag{D.5}
$$

Finally, I_5 is obtained as

$$
I_5 = \int_{-\infty}^{+\infty} (js)^{-3} G_{3,3}^{2,2} \left(\begin{matrix} 1, \frac{3}{2}+m, 1 \\ 1, \frac{3}{2}, m-1 \end{matrix} \,\middle|\, \frac{js\eta P_t \Omega}{c^4 m} \right)^3 \exp(-jsx) \mathrm{d}s
$$

$$
= \frac{1}{(2\pi j)^4} \int_{\mathcal{R}_1} \int_{\mathcal{R}_2} \int_{\mathcal{R}_3} \int_{\mathcal{R}_4} \prod_{i=1}^{3} \frac{\Gamma(r_i + \frac{3}{2})\Gamma(-r_i)\Gamma(\frac{-1}{2} - m - r_i)}{\Gamma(2 - m - r_i)}
$$

$$
\times \Gamma(1 - r_4) \int_{-\infty}^{+\infty} (js)^{-3} \left(\frac{js\eta P_t \Omega}{c^4 m} \right)^{-r_i} (-jsx)^{-r_4} \mathrm{d}s\mathrm{d}r_1\mathrm{d}r_2\mathrm{d}r_3\mathrm{d}r_4
$$

$$
= x^2 G_{1,0:3,3:3,3:3,3}^{0,1:2,2:2,2:2,2} \left(\begin{matrix} 3 \\ - \end{matrix} \,\middle|\, \begin{matrix} \mathbf{b}_5 \\ \mathbf{b}_6 \end{matrix} \,\middle|\, \begin{matrix} \mathbf{b}_5 \\ \mathbf{b}_6 \end{matrix} \,\middle|\, \begin{matrix} \mathbf{b}_5 \\ \mathbf{b}_6 \end{matrix} \,\middle|\, \frac{-\gamma}{x}, \frac{-\gamma}{x}, \frac{-\gamma}{x} \right). \tag{D.6}
$$